The 6th International Workshop on Microcavities and Their Applications

7-10 February, 2022
The Hong Kong University of Science and Technology,
Clear Water Bay, Hong Kong, China

Introduction

About WOMA2022:

The 6th WOMA will be held on the HKUST campus during the 7th -10th February 2022 in hybrid mode (in person and virtual). Scholars around the world of the optical microcavity community will share and discuss their latest work and insights in this rapidly expanding field. The four-day Workshop will include invited talks, contributed talks, student poster presentations and social activities (subject to the pandemic situation) in Hong Kong. Three Best Student Paper Awards will be awarded.

Topics:

The WOMA2022 will cover cutting-edge research topics relating to optical microcavity fundamentals and applications. Topics of interest include but are not limited to the following:

- Whispering-gallery-mode (WGM) resonators,
- High-Q cavity optics,
- Chip-integrated resonators,
- Crystalline WGM resonators,
- Optical microcavities in new materials,
- Deformed or chaotic microcavities,
- Ray dynamics and wave chaos in cavities,
- WGM resonator-based sensors,
- Machine learning applied to optical microcavities,
- Optical manipulation using microcavities,
- Microcavity lasers,
- Nonlinear optics in WGM resonators,
- Soliton phenomena in cavities,
- Kerr frequency microcombs,
- Atom-field interactions in microcavities,
- Quantum optics in microcavities.

Introduction

The organizers:

Prof. Andrew Poon
The Hong Kong University of Science and Technology
Hong Kong, China

Prof. Frank Vollmer
University of Exeter
Exeter, United Kingdom

Prof. Takahisa Harayama
Waseda University
Tokyo, Japan

Registration:
http://woma.ust.hk/Register.html

Webinar:
https://hkust.zoom.us/j/93267707356?pwd=VDRndzhEN2tUWCtlVjkwQ0lSblJkUT09

Program of Invited and Contributed Talks

WOMA2022 Program

17 January 2022 ~ 27 January 2022

Poster submissions (in pdf) to Organizers by email to woma2022@ust.hk.

Monday, 7 February 2022

8:00 – 8:10	Welcome by Organizers
	Session I: (Chair: Andrew Poon, The Hong Kong University of Science and Technology)
8:10 – 8:50 (invited)	Kerry Vahala California Institute of Technology **Earth-rate-sensitivity WGM Laser-Gyroscope**
8:50 – 9:30 (invited)	Marko Lončar Harvard University **Integrated Lithium Niobate Photonics and Applications**
9:30 – 10:00	Workshop photo (Zoom screen capture)/Break
	Session II: (Chair: Takahisa Harayama, Waseda University)
10:00 – 10:40 (invited)	Kartik Srinivasan National Institute of Standards and Technology **Connecting widely separated wavelength bands using chip-integrated nonlinear microresonators**
10:40 – 11:20 (invited)	Takasumi Tanabe Keio University **Ultrahigh-Q crystalline whispering gallery mode microcavity fabricated with mechanical machining**
11:20 – 12:00 (Invited)	Keiji Sasaki Hokkaido University **Multipolar lattice resonances in plasmonic crystal cavity**
12:00 – 14:00	Lunch
	Session III: (Chair: Kyungwon An, Seoul National University)
14:00 – 14:40 (invited)	Chil-Min Kim Daegu Gyeongbuk Institute of Science and Technology (DGIST) **Hybridization of Second Order Exceptional Point**
14:40 – 15:20 (invited)	Qinghai Song Harbin Institute of Technology (Shenzhen) **Lead halide perovskite based microlasers at the bounded states**
15:20 – 16:00 (invited)	Wenjie Wan University of Michigan-Shanghai Jiao Tong University Joint Institute **Non-Hermitian optics in a single nonlinear microcavity**
16:00 – 16:20	Fangxing Zhang

(contributed)	University of Michigan-Shanghai Jiao Tong University Joint Institute **Synthetic parity-time symmetry breaking in a single microcavity**
16:20 – 16:40	Break
	Session IV: (Chair: Frank Vollmer, University of Exeter)
16:40 – 17:20 (invited)	Tobias J. Kippenberg Ecole Polytechnique Fédérale de Lausanne (EPFL) **Soliton microcombs**
17:20 – 18:00 (invited)	Martina Hentschel University of Technology Chemnitz **Mesoscopic optics in complex microcavity systems**
18:00 – 18:40 (invited)	Síle Nic Chormaic Okinawa Institute of Science and Technology **Engineering whispering gallery resonators for nonlinear optics, photonics, and sensing applications**
18:40 – 19:00 (contributed)	Julius Kullig Otto-von-Guericke-Universität Magdeburg **Microcavities based on transmission at Brewster's angle**
19:00 – 19:20 (contributed)	Hsin-Yu Wu University of Exeter **Enhanced Chiroptical Signals through Coherent Perfect Absorption in a Parity-Time Symmetric System**

Program

Tuesday, 8 February 2022

	Session V: (Chair: Kerry Vahala, California Institute of Technology)
8:00 – 8:40 (invited)	Hui Cao Yale University **Tailoring microcavity lasers for parallel ultrafast random bit generation**
8:40 – 9:20 (invited)	Harald G. L. Schwefel University of Otago **Nonlinear crystalline WGM resonators – Quantum information & telecommunication**
9:20 – 10:00 (invited/IAS Distinguished Lecture)	A. Douglas Stone Yale University **Theory of Reflectionless Scattering Modes**
10:00 – 10:20 (contributed)	You Mengyu Waseda University **Universal single-mode lasing in fully-chaotic microcavity lasers**

10:20 – 10:40	Break
	Session VI: Student Poster Presentations (Chair: Andrew Poon, The Hong Kong University of Science and Technology)
10:40 – 12:00	WOMA website with interactive chat-box messaging
12:00	Lunch
	Session VII: (Chair: Takasumi Tanabe, Keio University)
14:00 – 14:40 (invited)	Toshihiko Baba Yokohama National University **Iontronic bio-chemical sensing using photonic crystal nanolasers**
14:40 – 15:20 (invited)	Yong-Zhen Huang Institute of Semiconductors, Chinese Academy of Sciences **Chaos microcavity lasers for random number generation due to internal mode injection**
15:20 – 16:00 (invited)	Jan Wiersig Otto-von-Guericke-Universität Magdeburg **Exceptional points in optical microdisk cavities**
16:00 – 16:20	Break
	Session VIII: (Chair: Martina Hentschel, University of Applied Sciences Chemnitz)
16:20 – 17:00 (invited)	Henning Schomerus University of Lancaster **Nonreciprocal response and transport theory of non-Hermitian materials**
17:00 – 17:40 (invited)	Roland Ketzmerick Technische Universität Dresden **Multifractal structure of chaotic resonance modes**
17:40 – 18:20 (invited)	Arno Rauschenbeutel Humboldt-Universitat Zu Berlin **Observation of Collective Superstrong Coupling of Cold Atoms to a 30-m Long Optical "Microresonator"**
18:20 – 18:40 (contributed)	Jolly Xavier University of Exeter **Advanced optoplasmonic single molecule sensing with tailored plasmonic particles**
18:40 – 19:00 (contributed)	Stefan Bittner Yale University **Spatio-temporal dynamics of wave-chaotic microlasers**
19:00 – 19:20 (contributed)	Manuel Crespo-Ballesteros Aston University **Optical Frequency Combs Generated via Parametric Acoustic Excitation of a SNAP Microresonator**

Program

Wednesday, 9 February 2022

	Session IX: (Chair: Hui Cao, Yale University)
8:00 – 8:40 (invited)	Lan Yang Washington University in St. Louis **Whispering-gallery-mode resonators: a versatile platform for fundamental science and applications**
8:40 – 9:20 (invited)	Warwick Bowen University of Queensland **Towards room temperature quantum control of cavity optomechanical devices**
9:20 – 10:00 (invited)	Sahin K. Ozdemir The Pennsylvania State University **Chiral perfect absorption on exceptional surfaces**
10:00 – 10:40	Break
	Session X: (Chair: Harold G. Schwefel, University of Otago)
10:40 – 11:20 (invited)	Howard Lee University of California, Irvine **Epsilon-near-zero resonances in planar and optical fiber platforms**
11:20 – 12:00 (invited)	Kyungwon An Seoul National University **Superradiance, superabsorption and a quantum engine**
12:00 – 14:00	Lunch
	Session XI: (Chair: Wenjie Wan, University of Michigan-Shanghai Jiao Tong University Joint Institute)
14:00 – 14:40 (invited)	Chunhua Dong University of Science and Technology of China **Non-reciprocity in the high Q microresonators**
14:40 – 15:20 (invited)	Yunfeng Xiao Peking University **Microcavity-enhanced surface nonlinear optics**
15:20 – 16:00 (invited)	Satoshi Sunada Kanazawa University **Scalable neuro-inspired photonic computing on a silicon chip**
16:00 – 16:20	Break
	Session XII: (Chair: Jan Wiersig, Otto-von-Guericke-Universität Magdeburg)
16:20 – 17:00 (invited)	Oliver G. Schmidt Chemnitz University of Technology **Microtube microcavities for on-chip integration**
17:00 – 17:40 (invited)	Misha Sumetsky Aston University

	Recent progress in the development and applications of SNAP technology
17:40 – 18:20 (invited)	Ingo Breunig University of Freiburg **Frequency conversion in microcavities made of non-centrosymmetric crystals**
18:20 – 19:00 (invited)	Melanie Lebental ENS-Paris **Möbius Strip Microlasers & Non-Euclidean Photonics**

Program

Thursday, 10 February 2022

	Session XIII: (Chair: Takahisa Harayama, Waseda University)
8:00 – 8:40 (invited)	Muhan Choi Kyungpook National University **Applications of GRIN microcavities based on transformation optics**
8:40 – 9:00 (contributed)	Qi-Tao Cao Peking University **Stimulated Scattering in Supermode Microcavities: Single- or Dual-mode Lasing?**
9:00 – 9:20 (contributed)	Hyundong Kim Daegu Gyeongbuk Institute of Science and Technology (DGIST) **The characteristics of exceptional points in asymmetric ellipse microdisks**
9:20 – 9:40 (contributed)	Beibei Li Institute of Physics, Chinese Academy of Sciences **Precision magnetic field sensing with a cavity optomechanical system**
9:40 – 10:00	Break
10:00 – 10:20	**Presentation of Best Poster Awards / Closing Remarks by Organizers / Introducing WOMA 2024**

Program of Posters

WOMA2022 Poster Program

Poster submissions (in pdf) to Organizers by email to woma2022@ust.hk.

8 February 2022, 10:40 – 12:00

P1	Shiqi Ai City University of Hong Kong **Dispersion and Nonlinearity Engineering for Hybrid Waveguide Comprised of Chalcogenide and Silicon Oxynitride**
P2	Xuanqi Chen The Hong Kong University of Science and Technology **BOSIM: Holistic Optical Switch Integration Model**
P3	Wai Lok Ho City University of Hong Kong **Manipulating and Trapping of Micro-Particles on Microring Resonators**
P4	Ming Jin Peking University **Highly Sensitive Detection with Heterodyne Waveguide Interferometry**
P5	Jinuk Kim Seoul National University **Lab-on-a-chip based Pneumatically Deformable Microfluidic Laser**
P6	Juman Kim Seoul National University **Unilluminable Room Problem and Wave Chaos in an Acoustic Penrose-cavity**
P7	Ching-Chi KWAN The Hong Kong University of Science and Technology **Dye-Doped Polymer-Coated Silicon Oxynitride Microresonator Lasers for Sensing**
P8	C.Lafargue Ecole Normale Supérieure de Paris-Saclay **Three-dimensional Microlasers: the Square Pyramid and Beyond**
P9	Yong-Hoon Lee Kyungpook National University **Active 3D FDTD Simulation in Limaçon Transformation Cavity**
P10	Seungwoo Lee Daegu Gyeongbuk Institute of Science and Technology **Chirality in an Asymmetric Microcavity**
P11	Jiayang Li The Hong Kong University of Science and Technology **Second-order Nonlinear and Quantum Photonics based on Integrated 3C-SiC-on-insulator Platform**

P12	Qiuli Li Ningbo University **Systematic Z-scan Measurements of the Third Order Nonlinearity of Chalcogenide Glasses**
P13	Xiaoting Li City University of Hong Kong **Efficiency-stable and Ultra-narrow Bandwidth-tunable Add-drop Filter Based on Quasicritical Coupling between Tapered Fiber and Microsphere**
P14	Yuhua Li City University of Hong Kong **High-harmonics Generation in Highly-doped Silica Microring Resonator**
P15	Liying Lin The Hong Kong University of Science and Technology **1.6 μm Continuous-wave Lasing from InAs AlGaInAs Quantum Dash Microdisk Lasers Grown on (001) Silicon**
P16	Shijie Liu Shanghai Jiao Tong University **Effective Four-wave Mixing in the Lithium Niobate on Insulator Microdisk by Cascading Quadratic Processes**
P17	Gabriele Maron Humboldt Universität zu Berlin **Trapping a single atom in the evanescent field of a WGM-microresonator**
P18	Songky Moon Seoul National University **Rainbow Refractometry for Deformed Microjets: Boundary Profiling and Chromatic Dispersion Measurement**
P19	Rui Niu University of Science and Technology of China **Repetition Rate Tuning of Soliton in Microrod Resonators**
P20	Yue Niu The Hong Kong University of Science and Technology **Field Programmable IIIV-on-Si Microresonator Switch Array**
P21	Zhongdi Peng University of Science and Technology of China **Gas Sensing through Thermal Effect in the High-Q Microbubble Resonators**
P22	Kalani Perera University of Exeter **Whispering Gallery Mode sensor for the Detection and Characterization of Organophosphorus Agro-chemical at Ultra- lower Concentrations**
P23	Tom Rodemund University of Applied Sciences Chemnitz **Coupling in Optical Microcavities**
P24	Lukas Seemann University of Applied Sciences Chemnitz **Optical Microcavities with Sources**
P25	Zhifei Wang

	The Hong Kong University of Science and Technology **FODON: Ultra-High-Radix Low-Loss Optical Switch Fabric**
P26	Kaiyi Wu The Hong Kong University of Science and Technology **Si_3N_4 Microring Resonators Toward Quantum Light Sources**
P27	Tan Bo Xue The Hong Kong University of Science and Technology **Second-order Nonlinear Frequency Conversion in AlGaAs-on-insulator Microcavities**
P28	Xiongshuo Yan Shanghai Jiao Tong University **Second Harmonic Generation in a Lithium Tantalate Microdisk Resonator**
P29	Donghai Zhang City University of Hong Kong **Plasmonic-cavity Integrated Graphene Photodetector**
P30	Qianni Zhang The Hong Kong University of Science and Technology **Photon Pairs and Heralded Single Photon Generation from Silicon-nitride Whispering-gallery-mode Microring Resonators**
P31	Zunyue Zhang The Chinese University of Hong Kong **High Resolution Silicon Nitride Spectrometer by Integrating Micro-rings and Arrayed Waveguide Gratings in Tandem**
P32	Yaojing Zhang The Chinese University of Hong Kong **Cavity Enhancement of Four-wave Mixing in a Silicon Racetrack Resonator**

Abstracts of Invited and Contributed Talks (in program order)

Earth-rate-sensitivity WGM Laser-Gyroscope

KERRY VAHALA[1*], YU-HUNG LAI[1], YU-KUN LU[2], MYOUNG-GYUN SUH[1]

[1]*Laboratory of Applied Physics, California Institute of Technology, Pasadena, California, 91125, USA*
[2] *School of Physics, Peking University, Beijing 100871, People's Republic of China*
[*]*vahala@caltech.edu*

Abstract: A chip-based gyroscope is described with sensitivity sufficient to measure the Earth's rotation. The device also features dissipative backscatter coupling that is used to study the gyro performance near an exceptional point.

1. Introduction

Counter-propagating lightwaves within a closed rotating loop experience different round-trip propagation times as a result of the Sagnac effect. Modern optical gyroscopes enhance this difference using long coiled optical fiber paths or by recirculation using active resonators. With the advent of the integrated photonics, there has been interest in creation of chip-based optical gyroscopes. Recent demonstrations using ultra-high-Q whispering-gallery-mode (WGM) resonators have provided encouraging results [1,2]. Here, a chip-based WGM laser gyroscope is described. Its sensitivity is high enough to measure the Earth's rotation. Moreover, there has been recent interest in parity time symmetric systems and exceptional-point (EP) enhancement of sensing systems [3,4] including gyroscopes [5]. The device features dissipative backscatter coupling of clockwise and counter-clockwise modes that allows investigation of gyroscope performance near an exceptional point.

2. Experiment

The gyroscope is demonstrated using offset counter-pumped stimulated Brillouin lasers (SBLs) in a 36 mm diameter ultra-high-Q silica disk resonator (Fig. 1a). By pumping the resonator from both directions, the Brillouin phase matching condition allows generation of counter-propagating SBLs within the same cavity mode (Fig.1b). We first tested the performance of the gyroscope by applying an external sinusoidal rotation. The gyroscope achieves a rotation amplitude sensitivity as low as 5°/h. As an additional test, the Earth's rotation was measured by switching the gyroscope axis between North and South directions. As a control test, the gyroscope axis was also switched between East and West directions (i.e., zero Earth rotation). This is the first time that the Earth's rotation has been measured using a chip-based optical gyroscope. Gyroscope scale factor enhancement by operation near the EP is also verified.

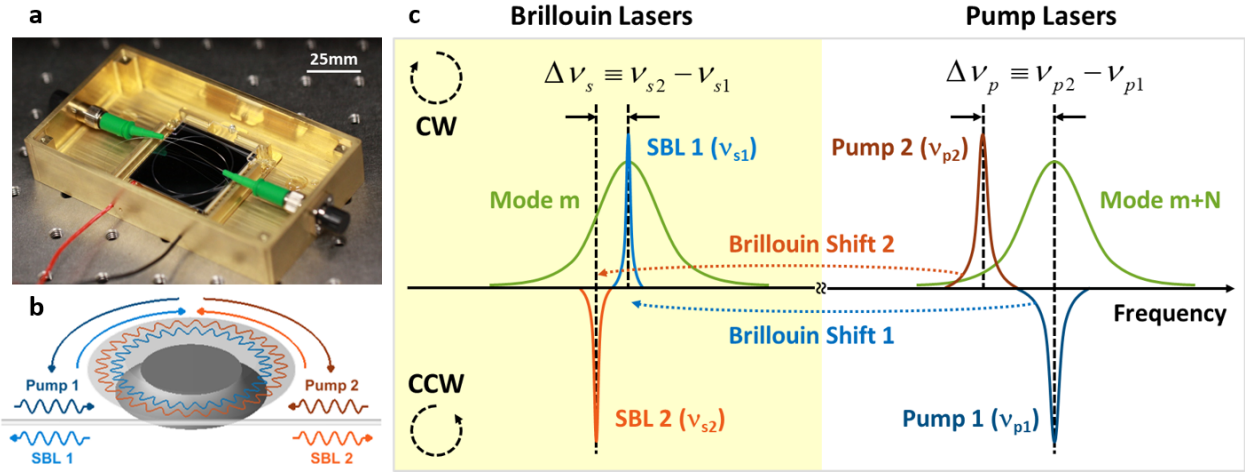

Fig. 1. **a)** Photograph of a packaged 36 mm-diameter silica resonator coupled with a fiber-connector pigtail. **b)** The circulation directions of the pumps and their corresponding SBLs. **c)** Spectral diagram of offset counter-pumping. The non-zero pump-detuning ($\Delta\nu_p$) unlocks the gyro readout ($\Delta\nu_s$) through Brillouin gain induced dispersion.

References

[1] Li, Suh and Vahala, "Microresonator Brillouin gyroscope," *Optica* **4**, 346 (2017)
[2] Liang, Ilchenko, Savchenkov, Dale, Eliyahu, Matsko and Maleki, "Resonant microphotonic gyroscope," *Optica* **4**, 114 (2017)
[3] Wiersig, "Sensors operating at exceptional points: General theory," *Phys. Rev. A* **93**, 033809 (2016).
[4] Chen, Ozdemir, Zhao, Wiersig, & Yang, "Exceptional points enhance sensing in an optical microcavity," *Nature* **548**, 192 (2017).
[5] Ren, et al. "Ultrasensitive micro-scale parity-time- symmetric ring laser gyroscope," *Opt. Lett.* **42**, 1556 (2017).

Integrated Lithium Niobate Photonics and Applications

Marko Lončar
John A. Paulson School of Engineering and Applied Sciences, Harvard University,
Cambridge, Massachusetts 02138, USA
loncar@seas.harvard.edu

Lithium niobate (LN) is an "old" material with many applications in optical and microwave technologies, owing to its unique properties that include large second order nonlinear susceptibility, large piezoelectric response, and wide optical transparency window. Conventional LN components, including modulators and frequency converters, have been the workhorse of the optoelectronic industry. They are reaching their limits, however, as they rely on weakly guiding ion-diffusion defined optical waveguides in bulk LN crystal.

I will discuss our work on an integrated LN platform, featuring sub-wavelength scale light confinement and dense integration of optical and electrical components, that has the potential to revolutionize optical communication networks and microwave photonic systems, as well as enable realization of quantum photonic circuits. Good example is integrated LN electro-optic (EO) modulator that supports data rates > 200 Gbps and that can be driven directly by a CMOS circuit [1], as well as an EO frequency comb [2] that leverages ultra-high Q optical cavities (Q ~ 10,000,000) operating both in telecom [3] and visible [4] wavelength range. Kerr frequency combs [5], super-continuum generation [6], and second harmonic generation in integrated periodically poled LN waveguides [7] will be discussed. Finally, programmable photonic molecule [8] and its application in microwave-to-optical conversion will be presented.

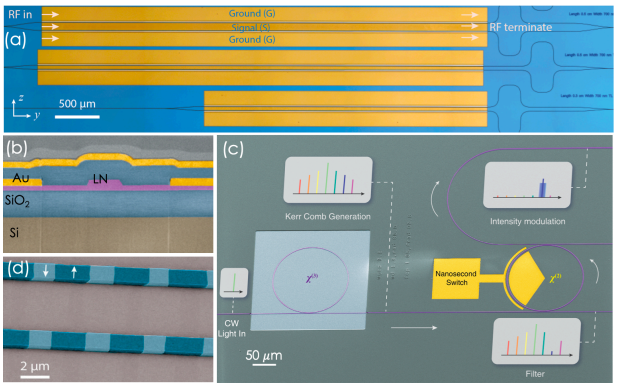

Integrated lithium niobate photonics. (a) EO modulator featuring low half-wave voltage ~ 1V, and bandwidth > 100 GHz. **(b)** Cross-section of EO frequency comb. **(c)** Kerr frequency comb integrated with tunable channel drop filters. **(d)** PPLN waveguide.

1. C. Wang, M. Zhang, X. Chen, M. Bertrand, A. Shams-Ansari, S. Chandrasekhar, P. Winzer, and M. Lončar. "Integrated lithium niobate electro-optic modulators operating at CMOS-compatible voltages." *Nature*, **562**, 101 (2018)
2. M. Zhang, B. Buscaino, C. Wang, A. Shams-Ansari, C. Reimer, R. Zhu, J. Kahn, and M. Lončar. "Broadband electro-optic frequency comb generation in an integrated microring resonator" *Nature*, **568**, 373 (2019)
3. M. Zhang, C. Wang, R. Cheng, A. Shams-Ansari, and M. Lončar, "Monolithic Ultrahigh-Q Lithium Niobate Microring Resonator." *Optica,* **4**, 1536 (2017).
4. B. Desiatov, A. Shams-Ansari, M. Zhang, C. Wang, M. Lončar, "Ultra-low-loss integrated visible photonics using thin-film lithium niobate", *Optica*, **6** 380 (2019)
5. C. Wang, M. Zhang, R. Zhu, H. Hu, and M. Lončar. "Monolithic lithium niobate photonic circuits for Kerr frequency comb generation, filtering and modulation." *Nature Communications*, **10**, 978 (2019)
6. M. Yu, B. Desiatov, Y. Okawachi, A. L. Gaeta, M. Loncar, "Coherent two-octave-spanning supercontinuum generation in lithium-niobate waveguides", *Optics Letters*, **44**, 1222 (2019)
7. C. Wang, C. Langrock, A. Marandi, M. Jankowski, M. Zhang, B. Desiatov, M. M. Fejer, and M. Lončar. "Ultrahigh-efficiency wavelength conversion in nanophotonic periodically poled lithium niobate waveguides." *Optica*, **5**, 1438 (2018)
8. M. Zhang, C. Wang, Y. Hu, A. Shams-Ansari, T. Ren, S. Fan, and M. Lončar. "Electronically Programmable Photonic Molecule." *Nature Photonics*, **13**, 36 (2019)

Connecting widely separated wavelength bands using chip-integrated nonlinear microresonators

KARTIK SRINIVASAN[1,2]

[1]*Physical Measurement Laboratory, National Institute of Standards and Technology, Gaithersburg, MD 20899-6811, USA*
[2]*Joint Quantum Institute, NIST/University of Maryland, College Park, MD 20742, USA*
[1]*kartik.srinivasan@nist.gov*

Abstract: I will discuss our laboratory's work in developing dispersion-engineered silicon nitride nonlinear microresonators to enable efficient connections between widely separated optical frequencies, for applications in time and frequency metrology and quantum information science.

Summary

The ability to coherently and efficiently connect visible and near-infrared wavelengths to the telecommunications band using chip-integrated nonlinear optics has relevance for both classical and quantum applications. In this talk, I will describe our efforts in developing such resources using Kerr nonlinear resonators based on the stoichiometric silicon nitride platform. I will discuss how phase- and frequency-matching can be satisfied for modes that are separated by >250 THz, and how the combination of high quality factors, small mode volumes, and interactions involving only fundamental spatial modes can result in wide-band four-wave mixing with efficiencies (e.g., translation efficiency at 1 mW of pump power) rivaling those of the best $c^{(2)}$ systems demonstrated to date [1]. Classical applications include spectral translation of telecom signals to the visible, for example, to connect high-performance chip-integrated lasers to atomic clocks [1]. By further engineering the dispersion of the resonator to suppress competing four-wave-mixing processes, sub-mW threshold optical parametric oscillation involving a visible signal and telecom idler is also shown [2]. On the quantum side, such resonators can be operated sub-threshold, resulting in visible-telecom entangled photon-pair sources suitable for connecting remote quantum memories, with the precise wavelengths of the two photons widely tunable by adjusting the resonator cross-section [3]. While such entangled photon-pair sources can be reasonably bright and low-noise, they are fundamentally probabilistic in nature (a consequence of the photon statistics of the underlying spontaneous four-wave-mixing process), and methods that enable a deterministic connection between disparate quantum nodes are needed. To that end, we are also investigating four-wave-mixing Bragg scattering (FWM-BS) in silicon nitride microresonators. Critical to quantum applications, FWM-BS directly converts signal photons to idler photons, making it suitable for operations down to the single photon level because there is no intrinsic noise source, unlike processes based on parametric amplification [4]. We demonstrate both narrow (few THz) and wide (100 THz) frequency shifts using FWM-BS in microresonators [5], and have recently demonstrated the ability to frequency shift single-photon Fock states [6] and make single photons indistinguishable [7] in such geometries. Finally, I will discuss other ongoing research activities based on Kerr nonlinear resonators.

References

1. X. Lu *et al.*, "Efficient telecom-to-visible spectral translation through ultralow power nonlinear nanophotonics," *Nature Photonics*, Jun. 2019.
2. X. Lu *et al.*, "manuscript in preparation."
3. X. Lu *et al.*, "Chip-integrated visible–telecom entangled photon pair source for quantum communication," *Nature Physics*, vol. 15, no. 4, pp. 373–381, Apr. 2019.
4. C. J. McKinstrie, J. D. Harvey, S. Radic, and M. G. Raymer, "Translation of quantum states by four-wave mixing in fibers," *Opt. Express*, vol. 13, no. 22, pp. 9131–9142, Oct. 2005.
5. Q. Li, M. Davanço, and K. Srinivasan, "Efficient and low-noise single-photon-level frequency conversion interfaces using silicon nanophotonics," *Nature Photonics*, vol. 10, no. 6, pp. 406–414, Apr. 2016.
6. A. Singh *et al.*, "Quantum frequency conversion of a quantum dot single-photon source on a nanophotonic chip," *Optica*, vol. 6, no. 5, p. 563, May 2019.
7. Q. Li *et al.*, "Tunable quantum beat of single photons enabled by nonlinear nanophotonics," *arXiv:1905.01698 [physics, physics:quant-ph]*, May 2019.

Ultrahigh-Q crystalline whispering gallery mode microcavity fabricated with mechanical machining

TAKASUMI TANABE[1], SHUN FUJII[1], YASUHIRO KAKINUMA[2]

[1]*Department of Electronics and Electrical Engineering, Keio University, 3-14-1 Hiyoshi, Kohoku-ku, Yokohama, Japan*
[2]*Department of System Design Engineering, Keio University, 3-14-1 Hiyoshi, Kohoku-ku, Yokohama, Japan*
takasumi@elec.keio.ac.jp

Abstract: High-Q cavity is fabricated without hand polishing which allows us to design the cross-section of the whispering gallery mode microcavity. This allows us to design the cavity dispersion.

1. Introduction

High-Q crystalline microresonators are attractive platforms for frequency comb generation, and they have been intensively studied in recent years. Since the generation of the frequency combs is dependent to the dispersion of the microcavity, the dispersion engineering is considered a hot topic. Although crystalline materials allow us to obtain ultatrhigh- Q, the precise structural control is a challenge, because crystalline resonators are usually fabricated with a hand polishing process. In this work, we demonstrate the dispersion engineering of a high-Q crystalline microresonator with a Q-factor exceeding 10^8 fabricated with computer-controlled machining.

2. Results

When we fabricate a crystalline microresonator by using a lathe cutting (Fig. 1(a)), we need to consider the critical cutting depth (Fig. 1(b)), which is the transition point from ductile mode cutting to brittle mode cutting. Ductile mode cutting enables us to realize a smooth surface, and it will be the key to achieving a high Q. In addition, the cutting surface also affects the critical cutting depth. We identified the critical cutting depth with an orthogonal cutting experiment, and fabricated a magnesium fluoride crystalline microresonator with fully computer-controlled ultraprecision machining.

Figure 1(d) shows the measured transmission spectrum of a MgF2 WGM microresonator whose diameter and curvature were 508 and 36 μm, respectively. The Q value was an ultrahigh-Q of 1.4×10^8 at 1552.2 nm, which is the highest Q fabricated with a machining process without polishing. The measured dispersion (blue dots) is shown in Fig. 1(e), where the theoretical dispersion (solid red line) is shown with $\omega_\mu-\omega_0+D_{1\mu} = D_2\mu^2/2+D_3\mu^3/12+ D_4\mu^4/24+\cdots$. These results confirmed that our pre-designed structure was precisely fabricated, and attractive with respect to dispersion engineering for microresonator frequency comb generation.

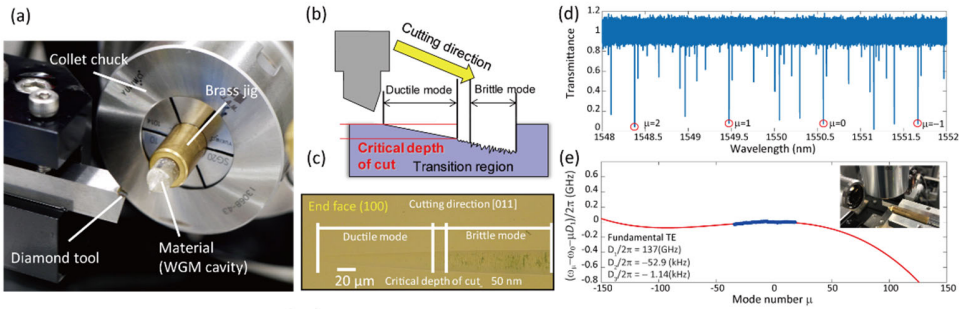

Figure 1 (a) Fully computer-controlled ultraprecision lathe for WGM microresonator fabrication. (b) Schematic illustration of the setup used to test the critical cutting depth. (c) Microscope image of CaF2 when we cut in the [011] direction with end-face orientation (100). The ductile mode to brittle mode transition is observed at a critical cutting depth of ~50 nm. (d) Observed transmission spectrum of fabricated MgF_2 microresonator. (e) The calculated (solid red line) and measured (blue dots) dispersion for the pump mode.

3. Summary

A microcavity with a Q of 1.4×10^8 is fabricated with mechanical machining by cutting the MgF_2 at ductile mode. The measured dispersion agrees perfectly with the design.

References

1. S. Fujii, *et al.* "Octave-wide phase-matched four-wave mixing in dispersion engineered crystalline microresonators," Opt. Lett. **44**, 3146 (2019).

Multipolar lattice resonances in plasmonic crystal cavity

KEIJI SASAKI

Research Institute for Electronic Science, Hokkaido University, Sapporo, Hokkaido, Japan
sasaki@es.hokudai.ac.jp

Abstract: We demonstrate that multipolar lattice resonances in plasmonic crystal cavity can be excited by both Gaussian beam and cylindrical vector beam. The simulation shows that spatial distributions of the lattice resonances exhibit characteristic patterns conserving the chirality.

1. Introduction

Plasmon damping and losses limit the enhancement of the localized field in plasmonic nanocavity and thus represent one of the main barriers to the evolution of plasmonics into a prominent technology. It should be possible to reduce damping by controlling the material properties, whereas radiative losses can be managed by the following two approaches. The first approach is to exploit the dark modes of the plasmonic cavity. We have recently reported a method of exciting dark-mode multipole plasmons by using vortex beams with specific angular momentum. The second approach to managing radiative losses is to take advantage of the lattice resonances in periodic metal nanoparticles, i.e., plasmonic crystal cavity, in which collective resonances are mediated by the diffractive coupling of localized plasmons. In this presentation, we report a combination of the two above approaches applied to the management of radiative losses, taking advantage of multipolar dark lattice resonances, which can be excited from free space. We theoretically demonstrate that the quadrupole lattice resonances in square lattice plasmonic crystals composed of nanodisks can be excited both by vertically incident cylindrical vector (CV) beam and by a linearly polarized Gaussian beam. The spatial distributions of the lattice resonances in the plasmonic crystal cavity exhibit characteristic patterns where the chirality of the spatial patterns conserve the chirality of the incident structured light and the excited plasmonic fields in the individual nanodisks.

2. Results and discussion

We consider a square lattice plasmonic crystal consisting of 9 x 9 array of gold nanodisks. The lattice period is set such that normally incident light along the z direction is diffracted in the *x* or *y* directions. When the CV beam is used as the excitation beam (Fig. 2(a)), the near-field intensity spectrum exhibits two clear peaks (Fig. 2(g)). The FWHM of the quadrupole resonance at 805 nm is ~30 nm, which is much narrower than that of a isolated nanodisk. This result indicates that the lattice resonance decreases the radiative loss even in a finite plasmonic crystal. The field enhancement reaches 5 x 10^4. Figure 2(c) shows the near-field distribution at 805 nm, in which the single-lobed envelope function peaks at the center, even though the incident beam has a ring-shaped intensity profile. In contrast, the near-field distribution of the dipole resonance at 1040 nm shown in Fig. 2(e) exhibits a ring-shaped envelope function. An inset of Fig. 2(g) shows the electric field profile around the central nanodisk of Fig. 2(c), thus indicating that this 805-nm lattice resonance corresponds to quadrupole mode. The quadrupole lattice resonance is also excited even using a Gaussian incident beam (Fig. 2(b)). Figure 2(h) shows the corresponding intensity spectrum. The near-field distribution at 805 nm in Fig. 2(d) shows a double-lobed higher-order envelope function along the *x* axis. The phases of the left and right-hand parts are π shifted. As a result, the quadrupole mode is cancelled out, and only a small dipole mode can be observed in the central column. The detailed field distribution around the nanodisk is shown in the inset of Fig. 2(h). At 1040 nm, the near-field distribution exhibits dipole lattice resonances with a single-lobed fundamental envelope function, as shown in Fig. 2(f).

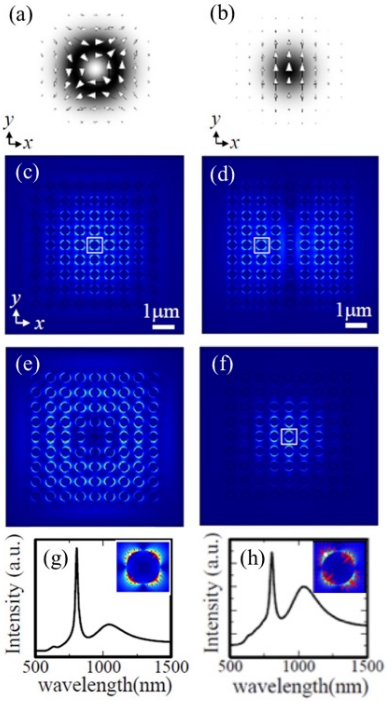

Figure 2. Cross-section profiles of (a) CV beam and (b) linearly-polarized Gaussian (G) beam. Electric field norm distributions of plasmonic crystal excited by (c) CV- and (d) G-beams at 805 nm, (e) CV- and (f) G-beams at 1064 nm. Near-field intensity spectra under the excitation with (g) CV- and (h) G-beams.

Hybridization of Second Order Exceptional Point

Jinhyeok Ryu, Chang-Hwan Yi, and Chil-Min Kim
Department of Emerging Materials Science, DGIST, Daegu 42988, Republic of Korea

Exceptional point (EP) is a unique point in non-Hermitian systems, where the eigenvalues as well as their corresponding eigenvectors coalesce simultaneously. Up to now, several types of second order EPs have been found depending on coupling mechanism: a parity-time symmetry, an asymmetric back scattering, a supermode coupling, an internal-external mode pair, a concentric layered microdisk, and a resonance assisted tunneling. Among them, a chiral EP is an even and an odd parity mode coalescence, which result in maximum chirality, due to asymmetric backscattering and a supermode EP is a coalescence of optical modes at two remote microdisks.

Recently, higher order EPs are another new issue, finding systems, formation of EPs, and their coupling mechanism. In several systems, higher order EPs have been found. In higher-order EPs, each of them uses its own single coupling mechanism. Among the second order EPs, we focus on the chiral and the supermode EP and achieve a new heterogeneous third-order EP, for the first time, by hybridizing these two different types of second order EPs. Our heterogeneous third-order EP is demonstrated in a system comprised of two microdisks and one scatterer. This surprising EP is analyzed by calculating the overlaps of spatial mode distributions as well as chirality of modes. Through the analysis, we show that our third order EP should be described by a 4×4 Hamiltonian. It is confirmed that our EP has a 1/3 scaling-low response to external perturbations. Most importantly, since this hybridization mechanism can extend to achieving various different types of higher-order EPs, we believe that our finding will initiate new directions of studying EPs.

References

1. C. M. Bender and S. Boettcher, Phys. Rev. Lett. 80, 5243–5246 (1998).
2. J. Wiersig, A. Eberspächer, J.-B. Shim, J.-W. Ryu, S. Shinohara, M. Hentschel, and H. Schomerus, Phys. Rev. A 84, 023845 (2011).
3. J.-W. Ryu, S.-Y. Lee, and S. W. Kim, Phys. Rev. A 79, 053858 (2009).
4. C.-H. Yi, J. Kullig, M. Hentschel, and J. Wiersig, Photon. Res. 7, 464–472 (2019).
5. J. Kullig, C.-H. Yi, M. Hentschel, and J. Wiersig, New J. Phys. 20, 083016 (2018).
6. C.-H. Yi, J. Kullig, and J. Wiersig, Phys. Rev. Lett. 120, 093902 (2018).

Lead halide perovskite based microlasers at the bounded states in the continuum

Qinghai Song
Harbin Institute of Technology, Shenzhen, China

Abstract:

Mode interaction in optical microcavities have been intensively studied for decades. A large number of novel phenomena have been proposed and experimentally realized, e.g. high Q resonances, unidirectional emissions, and coherent destruction of the tunneling etc. In past few years, a different type of phenomenon that was initially proposed in quantum mechanism has been revisited in optical region. This kind of phenomenon is known as the optical bounded states in the continuum (BICs). With the destructive interference of two modes in their radiative channels, the Q factor at the BICs can be infinitely large. While the optical BICs have been intensively studied, they are mostly restricted in passive systems. Herein, by combing the optical BICs with the gain materials (lead halide perovskites), we have explored the BICs in active systems and the corresponding laser emissions. Owing to the topological nature of BICs and their infinitely high Q factors, the BICs lasers have shown a series of unique laser characteristics including single-mode operation, ultralow threshold, and vortex emissions. The BICs based vortex lasers are intrinsically better than the previous approaches, which strongly rely on the asymmetrical scattering and have much higher energy consumption than their linear counterparts.

Non-Hermitian optics in a single nonlinear microcavity

WENJIE WAN[1*]

[1]*University of Michigan-Shanghai Jiao Tong University Joint Institute, Shanghai Jiao Tong University, Shanghai 200240, China*
*wenjie.wan@sjtu.edu.cn

Optical microcavities are inherently non-Hermitian in nature, offering a fertile ground to test recent emerging development in non-Hermitian physics. Among them, representative examples include coherent perfect absorption (CPA)/critical coupling [1], electromagnetically induced transparency (EIT)[2], parity-time symmetric coupled resonators, exceptional points (EP). These works conducted in microcavities by manipulating additional factors like gain and loss reveal rich physics beyond the Hermitian regime. However, realizations of these experiments have been mainly limited to the spatial domain, for example, using two coupled microcavities to achieve PT symmetry. In this talk, we shall discuss our group's efforts in non-Hermitian optics in a single microcavity by extending *an additional dimension such as frequency* through internal nonlinear optical processes. Within a single whispering-gallery-mode type microcavity, we show nonlinearity can alter the total transmission of a CPA, examining such a critical coupling mechanism in the nonlinear regime[1]. Similarly, we demonstrate a new mechanism of optically induced transparency in a micro-cavity by introducing a four-wave mixing gain to nonlinearly couple two separated resonances of the micro-cavity in an ambient environment. We also show that the unidirectional gain of the four-wave mixing can lead to the remarkable effect of non-reciprocal transmission at the transparency windows[2]. On the PT-symmetry problem, we theoretically and experimentally demonstrate anti-PT symmetry in a synthetic spectral dimension induced by nonlinear Brillouin scattering in a single optical microcavity, where electromagnetically induced transparency or absorption in two spectral resonances provides the optical gain and loss to observe a phase transition between two symmetry regimes [3]. Moreover, we will also show our studies on nonlinear bistable behaviors of such microcavity-based SBS near its EP, revealing a surprising memory effect depending not only on the perturbation variations and Hermiticity of the systems.

Particularly, in our anti-PT symmetry work, two *spectrally* separated optical resonances in a *single* microcavity are coupled by nonlinear frequency conversion through stimulated Brillouin scattering (Fig. 1a), without the need of having a second microcavity in the spatial PT case. These two nonlinear-coupled resonances can interfere with each other and result in either electromagnetically induced transparency (EIT) or absorption (EIA), as shown in Fig. 1d and Fig.1e, similar to their counterparts in atomic physics. By using a detuning technique, i.e. through the detuning factor $\delta = \Delta_p - \Delta_s$, the difference of detuning of probe and stokes (Fig. 1c), we can change the eigenvalue of the non-Hermitian Hamiltonian, $\lambda_{\pm} = \pm\sqrt{\delta^2 - |g|^2}$ (g is the nonlinear coupling factor). Such that, a striking phase transition between the broken and unbroken phases of the synthetic anti-PT symmetry at an exceptional point $\left|\left(\Delta_p - \Delta_s\right)/g\right| = 2$. These results expand the scope of non-Hermitian optics into the synthetic spectral dimension, providing a new paradigm to exploit the benefits of PT-symmetry and the emerging pseudo-Hermitian physics.

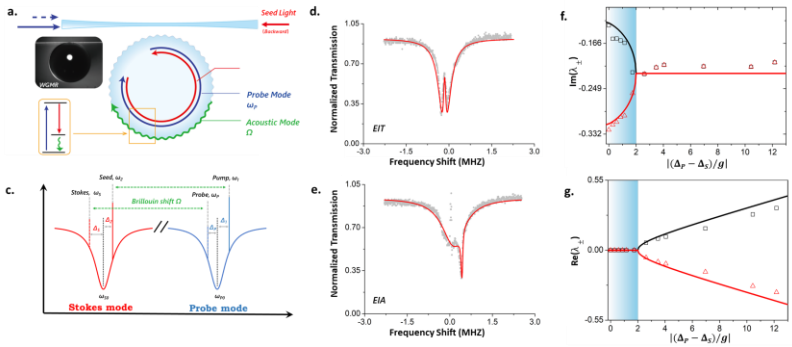

Fig. 1. Anti-PT symmetry in a single microsphere cavity through nonlinear Brillion scattering process.

References

1. W. Wan, Y. Chong, L. Ge, H. Noh, A.D. Stone, H. Cao, *Science* **331**,889 (2011).
2. Y. Zheng, W Wan, et.al, *Light: Science & Applications* **5** , e16072-e16072 (2016)
3. F. Zhang, Y. Feng, X. Chen, L. Ge, W. Wan, *Physical review letters* **124**, 053901 (2020)

Synthetic parity-time symmetry breaking in a single microcavity

FANGXING ZHANG [1], LI GE [2], AND WENJIE WAN [1]

[1]*University of Michigan-Shanghai Jiao Tong University Joint Institute, Shanghai Jiao Tong University, Shanghai 200240, China*
[3]*Department of Physics and Astronomy, College of Staten Island, the City University of New York, NY 10314*
[1] wenjie.wan@sjtu.edu.cn *or* [2] li.ge@csi.cuny.edu

Non-Hermitian systems based on parity–time (PT) symmetry reveal rich physics beyond the Hermitian regime. So far, realizations of PT-symmetric systems have been limited to the spatial domain [1,2]. Here we theoretically and experimentally demonstrate PT symmetry in a synthetic spectral dimension induced by nonlinear Brillouin scattering in a single optical microcavity, where electromagnetically induced transparency or absorption in two spectral resonances provides the optical gain and loss to observe a phase transition between two symmetry regimes. This scheme provides a new paradigm towards the investigation of non-Hermitian physics in a synthetic photonic dimension for all-optical signal processing and quantum information science.

In our work, two *spectrally* separated optical resonances in a *single* microcavity are coupled by nonlinear frequency conversion through stimulated Brillouin scattering (Fig. 1a), without the need of having a second microcavity in the spatial PT case. These two nonlinear-coupled resonances can interfere with each other and result in either electromagnetically induced transparency (EIT) or absorption (EIA), as shown in Fig. 1d and Fig.1e, similar to their counterparts in atomic physics. By using a detuning technique developed specifically for this framework, we can control the parameter $\delta = \Delta_p - \Delta_s$, which is the difference of detuning of probe and stokes light shown in Fig. 1c. Then, change the eigenvalue of the non-Hermitian Hamiltonian, $\lambda_\pm = \pm\sqrt{\delta^2 - |g|^2}$. Hence, we are able to observe a striking phase transition between the broken and unbroken phases of the synthetic PT symmetry at an exceptional point $\left|(\Delta_p - \Delta_s)/g\right| = 2$, where g is the coupling efficiency of two optical modes. These results expand the scope of non-Hermitian optics into the synthetic spectral dimension, providing a new paradigm to exploit the benefits of PT symmetry and the emerging pseudo-Hermitian physics.

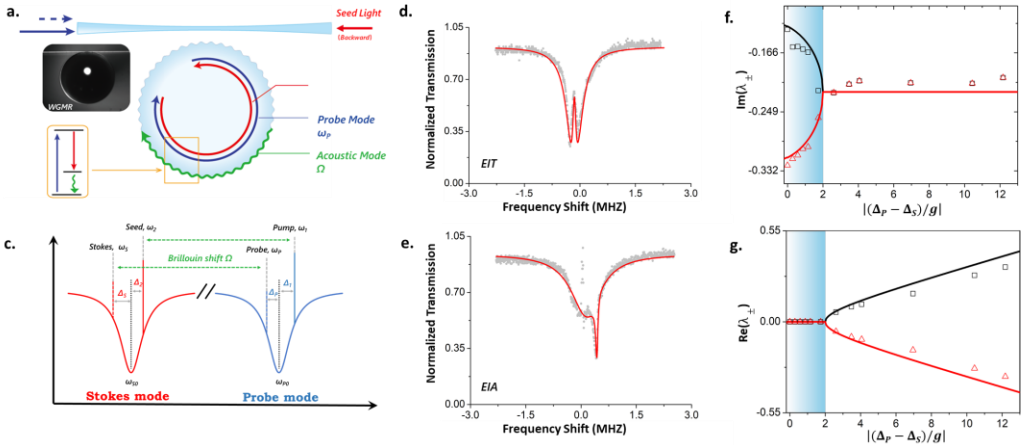

Fig. 1. (a) Brillion scattering in a WGM microcavity with two optical modes, i.e., the probe and Stokes modes, together with an acoustic mode. Lower inset: Energy transition diagram. Upper inset: Picture of one high-Q microsphere coupled to the tapered fiber. (b) Spectrally Illustration of coupling modes system, which established by the pump-seed set up in the experimental. (c) EIT and EIA result from nonlinear-coupling, near the seed and pump frequency respectively. (b, c) The real parts (b) and imaginary parts (c) of the dynamical eigenfrequencies measured in the synthetic PT system. The exceptional point at $\left|(\Delta_p - \Delta_s)/g\right| = 2$ marks the phase transition boundary. The solid lines are obtained from the theoretical simulation.

References

1. Guo A, et al. Observation of PT-symmetry breaking in complex optical potentials. *Phys. Rev. Lett.* **103**, 093902 (2009).
Peng B., Özdemir Ş. K., Lei F., Monifi F., Gianfreda M., Long G. L., Fan S., Nori F., Bender C. M., & Yang L. Parity–time-symmetric whispering-gallery microcavities. *Nat. Phys.* **10**, 394 (2014).

Soliton microcombs

Tobias J. Kippenberg (PhD)
EPFL, Switzerland

Optical frequency combs[1,2] provide equidistant markers in the IR, visible and UV and have become a pivotal tool for frequency metrology and are the underlying principle of optical atomic clocks, but are also finding use in other areas, such as broadband spectroscopy or low noise microwave generation. In 2007 a new method to generate optical combs was discovered based on high Q optical microresonators[3,4]. Such microresonator frequency combs have since then emerged as a new and widely investigated method with which combs can be generated via parametric frequency conversion of a continuous wave (CW) laser inside a high Q resonator via the Kerr nonlinearity. Over the past years the a detailed understanding of the comb formation process has been gained, and regimes identified in which dissipative temporal solitons (DKS) can be generated, that not only provide low noise optical frequency combs but moreover give access to femtosecond pulses. Such DKS have unlocked the full potential of soliton micro-combs by providing access to fully coherent and broadband combs and soliton broadening effects. Dissipative Kerr solitons have now been generated in a wide variety of resonators, including those compatible with photonic integration based on silicon nitride (Si_3N_4). We will discuss the DKS regime, first discovered in crystalline resonators, and our current understanding including the observation of the breather soliton regime, the influence of avoided mode crossings on breather and the repetition rate, as well as methods to deterministically access the single soliton regime. Taken together this has enabled to reliably access single soliton states in photonic chip based resonators, in particular those utilizing the photonic damascene process. Dissipative Kerr solitons enable to obtain combs that can span more than a full octave using soliton induced Cherenkov radiation, which extends the combs bandwidth and power in the spectral wings via dispersive waves. Such DKS have been enabled to count the cycles of light, allow 2f-3f self referencing. Using such soliton Kerr optical frequency combs in a SiN microresonator we have recently demonstrated with the group of C. Koos (KIT) massively parallel coherent communication, with dual combs for both the source and as massively parallel LO for the coherent receiver[1]. Moreover, we have demonstrated using a pair of photonic chip based frequency combs dual comb distance measurements, with record acquisition rates due to the combs large mode spacing (100 GHz). Recent work moreover has shown that DKS can be extended to the biological imaging window at 1 micron, relevant for e.g. Raman spectral imaging or OCT. Soliton microcombs have the potential to advance timekeeping, metrology or telecommunication by providing a technology amenable to full photonic integration, low power consumption and large comb bandwidth and repetition rate.

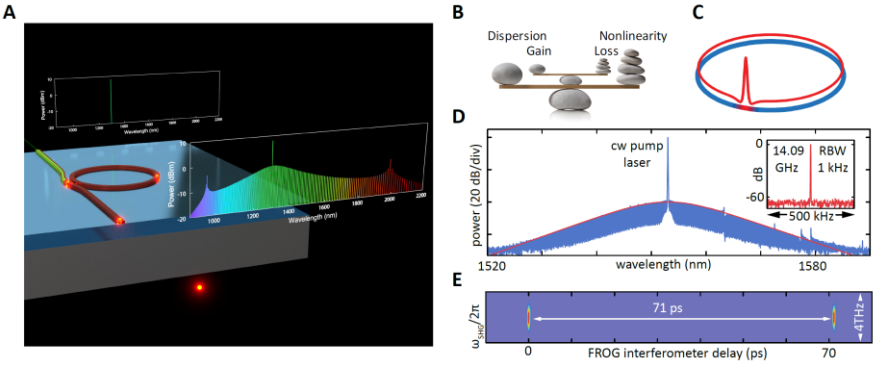

Figure 1 : Dissipative Kerr solitons in microresonators. (B) Principle of a DKS that balances dispersion and nonlinearity, as well as parametric gain and cavity loss. (C) temporal dissipative soliton waveform envelope in a microresonator (D) First demonstration of a DKS in a crystalline microresonator. (E) The FROG profile of a single DKS.

1 Cundiff, S. T. & Ye, J. Colloquium: Femtosecond optical frequency combs. *Rev. Mod. Phys.* **75**, 325-342 (2003).
2 Udem, T., Holzwarth, R. & Hansch, T. W. Optical frequency metrology. *Nature* **416**, 233-237 (2002).
3 Del Haye, P. *et al.* Optical frequency comb generation from a monolithic microresonator. *Nature* **450**, 1214 (2007).
4 Kippenberg, T. J., Holzwarth, R. & Diddams, S. A. Microresonator-based optical frequency combs. *Science* **332**, 555-559, doi:10.1126/science.1193968 (2011).
5 Del'Haye, P. *et al.* Octave Spanning Tunable Frequency Comb from a Microresonator. *Physical Review Letters* **107**, doi:10.1103/PhysRevLett.107.063901 (2011).
6 Herr, T. *et al.* Universal formation dynamics and noise of Kerr-frequency combs in microresonators. *Nature Photonics* **6**, 480-487, doi:10.1038/nphoton.2012.127 (2012).
7 Alnis, J. *et al.* Thermal-noise-limited crystalline whispering-gallery-mode resonator for laser stabilization. *Physical Review A* **84**, doi:10.1103/PhysRevA.84.011804 (2011).
8 Kudryashov, A. V. *et al.* Terabit/s data transmission using optical frequency combs. **8600**, 860009, doi:10.1117/12.2003701 (2013).
9 Wang, C. Y. *et al.* Mid-infrared optical frequency combs at 2.5 mum based on crystalline microresonators. *Nature communications* **4**, 1345, doi:10.1038/ncomms2335 (2013).10 Herr, T. *et al.* Temporal solitons in optical microresonators. *Nature Photonics* **8**, 145-152, doi:10.1038/nphoton.2013.343 (2013).

Invited Contribution 6th WOMA Hongkong 2019

Mesoscopic optics in complex microcavity systems

Martina Hentschel, TU Chemnitz, Germany

Microcavity lasers made of deformed dielectric disk resonators such as the Limaçon-shaped cavity have attracted a lot of interest due to their directional light emission from high quality factor modes. Inspired by setups of mesoscopic physics of electronic system, we combine individual microdisk resonators to one- and two-dimensional arrays and investigate their behavior in dependence on the inter-cavity distance and the array configuration. For chains of several Limaçon-shaped microcavities we show that the directionality of emission is enhanced dramatically for weakly coupled resonators with inter-cavity spacings D on the order of the wavelength [1].

Furthermore, we study the coupling mechanisms between Limaçon resonators in different array configurations. We show that far-field properties depend sensitively on the coupling between the resonators in the array and are mostly determined by the inter-cavity distance, cf. Fig. 1, as well as by geometric imperfections of the configuration. We find the directionality enhancement to be even more pronounced at smaller inter-cavity distances $D/R < 1$ (where R is the mean cavity radius), see Fig. 1a. Moreover, for certain resonances we find a reversal of the main emission direction at only a slightly different D/R, see Fig. 1a. Both effects, the superdirectional emission and the emission reversal, result from the strong coupling of the cavities for smaller cavity spacings and sensitively depend on resonance properties and the array geometry. We use phase-space methods to model and capture the collective behavior of generic complex ensemble structures. We discuss the coupling induced, emergent dynamics, the role of geometric imperfections, and relate our findings observations made for to billiards with sources.

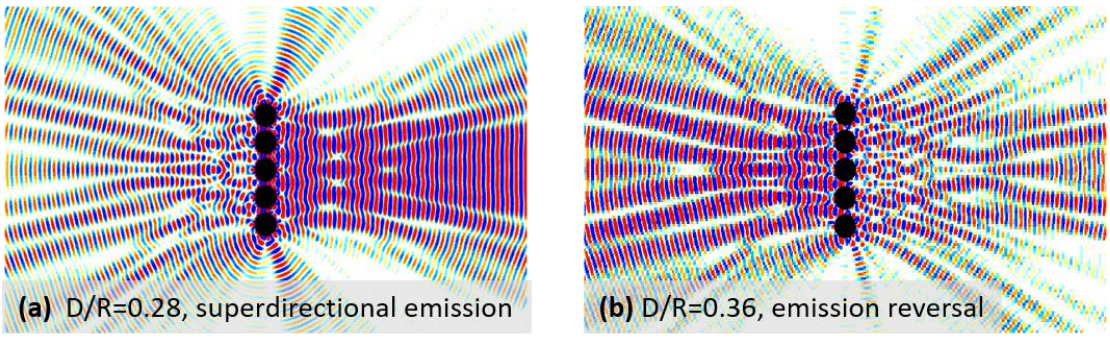

Fig. 1: Linear arrangements of resonant optical elements show very different behavior in dependence on the inter-cavity distance D. Limaçon cavities with dimensionless wave number kR ~7, refractive index n=3, shape parameter ε=0.43.

[1] J. Kreismann, J. Kim, M. Bosch, S. Sinzinger, M. Hein, and M. Hentschel, *Super-directional light emission and emission reversal from micro cavity arrays,* Phys. Rev. Res. **1**, 033171 (2019).

Engineering whispering gallery resonators for nonlinear optics, photonics, and sensing applications

SHO KASUMIE, JEAN-BAPTISTE CEPPE, FUCHUAN LEI, JONATHAN M. WARD, SÍLE NIC CHORMAIC[1]

Light-Matter Interactions for Quantum Technologies Unit, OIST Graduate University, Onna-son, Okinawa, Japan
[1]sile.nicchormaic@oist.jp

Abstract: We discuss recent progress on whispering gallery resonator research, including topics related to lasing and sensing applications. We also introduce some novel resonator and coupler designs that may improve functionality.

1. Introduction

As is well-known by now, whispering gallery resonators (WGRs) are neat experimental tools that offer a range of uses covering topics as diverse as miniature lasers when made from active materials [1], to sensing and trapping devices for nanoparticles [2]. One major challenge in this field is to move WGRs from the laboratory environment into real-life scenarios when they can be put into practical, everyday usage. Stability of coupling schemes is one drawback, for example when using the standard tapered fiber coupler. Another issue is the repeatability of fabrication techniques used for many designs of WGRs such as microspheres and microbubbles. In this work, we will discuss some of our laboratory-based work on WGR applications and present some alternatives for light coupling and device design that may allow a more applications-based progression in this field in the coming years.

2. Resonator design

The whispering gallery resonator of choice for many of our experimental endeavors is the microbubble, an image of which is shown in Fig. 1. The microbubble has unique advantages over most other types of WGR due to the fact that it can be incorporated into microfluidic systems for sensing and spectroscopy purposes [3], and the geometry of the bubble can be engineered to facilitate the study of nonlinear optics effects, such as frequency comb generation [4]. Several of our advances using this device (or the more standard solid microsphere) will be discussed, but we will also present some of our recent advances in WGR techniques, such as light coupling via a nano-antenna [5], see Fig. 1, and fabrication using 3D printing methods.

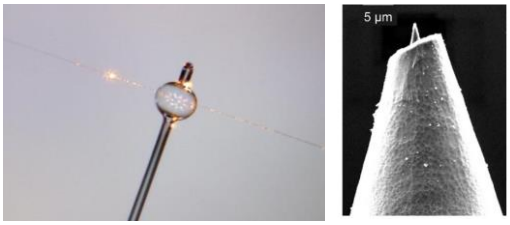

Fig. 1. Left: Image of light coupled into a microbubble via a tapered optical fiber. Right: Image of a nano-antenna [5].

3. Summary

We report on advances for whispering gallery resonators to increase their functionality for real-life applications. While we also present work on our current research, we hope to encourage researchers to push these devices towards everyday applications in the near-future.

References

1. X. Wang, Y. Yu, S. Zhou, S. Wang, Z. Gao, J.M. Ward, S. Nic Chormaic, and P. Wang, "Single mode green lasing and multicolor luminescent emission from an Er3+-Yb3+ co-doped compound fluorosilicate glass microsphere resonator," OSA Continuum (2018).
2. J.M. Ward, Y. Yang, F. Lei, X.-C. Yu, Y.-F. Xiao, and S. Nic Chormaic, "Nanoparticle sensing beyond evanescent field interaction with a quasi-droplet microcavity," Optica (2018).
3. L.T. Hogan, E.H. Horak, J.M. Ward, K.A. Knapper, S. Nic Chormaic, and R.H. Goldsmith, "Toward real-time monitoring and control of nanoparticle properties with a microbubble resonator spectrometer," chemrxiv.org/s/e1f0342422952b9a9e6c (2019).
4. Y. Yang, X. Jiang, S. Kasumie, G. Zhao, L. Xu, J. Ward, L. Yang, and S. Nic Chormaic, "Four-wave mixing parametric oscillation and frequency comb generation at visible wavelengths in a silica microbubble resonator," Opt. Lett. (2016).
5. J.M. Ward, F. Lei, S. Vincent, P. Gupta, S.K. Mondal, J. Fick, and S. Nic Chormaic, "Excitation of whispering-gallery-modes with a "point-and-play" fiber-based, optical nano-antenna," Opt. Lett. (2019).

Microcavities based on transmission at Brewster's angle

JULIUS KULLIG[1,*] AND JAN WIERSIG[1]

[1] *Institut für Physik, Otto-von-Guericke-Universität Magdeburg, Postfach 4120, D-39016 Magdeburg, Germany*
[*] *julius.kullig@ovgu.de*

Abstract: We report on microcavities that utilize transmission at Brewster's angle for the light confinement. The design is based on rays that sequentially leave and reenter the cavity without intensity loss which leads to high-Q modes.

1. Microstar cavity for light confinement without reflection

Whispering-gallery cavities confine light via total internal reflection for long times. Therefore, the long-lived optical modes are localized inside the cavity and only leak evanescently to the surrounding area. In our approach this is fundamentally different [1]. We construct a star-shaped microdisk cavity where a family of rays intersect the dielectric interface under Brewster's angle such that these rays leave and reenter the cavity without loss of intensity and therefore without beam splitting effects, see Fig. 1a. If the refractive index and the shape of the microstar are adjusted properly these specific rays are guided along marginally stable periodic orbits. Consequently, in the wave mechanics long-lived optical modes are formed that are supported by these rays, see Fig. 1b. At first glance these modes look similar to whispering-gallery modes, however, there are two main differences. First, these modes are not supported by total internal reflection. Hence, they live in the so-called leaky region of the phase space. Second, a large fraction of the mode's intensity is trapped in the exterior of the microstar between the spikes. Especially the latter property enables interesting applications such as an enhanced light matter interaction with the surrounding material which can be beneficial for, e.g., detection of nanoparticles.

In order to improve the Q-factor of the optical modes a deformation can be applied to the (polygonal) microstar by rounding the straight line segments. Thus, the marginally stable periodic orbit become stable and the optical modes are focused along it, compare Figs. 1c and 1d.

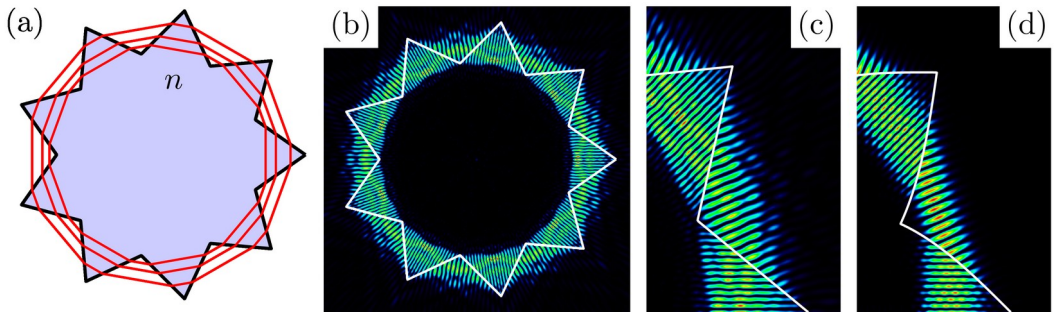

Fig. 1: (a) Ray dynamics in the microstar cavity. (b) Intensity pattern of a long-lived mode based on transmission at Brewster's angle. A magnification of the mode intensity pattern in a microstar with (c) straight line segments and with (d) deformed segments.

2. Whispering-gallery cavities with a Brewster notch

The concept of light confinement via transmission at Brewster's angle can be combined with traditional whispering-gallery cavities [2]. Therefore, a polygonal cavity is considered where one of the total internal reflections is replaced by a transmission through a notch, see Fig. 2a. The notch is again adjusted such that the perfect transmittance at Brewster's angle prevents beam splitting effects and therefore leads to a lossless periodic orbit. Accordingly, there exist long-lived optical modes passing trough the notch, see Fig. 2b. Next, a deformation to the notched cavity can be applied to selectively increase the Q-factor of those modes and to discriminate the Q-factor of other remaining modes that are supported solely by total internal reflection. As a result, the deformed notched cavity is suited to be efficiently coupled to a waveguide (see Fig. 2c). Therefore, the notch-supported modes can be conveniently excited and measured via the waveguide transmission spectra.

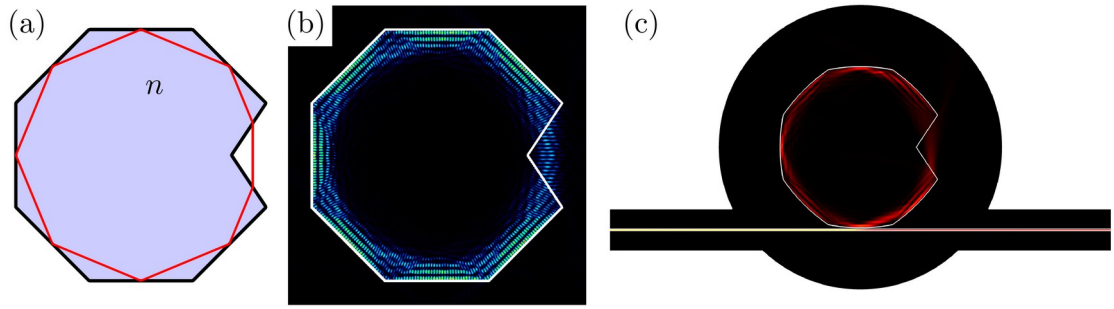

Fig. 2: (a) Ray dynamics in the notched cavity. (b) Intensity pattern of a long-lived mode. (c) Waveguide excitation of a long-lived mode in a deformed notched cavity.

Alternatively, an asymmetric boundary deformation can be applied to a notched cavity to destroy the mirror reflection symmetry. In general this leads to a coupling between clockwise and counterclockwise propagating waves in the cavity. With an additional further adjustment of the refractive index the notched cavity can be be tuned very close to an exceptional point where two modes (and their complex frequencies) coalesce to a single clockwise propagating mode. This is in particular interesting for sensing applications as it combines the exceptional point enhanced sensing with the strong light-matter interaction from the modes with their intensity trapped inside the notch. We verify the outstanding sensor performance by analyzing the complex frequency splitting induced by a targetparticle placed inside the notch.

References

1. J. Kullig, X. Jiang, L. Yang, and J. Wiersig, “Microstar cavities: An alternative concept for the confinement of light”, Phys. Rev. Research 2, 012072(R) (2020)
2. J. Kullig and J. Wiersig, “Microdisk cavities with a Brewster notch”, Phys. Rev. Research 3, 023202 (2021)

Enhanced Chiroptical Signals through Coherent Perfect Absorption in a Parity-Time Symmetric System

Hsin-Yu Wu* and Frank Vollmer

Department of Physics and Astronomy, Living Systems Institute, University of Exeter, Exeter, United Kingdom
**email: h.wu@exeter.ac.uk*

Abstract: We report how a coherent perfect absorber (CPA) enabled by an achiral optical system obeying parity-time (PT) symmetry has an enhanced ability to effectively sense molecular chirality of monolayered substances with unprecedented sensitivities.

Coherent amplification of chiroptical activity from a molecularly-thin optically-active substance has been a long-standing challenge due to the inherently weak nature of chiral responses. Here we report how a coherent perfect absorber (CPA) enabled by an achiral optical system obeying parity-time (PT) symmetry has an enhanced ability to effectively sense molecular chirality of monolayered substances. We demonstrate that such a CPA-based *PT*-symmetric system enables us in complete darkness to probe a subtle signal change induced by the introduction of a small disturbance, such as adsorbed chiral monolayer, to the unperturbed *PT*-symmetric system, and allows for absolute measurement and quantitative detection of the magnitude and sign of both real and imaginary parts of the chirality parameter in a background-free environment. Moreover, the CPA-based *PT*-symmetric system also exhibits three orders of magnitude enhancement in chiroptical responses of molecules, which is consistent with analytical calculations of differential absorption.

Since chiral molecules only manifest their handedness during their interaction with the chiral state of light (such as circularly-polarized (CP) light), the vectorial electromagnetic waves are represented in terms of the unit circular basis vectors and then expressed as in the form of circular Jones vectors (**Fig. 1a**). a, d and b, c represent the complex electric-field amplitudes of normally incident and scattered CP waves propagating along the z-axis, respectively. The $+$ ($-$) sign in subscript indicates left- and (right-) handed CP [LCP and (RCP)] states, respectively. The geometry is infinite in the x and y directions with water as a background medium. As shown in **Fig. 1b**, the eigenvalue spectrum of S^{PT}, the absolute value of the eigenvalues of S^{PT} as a function of wavelength λ, clearly illustrates two distinct regimes of the PT phase separated by a phase transition point or an EP at which all four eigenvalues coalesce with two degenerate pairs of eigenstates, $\psi_1 = \psi_3$ and $\psi_2 = \psi_4$. In addition, the eigenstates of S^{PT} display very intriguing and unique properties in different PT phases. **Fig. 1d** specifies that the phase difference between the two counter-propagating oppositely-handed CP incident beams of the same wavelength is exactly $\pi/2$ in the PT-broken phase. By fixing their relative phase at $\pi/2$, we can achieve coherent switching between the same-handed pair of absorbing and amplifying eigenstates, that is, $(\psi_3 \leftrightarrow \psi_1)$ and $(\psi_4 \leftrightarrow \psi_2)$, by simply varying the intensity ratio of the two CP incident beams, as indicated in **Fig. 1c**. The output coefficient (Θ) is defined as $\Theta = (|b_- + b_+|^2 + |c_+ + c_-|^2)/(|a_+ + a_-|^2 + |d_- + d_+|^2)$. **Fig. 1e** shows how Θ varies with the wavelength of the coherent incident beams for the lasing- and CPA-locked *PT*-symmetric systems. It is obvious that the CPA-locked S^{PT} has a higher sensitivity owing to its sharp feature at λ_{CPAL} than the lasing-locked S^{PT}.

Now let us consider that a one-nanometer-thick layer of a chiral substance adheres to both surfaces of the *PT*-symmetric structure (layer 2 and 5 in **Fig. 2**) as the substrate is immersed in a solution containing chiral molecules. The adsorbed chiral layer has an average refractive index $n_c = 1.33 + 10^{-4}i$ and a variable chirality parameter κ. As shown in **Fig. 2**, we demonstrate the capability to detect chiroptical signals from molecularly-thin chiral layers bound to the exterior surfaces of the *PT*-symmetric structure. For one-nanometer-thick layers of chiral substance with $\kappa = \pm 10^{-5}$ and $\pm 10^{-5}i$ (typical values for the chirality parameter of chiral molecules), ϑ (arising from circular birefringence) and χ (originating from circular dichroism (CD)) are as large as 10 mdeg near λ_{CPAL} and highly sensitive to the sign of κ. Furthermore, it is feasible to achieve the absolute chirality measurements since such a *PT*-symmetric system composed of a gain-loss bilayer does not make any contributions to the total chiroptical signals owing to its structurally achiral nature. As a comparison, the reference chiroptical signals (ϑ^{Ref} and χ^{Ref}) contributed by the pure chiral layers of the same thickness in the absence of the *PT*-symmetric substrate under the identical illumination are as small as 9 μdeg, thus achieving three orders of magnitude enhancement in the chiroptical responses using the CPA-locked *PT*-symmetric detection scheme.

To further understand the underlying mechanism of how the CPA-locked S^C enhances chiroptical signals, especially CD, we first investigate the optical absorption of two independent pairs of internal and beams in response to their respective input states, ψ_3^{CPA} and ψ_4^{CPA}, as schematically illustrated in **Fig. 3**. As shown in **Fig. 3a**, the signs of the chirality-dependent $\Delta\alpha(z_6)$, denoted by blue downward and red upward arrows corresponding respectively to $\mathrm{Im}(\kappa) > 0$ and $\mathrm{Im}(\kappa) < 0$, are in accord with those of the calculated χ shown in **Fig. 2**. The magnitudes of the chirality-dependent $\Delta\alpha(z_6)$ get considerably increased by a factor of up to approximately 10^3 compared to those of the reference differential absorption ($\Delta\alpha(z_6)^{Ref}$) from the pure chiral layers of the same thickness in the absence of the *PT*-symmetric substrate under the identical illumination shown in **Fig. 3b**, which are consistent with the aforementioned enhancement of three orders of magnitude in the chiroptical responses.

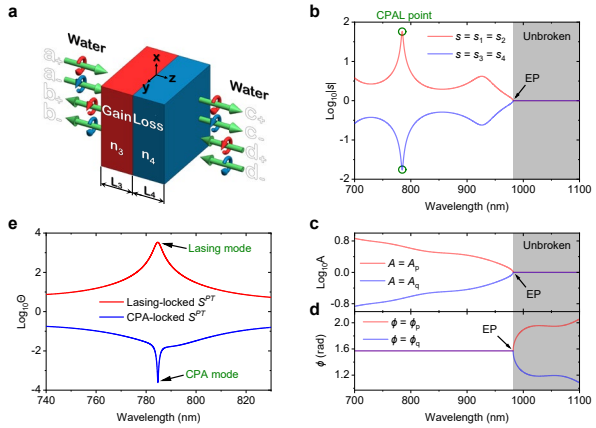

Fig. 1: Eigen characteristics of *PT*-symmetric system S^{PT}. **a** *PT*-symmetric system composed of two homogeneous gain and loss slabs of equal length is characterized by a scattering matrix S^{PT} in circular polarization representation. **b** Semi-log plot of the modulus of the eigenvalues of S^{PT} as a function of wavelength λ. **c**, **d** Semi-log plot of the relative amplitude A and phase ϕ of the two counter-propagating oppositely-handed CP incident waves of the same wavelength, extracted from the eigenstates of S^{PT}, as a function of λ. **e** Semi-log plot of the output coefficient Θ as a function of λ for the lasing- and CPA-locked S^{PT}. EP separates two distinct PT phases.

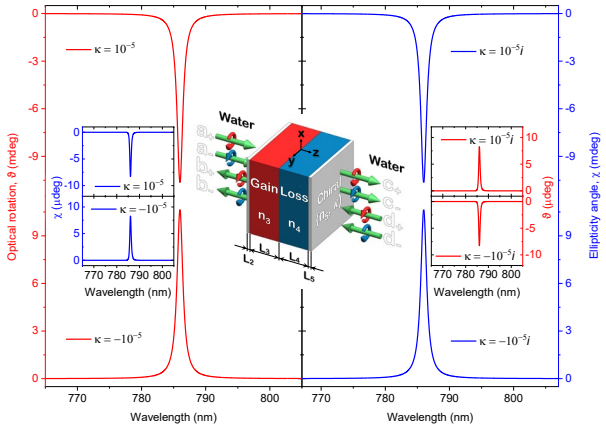

Fig. 2: Spectra of chirality-dependent optical rotation ϑ and ellipticity angle χ. The exterior surfaces of S^{PT} are decorated with a chiral substance characterized by a chirality parameter $\kappa = \kappa_2 = \kappa_5$ and an average refractive index $n_c = n_2 = n_5$ to form S^C system. Spectra of ϑ and χ (inset) for the purely real chirality parameter $\kappa = \pm 10^{-5}$ (left column). Spectra of χ and ϑ (inset) for the purely imaginary chirality parameter $\kappa = \pm 10^{-5}i$ (right column). ϑ and χ are obtained from the CPA-locked S^C system ($n_c = 1.33 + 10^{-4}i$ and $L_2 = L_5 = L_c = 1$ nm).

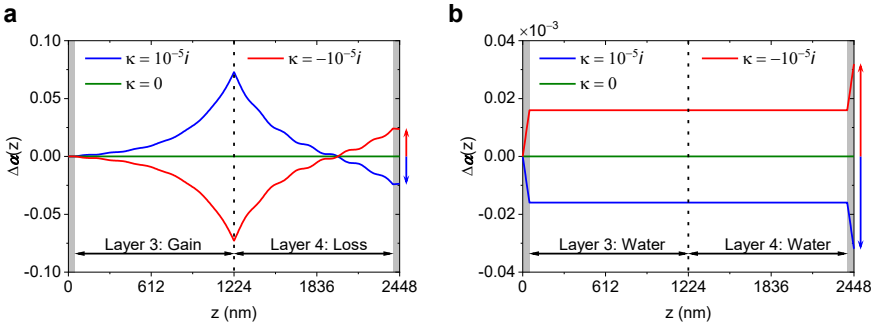

Fig. 3: Spatially-dependent differential absorption $\Delta\alpha(z)$ of two independent pairs of internal and beams. The profile of $\Delta\alpha(z)$ at λ_{CPAL} as a function of the propagation distance z for $\kappa = 0$ and $\kappa = \pm 10^{-5}i$, obtained from the CPA-locked S^C with $n_3 = 2.1 - 0.207i$ and $n_4 = 2.1 + 0.207i$ (**a**) and from the pure chiral layers of the same thickness in the absence of the *PT*-symmetric substrate, $n_3 = n_4 = n_1 = n_6 = 1.33$, (**b**). For visibility, $L_c = L_2 = L_5 = 50$ nm with $n_c = 1.33 + 10^{-4}i$ is used and represented by gray shaded areas. Chirality-dependent $\Delta\alpha(z_6)$ is denoted by blue downward and red upward arrows.

References

[1] Chong YD, Ge L, Stone AD. "PT-symmetry breaking and laser-absorber modes in optical scattering systems," *Phys Rev Lett* 2011, **106**(9)**:** 093902.

[2] Lindell IV, Sihvola AH, Tretyakov SA, Viltanen AJ., *Electromagnetic Waves in Chiral and Bi-Isotropic Media,* Artech House Publishers, 1994.

[3] Deparis O., "Poynting vector in transfer-matrix formalism for the calculation of light absorption profile in stratified isotropic optical media," *Opt Lett* 2011, **36**(20)**:** 3960-3962.

Tailoring microcavity lasers for parallel ultrafast random bit generation

HUI CAO

Department of Applied Physics, Yale University, New Haven, USA
hui.cao@yale.edu

Abstract:

Random numbers are widely used for information security, cryptography, stochastic modeling, and quantum simulations. Key technical challenges for physical random number generation are speed and scalability. We demonstrate a method for ultrafast generation of hundreds of random bit streams in parallel with a single laser diode. Spatio-temporal interference of many lasing modes in a specially designed microcavity is introduced as a scheme for greatly accelerated random bit generation. Spontaneous emission, caused by quantum fluctuations, produces stochastic noise that makes the bit streams unpredictable and nonreproducible. We achieve a total bit rate of 250~Tb/s with off-line post-processing, which is more than two orders of magnitude higher than the current post-processing record. Our approach is robust, compact, energy efficient, and should impact applications in secure communication and high-performance computation.

Nonlinear crystalline WGM resonators – Quantum information & telecommunication

HARALD G. L. SCHWEFEL[1,2]

[1]*The Dodd-Walls Centre for Photonic and Quantum Technologies, New Zealand*
[2]*Department of Physics, University of Otago, Dunedin, New Zealand*
[1]*harald.schwefel@otago.ac.nz*

Abstract: I will present two related but different means of communication between 1) quantum computers based on microwave circuits and 2) classical communication based on coherent frequency combs. Central to both are nonlinear crystalline WGM resonators.

1. Introduction

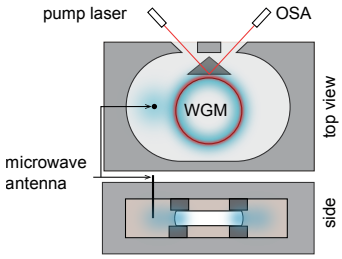

Fig. 1 Optical and Microwave cavity used

Quantum information technology based on superconducting microwave qubits has boosted the interest in converting quantum states from the microwave to the optical domain. Optical photons, unlike microwave photons, do not face high transmission losses or strong decoherence at room temperature making them suitable for long distance quantum communication. Moreover, the optical domain offers access to a large set of very well developed quantum optical tools, such as highly efficient single-photon detectors and long-lived quantum memories.

I will present a method to efficiently mix microwave and optical fields within a high quality crystalline whispering gallery mode (WGM) resonator [1]. The system is based on a high-quality diamond turned and polished, millimetre sized lithium niobate (LN) WGM resonator, coupled to a microwave cavity (see Fig. 1).

In the WGM resonator both the microwave and the optical fields are enhanced close to the rim of the WGM resonator and strong mixing mediated by the high second order nonlinearity in LN allows for both Sum- and Difference Frequency Generation (SFG & DFG).

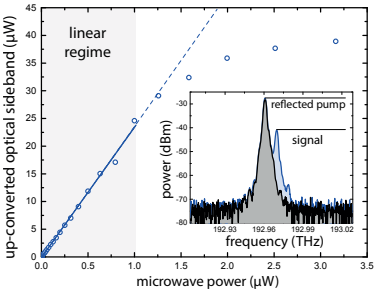

Fig. 2 Single sideband up-conversion

2. Microwave-to-optical frequency conversion

In the limit of low microwave powers only the first sidebands exist (see Fig. 2). Carefully selecting an avoided crossing of two intrinsically coupled optical modes results in an asymmetric spectrum of the optical modes, which can be tuned such that only SFG is allowed. This fundamentally noiseless process can transfer the quantum state of an individual microwave photon into the optical domain [2]. I will discuss the current state of our efforts in achieving this conversion in a cryogenic environment.

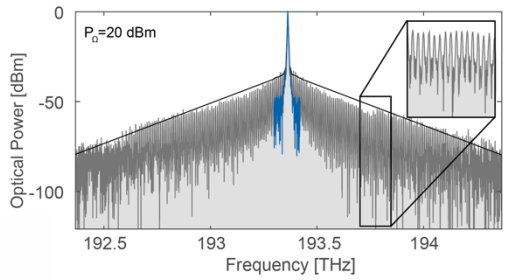

Fig. 3 More than 180 frequency comb lines.

3. Electro-optic frequency comb generation

In a system with symmetrically spaced optical modes and high microwave powers, both SFG and DFG can cascade leading to a comb with more than 180 comb lines at modest microwave and optical powers [3] (Fig. 3). I will discuss the width of the comb and its use in wavelength division multiplexing in the telecommunication domain.

[1] D. V. Strekalov, C. Marquardt, A. B. Matsko, H. G. L. Schwefel, and G. Leuchs, J. Opt. **18**, 123002 (2016).
[2] A. Rueda, F. Sedlmeir, M. C. Collodo, U. Vogl, B. Stiller, G. Schunk, D. V. Strekalov, C. Marquardt, J. M. Fink, O. Painter, G. Leuchs, and H. G. L. Schwefel, Optica, **3**, 597–604 (2016).
[3] A. Rueda, F. Sedlmeir, M. Kumari, G. Leuchs, and H. G. L. Schwefel, Nature **568**, 378 (2019).

Theory of Reflectionless Scattering modes

A. DOUGLAS STONE[1]

[1]*Department of Applied Physics and Yale Quantum Institute, Yale University, New Haven, CT USA*

Abstract: We present a general theory of reflectionless excitation of arbitrary resonant electromagnetic structures based on analytic properties of the S-matrix and a generalized reflection matrix. New types of exceptional points are identified with interesting physical properties.

1. Summary

Coupling an input wave into or through a scattering structure without any reflection is a ubiquitous challenge in all of wave physics, both classical and quantum. While reflectionless perfect transmission through parity symmetric 1D resonant structures is a familiar text book topic, the conditions for reflectionless excitation of general, non-symmetric structures in multi-channel, 2D and 3D geometries have not previously been elucidated in terms of a general theoretical and computational framework. Here I will describe such a theory[1,2], which is based on general analytic properties of the scattering matrix, and applies to the linear wave equations of optics and photonics, acoustics and quantum mechanics. It is shown that for finite resonant structures there exist a countably infinite number of complex frequencies at which such reflectionless harmonic solutions occur, which correspond to adapted input wavefronts, determined by eigenvectors of a generalized reflection matrix with eigenvalue equal to zero. We refer to such discrete solutions as R-zeros when they are complex, and as reflectionless scattering modes (RSMs), when they occur at real frequency. A special case of this is Coherent Perfect Absorption or time-reversed lasing, for which the energy is completely absorbed when the time-reverse of the analogous lasing mode is imposed on the system[3]. However in the new, more general theory, these solutions can be fully transmitted into any specified set of output channels of a lossless structure, as well being partially absorbed or amplified in systems with absorption or gain. RSMs correspond to steady-state harmonic solutions and either require the system to have a symmetry (typically Parity-Time (PT)), or require the existence of one tunable structural parameter to achieve RSM. However R-zeros can also be excited with transient (pulsed) inputs corresponding to a complex frequency excitation. Degeneracy of two RSMs corresponds to a new kind of exceptional point (EP), not previously studied, and leads to an increase in the bandwidth of the perfect absorption or transmission resonance[1,2,4]. We will present experimental results showing excitation of RSMs and RSM-EPs in ring resonators[4] and in microwave circuits. We will also show simulations and experimental results for microwave frequencies demonstrating that RSMs can be optimized to perform photonic processing functions such as demultiplexing of signals

References

1. William R. Sweeney, Chia Wei Hsu, and A. D. Stone, "Theory of Reflectionless Scattering Modes", Phys. Rev. A, 2020, https://link.aps.org/doi/10.1103/PhysRevA.102.063511
2. "Reflectionless excitation of arbitrary photonic structures: A general theory", A. D. Stone, W.R. Sweeney,C._W. Hsu,K. Wisal, and Z. Wang, Nanophotonics, 10.1515/nanoph-2020-0403.
3. Y.D. Chong, L. Ge, H. Cao, and A.D. Stone, "Coherent Perfect Absorbers: Time-reversed lasers", Phys. Rev. Lett., **105**, 053901 (2010).
4. C. Wang, W. R. Sweeney, A. D. Stone, and Lan Yang, "Coherent perfect absorption at an exceptional point", *Science* **373** (6560), 1261-1265, (2021).

Universal Single-Mode Lasing in Fully-Chaotic Microcavity Lasers

MENGYU YOU[1,*], KOTA MAKINO[1], DAISUKE SAKAKIBARA[1], YONOSUKE MORISHITA[1], SUSUMU SHINOHARA[2], SATOSHI SUNADA[3], TAKAHISA HARAYAMA[1]

[1]*Department of Pure and Applied Physics, School of Advanced Science and Engineering, Waseda University, 3-4-1 Okubo, Shinjuku-ku, Tokyo 169-8555, Japan*
[2]*Telecognix Corporation, 58-13 Shimooji-cho, Yoshida, Sakyo-ku, Kyoto 606-8314, Japan*
[3]*Faculty of Mechanical Engineering, Institute of Science and Engineering, Kanazawa University, Kakuma-machi Kanazawa, Ishikawa 920-1192, Japan*
[*]*mengyuyou@akane.waseda.jp*

Abstract: By numerically and experimental investigating the lasing states with three different fully-chaotic microcavity lasers, we showed that single-mode lasing occurs even when many resonant modes have positive gain. This result supports the universal single-mode lasing conjecture in fully-chaotic microcavity lasers.

Recently, the dependence of a cavity shape on the spectral properties of lasing states has been studied [1-3]. In case of continuous-wave pumping, it was experimentally observed that semiconductor microlasers with a fully-chaotic cavity exhibit single-mode lasing, while those with a non-chaotic cavity (e.g., ellipse) show multi-mode lasing [2]. For fully-chaotic cavities, the field intensity distributions of resonant modes tend to spread over the cavity, which results in a high modal overlap between any pair of resonant modes. This modal property can lead to suppression of the lasing of secondary modes [4]. Because the high modal overlap is a general property of fully-chaotic cavities, the single-mode lasing is expected to be universal for these cavities [4]. The validity of this universal single-mode lasing conjecture has been numerically verified for relatively small cavities where a limited number of modes interact [5]. However, its validity has not yet been systematically studied for a larger cavity where many modes compete with each other for obtaining gain.

In this study, we used the Schrödinger-Bloch (SB) model [6], an approximate model of the MB model, for numerically simulating lasing states for three different fully-chaotic cavities shown in Fig. 1, i.e., the D-shaped, cardioid, and stadium cavities, all of which are rigorously proved to exhibit fully-chaotic ray dynamics. The SB model is numerically much less expensive than the MB model. Thus, it is suitable for simulating a relatively large cavity.

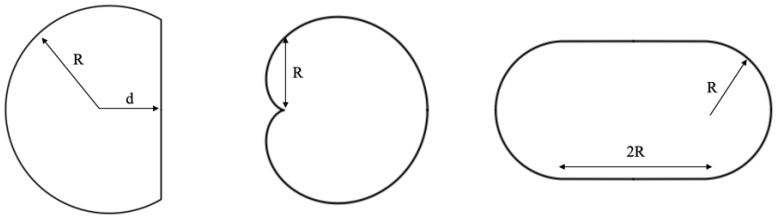

Fig. 1. Fully-chaotic cavities used in this study. From left to right: D-shaped, cardioid, and stadium.

Figure 2 shows a resonance distribution of the D-shaped cavity with refractive index 3.3 superposed by a gain region (blue area). Although many modes are in the gain region and thus have positive gain, we found that the stationary lasing state of the SB model is a single mode. Figure 3 shows a typical field intensity distribution of the single-mode stationary lasing state, whose spectrum is shown in Fig. 4. The semi-log plot of the spectral data clearly shows that there is no secondary lasing mode. Although the single-mode lasing has been already reported for a relatively small cavity ($nkR \approx 15$) [5], here we confirmed it for a much larger cavity ($nkR \approx 100$) where many modes are in the gain region. For the other fully-chaotic cavities (i.e., cardioid ($nkR \approx 100$), and stadium cavities ($nkR \approx 70$)), we confirmed qualitatively similar results. In addition, fabricating semiconductor microlasers with the above three cavity shapes, we experimentally observed single-mode lasing for higher pumping powers.

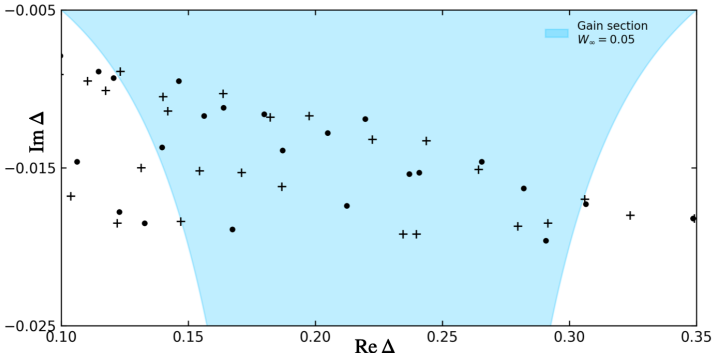

Fig. 2. Resonance distribution in the complex wavenumber plane for the D-shaped cavity. The filled circles and pluses represent even parity and odd parity modes, respectively.

In conclusion, we numerically and experimentally demonstrated that single-mode lasing occurs in all of these three cavities. This result validates the universal single-mode lasing conjecture. Detailed conditions for the occurrence of the single-mode lasing will be reported in the presentation.

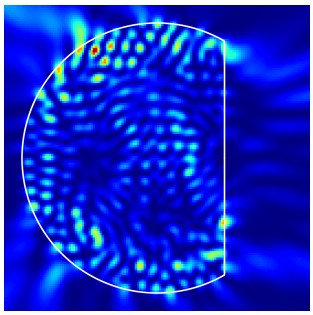

Fig. 3. Typical field intensity distribution of the single-mode stationary lasing state of the D-shaped microcavity laser numerically simulated by the Schrödinger-Bloch model.

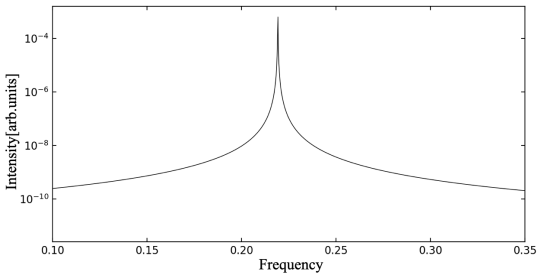

Fig. 4. Spectrum (semi-log plot) of the single-mode stationary lasing state corresponding to Fig. 3.

References

1. S. Sunada, S. Shinohara, T. Fukushima, T. Harayama, and M.Adachi, "Stable Single-Wavelength Emission from Fully Chaotic Microcavity Lasers", Phys. Rev. A. **88**, 013802 (2013).
2. S. Sunada, S. Shinohara, T. Fukushima, and T. Harayama, "Signature of Wave Chaos in Spectral Characteristics of Microcavity Lasers", Phys. Rev. Lett. **116**, 203903 (2016).
3. B. Redding, A. Cerjan, X. Huang, M. L. Lee, A. D. Stone, M. A. Choma, and H. Cao, "Low spatial coherence electrically pumped semiconductor laser for speckle-free full-field imaging." Proceedings of the National Academy of Sciences **112**.5, 1304-1309 (2015).
4. T. Harayama, S. Sunada, and S. Shinohara, "Universal Single-Mode Lasing in Fully Chaotic Two-Dimensional Microcavity Lasers under Continuous-Wave Operation with Large Pumping Power", Photon. Res. **5**, B39-B46 (2017).
5. M. Yoshikawa, M. Tonosaki, S. Shinohara, S. Sunada and T. Harayama, "Numerical Verification of Single-Mode Lasing in a D-Shaped Microcavity Laser", The 2nd International Workshop on Asymmetric Microcavity and Wave Chaos (2018).
6. T. Harayama, S. Sunada, and K.S. Ikeda, "Theory of Two-Dimensional Microcavity Lasers", Phys. Rev. A **72**, 013803 (2005).

Iontronic bio-chemical sensing using photonic crystal nanolasers

TOSHIHIKO BABA

Department of Electronic and Computer Engineering, Yokohama National University, Japan
baba-toshihiko-zm@ynu.ac.jp

Abstract: GaInAsP semiconductor photonic crystal nanolaser can be a bio-chemical sensor that detects both environmental index and iontronic properties, which allow simple sensing and/or ultrahigh sensitivity. Principles and examples of the sensing will be presented.

The GaInAsP semiconductor photonic crystal nanolaser operates at room temperature by photopumping and emits near-infrared light at a wavelength longer than 1.3 μm [1-3]. Immersion of the nanolaser in a solution causes its laser characteristics to change. Observation of this phenomenon makes it possible to perform biosensing without a fluorescent label or a chromogenic substrate. The most common phenomenon between many photonic sensors is that the resonance wavelength reflects the refractive index of attached media; an index change of 2.5×10^{-4} in the surrounding liquid can be measured through an emission wavelength shift without stabilization [1,4]. This effect is applicable to detecting environmental toxins and cell behaviors [5,6]. The laser emission intensity also reflects the electric charge of surface ions [7,8]. The intensity varies when an electrolyte or a negatively charged deoxyribonucleic acid (DNA), which is positively or negatively charged in water, is accumulated on the surface. This effect allows us to detect the antigen-antibody reaction of a biomarker protein from only the emission intensity without any kind of spectroscopy [9]. In detecting a small amount of DNA or protein, a wavelength shift also appears from its concentration that is 2–3 orders of magnitude lower than those of the conventional chemical methods, such as the enzyme-linked immuno-solvent assay [10-12]. It is unlikely that this wavelength behavior at such low concentrations is due to the refractive index of the biomolecules. It is observed that the electric charge of surface ions is induced by various means, including plasma exposure and an electrochemical circuit shifting the wavelength [13,14]. This suggests that the superhigh sensitivity is also due to the effect of charged ions. Thus, we call this device an iontronic photonic sensor. This presentation focuses on such a novel sensing scheme of nanolaser sensor, as an example of resonator-based photonic sensors, in addition to the conventional refractive index sensing.

This work was supported by Grant-in-Aid #16H06334 from the Ministry of Education Culture, Sports, Science and Technology, Japan.

References

1. S. Kita, K. Nozaki, S. Hachuda, H. Watanabe, Y. Saito, S. Otsuka, T. Nakada, Y. Arita and T. Baba, “Photonic crystal point-shift nanolaser with and without nanoslots --- design, fabrication, lasing and sensing characteristics”, IEEE J. Sel. Top. Quantum Electron. (2011)
2. M. Narimatsu, S. Kita, H. Abe and T. Baba, “Enhancement of vertical emission in photonic crystal nanolasers,” Appl. Phys. Lett. (2012).
3. T. Watanabe, H. Abe, Y. Nishijima and T. Baba, "Array integration of thousands of photonic crystal nanolasers", Appl. Phys. Lett., (2014).
4. S. Kita, K. Nozaki and T. Baba, “Refractive index sensing utilizing a cw photonic crystal nanolaser and its array configuration”, Opt. Express (2008).
5. D. Takahashi, S. Hachuda, T. Watanabe, Y. Nishijima and T. Baba, "Detection of endotoxin using a photonic crystal nanolaser", Appl. Phys. Lett. (2015).
6. H. Abe, M. Narimatsu, T. Watanabe, T. Furumoto, Y. Yokouchi, Y. Nishijima, S. Kita, A. Tomitaka, S. Ota, Y. Takemura and T. Baba, “Living-cell imaging using a photonic crystal nanolaser array,” Opt. Express (2015).
7. K. Watanabe, Y. Kishi, S. Hachuda, T. Watanabe, M. Sakemoto, Y. Nishijima and T. Baba, "Simultaneous detection of refractive index and surface charges in nanolaser biosensors", Appl. Phys. Lett. (2015).
8. M. Sakemoto, Y. Kishi, K. Watanabe, H. Abe, S. Ota, Y. Takemura and T. Baba, “Cell imaging using GaInAsP semiconductor photoluminescence”, Opt. Express (2016).
9. K. Watanabe, M. Nomoto, F. Nakamura, S. Hachuda, A. Sakata, T. Watanabe, Y. Goshima and T. Baba, “Label-free and spectral-analysis-free detection of neuropsychiatric disease biomarkers using an ion-sensitive GaInAsP nanolaser biosensor”, Biosen. Bioelectron. (2018).
10. S. Kita, S. Otsuka, S. Hachuda, T. Endo, Y. Imai, Y. Nishijima, H. Misawa and T. Baba, “Super-sensitivity in label-free protein sensing using nanoslot nanolaser”, Opt. Express (2011).
11. S. Hachuda, S. Otsuka, S. Kita, T. Isono, M. Narimatsu, K. Watanabe, Y. Goshima and T. Baba, “Selective detection of sub-atto-molar streptavidin in 1013-fold impure sample using photonic crystal nanolaser sensors”, Opt. Express (2013).
12. S. Hachuda, T. Watanabe, D. Takahashi and T. Baba, “Sensitive and selective detection of prostate-specific antigen using a photonic crystal nanolaser”, Opt. Express (2016).
13. T. Watanabe, Y. Saijo, Y. Hasegawa, K. Watanabe, Y. Nishijima and T. Baba, "Ion-sensitive photonic-crystal nanolaser sensors," Opt. Express (2017)
14. Y. Saijo, K. Watanabe, T. Watanabe, Y. Terada, Y. Nishijima and T. Baba, "Iontronic control of GaInAsP photonic crystal nanolaser", Appl. Phys. Lett. (2019).

Chaos microcavity lasers for random number generation due to internal mode injection

YONG-ZHEN HUANG, CHUN-GUANG MA, ZHI-XIONG XIAO, JIN-LONG XIAO, YUE-DE YANG

State Key Laboratory of Integrated Optoelectronics, Institute of Semiconductors, Chinese Academy of Sciences, Beijing 100083, China & Center of Materials Science and Optoelectronics Engineering, University of Chinese Academy of Sciences, Beijing 100049, China. Email: *yzhuang@semi.ac.cn*

Abstract: Chaos state was realized in a circular-side hexagonal microcavity laser with multiple mode interaction, and was applied to generate high speed random numbers.

The generations of truly random numbers are greatly demanded for classical and quantum cryptography systems require to ensure unpredictable parameters. Chaos external-cavity semiconductor lasers have been investigated for physical random bit generations, which usually have the time-delay periodicity and requires a fine-tuning of the external cavity. In this talk, a compact physical random number generator is demonstrated utilizing a chaos microlaser by adjusting multiple mode oscillation for realizing internal mode injection. A circular-side hexagonal resonator (CSHR) was designed for enhancing mode Q factors and controlling mode structure with a ring p-electrode [1,2]. As shown in Fig. 1(a), circular-side was introduced to enhance mode Q factors for realizing dual-mode lasing as in square microcavity lasers [3], and the ring electrode was used to adjust transverse mode interval [1]. For a 10-μm-side-length CSHR microlaser with a circular deformation of 1.015 μm, the wavelength interval between two transverse modes was varied from 0.176 to 0.1 nm with an intensity ratio less than 3 dB by increasing injection current. The lasing spectra and corresponding radio-frequency (RF) spectra were measured by an optical spectrum analyzer and a setup in Fig. 1(b). The lasing spectra and RF spectra indicate that the microlaser can be adjusted among chaos state, four-wave mixing state and period-two oscillation state buy varying injection current. For the chaos state, the microwave signal shows a large bandwidth without any significant narrow peak suitable generate random bit. Random bit generation with a bit-rate of 10 Gbit/s is demonstrated using the microlaser under the spontaneous chaos state. The Correlation Dimension of 5.46 is calculated from obtained random data. Furthermore, three mode with frequency intervals about 10 GHz and Q factors larger than 1000 were obtained by a 2D finite-element method, the corresponding mode field patterns are shown in Fig. 1(c) where intensities in the upper regions are magnified. The triple modes are composed the fundamental and the first order transverse modes of hexagonal periodic orbits and one triangular periodic orbit [4]. The tri-mode rate equation with interactional injection terms can also yield chaos state.

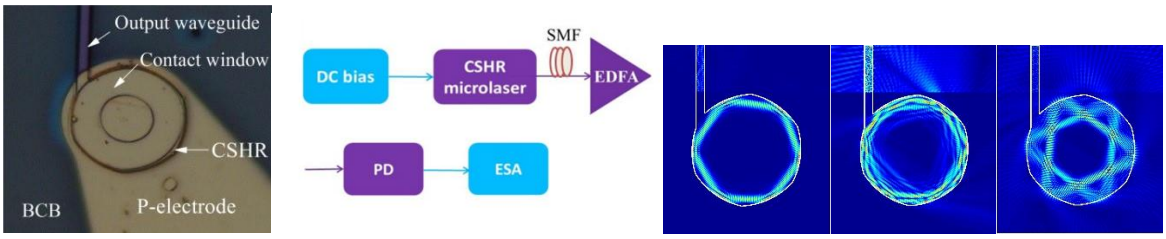

(a) (b) (c)

Fig. 1. (a) Microscope picture of a CSHR microlaser, (b) schematic for RF signal generation, SMF: single-mode fiber, EDFA: erbium-doped fiber amplifier, PD: photodetector, ESA: electric spectrum analyzer, and (c) mode field patterns of three near degenerate modes

References

1. H. Long, Y. Z. Huang, X.W. Ma, Y. D. Yang, J. L. Xiao, L. X. Zuo, and B. W. Liu "Dual-transverse-mode microsquare lasers with tunable wavelength interval," Opt. Lett. 40, 3548-3551 (2015).
2. Z. X. Xiao, Y. Z. Huang, Y. D. Yang, M. Tang, and J. L. Xiao, "Modulation bandwidth enhancement for coupled twin-square microcavity lasers," Opt. Lett. 42, 3173-3176 (2017).
3. H. Z. Weng, Y. Z. Huang, Y. D. Yang, X. W. Ma, J. L. Xiao, and Y. Du, "Mode Q factor and lasing spectrum controls for deformed square resonator microlasers with circular sides," Phys. Rev. A, 95, 013833(2017).
4. Y. D. Yang, M. Tang, F. L. Wang, Z. X. Xiao, J. L. Xiao, and Y. Z. Huang, "Whispering-gallery mode hexagonal micro/nano-cavity lasers," Photon. Res., 7, 594-607(2019)

Exceptional points in optical microdisk cavities

JAN WIERSIG[1,*]

[1] *Institut für Physik, Otto-von-Guericke-Universität Magdeburg, Postfach 4120, D-39016 Magdeburg, Germany*
[*] *jan.wiersig@ovgu.de*

Abstract: First, we theoretically demonstrate exceptional points in weakly deformed whispering-gallery cavities. Second, we discuss the relation between Hamiltonian and Liouvillian exceptional points in systems with parametric noise.

1. Introduction

Optical microcavities are the key elements for modern light-emitting devices such as single-photon emitters, ultralow-threshold lasers, and sources of entangled photon pairs. An important subclass are whispering-gallery cavities, e.g. microdisks and microtoroids, where the light is trapped for a long time by total internal reflection at the boundary of the cavity. Deforming or perturbing the boundary of whispering-gallery cavities can be beneficial for several applications [1], e.g. directional free-space light emission and mode discrimination.

Optical microcavities, and in fact all real physical systems, are open systems. The emerging field of non-Hermitian physics deals with the resulting phenomena such as mode nonorthogonality and spectral degeneracies, so-called exceptional points (EPs). In contrast to conventional degeneracies, at an EP not only eigenvalues but also the corresponding eigenstates of the non-Hermitian Hamiltonian coalesce. A number of experiments have proven the existence of EPs in various physical systems including optical microcavities. Applications of EPs are, for instance, ultrasensitive sensors for single-particle detection and orbital angular momentum microlasers.

2. EPs in weakly deformed microdisk cavities

Exploiting a perturbation theory for weakly deformed cavities we derive a non-Hermitian Hamiltonian for up to four modes with nearly-degenerate frequencies. From the non-Hermitian Hamiltonian we deduce boundary deformations which give rise to EPs of second, third, and fourth order. We confirm the existence of EPs in extremely weakly deformed microdisks by a comparison to full numerics [2,3].

3. Hamiltonian and Liouvillian EPs in noisy non-Hermitian systems

We discuss the impact of fluctuating system parameters on the performance of EP-based sensors. We adapt a transparent Lindblad-type formalism which allows us to study the resolvability of the energy splitting and the dynamical stability of the sensor in a unified manner by comparing the behavior of Hamiltonian and Liouvillian EPs.

References

1. H. Cao and J. Wiersig, "Dielectric microcavities: Model systems for wave chaos and non-Hermitian physics", Rev. Mod. Phys. 87, 61 (2015)
2. J. Kullig, C.-H. Yi, and J. Wiersig, "Exceptional points by coupling of modes with different angular momenta in deformed microdisks: A perturbative analysis", Phys. Rev. A 98, 023851 (2018)
3. J. Kullig and J. Wiersig, "High-order exceptional points of counterpropagating waves in weakly deformed microdisk cavities", Phys. Rev. A 100, 043837 (2019)
4. J. Wiersig, “Robustness of exceptional-point-based sensors against parametric noise: The role of Hamiltonian and Liouvillian degeneracies”, Phys. Rev. A 101, 053846 (2020)

Nonreciprocal response and transport theory of non-Hermitian materials

HENNING SCHOMERUS

[1] *Department of Physics, Lancaster University, Lancaster, LA1 4YB, UK*

Abstract: I describe the response and transport characteristics of non-Hermitian systems with directed couplings, and highlight the effect on topological states.

1. Introduction

Photonic crystals and metamaterials present versatile band structure effects that allow to efficiently confine and guide light to predestined locations. In recent years, the range of such mechanisms has been enhanced by topological concepts, which have been transferred from the electronic to the photonic domain. An important new ingredient appearing the photonic setting are losses through leakage or in the medium. These make the effective description of the systems non-Hermitian, a situation for which structural confinement and topological protection is not well understood. Additional complications arise when these losses are directed, and hence break non-reciprocity.

2. Details

I present two general and complementary frameworks addressing the response [1] and transport [2] of nonreciprocal non-Hermitian systems, and use this to describe a range of unique effects related to topological zero-modes in such systems. On the response side, this concern a dynamical phase transition, where the system becomes a directed sensor as the zero mode changes its biorthogonal structure. On the transport side, this concerns the reflectionless transport in a direction that depends on the topological phase, invisibility coinciding with the skin-effect phase transition of topological edge states, and coherent perfect absorption in a system that is transparent when probed from one side.

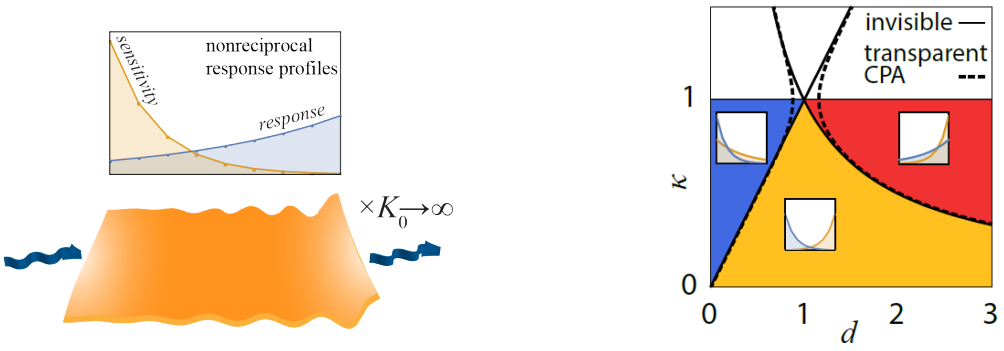

Fig. 1. (a) Directional instability induced by a nonreciprocity-driven phase transition of a topological zero mode. (b) Transport phase diagram relating this transition to conditions of invisibility, transparency, and coherent perfect absorption (CPA).

References

[1] Henning Schomerus, Phys. Rev. Research 2, 013058 (2020).
[2] Hamed Ghaemi-Dizicheh and Henning Schomerus, Phys. Rev. A 104, 023515 (2021)

Chaotic modes in dielectric cavities: What we know and don't know

ROLAND KETZMERICK

Technische Universität Dresden, Institut für Theoretische Physik, 01062 Dresden, Germany

Abstract: We explain the multifractal structure of chaotic modes, how it depends on the quality factor, and its universal fluctuations. We analyze 10^4 modes at small wave lengths ($nkR=10^4$) for a limaçon dielectric cavity.

The talk presents unpublished work [1] on the structure of chaotic modes in dielectric cavities in position and phase space, see Fig.1. This is done about an order of magnitude further in the small wave length limit ($nkR=10^4$) than previous work and corresponds to experimental settings. The analysis is motivated by recent findings for quantum maps with escape [2-5]. We explain the average multifractal structure of modes depending on the quality factor, based on unstable and stable directions of chaotic ray dynamics. Intensity fluctuations of individual modes on top of the average multifractal structure are shown to be universally exponentially distributed, as in chaotic quantum billiards. Open questions are addressed.

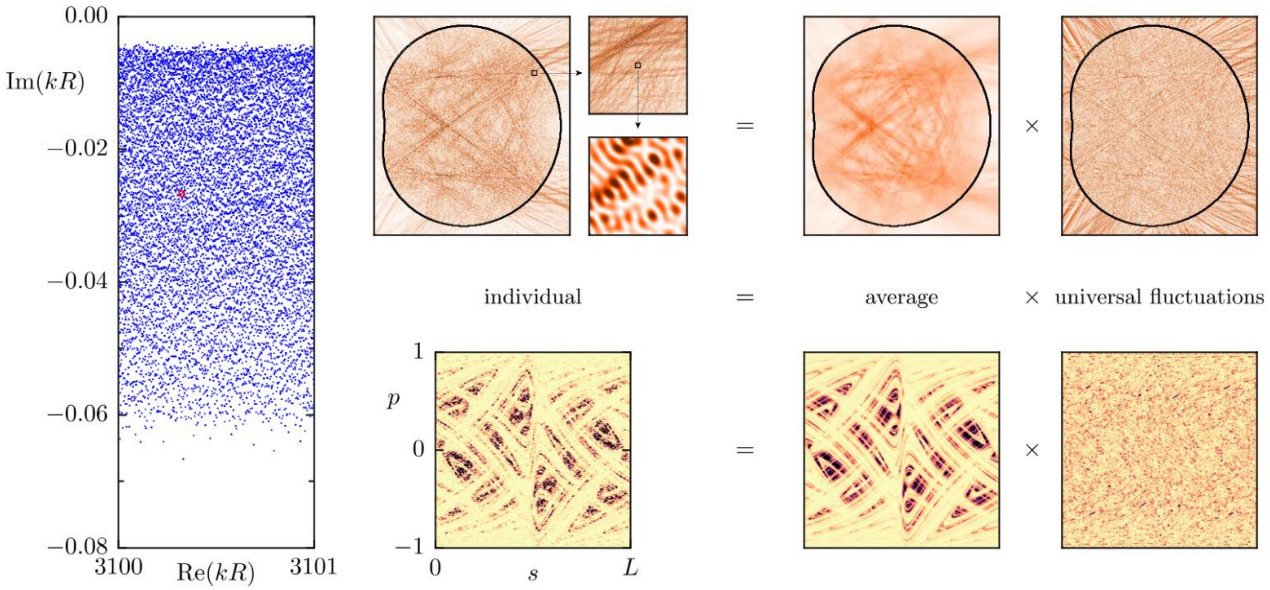

Fig. 1. (Left) Spectrum of 9964 antisymmetric TM polarized modes of limaçon cavity with n=3.3. (Top) Highlighted mode shown in position space with two consecutive magnifications by a factor 20 each and (bottom) on boundary phase space. Intensities in both cases are described by average multifractal mode structure at this quality factor multiplied by universal fluctuations.

References

1. Ketzmerick, Clauß, Fritzsch, Bäcker, in preparation.
2. Clauß, Körber, Bäcker, Ketzmerick, "Resonance eigenfunction hypothesis for chaotic systems," Phys. Rev. Lett. **121**, 074101 (2018).
3. Clauß, Altmann, Bäcker, Ketzmerick, "Structure of resonance eigenfunctions for chaotic systems with partial escape," Phys. Rev. E **100**, 052205 (2019).
4. Clauß, Kunzmann, Bäcker, Ketzmerick, "Universal intensity statistics of multifractal resonance states", Phys. Rev. E **103**, 042204 (2021).
5. Clauß, Ketzmerick, "Local random wave model for semiclassical fractal structure of chaotic resonance states", arXiv:2112.12626

Observation of Collective Superstrong Coupling of Cold Atoms to a 30-m Long Optical "Microresonator"

ARNO RAUSCHENBEUTEL

Institute of Physics, Humboldt-Universität zu Berlin, 10099 Berlin, Germany
arno.rauschenbeutel@hu-berlin.de

Abstract: A largely unexplored regime of cavity QED is reached when emitters interact strongly with several longitudinal cavity modes. We realize this superstrong coupling with a small atomic ensemble coupled to a 30-m long optical resonator.

1. Introduction

A milestone in the endeavor of controlling light–matter interaction at the fundamental quantum-mechanical level was the realization of strong coupling between single quantum emitters and single photons in cavity QED [1]. In ensuing experiments, this achievement led to a variety of applications [2]. Interfacing the resonator mode simultaneously with many identical quantum emitters such as neutral atoms not only allowed extremely large collective light-matter coupling strengths to be reached [3], but also initiated new approaches for quantum devices. Furthermore, in such systems, the resonator mode can be employed to provide an infinite-range interaction between the different atomic qubits, a key ingredient for the study of the quantum dynamics of collective light-matter systems.

2. Realizing the Superstrong Coupling Regime in Cavity QED

A largely unexplored regime of cavity QED is reached when a single emitter or an ensemble of emitters interacts strongly with several nondegenerate, longitudinal modes of a long cavity. This scenario bridges the gap between two archetypical regimes of light-matter interaction: the strong coupling of emitters to a single resonantly enhanced field mode, giving rise to, e.g., vacuum-induced Rabi oscillations [4], and the coupling of emitters to a single spatial mode with a continuous spectrum, enabling applications such as efficient single-photon sources. In this regime of so-called superstrong coupling [5], the emitter-resonator coupling strength exceeds the free-spectral range (FSR) of the resonator as well as the single-emitter decay rate. Here, we report on the realization of superstrong coupling (SSC) with a small ensemble of atoms that is coupled to a 30-m long optical fiber ring resonator [6]. In the transmission spectrum, several longitudinal cavity resonances are significantly modified and collective coupling strengths largely exceeding the FSR are observed. Remarkably, SSC is reached in our experiment with as little as 200 atoms. At the same time, we infer an intrinsic single-atom cooperativity of 0.13, meaning that the system's dynamics depends on a quantized degree of freedom and its response will be nonlinear at the level of a few photons.

3. Summary

The experimental realization of superstrong coupling sets the stage for devising novel applications and for the scientific exploration of optical cavity QED in an entirely new regime. For example, the expected non-Markovian dynamics of our experimental system is challenging theoretically and uncharted experimentally. In this context, pulsed revivals of the atomic inversion on the time scale of the round-trip time of the resonator, rather than sinusoidal vacuum Rabi oscillations, have been predicted [7]. Moreover, the interaction of different cavity modes that occurs under the condition of SSC, in conjunction with the substantial single-atom cooperativity, should enable resonator-enhanced wave mixing of fields containing only a few photons each. Finally, our system may also pave the way towards the implementation of quantum annealing algorithms using atoms or photons as carriers of information.

References

1. H. J. Kimble, "Strong interactions of single atoms and photons in cavity QED," Phys. Scr. **T76**, 127 (1998).
2. A. Reiserer and G. Rempe, "Cavity-based quantum networks with single atoms and optical photons," Rev. Mod. Phys. **87**, 1379 (2015).
3. Y. Colombe, T. Steinmetz, G. Dubois, F. Linke, D. Hunger, and J. Reichel, "Strong atom–field coupling for Bose–Einstein condensates in an optical cavity on a chip," Nature **450**, 272 (2007).
4. M. Brune, F. Schmidt-Kaler, A. Maali, J. Dreyer, E. Hagley, J. M. Raimond, and S. Haroche, "Quantum Rabi Oscillation: A Direct Test of Field Quantization in a Cavity," Phys. Rev. Lett. **76**, 1800 (1996).
5. D. Meiser and P. Meystre, "Superstrong coupling regime of cavity quantum electrodynamics," Phys. Rev. A **74**, 065801 (2006).
6. A. Johnson, M. Blaha, A. E. Ulanov, A. Rauschenbeutel, P. Schneeweiss, and J. Volz, "Observation of Collective Superstrong Coupling of Cold Atoms to a 30-m Long Optical Resonator," Phys. Rev. Lett. **123**, 243602 (2019).
7. D. O. Krimer, M. Liertzer, S. Rotter, and H. E. Türeci, "Route from spontaneous decay to complex multimode dynamics in cavity QED," Phys. Rev. A **89**, 033820 (2014).

Advanced optoplasmonic single molecule sensing with tailored plasmonic particles

JOLLY XAVIER[1], FRANK VOLLMER

Living Systems Institute, Department of Physics and Astronomy, University of Exeter, Exeter, UK
[1]j.xavier@exeter.ac.uk

Abstract: We present our computational as well as experimental investigations on advanced optoplasmonic biosensors comprising of dielectric whispering gallery mode micro resonators combined with tailored plasmonic resonant nanoparticles for field enhanced ultra-sensitive single molecule bio-detection.

1. Introduction

The coupled photonic-plasmonic resonator system promises a leap forward in the detection and analysis of physical, chemical, and biological entities even to single molecular level. Optoplasmonic sensing schemes combine optically resonant dielectric nano/microcavities with plasmonically resonant metal nanostructures to enable detection at the nanoscale with extraordinary sensitivity even to single-ion sensing [1-3].

2. Discussion

We studied multi-wavelength optoplasmonic high sensitivity detection scheme for sensing of single biomolecules and processes by meticulously tuning the light-matter interaction in the visible and near infrared spectral regions. Our advanced optoplasmonic biosensor consists of dielectric whispering gallery mode (WGM) micro resonators combined with tailored plasmonic resonant nanoparticles for field-enhanced sensing. The computational as well as experimental observations exhibit that the controlled tailoring of the surface features of plasmonic particle such as spiked nanostructures could deterministically influence the field enhancement in optoplasmonic sensors for ultra-sensitive single molecular level biosensing which could be extended further for point-of care applications. [1, 3].

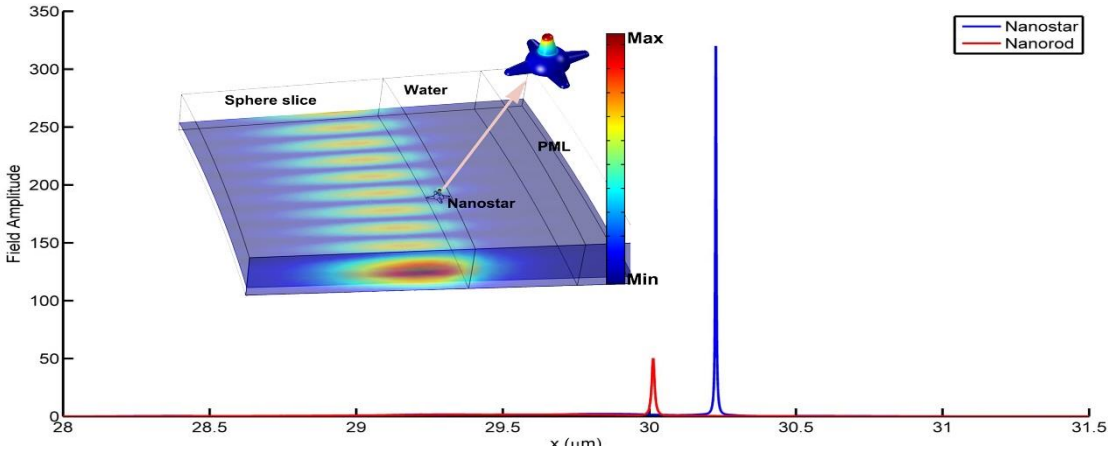

Fig. 1. Optoplasmonic sensing scheme and computational simulation exhibiting the large field enhancement for spiked plasmonic particle in comparison to plasmonic nanorods .

References

1. J. Xavier, S. Vincent, F. Meder and F. Vollmer, "Advances in optoplasmonic sensors – combining optical nano/microcavities and photonic crystals with plasmonic nanostructures and nanoparticles," Nanophotonics **7**, 1 (2018).
2. M. D. Baaske and F. Vollmer, "Optical observation of single atomic ions interacting with plasmonic nanorods in aqueous solution," Nature Photonics **10**, 733 (2016).
3. S. Subramanian H-Y. Wu, T. Constant, J. Xavier, and F. Vollmer, "Label-free optical single-molecule micro- and nanosensors," Adv. Mater. **30**, 1801246 (2018).

Spatio-temporal dynamics of wave-chaotic microlasers

Stefan Bittner[1,2], Kyungduk Kim[1], Stefano Guazzotti[3], Yongquan Zeng[4], Qi Jie Wang[4], Ortwin Hess[3], Hui Cao[1]

[1]*Department of Applied Physics, Yale University, New Haven, USA*
[2]*Chair in Photonics, LMOPS, CentraleSupélec, Université Paris-Saclay, Metz, France*
[3]*Department of Physics, Imperial College, London, United Kingdom*
[4]*School of Electrical and Electronic Engineering, Nanyang Technological University, Singapore*
[2]*stefan.bittner@centralesupelec.fr*

Abstract: We compare the spatio-temporal dynamics of wave-chaotic semiconductor microlasers and conventional broad-area lasers. While the regular Fabry-Perot cavities exhibit instabilities, the wave-chaotic microlasers exhibit stable dynamics, and their intensity distributions agree with ray dynamics predictions.

1. Introduction

The temporal dynamics of lasers is strongly influenced both by the properties of the active medium and outside perturbations such as feedback or optical injection. In particular semiconductor lasers are easily destabilized by external signals or interactions between different lasing modes, often leading to chaotic dynamics [1]. Broad-area lasers with Fabry-Perot (FP) cavities of width 50 µm or more can exhibit complex spatio-temporal instabilities due to the interaction of different transverse modes. These instabilities present serious problems for high-power applications, e.g., as pump sources or in medical surgery, and controlling them remains an important problem.
Another important factor determining the properties of a laser is of course the resonator. Asymmetric microcavities have attracted a lot of attention since their ray dynamics can be chaotic and strongly influences for example their spectra and emission directions [2]. We investigated how the spatio-temporal dynamics of wave-chaotic microlasers is influenced by cavity geometry and ray dynamics compared with conventional broad-area FP-cavities [3].

2. Experimental results

2.1 Experimental setup and fabrication

Three different cavity geometries are considered in the following (see Fig. 1 bottom): conventional broad-area FP-cavities, so-called D-cavities that are a circle from which a straight segment has been cut off, and stadium cavities that consist of a square between two semicircles. D-cavity and stadium have completely chaotic ray dynamics. The cavities are fabricated from a commercial AlGaAs quantum well epiwafer using photolithography and dry etching.
The microlasers are pumped electrically with microsecond pulses at room temperature. Their spatio-temporal dynamics is investigated by imaging one of the cavity sidewalls (see Fig. 1) onto a streak camera for time-resolved measurements or onto a CCD camera for measuring the time-integrated intensity distributions at the sidewalls using an objective with NA = 0.4.

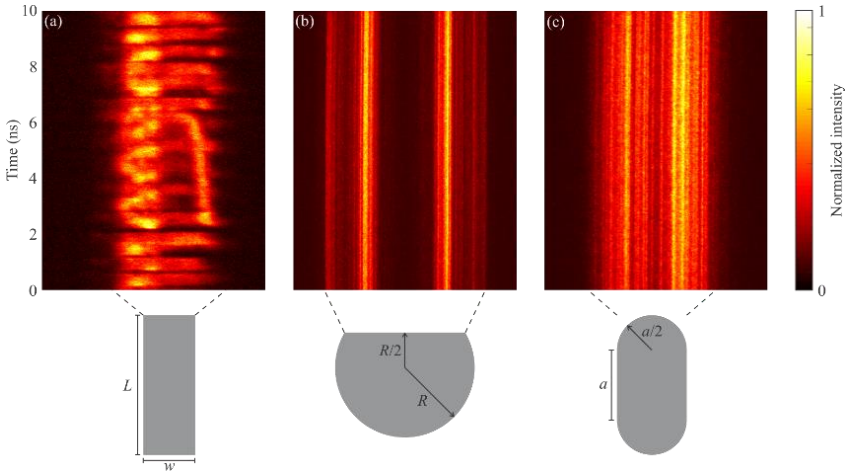

Fig. 1. Spatio-temporal dynamics of different microlasers. One of the cavity sidewalls was imaged onto the streak camera as indicated. (a) Fabry-Perot cavity with width w = 80 mm and length L = 1 mm. (b) D-cavity with R = 200 µm. (c) Stadium with a = 119 µm.

2.2 Spatio-temporal dynamics

The FP-cavities exhibit spatio-temporal instabilities and filamentation [see Fig. 1(a)], with rapid fluctuations of the output profile on a sub-nanosecond time scale. Complex, unstable spatio-temporal structures are formed due to the interaction of the optical field with the gain medium: regions of high intensity create a lensing effect due to gain depletion and the resulting increase of the refractive index caused by the decrease of the carrier density. This results in a self-focusing instability and renders broad-area FP-cavity lasers intrinsically unstable.
The spatio-temporal dynamics of the wave-chaotic D-cavity and stadium microlasers [see Figs. 1(b, c)], in contrast, shows no rapid fluctuations of the intensity profiles or the total output intensity. The complex wave interference due to the chaotic ray dynamics in these cavities prevents the formation of a lensing effect and hence self-focusing instabilities. The remaining fluctuations of the laser output are on time scales longer than 100 ns and thermally induced, whereas the intrinsic dynamics is stable [2].

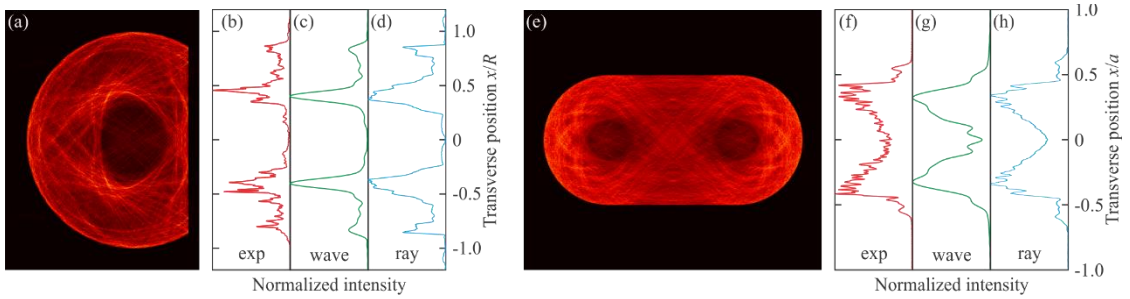

Fig. 2: Intensity distributions of (a-d) D-cavity and (e-h) stadium microcavities. (a) Average intensity distribution of 11 high-*Q* modes and sidewall emission intensity distributions from experiments (b), passive mode simulation (c) and ray tracing (d). (e) Average intensity distribution of 25 high-*Q* modes and sidewall emission intensity distributions from experiments (f), passive mode simulations (g) and ray tracing (h). The wave simulations are for cavities with refractive index $n = 3.37$, where $R = 20$ µm for the D-cavity and $a = 23.8$ µm for the stadium.

2.3 Sidewall emission intensity distributions

While the emission intensity distributions from the wave-chaotic cavities show no significant temporal variation, the intensity profiles in Figs. 1(b, c) are spatially inhomogeneous. To investigate the origin of the sidewall emission profiles, we perform numerical simulations of the passive cavity modes and the ray dynamics. Since the microlasers operate in a multi-mode regime, we consider the average of several high-*Q* modes for comparison. Figs. 2(a, e) show the average intensity distribution of several high-*Q* modes of passive resonators with D-cavity and stadium shape, respectively. The intensity distributions are inhomogeneous with caustic-like structures at the centers of the circular boundary parts due to the leakage by refractive escape from the cavities.
The measured, time-averaged sidewall emission intensity distributions in Figs. 2(b, f) show an inhomogeneous profile as well, with regions of low intensity in the middle corresponding to the caustic-like structures in Figs. 2(a, e). For a quantitative comparison of the simulations with experiments, the finite NA of the imaging optics is taken into account, resulting in the intensity distributions in Figs. 2(c, g). Furthermore, ray simulations of the long-time dynamics in the open wave-chaotic cavities were performed [see Figs. 2(d, h)]. The results from experiments, wave simulations and ray tracing show very good agreement. The inhomogeneous intensity profiles are due to the localization of the lasing modes on the unstable manifold of the chaotic saddle of the corresponding billiard systems [4]. This demonstrates that the spatial emission profiles of the wave-chaotic cavities result from their geometry alone, whereas nonlinear interactions with the active medium have no observable influence in contrast to the case of FP-cavities.

3. Summary

We demonstrated that complex interference effects in wave-chaotic cavities result in the suppression of the spatio-temporal instabilities observed in conventional broad-area Fabry-perot semiconductor lasers. Whereas the output profiles of the FP-cavities fluctuate strongly due to the nonlinear interaction of optical field and active medium, the output profiles of D-cavity and stadium microlasers are stable and are determined by the cavity geometry alone.

References

1. J. Ohtsubo, “Semiconductor Lasers - Stability, Instability and Chaos” (3rd edition, Springer, 2013).
2. H. Cao and J. Wiersig, “Dielectric microcavities: Model systems for wave chaos and non-Hermitian physics”, Rev. Mod. Phys. **87**, 61 (2015)
3. Bittner *et al*., “Suppressing spatio-temporal lasing instabilities with wave-chaotic microcavities”, Science **361**, 1225 (2018).
4. E. G. Altmann, J. S. E. Portela and T. Tél, “Leaking chaotic systems”, Rev. Mod. Phys. **85**, 869 (2013).

Optical Frequency Combs Generated via Parametric Acoustic Excitation of a SNAP Microresonator

MANUEL CRESPO-BALLESTEROS[1,2] AND MISHA SUMETSKY[1]

[1]*Aston Institute of Photonic Technologies, Aston University, Birmingham B4 7ET, UK*
[2]*m.crespo@aston.ac.uk*

Abstract: We model optical frequency comb (OFC) spectrum generated parametrically by acoustic resonant oscillations of a parabolic SNAP microresonator. We demonstrate the moderately broadband OFC generated by unstable parametric excitation.

1. Introduction

Optical frequency combs (OFC) with low repetition rates (~ 100 MHz) are critical for sensing and high-resolution spectroscopy [1-3]. Although low repetition rates can be achieved with mode-locked laser frequency combs, they are difficult to obtain by on-chip technologies such as Kerr frequency combs microresonators. Proposed solutions include the use of optomechanical effects in combination with other nonlinear phenomena [4]. A different solution has been proposed theoretically in [5], where an acoustic mode parametrically excites the optical whispering gallery modes (WGM) of a bottle microresonator. The matching condition between optical WGM frequencies and natural acoustic frequencies (~ 100 MHz) can be achieved by the ultraprecise fabrication of microresonators using the surface nanoscale axial photonics (SNAP) technology [6,7]. Here, we simulate the parametric excitation of a parabolic SNAP microresonator and analyze the regions of stability that lead to the creation of a moderately wide OFC spectrum.

2. Model

Fig. 1(a) illustrates the device proposed for the generation of OFC via parametric resonance. The system consists of a parabolic SNAP microresonator and a transverse biconical optical fiber taper with micron-diameter waist coupled to the resonator that serves as an input-output port. The microresonator is introduced by the nanoscale effective radius variation (ERV) of an optical fiber of radius r_0 (see Fig. 1(b)). To excite the appropriate acoustic mode, we propose to use the radiation pressure exerted by the light of a beating mode inside the resonator. The advantage of using the SNAP platform is that we can engineer the separation between the axial optical modes of the parabolic resonator, $\Delta\nu_{\mathrm{op}}$, so that the acoustic mode frequency is $\nu_{\mathrm{ac}} = 2\Delta\nu_{\mathrm{op}}$. The microresonator in this configuration works in the parametric resonant regime, noticeably increasing the number of modes excited.

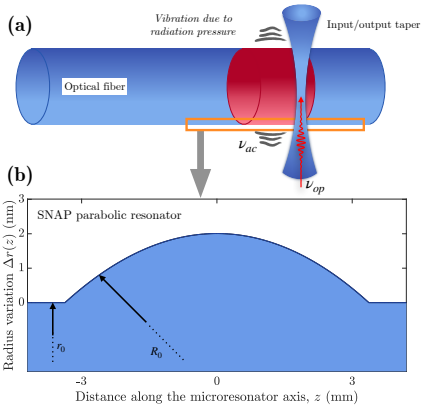

Fig. 1. (a) Illustration of the device proposed. (b) Parabolic SNAP resonator created by the nanoscale ERV of an optical fiber.

3. Theory

The propagation of a WGM with eigenfrequency ν near to a cutoff frequency ν_c obeys the Schrödinger equation [5]

$$i\frac{1}{2\pi\nu_c}\partial_t\psi = -\frac{1}{2\beta_c^2}\partial_z^2\psi - \frac{\Delta r(z,t)}{r_0}\psi + i\gamma\psi + D_0\delta(z-z_0)\psi + A_{in}(t)\delta(z-z_0) \quad (1)$$

where $\beta_c = 2\pi n_r\nu_c/c$ is the cutoff wavenumber, n_r is the refractive index of the fiber and c is the speed of light. The parameter γ accounts for the absorption losses in the fiber while parameter D_0 is the coupling of the optical fiber to the taper [8]. The source term $A_{in}(t)\delta(z-z_0)$ represents the input of light from a microfiber couple to the microresonator at position $z = z_0$. We assume that $A_{in}(t)$ is a monochromatic light source with certain switching time [5]. In equation (1), the ERV $\Delta r(z,t)$ acts as a potential well that varies in time accordingly to the mechanical vibration due to the exerted radiation pressure. For a parabolic resonator, the ERV takes the form $\Delta r(z,t) = -1/2 \cdot \Omega(t)^2 z^2$. For the breathing acoustic mode, it is reasonable to model the time-varying frequency as $\Omega(t)^2 = 1/R_0(1 + 2\epsilon\sin(2\pi\nu_{ac}t))$, where R_0 is the curvature of the fiber and $|\epsilon| \ll 1$ determines the amplitude of the mechanical oscillations. The periodic acoustic oscillation of the resonator will modulate the optical mode giving rise to many harmonics around the input frequency ν_{op} equally spaced by the acoustic frequency.

In this work, we consider the case of parametric resonance which condition corresponds to the situation when the acoustic frequency is $\nu_{ac} = 2\Delta\nu_{op}(2+\delta)$, where $\Delta\nu_{op} = c/2\pi n_r\sqrt{r_0 R_0}$ and $|\delta| \ll 1$ is the relative deviation of the acoustic frequency from the optical eigenfrequency spacing. Under the conditions of $|\epsilon| \ll 1$ and $|\delta| \ll 1$, the transition amplitudes between quasi-states depends only on the ratio ϵ/δ [5]. In the region of instability of the Mathieu equation ($|\epsilon| > |\delta|$), we expect a strong excitation of the parabolic resonator and a noticeable increase in the number of comb teeth [9]. The number of these lines will be limited by the finite size of the SNAP resonator and the optical Q-factor. On the other hand, in the region of stability ($|\epsilon| < |\delta|$), we expect to excite only a certain number of comb lines.

4. Example of an OFC

As an example, we have simulated the dynamics of a SNAP parabolic resonator with $r_0 = 20\ \mu$m and maximum ERV $\Delta r_0 = 2$ nm. For a curvature of $R_0 = 3.3$ km, the length of this resonator is $L = 7.26$ mm (Fig. 1(b)). Attenuation of the resonator are set to $\gamma = 3$ MHz, which corresponds to a Q-factor of $\sim 2\times10^8$. The coupling between the taper and the resonator is set to $D_0 = 0.05\ \mu\text{m}^{-1}$. Using theory in [10], the acoustic frequency for such a resonator can be estimated to $\nu_a = 2\Delta\nu_o = 253$ MHz. In our simulations, we set the value of $\epsilon = 0.005$ which corresponds to a maximum deviation of $2\epsilon\Delta r_0/r_0 \approx 20$ pm from the resonator equilibrium point. We excite the WGM corresponding to $q = 34$ (bold green line in Fig. 2) and measure the spectrum at the center of the resonator ($z_0 = 0$). We show the resulting spectra in the region of instability when $\epsilon/\delta = 10$ (Fig. 2(a)) and in the stability zone $\epsilon/\delta = 0.1$ (Fig. 2(b)). The number of combs in the unstable case reaches its maximum, a number that is determined by the size of the resonator and given approximately by $\nu_{op}\Delta r_0/\Delta\nu_{op} r_0 \approx 158$. In the stable case however, the bandwidth of the spectrum is limited. The plots in Fig. 2 also show that the OFC spectrum is asymmetric with respect to the excited mode. This asymmetry is expected since there are no more modes to fill below the ground state $q = 0$ (region of evanescent waves).

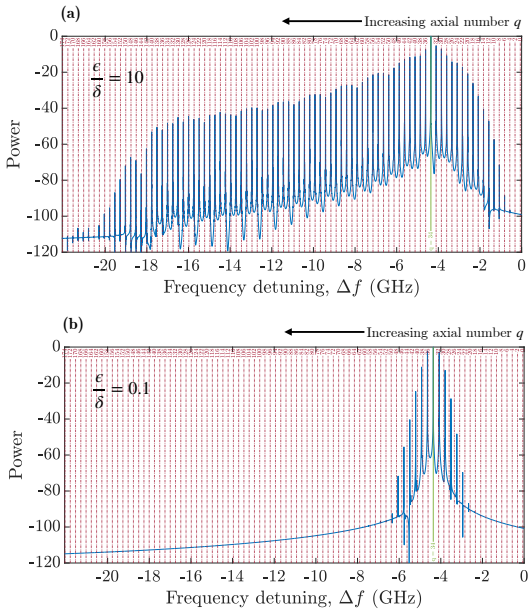

Fig. 2. OFC spectrum of the parametrically excited SNAP resonator. (a) Resonator working in the region of instability $|\epsilon| > |\delta|$. (b) Stable case when $|\epsilon| < |\delta|$.

5. Discussion

We have shown that a moderately broadband OFC spectrum can be generated when a parabolic microresonator is parametrically excited by its breathing acoustic mode. The OFC has a low repetition rate on the order of $\sim$ 100 MHz. The bandwidth of the OFC spectrum can be further increased by increasing the axial size of the SNAP resonator while keeping its parabolic shape determined by the required OFC repetition rate. We suggest that the SNAP technology enables fabrication of microresonators with the precision sufficient for the experimental realization of the OFCs described here.

References

[1] T. Udem, R. Holzwarth, and T. W. Hänsch, "Optical frequency metrology", Nature (London) **416**, 233 (2002).
[2] T. J. Kippenberg, R. Holzwarth, and S. A. Diddams, "Microresonator-based optical frequency combs", Science, **332**, 555 (2011).
[3] M. L. Weichman, P. B. Changala, J. Ye, Z. Chen, M. Yan, N. Picqué, "Broadband molecular spectroscopy with optical frequency combs", J. Mol. Spectrosc., **355**, 66 (2019)
[4] Yong Hu, Shulin Ding, Yingchun Qin, Jiaxin Gu, Wenjie Wan, Min Xiao, and Xiaoshun Jiang, "Generation of Optical Frequency Comb via Giant Optomechanical Oscillation", Phys. Rev. Lett., **127**, 134301 (2021).
[5] M. Sumetsky, "Optical frequency combs generated mechanically", Opt. Lett., **42,** 3197 (2017).
[6] M. Sumetsky, "Nanophotonics of optical fibers", Nanophotonics, **2**, 393 (2013)
[7] N. A. Toropov, M. Sumetsky, "Permanent matching of coupled optical bottle resonators with better than 0.16 GHz precision", Opt. Lett., **41**, 2278 (2016)
[8] M. Sumetsky, "Theory of SNAP devices: Basic equations and comparison with the experiment", Opt. Express, **20**, 22537 (2012).
[9] V. S. Popov, A. M. Perelomov, "Parametric excitation of a quantum oscillator", Sov. Phys. JETP, **29**, 738 (1969)
[10] M. Sumetsky, "Optical bottle versus acoustic bottle and antibottle resonators", Opt. Lett., **42**, 923 (2017)

Whispering-gallery-mode resonators: a versatile platform for fundamental science and applications

Lan Yang

In the past ten years, there has been rapid progress in the field of optical resonators, which have been demonstrated as an excellent platform to explore both fundamental science and technology development. In this talk, I will report some recent research discoveries from my group in this exciting field. I will present a few cases demonstrating the great potentials of high-Q WGM microresonators and microlasers for both fundamental science and engineering applications. Specifically, I will start with a review of non-Hermitian physics in high-quality WGM resonators. Examples including nonreciprocal light transmission, loss engineering in a lasing system, chiral modes at EPs for directional lasing emission, EPs enhanced sensing, and chiral EP-assisted electromagnetically induced transparency (EIT) will be introduced. Afterwards, I will discuss our recent exploration of a barcode technology leveraging collective behaviors of multiple resonances for sensing applications. Later, an interesting finding of mechanical solitons through optomechanical effects in a microtoroid resonator will also be presented. In the end, I will present a new generic and hand-held microresonator platform transformed from a table-top setup, which will help release the power of high-Q WGM resonator technologies.

Coherent vortex dynamics observed using an optical microcavity

Yauhen Sachkou[1], Christopher Baker[1], Glen Harris[1], Oliver Stockdale[2], Stefan Forstner[1], Matthew Reeves[2], Xin He[1], Andreas Sadawsky[1], Yasmine Sfendla[1], David McAuslan[1], Ashton Bradley[3], Matthew Davis[1,2] and Warwick Bowen[1]

[1] Australian Centre for Engineered Quantum Systems, University of Queensland, Australia

[2] Australian Centre in Future Low Energy Electronic Technologies, University of Queensland, Australia

[2] Dodd-Walls Centre for Photonic and Quantum Technologies, Otago University, New Zealand

E-mail: w.bowen@uq.edu.au

Kosterlitz and Thouless were awarded the 2016 Nobel Prize in Physics for discovering that two-dimensional superfluidity occurs due to a topological phase transition involving the binding of quantized vortices. Quite remarkably, however, even after almost a half century, coherent vortex dynamics have yet to be directly seen in any strongly-interacting two-dimensional superfluid. Here, we address this longstanding challenge, observing the coherent dynamics of nonequilibrium clusters of vortices in quasi-two-dimensional helium as they evolve, dissipate and annihilate using an on-chip optical microcavity.[1]

The importance of strongly-interacting superfluids ranges from string theory to astrophysics; including dark matter, the quark-gluon plasma in the early universe, and the dense cores of neutron stars. However, progress is impeded across this full range of areas by the lack of an underpinning microscopic theory. There is contentious debate, even at the most basic level. For instance, proposed values for the effective mass of a vortex range from zero to infinity, while it remains unclear whether an Iordanskii force exists between vortices and colocalized normal fluid. Our ability to observe vortex dynamics allows direct tests of these questions in the laboratory. We conclude that, for our experiments, neither a vortex mass nor an Iordanskii force is required.

It had generally been thought that surface interactions would prohibit experiments such as ours in two-dimensional helium. We overcome them by greatly enhancing the coherent interactions between vortices. This is achieved by confining the superfluid orders-of-magnitude more strongly than has previously been possible on the atomically smooth surface of a silicon chip. We further show that thermal vortex diffusion is suppressed by six orders-of-magnitude, verifying a thirty-year-old prediction, and realize laser control and imaging of vortex clusters for the first time in helium, leveraging techniques from quantum optomechanics (see Fig. 1).[2]

By observing coherent vortex dynamics for the first time in a strongly-interacting two-dimensional superfluid, and achieving this on a silicon-chip with integrated laser observation and control capabilities, the research reported here opens a pathway to explore the rich dynamics of quantized vortices in strongly-interacting systems, to build new quantum technologies based on superfluid helium matter-waves on a chip, for laboratory-based tests of astrophysical phenomena, and to test predictions from quantum turbulence, such as the existence of anomalous hydrodynamics and inverse energy cascade.

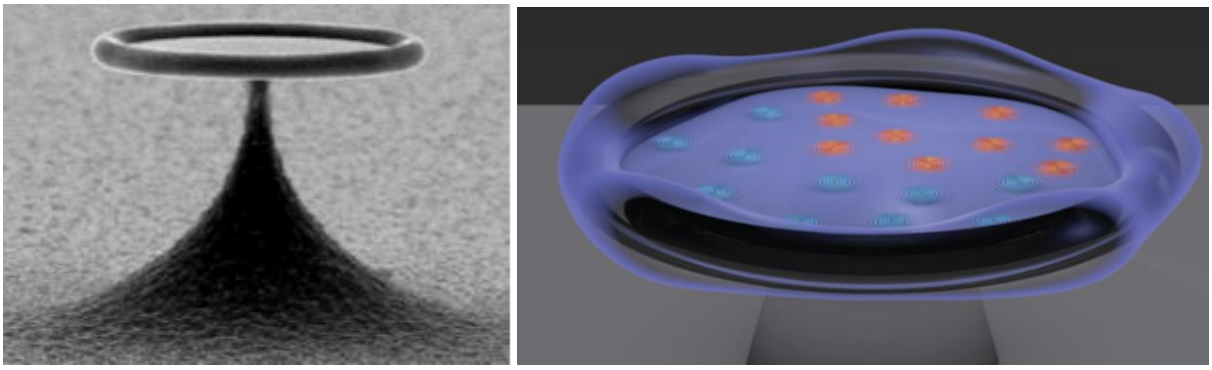

Figure 1: Left: SEM image of a microtoroidal resonator. Right: Illustration of a two-dimensional vortex ensemble confined to the surface of a microtoroidal resonator.

[1] Sachkou *et al*, *Coherent vortex dynamics in a strongly-interacting superfluid on a silicon chip*, arXiv:1902.04409 (2019).

[2] G. I. Harris *et al*, Nature Physics **12**, 788-793 (2016); D. L. McAuslan, PRX **6**, 021012 (2016); Baker *et al*, New Journal of Physics **18** 123025 (2016); Forstner *et al*, *Modelling of vorticity, sound and their interaction in two-dimensional superfluids*, arXiv:1901.05167 (2019).

Title: Chiral perfect absorption on exceptional surfaces

Authors: S. Soleymani, Q. Zhong, M. Mokim, S. Rotter, R. El-Ganainy, and S. K. Ozdemir

Abstract:

An exceptional surface (ES) is a hypersurface in the parameter space that is a continuous collection of exceptional points (EPs) - spectral degeneracies of non-Hermitian systems with degenerate eigenvalues and coalesced eigenvectors. Contrary to isolated EPs in the parameter space, ES are more robust and stable against fluctuations in the experimental environment (e.g., fluctuations in the coupling, fabrication errors, temperature fluctuations, etc). By establishing non-reciprocal coupling between clockwise (CW) and counterclockwise (CCW) modes of a whispering-gallery-mode resonator, such that CW mode is coupled to the CCW, but CCW mode does not couple to the CW mode, we have experimentally demonstrated the emergence of exceptional surfaces and characterized their stability against perturbations. Operating the system on the ES and hence exactly at EPs enabled clear observation of squared Lorentzian reflection spectra for the CW input and no resonance in the reflection spectra for the CCW input. Transmission spectra exhibit Lorentzian form for both input directions. This asymmetry in reflection spectra is a hallmark of the system being operated at an EP. Utilizing this, we also demonstrated tunable and chiral perfect absorption: input in the CW direction is perfectly absorbed exhibiting squared Lorentzian absorption spectra whereas input in the CCW direction is partially absorbed with Lorentzian absorption spectra. In this talk we will discuss various exotic features of exceptional surfaces and their use in practical applications.

Superradiance, superabsorption and a quantum engine

KYUNGWON AN

Department of Physics, Seoul National University, Seoul 08826, Korea
kwan@phya.snu.ac.kr

Abstract: By using two-level atoms in the same superposition state, we have demonstrated coherent single-atom superradiance, the long-sought superabsorption as a time reversal of the superradiance and a superradiant quantum heat engine with near-unity efficiency.

Two-level atoms prepared in identical superposition states of the same phase can undergo superradiance in a cavity. We observed that coherent superradiance occurs even when the atoms interact with the cavity one by one as long as they are correlated by the cavity field. As we increased the number N_c of atoms traversing the cavity during the cavity field decay time, the number of photons in the cavity grew nonlinearly, proportional to N_c^2 [1]. In this process, the phase imprinted on the atomic superposition states was transferred to the superradiant field. If we suddenly change the sign of the atomic phase, the atoms undergo a time-reversal process of superradiance, absorbing photons instead of emitting photons. We have recently realized the so-called superabsorption, the opposite of superradiance, of a probe field of an arbitrary phase in this way [2]. The number of photons absorbed for a given time was observed to be proportional to the number of atoms squared as expected. Coherent superradiance can also be utilized to build a quantum engine that would operate with only a single heat reservoir. We constructed a four-cycle photonic engine with an atomic beam serving as a heat reservoir providing heat to the engine in a form of photons, exerting a radiative pressure on mirrors as a piston. In the expansion stage under the same reservoir temperature as the contraction stage, the common atomic phase was turned on to induce the coherent superradiance. About 40 times more heat (photons) were transferred to the engine and performed a work. The resulting engine efficiency surpassed the Carnot efficiency, even approaching a unity.

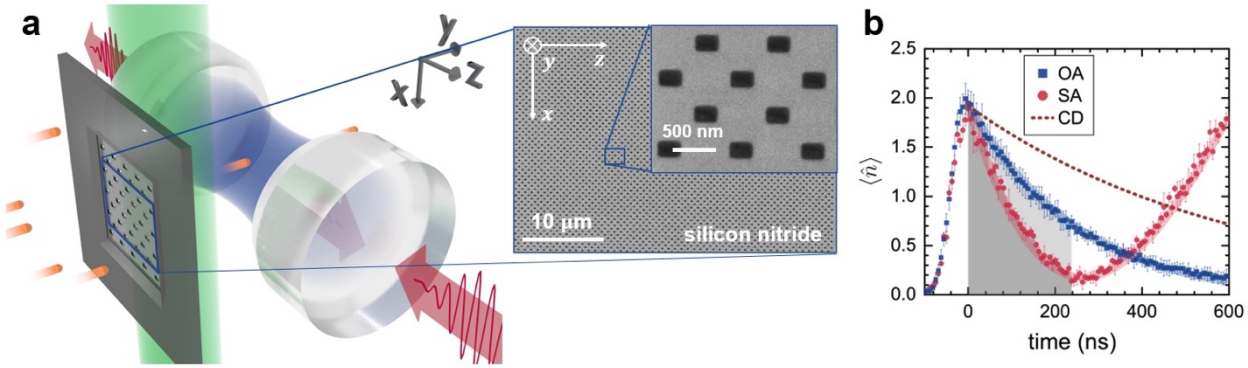

Fig. 1. **a.** Experimental setup for superabsorption. Atoms are prepared in a superposition state after going through a nanohole aperture with a hole spacing matching the transition wavelength (791nm, $^1S_0$-$^3P_1$ transition) of atomic barium. A probe field is prepared in the cavity at t=0. **b.** Ordinary absorption (OA) occurs for ground state atoms. By adjusting the phase of the atomic superposition state, we can induce superabsorption (SA), which depletes the cavity field much faster than OA. The number of atoms in the cavity was about 10. In order to induce OA as strong as SA, we needed 10 times more atoms than SA. Excerpted from Ref. 2.

References

1. Junki Kim, Daeho Yang, Seunghoon Oh, and Kyungwon An, "Coherent single-atom superradiance," Science **359**, 662–666 (2018).
2. Daeho Yang Seung-hoon Oh, Junseok Han, Gibeom Son, Jinuk Kim, Junki Kim, Moonjoo Lee and Kyungwon An, "Realization of superabsorption by time reversal of superradiance," Nat. Photonics **15**, 272 (2021).

Non-reciprocity in the high Q microresonators

CHUNHUA DONG*

CAS Key Laboratory of Quantum Information, University of Science and Technology of China, Hefei 230026, P. R. China.
**chunhua@ustc.edu.cn*

Abstract: Non-reciprocal optical devices are indispensable components in classical and quantum information processing in integrated photonic circuits. Here, our recent theoretical and experimental progresses are introduced for innovative technology as well as for fundamental science.

1. Introduction

The non-reciprocity has many applications for photonic isolators and circulators, which have been recently demonstrated in our experiment. A reconfigurable non-reciprocal device with alternative functions as either a circulator or a directional amplifier via optomechanically induced coherent photon-phonon conversion or gain was demonstrated. The underlying mechanism of the non-reciprocity demonstrated here is actually universal and can be generalized to any traveling wave resonators with a mechanical oscillator, such as the integrated disk-type microresonator coupled with a nanobeam. In addition, I will present some new results about the multi-modes interaction and spin-orbit coupling in the high Q microresonators for the non-reciprocity.

2. Some details

In this study, the optomechanically induced non-reciprocity is experimentally demonstrated for the first time. Optomechanically induced non-reciprocal transparency and amplification are observed, and a non-reciprocal phase shift of up to 40 degrees is demonstrated in this study. Optomechanically induced non-reciprocity has applications for photonic isolators and circulators, which have been recently demonstrated in our experiment. A reconfigurable non-reciprocal device with alternative functions as either a circulator or a directional amplifier via optomechanically induced coherent photon-phonon conversion or gain was also demonstrated.

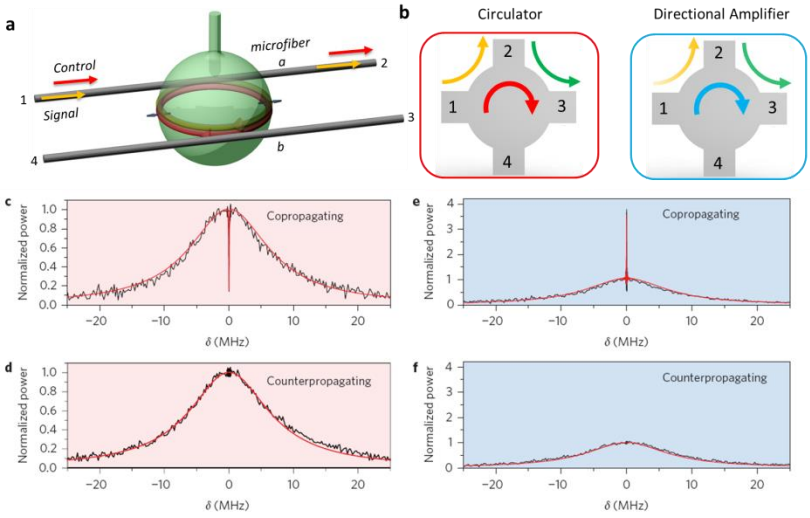

Fig. 1. a,b, Schematic of the optomechanical circulator and directional amplifier. The device consists of an optomechanical resonator and two coupled microfibres. A control field launched into port 1 excites the coupling between the mechanical motion and the CW optical field. The routing direction of the signal light coincides with the control field (i.e., CW direction). c,d, The emission power spectra in the OMIT response are obtained using co- and counterpropagating signal pulses. The incident driving power is 10 mW. The solid red lines are the results of calculations. e,f, The emission power spectra in the OMIA response are obtained using co- and counterpropagating signal pulses. The incident driving power is 5.5 mW. The solid red lines are the results of calculations.

References

1. M. Hafezi, and P. Rabl, Opt. Express 20, 7672 (2012).
2. C.-H. Dong, et al. Brillouin-scattering-induced transparency and non-reciprocal light storage. Nature Commun. 6, 6193 (2015).
3. C.-H. Dong, et al. Optomechanical dark mode. Science 338, 1609-13 (2012).

4. Z. Shen, Y.-L. Zhang, Y. Chen, C.-L. Zou, Y.-F. Xiao, X.-B. Zou, F.-W. Sun, G.-C Guo, and C.-H. Dong, Experimental realization of optomechanically induced non-reciprocity. Nature Photonics 10, 657 (2016).
5. F. Ruesink, M. Miri, A. Alù and E. Verhagen, Nature Communications 7, 13662 (2016).
6. Kim, J., Kuzyk, M. C., Han, K., Wang, H. & Bahl, G. Nat. Phys. 11, 275–280 (2015).
7. K. Fang, J. Luo, A. Metelmann, M. H Matheny, F. Marquardt, A. A Clerk, O. Painter, Nat. Phys. 13, 465 (2017).
8. Z. Shen, Y. Zhang, Y. Chen, F. Sun, X. Zou, G.-C. Guo, C.-L. Zou, and C.-H. Dong, Reconfigurable optomechanical circulator and directional amplifier, Nature Communications 9, 1797 (2018).

Symmetry-broken Microcavity Optics

YUN-FENG XIAO

State Key Laboratory of Mesoscopic Physics, School of Physics, Peking University
yfxiao@pku.edu.cn

Abstract: Confinement and manipulation of photons using microcavities have triggered intense research interest in both fundamental and applied photonics for more than two decades. Prominent examples are ultrahigh-Q whispering gallery microcavities which confine photons by means of continuous total internal reflection along a curved and smooth surface. The long photon lifetime, strong field confinement, and in-plane emission characteristics make them promising candidates for enhancing light-matter interactions on a chip. In the first part of this talk, I will introduce some representative photonics applications of ultrahigh-Q microcavities. In the second part, I will focus on (1) chaos-assisted momentum transformation in an asymmetrical microcavity, (2) spontaneous symmetry breaking of optical fields in a single ultrahigh-Q microcavity, and (3) second-order nonlinear optics induced by symmetry breaking at the surface of a silica microcavity under a sub-milliwatt continuous-wave pump. By dynamically coordinating the double-resonance phase matching, a second harmonic is achieved with a conversion efficiency of 0.049% W^−1, 14 orders of magnitude higher than that of the non-enhancement case.

References

1. Xueyue Zhang, Qi-Tao Cao, Zhuo Wang, Yu-xi Liu, Cheng-Wei Qiu, Lan Yang, Qihuang Gong and Yun-Feng Xiao, "Symmetry-breaking-induced nonlinear optics at a microcavity surface," Nature Photonics 13, 21–24 (2019).
2. Xuefeng Jiang, Linbo Shao, Shu-Xin Zhang, Xu Yi, Jan Wiersig, Li Wang, Qihuang Gong, Marko Lončar, Lan Yang, and Yun-Feng Xiao, "Chaos-assisted broadband momentum transformation in optical microresonators," Science 358, 344 (2017).
3. Qi-Tao Cao, Heming Wang, Chun-Hua Dong, Hui Jing, Rui-Shan Liu, Xi Chen, Li Ge, Qihuang Gong, and Yun-Feng Xiao, "Experimental demonstration of spontaneous chirality in a nonlinear microresonator," Phys. Rev. Lett. 118, 033901 (2017).

Scalable neuro-inspired photonic computing on a silicon chip

SATOSHI SUNADA[1,2] , ATSUSHI UCHIDA[3]

[1] *Faculty of Mechanical Engineering, Institute of Science and Engineering, Kanazawa University, Kakuma-machi Kanazawa, Ishikawa, 920-1192, Japan*
[2] *Japan Science and Technology Agency (JST), PRESTO, 4-1-8 Honcho, Kawaguchi, Saitama 332-0012, Japan*
[3] *Department of Information and Computer Sciences, Saitama University, 255 Shimo-Okubo, Sakura-ku, Saitama City, Saitama, 338-8570, Japan*
[1]*sunada@se.kanazawa-u.ac.jp*

Abstract: We report a neuro-inspired photonic computing, which allows for large-scale, high-density, high-speed neural processing on a tiny silicon chip.

The recent rapid advancement of machine learning technologies has been driven by massive computing power, developments in special purpose hardware, and the availability of large datasets. Although the accelerated increase in the volume of data in modern society enables the development of larger and more complex machine learning models, it poses considerable challenges for the present electronic computing hardware in terms of both computing speed and power consumption. Such issues have emerged as a major bottleneck for artificial intelligence (AI) and motivated the development of novel AI computing hardware and concepts.

In this presentation, we show a novel photonic neuro-inspired computing architecture [1]. The key operation is based on the continuous spatial degrees of freedom of an optical field, which is generated by a complex interference of the guided modes in a multimode waveguide [1,2] or resonance modes in an optical cavity [3]. Such an optical field works as a spatially continuous neural network with complex internal connections, i.e., a *photonic neural field*. In contrast to existing photonic neural networks, the photonic neural field is a spatially continuous field that nonlinearly responds to optical inputs, and its high spatial degrees of freedom allow for large-scale and high-density neural processing on a tiny chip. In this study, we used the on-chip photonic neural field as a reservoir of information and demonstrate a high-speed chaotic time-series prediction and vowel recognition with low errors using a training approach similar to reservoir computing. We show that the photonic neural field is potentially capable of executing more than one peta multiply-accumulate operations per second for a single input wavelength on a footprint as small as a few square millimeters. The processing rate is boosted by more than an order of magnitude compared to previous approaches. The operation of the neural field is energy efficient due to a passive scattering process, for which the required power comes only from the optical input.

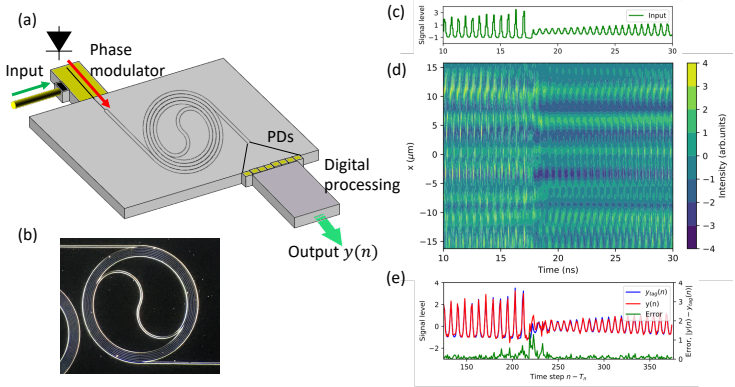

Fig. 1 (a) Conceptual schematic of the proposed photonic architecture. (b) Fabricated photonic neural field generator. (c-e) Demonstration of a chaotic time-series prediction. (c) Input signal. (d) Spatiotemporal evolution of the neural field. (e) Prediction results.

References

1. S. Sunada and A. Uchida, "Photonic neural field on a silicon chip: Large-scale, high-speed neuro-inspired computing and sensing," Optica, *in press*; arXiv:2105.10672
2. S. Sunada, K. Kanno, and A. Uchida, "Using multidimensional speckle dynamics for high-speed, large-scale, parallel photonic computing," Opt. Express 28, 30349 (2020).
3. S. Sunada and A. Uchida, "Photonic reservoir computing based on nonlinear wave dynamics at microscale," Sci. Rep. 9, 19078 (2019).

Microtube microcavities for on-chip integration

Oliver G. Schmidt
Research Center MAIN, Chemnitz University of Technology, Germany
oliver.schmidt@main.tu-chemnitz.de

This talk will focus on microtube microcavities that can be fabricated in parallel with high throughput and high yield on a single chip. The presentation reports about wafer-scale fabrication techniques [1], sensor schemes [2] and new ways to optically couple and extract light from microcavities [3-5]. The flexibility in materials choice is exploited to demonstrate geometry-programmable lasing with perovskite materials [6] opening up new perspectives for on-chip optoelectronic device integration.

[1] C. N. Saggau *et al.*, Adv. Mater. 32, 2003252 (2020)
[2] J. Wang *et al.*, ACS Sensors 1476 (2019)
[3] S. Valligatla *et al.*, Adv. Opt. Mater. 8, 2000782 (2020)
[4] X. Wang *et al.*, ACS Nano 15, 18411 (2021)
[5] J. Wang *et al.*, Laser Photonics Rev. 14, 2000118 (2020)
[6] H. Dong *et al.*, Adv. Funct. Mater. 31, 2109080 (2021)

Recent progress in the development and applications of SNAP technology

M. SUMETSKY

Aston Institute of Photonic Technologies, Aston University, Birmingham B4 7ET, United Kingdom
m.sumetsky@aston.ac.uk

Abstract: Recent progress in the development and applications of Surface Nanoscale Axial Photonics (SNAP) technology is reviewed.

1. Introduction

Since its introduction in 2011 [1, 2], Surface Nanoscale Axial Photonics (SNAP) technology – which enables the fabrication of nanoscale-shallow complex high Q-factor microresonator structures at the surface of an optical fiber with subangstrom precision – exhibited noticeable theoretical and experimental development. Originally, SNAP structures were fabricated with a CO_2 laser, which locally anneals the fiber surface. Later, the techniques based on femtosecond laser inscription and temporary local heating of optical fibers have been demonstrated [3, 4].

2. Theory, fabrication principles, and recent development

In this presentation, I briefly review the theory and fabrication principles of SNAP microresonators [5] and then proceed with recent results obtained in 2018-2019. In particular, I review new fabrication technique of droplet-induced microresonator structures in optical capillaries [6], microresonators induced by bending of optical fibers [7], precise relative tuning of coupled microresonators [8], and slow-cooked microresonators [9]. Next, I discuss our recent experiments on resonant tunneling through a SNAP microresonator [10] and tunneling and slow propagation of light near a cutoff wavelength of a uniform optical fiber [11].

3. Future development

Finally, I discuss the potential applications of SNAP for the fabrication of miniature delay lines [12], microlasers [13], frequency comb generators [14, 15], optomechanical microdevices [16, 17], optical buffers [18], and single photon microprocessors [19].

References

[1] M. Sumetsky, Localization of light in an optical fiber with nanoscale radius variation, in: CLEO Europe and EQEC 2011 Conference Digest, Postdeadline Paper PDA_8 (2011).
[2] M. Sumetsky, D.J. DiGiovanni, Y. Dulashko, J.M. Fini, X. Liu, E.M. Monberg, T.F. Taunay, Surface nanoscale axial photonics: robust fabrication of high-quality- factor microresonators, Opt. Lett. **36**, 4824 (2011).
[3] F.C. Shen, X.W. Shu, L. Zhang, M. Sumetsky, Fabrication of surface nanoscale axial photonics structures with a femtosecond laser, Opt. Lett. **41**, 2795 (2016).
[4] A. Dmitriev, N. Toropov, M. Sumetsky, Transient reconfigurable subangstrom-precise photonic circuits at the optical fiber surface, in: IEEE Photonics Conference (IPC), Postdeadline paper (2015).
[5] M. Sumetsky, Theory of SNAP devices: basic equations and comparison with the experiment, Opt. Express **20**, 22537 (2012) .
[6] T. Hamidfar, K.V. Tokmakov, B.J. Mangan, R.S. Windeler, A.V. Dmitriev, D.L.P. Vitullo, P. Bianucci, M. Sumetsky, Localization of light in an optical microcapillary induced by a droplet, Optica **5**, 382 (2018).
[7] D. Bochek, N. Toropov, I. Vatnik, D. Churkin, and M. Sumetsky, SNAP microresonators introduced by strong bending of optical fibers, Opt. Lett. **44**, 2318 (2019).
[8] D.L.P. Vitullo, S. Zaki, G. Gardosi, B.J. Mangan, R.S. Windeler, M. Brodsky, M. Sumetsky, Tunable SNAP microresonators via internal Ohmic heating, Opt. Lett. **43**, 4316 (2018).
[9] G. Gardosi, Y. Yang, M. Sumetsky, Slow cooking of SNAP microresonators, CLEO: Applications and Technology (2019) paper JTh2A.50, and in preparation.
[10] M. Crespo-Ballesteros, Y. Yang, N. Toropov, and M. Sumetsky, Four-port SNAP microresonator device, Opt. Lett. **44**, 3498 (2019).
[11] Y. Yang and M. Sumetsky, Tunnelling and free propagation of slow whispering gallery modes near the cutoff wavelength of an optical fbre, CLEO-Europe, paper CK-11.4 (2019) and in preparation.
[12] M. Sumetsky, Delay of light in an optical bottle resonator with nanoscale radius variation: dispersionless, broadband, and low loss, Phys. Rev. Lett. **111**, 163901(2013).
[13] M. Sumetsky, Lasing microbottles, Light Sci. Appl. **6** , e17102 (2017).
[14] V. Dvoyrin, M. Sumetsky, Bottle microresonator broadband and low-repetition-rate frequency comb generator, Opt. Lett. **41**, 5547 (2016).
[15] S.V. Suchkov, M. Sumetsky, A.A. Sukhorukov, Frequency comb generation in SNAP bottle resonators, Opt. Lett. **42**, 2149 (2017).
[16] M. Sumetsky, Optical frequency combs generated mechanically, Opt. Lett. **42**, 3197 (2017).
[17] M. Sumetsky, Optical bottle versus acoustic bottle and antibottle resonators, Opt. Lett. **42** 923 (2017).
[18] M. Sumetsky, Microscopic optical buffering in a harmonic potential, Sci. Rep. **5** 18569 (2015).
[19] M. Sumetsky, Mahaux-Weidenmüller approach to cavity quantum electrodynamics and complete resonant down-conversion of the single photon frequency, Phys. Rev. A **100**, 013801 (2019).

6th International Workshop on Microcavities and Their Applications (WOMA)

Frequency conversion in microcavities made of non-centrosymmetric crystals

Ingo Breunig(1,2)
(1) Laboratory for Optical Systems, Department of Microsystems Engineering - IMTEK, University of Freiburg, Georges-Köhler-Allee 102, 79110 Freiburg, Germany
(2) Fraunhofer Institute for Physical Measurement Techniques IPM, Heidenhofstraße 8, 79110 Freiburg, Germany

Abstract:
Whispering gallery resonators (WGRs) made of non-centrosymmetric crystals nowadays serve as compact, efficient and wavelength flexible frequency converters. Conventionally, they are based on nonlinear optical three-wave mixing processes such as frequency doubling, sum-frequency generation and optical parametric oscillation. Here, we review our work on WGR based optical parametric oscillators. Devices made of radially poled $LiNbO_3$ are tunable in the near infrared between 1.7 and 2.8 µm wavelength and they reach conversion efficiencies beyond 50 % at milliwatt pump powers. WGRs made of non-oxide crystals such as $CdSiP_2$ and $AgGaSe_2$ extend the tuning range into the mid infrared (Figs. a, b), the latter even beyond 8 µm wavelength. Active stabilization and mode-hop free tuning is achieved by integrating a piezo translator inside the cavity. Despite of their intrinsic triple resonance, WGR based parametric oscillators are suitable for high-resolution spectroscopy.

For chip-integration, we use the following procedure: imprinting a quasi-phasematching structure into a bulk $LiNbO_3$ crystal, bonding it onto crystalline SiO_2, thinning down the structured $LiNbO_3$ layer down to some µm, etching the resonator and chemo-mechanically polishing the sidewalls. The final resonators (Fig. c) have regularly quality factors beyond 10^6. This technique can be adopted to any non-centrosymmetric material.

Furthermore, we will show adiabatic frequency conversion in WGRs based on $LiNbO_3$ crystals. Here, the refractive index of the resonator material is changed faster than the round-trip time using the linear electro-optic effect. As a result, the intracavity light changes its frequency according to the shift of the resonances. In contrast to the abovementioned three-wave mixing processes, this technique has no constraints regarding pump power or phasematching.

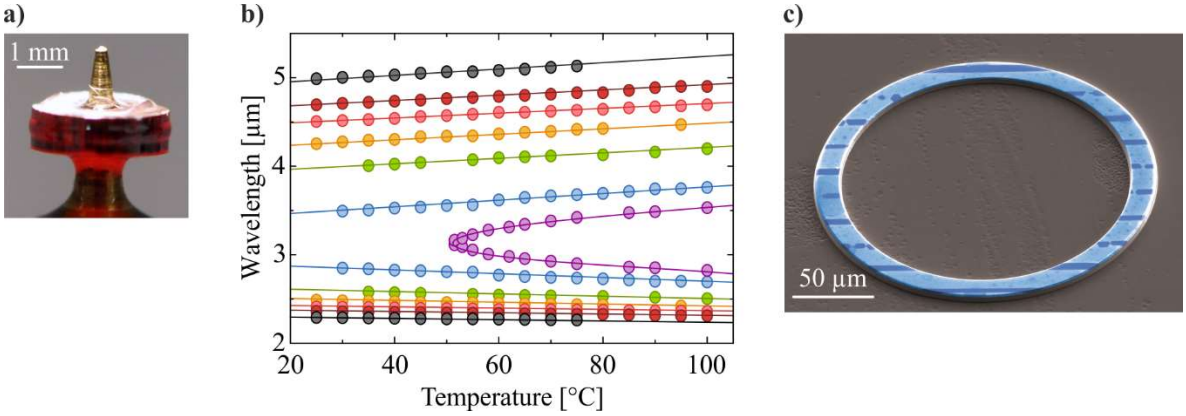

a) Whispering gallery resonator made of bulk $CdSiP_2$. b) Wavelength tuning of a whispering gallery optical parametric oscillator based on a $CdSiP_2$ resonator. c) Chip-integrated ring resonator made of periodically poled $LiNbO_3$.

Möbius Strip Microlasers & Non-Euclidean Photonics

YALEI SONG[1,2], STEFAN BITTNER[3], CLEMENT LAFARGUE[2], BARBARA DIETZ[1], DOMINIQUE DECANINI[4], XAVIER CHECOURY[4], JOSEPH ZYSS[2], MELANIE LEBENTAL[2].

[1]*Lanzhou Center for Theoretical Physics and the Gansu Provincial Key Laboratory of Theoretical Physics, Lanzhou University, Lanzhou, 730000 Gansu, China.*
[2]*Laboratoire Lumière, Matière et Interfaces (LuMIn), CNRS, ENS Paris-Saclay, Université Paris-Saclay, CentraleSupélec, 91190 Gif-sur-Yvette, France.*
[3]*Chair in Photonics, LMOPS EA-4423 Laboratory, CentraleSupélec and Université de Lorraine, 2 rue Edouard Belin, 57070 Metz, France.*
[4] *Centre de Nanosciences et de Nanotechnologies, CNRS, Université Paris-Saclay, 10 Boulevard Thomas Gobert, 91120 Palaiseau, France.*

lebental@ens-paris-saclay.fr

Abstract: We report on experiments with Möbius strip microlasers which were fabricated with high optical quality by direct laser writing. Comparison between experiments and 3D FDTD simulations reveals that the resonances are localized on periodic geodesics.

Direct laser writing [1] enables the fabrication of almost arbitrary three-dimensional (3D) microstructures with feature sizes of less than 1 µm and allows to create 3D organic microlasers such as pyramids with high quality and low surface roughness [2]. Apart from 3D bulk resonators, it is also possible to fabricate thin, curved waveguides to investigate how light propagates along a curved surface. We fabricate organic microlasers in the shape of a Möbius strip [Fig. 1(a)] made of a photoresist doped with a laser dye and investigate the consequences of such a non-Euclidean geometry on the properties of a microlaser [3].

The Möbius strip is of particular interest since it exhibits topological properties impossible in two dimensions: it has only one surface and one boundary. We investigate how the non-Euclidean geometry of the Möbius strip influences the structure of the lasing modes. In particular, the formation of whispering gallery modes propagating along the boundary as commonly observed for conventional ring resonators is impossible for the Möbius strip since its boundary features both concave and convex parts.

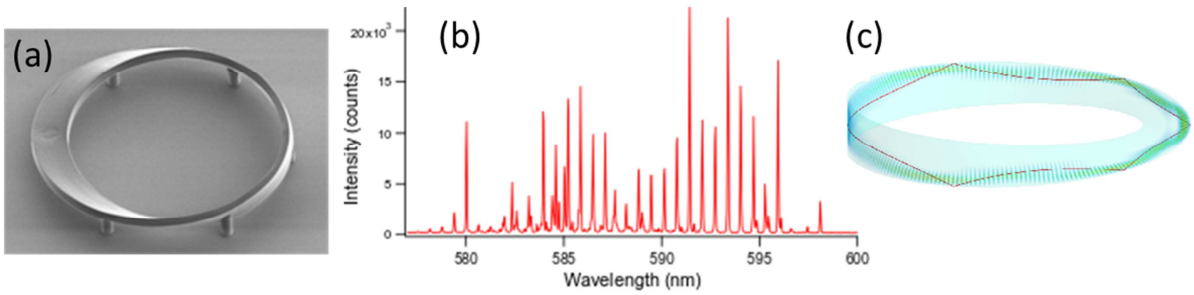

Fig. 1. (a) Scanning Electronic Microscope (SEM) image of a Möbius strip microlaser with diameter 100 µm. (b) Typical experimental laser spectrum from a Möbius strip microlaser. (c) High-Q wavefunction of a Möbius strip resonator calculated by 3D FDTD simulation, which is located on the periodic geodesic in red line.

The spectrum of a Möbius microlaser [Fig. 1(b)] is dominated by a series of equidistant peaks, which is the fingerprint of longitudinal modes propagating along a periodic ray trajectory. The classical ray trajectories in a resonator are determined by Fermat's principle, and on a curved surface, the shortest path between two points is a geodesic. We hence surmise that the lasing modes of a Möbius microcavity are localized on periodic geodesics. We calculate the modes of a Möbius strip resonator with 3D FDTD simulations and its periodic geodesics with a ray tracing code based on Fermat's principle. Figure 1(c) shows the intensity distribution of a high Q resonant mode, and its structure is in good agreement with a periodic geodesic with 5 reflections at the boundary. The optical length

of this geodesic - as well as a few other periodic geodesics - agrees well with the optical length obtained from the measured lasing spectrum. In conclusion, the experiments and simulations strongly indicate that the lasing modes of the Möbius microcavity are localized on periodic geodesics.
These results open the way to further investigations of non-Euclidean photonic devices which can provide new ways of confining and manipulating light in optical microstructures.

References

1. J. Fischer and M. Wegener, *Three-dimensional optical laser lithography beyond the diffraction limit*, Laser & Phot. Rev. 7, 22 (2013).
2. M. A. Guidry, Y. Song, C. Lafargue, R. Sobczyk, D. Decanini, S. Bittner, B. Dietz, L. Huang, J. Zyss, A. Grigis, and M. Lebental, *Three dimensional micro-billiard lasers: The square pyramid*, Europhys. Lett. 126, 64004 (2019).
3. Y. Song, Y. Monceaux, S. Bittner, K. Chao, H. M. Reynoso de la Cruz, C. Lafargue, D. Decanini, B. Dietz, J. Zyss, A. Grigis, X. Checoury, and M. Lebental, *Möbius strip microlasers: a testbed for non-Euclidean photonics.* arXiv:2011.12088. To appear in Physical Review Letters. Editor's suggestion.

Applications of GRIN microcavities based on transformation optics

MUHAN CHOI[1,2,*], INBO KIM[2], AND SUNGHWAN RIM[2]

[1]*School of Electronics Engineering, Kyungpook National University Daegu, 41566, South Korea*
[2]*Digital Technology Research Center, Kyungpook National University, Daegu 41566, South Korea*
[*]*mhchoi@ee.knu.ac.kr*

Abstract: we report gradient index (GRIN) microcavities based on conformal transformation optics working in optical frequency regime and their unique optical properties. The spatially varying refractive index profile can be implemented by drilling subwavelength-scale air holes in a dielectric slab.

A new type of inhomogeneous optical resonators based on transformation optics are intriguing optical devices since they enable us to manipulate properties of the resonant modes of dielectric cavities such as emission directionality, chirality, inter-mode couplings between resonance modes while maintaining their high Q-factor.[1-4] Although the theoretical concept was well established and the experimental feasibility was shown in microwave regime, the realization of such transformation cavities working on optical frequency regime still remains a challenging goal despite its great potential in the optical applications.

Here, we report GRIN microcavities designed by conformal transformation optics working in optical frequency regime and their unique optical properties. The spatially varying refractive index profile can be implemented by drilling subwavelength-scale air holes in a dielectric slab. Transformation optics-based microcavities will open a new horizon of application beyond that of conventional homogeneous optical dielectric microcavities.

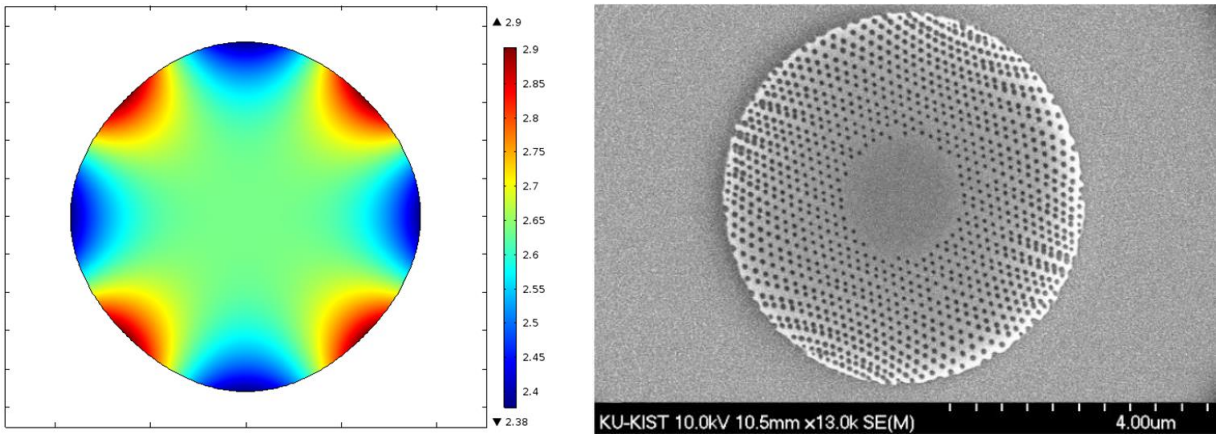

Fig. 1. Top-view of a microcavity (right) designed by transformation optics with the spatially varying refractive index profile (left) implemented by drilling subwavelength-scale air holes.

References

1. K. J. Vahala *et. al*. "Optical microcavities," Nature, **424**, 839-846 (2003).
2. J. B. Pendry, D. Schurig, and D. R. Smith, "Controlling Electromagnetic Fields," Science , **312**, 1780-1782 (2006).
3. U. Leonhardt, "Optical conformal mapping," Science, **312**, 1777-1780 (2006).
4. Y. Kim, S.Y. Lee, J.W. Ryu, I. Kim, J.H. Han, H.S. Tae, M. Choi and B. Min, "Designing Whispering Gallery Modes via Transformation Optics" Nature photonics, **10**, 647–652 (2016).

Stimulated Scattering in Supermode Microcavities: Single- or Dual-mode Lasing?

QI-TAO CAO[1,*], YUN-FENG XIAO[1]

[1] *State Key Laboratory for Mesoscopic Physics and Frontiers Science Center for Nano-optoelectronics, School of Physics, Peking University, Beijing 100871, China*
**caoqt@pku.edu.cn*

Abstract: We experimentally elucidate the lasing spectral paradox by investigating the lasing dynamics of supermode Raman microlasers. The single-mode lasing behavior is confirmed, and the beating signal has been recognized as the transient interference during the lasing switching.

1. Introduction

Microlasers in near-degenerate supermodes have drawn much attention in the past decades, promoting various advances such as spontaneous symmetry breaking, exceptional points, and novel light sources. Single microcavities supporting high-Q whispering-gallery modes (WGMs) are found as a natural platform for studying supermodes, and supermode lasers in WGM microcavities have been demonstrated with not only intrinsic gain materials but also nonlinear optical effects by stimulated scattering. Given that the energy splitting of supermodes is sensitive to the external perturbation, the stimulated scattering, such as Raman or Brillouin lasers in supermode microcavities, has also shown unique merit for nanoparticle detection, featuring a beat note corresponding to the splitting [1,2].

Different from the conventional inversion lasers, stimulated scattering holds a homogeneous gain and thus the energy in the pump field should be clamped at a fixed value once the lasing threshold is reached, leading to a single-mode lasing [3,4]. However, beat notes are widely observed in supermode microlaser output, so that these lasers are generally regarded as dual-mode lasers. In this work, we experimentally elucidate this lasing spectral paradox by investigating the dynamics of a supermode Raman laser in an ultrahigh-Q microcavity [5].

2. Results

The Raman microlaser is generated by optically pumping a WGM microcavity and propagates in both the clockwise (CW) and counterclockwise (CCW) directions. The intracavity counterpropagating waves are coupled by a scatterer at the surface, which forms a pair of standing-wave supermodes, the symmetric a_+ and antisymmetric a_-. The losses and frequencies of the two supermodes are slightly different due to the relative position between the mode distribution and the scatterer. According to the mode competition theory, only the mode with the smaller loss can reach the lasing condition, accompanied with the clamped pump field. Experimentally, a silica microsphere cavity with the Q factor over 4×10^7 is applied. A tapered fiber is evanescently coupled to the cavity, and the transmission of the Raman supermodes is measured with a modal splitting of $2g = 2\times5.49 \pm 0.01$ MHz. By tuning the pump laser (~1,490 nm) into the resonance of the cavity mode, the first-order Raman laser is observed as a single line at 1,610 nm (Fig. 1(a)) with the threshold of 213 μW.

The clamping of the pump field is investigated by monitoring the intracavity pump power via an add–drop coupling scheme. As the pump laser scans from the blue-detuned region toward the resonance, the intracavity pump power increases and reaches the threshold, after which the power of the Raman laser grows monotonically. Simultaneously, the intracavity pump power is clamped at a constant value (Fig. 1(b)), indicating that the gain, matching the loss of the higher-Q supermode, remains unchanged. Hence, the loss of the other supermode cannot be compensated, and the laser operates in the single-mode regime. Quantitatively, a probe laser with the frequency slightly higher than the supermode is introduced to interfere with the output laser, and the frequency spectrum is presented in Fig. 1(c). The peak with the center frequency of f_+ (f_-) is attributed to the interference between the probe laser and the signal from the symmetric (antisymmetric) supermode, while the tiny peak located at $\delta f = 12.5$ MHz corresponds to the interference between the two supermodes. The intensity of the $f-$ peak is much higher than that of the f_+ peak, indicating a single-mode emission with a large side-mode suppression ratio (SMSR) over 1000.

The temporal oscillations in the laser output cannot be observed due to the large SMSR (Fig. 1(c)), which contradicts the strong beat notes reported previously. To reveal the underlying physics, we study the lasing dynamics dependent on the loss difference of the two supermodes, so that the self-injection technique is introduced to modulate the mode loss. Experimentally, a flat end face of the output fiber, serving as a reflector, reinjects partial output laser

into the cavity. To regulate the injection phase ϕ, we dynamically tune the Raman laser wavelength via the Kerr and thermo-optic effects by controlling the pump detuning. The beat notes emerge during the pump scanning in Fig. 1(d), which is also predicted by the theoretical calculation. By extracting the a_+ and a_- components of the hopping supermode laser, it is found that the beat note arises from the transient interference during the switching between an emerging laser and a decaying laser (Fig. 1(e)). As a result, simultaneous lasing from both supermodes occurs only under nonequilibrium evolution, and stable dual-mode lasing cannot be obtained. During scanning, the intracavity pump power exhibits a periodic fluctuation due to the loss modulation (Fig. 1(d)), indicating that the pump field is not clamped under the self-injection. To further prove the established theory of lasing dynamics, we experimentally study the hopping period as a function of the feedback length. The hopping period of the supermode lasers (T_1 in Fig. 1(d)) reads $T_1 = 2\pi/\dot{\phi} = c\pi/(nL\dot{\omega})$, where $\dot{\omega}$ is the frequency shift speed of the Raman laser. Experimentally, the fiber length L between the coupling point and the reflector is changed by cutting the fiber sequentially, and the measured hopping period exhibits a linear dependence on L, consistent with the theoretical result (Fig. 1(f)).

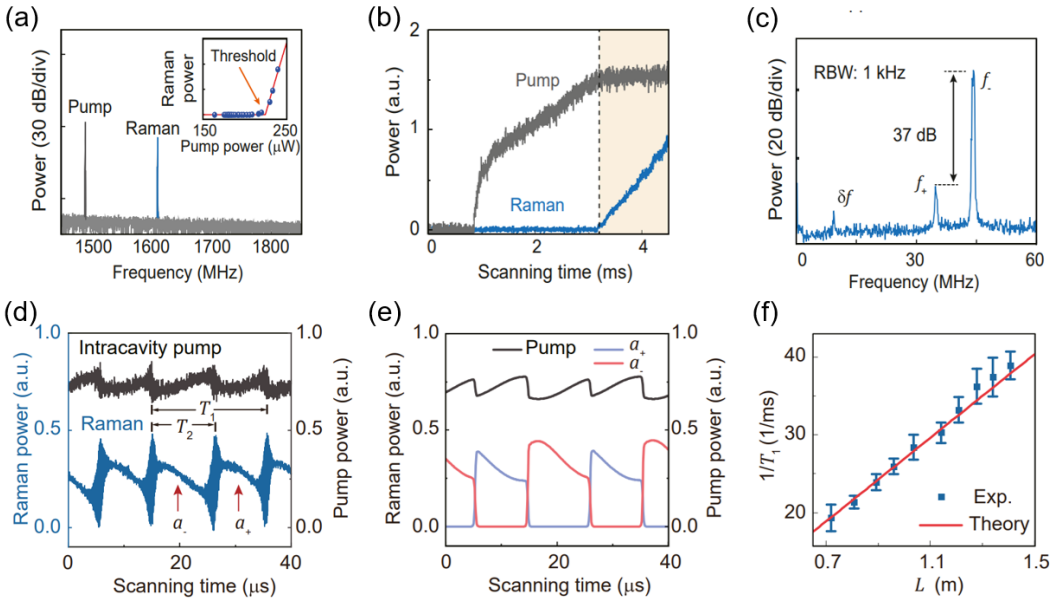

Fig. 1. (a) Optical spectrum of the Raman laser. (Inset) Threshold curve of the Raman laser. (b) Experimental observation of the clamping effect on the pump field. (c) Frequency spectrum of the combined probe light and Raman emission, in which the wavelength of the pump beam is unchanged. (d) Measured intracavity pump power (gray) and Raman laser output (blue) versus scanning time with self-injection. T1 ~ 20.6 μs is the hopping period, and T2 ~ 11.3 μs is the duration of the antisymmetric mode lasing in one period. (e) Simulated dynamics of lasing mode switching with self-injection. (f) Dependence of hopping frequency on optical length L.

3. Summary

In summary, we have clarified the controversy between the single-mode nature of stimulated scattering lasers and the previous observed “dual-mode” beat note in near-degenerate supermodes. Experimentally, the pump field is clamped to the mode with lower loss, while the laser is single mode with a SMSR up to 37 dB. The beating phenomenon is retrieved by introducing a self-injection feedback to the microcavity and identified as the transient interference when the lasing mode switches between the supermodes. This work provides an insightful guidance for microlaser-based precision measurements and paves the way to reconfigurable light sources and low-power-consumption optical memories.

References

1. B.-B. Li et al., Single nanoparticle detection using split-mode microcavity Raman lasers. *PNAS* 111, 14657–14662 (2014).
2. S. K. Ozdemir et al., Highly sensitive detection of nanoparticles with a self-referenced and self-heterodyned whispering-gallery Raman microlaser. *PNAS* 111, E3836–E3844 (2014).
3. T. J. Kippenberg, S. M. Spillane, B. Min, K. J. Vahala, Theoretical and experimental study of stimulated and cascaded Raman scattering in ultrahigh-Q optical microcavities. *IEEE J. Sel. Top. Quant. Electron.* 10, 1219–1228 (2004).
4. Q. T. Cao et al., Reconfigurable symmetry-broken laser in a symmetric microcavity. *Nat. Commun.* 11, 1–7 (2020).
5. P.-J. Zhang et al., "Single-mode characteristic of a supermode microcavity Raman laser," *PNAS* 118(22), e2101605118 (2021).

The characteristics of exceptional points in asymmetric ellipse microdisks

HYUNDONG KIM[1], SUN-JAE GWAK[1], CHANG-HWAN YI[2], JINHYEOK RYU[1], YOUNG MIN EOM[3], CHIL-MIN KIM[1,3*]

[1]*Department of Emerging Materials Science, Daegu Gyeongbuk Institute of Science and Technology (DGIST), Daegu 42988, Republic of Korea*
[2]*Center for Theoretical Physics of Complex Systems, Institute for Basic Science (IBS), Daejeon 34126, Republic of Korea*
[3]*School of Undergraduate Studies, Daegu Gyeongbuk Institute of Science and Technology (DGIST), Daegu 42988, Republic of Korea*
[*]*chmkim@dgist.ac.kr*

Abstract: We study exceptional points in asymmetric ellipse microdisks. Even and odd modes in an ellipse split depending on eccentricity. By applying asymmetric deformation to the ellipse, an exceptional point of these two modes is obtained.

1. Introduction

Non-Hermitian systems differ from Hermitian ones, since eigenvalues and their corresponding eigenstates in non-Hermitian systems can coalesce into a single point [1, 2] in parameter space. These points are called exceptional points (EPs) on the Riemann surface. EPs in microcavities have been studied intensively because these EPs have great potentials in sensor-based applications. So far, various types of cavities, such as, an asymmetric limaçon and coupled cavities, have been proposed to reveal detailed properties of EPs. By devising asymmetric ellipse microdisks (AEMs), which can be controlled by three deformation parameters, we investigate the more detailed properties of EPs.

2. Exceptional points in asymmetric ellipse microdisks

Asymmetric ellipse microdisks are given by $r(\theta) = [r_0(1 + \varepsilon_2 \cos(\theta + \varepsilon_3\pi))]/\sqrt{\sin^2\theta + \left(\cos\theta\sqrt{1-\varepsilon_1^2}\right)^2}$: ε_1 and ε_2 are the two symmetric deformation parameters, and ε_3 induces the asymmetric deformation. By controlling these three parameters carefully, we can achieve EP formed by a pair of modes having the same radial mode number and the same angular mode number (l, m). This EP obtained shows $|\Delta kr| \sim 10^{-8}$ with chirality ($\alpha > 0.9$). Both modes at this EP become purely traveling waves along the clockwise (CW) or counter clockwise (CCW) directions. For elucidating process to be EPs, 2×2 effective Hamiltonian matrix is adopted with basis modes, $\varepsilon_3 = 0$. With various boundary parameters, EPs show continuous branch-cuts structure on the parameters space, as shown in Fig.1 (a), (b). They are all 2nd order EPs.

As is well known, the frequency splittings at EPs are much sensitive against external perturbations than the diabolic points [3], because the Riemann surfaces have a square-root-topology [4]. The frequency splittings at EPs are examined by applying refractive index perturbation Δn outside of disks. As a result, a relation $\Delta kr \sim \beta(\Delta n)^{1/2}$ is confirmed. More interestingly, we have revealed that the value β in the frequency splitting at EPs depends on the eccentricity ε_1 in AEMs. This $\varepsilon_1$dependency in β originates from the fact that the splittings of even and odd parity mode are induced by couplings between CW and CCW modes in an ellipse [5]. Since this coupling is qualitatively proportional to ε_1, the splittings of modes at EPs in the higher ε_1 results in the higher values of β. These results suggest that the frequency splitting of EPs can be changed by controlling parameters adequately. The all calculations are performed numerically [6, 7].

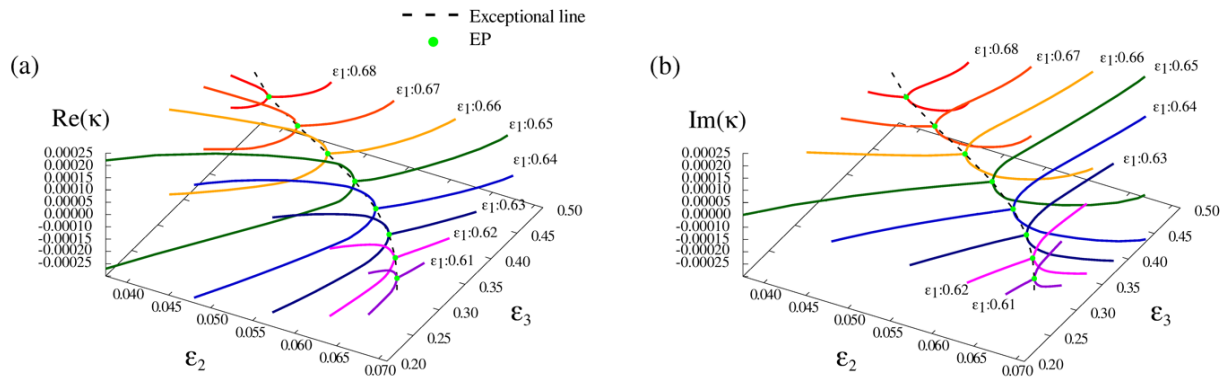

Fig. 1. (a) and (b) show exceptional points (green dots) for different eccentricities of AEMs on the continuous branch-cuts structure. The involved modes in calculations have the same radial mode number l=1 and angular mode number m= 10.

3. Summary

We have investigated EPs in AEMs. The coupled modes of even and odd parity have strong chirality at EPs. We calculated numerical processes to be EPs and presented continuous branch-cuts structure with EPs. As these results, it is revealed that the frequency splitting of EPs is further associated with the primary parameter of eccentricity in ellipses on the fundamental square-root dependency against to perturbations. We believe our results will contribute to the development of a high-resolution sensor in cutting edge state.

References

1. Heiss, W. D. Repulsion of resonance states and exceptional points. *Physical Review E*, *61*(1), 929. (2000).
2. Berry, M. V. Physics of nonhermitian degeneracies. *Czechoslovak journal of physics*, *54*(10), 1039-1047. (2004).
3. Wiersig, J. Sensors operating at exceptional points: general theory. *Physical Review A*, *93*(3), 033809. (2016).
4. Chen, W., Özdemir, Ş. K., Zhao, G., Wiersig, J., & Yang, L. Exceptional points enhance sensing in an optical microcavity. *Nature*, *548*(7666), 192. (2017).
5. Yi, C. H., Kullig, J., Kim, C. M., & Wiersig, J. Frequency splittings in deformed optical microdisk cavities. *Physical Review A*, *96*(2), 023848. (2017).
6. Wiersig, J. Boundary element method for resonances in dielectric microcavities. *Journal of Optics A: Pure and Applied Optics*, *5*(1), 53. (2002).
7. Nelder, J. A., & Mead, R. A simplex method for function minimization. *The computer journal*, *7*(4), 308-313. (1965).

Precision magnetic field sensing with a cavity optomechanical system

Bei-Bei Li[1,2]*, Jan Bilek[3], Douglas Bulla[4], Ulrik L. Andersen[3], Warwick P. Bowen[2]

[1]*Institute of Physics, Chinese Academy of Sciences, Beijing, 100094, China.*
[2]*University of Queensland, St Lucia, QLD 4072, Australia.*
[3]*Technical University of Denmark, 2800 Kgs. Lyngby, Denmark.*
[4]*Defence Science and Technology Group, Edinburgh, SA 5111, Australia.*
**Email address: libeibei@iphy.ac.cn*

Abstract: A broad band and sensitive magnetometry has been demonstrated by integrating a magnetostrictive material with a high Q optical microcavity. We have developed a scalable fabrication method and demonstrated quantum light enhanced optomechanical magnetometry.

1. Introduction

The resonant enhancement of both mechanical and optical response in microcavity optomechanical devices allows exquisitely sensitive measurements of stimuli such as acceleration, mass and magnetic fields. For example, ultrasensitive magnetometry has been realized by integrating a magnetostrictive material Terfenol-D into a high Q optical microcavity [1]. Here we report a magnetic field sensitivity of 26.5 pT/Hz$^{1/2}$, which is comparable to that of the similar-sized superconducting quantum interference device (SQUID) based magnetometry [2], but without using cryogenic cooling. We also developed a scalable and reproducible fabrication pathway for cavity optomechanical magnetometers, through sputter coating a thin film of Terfenol-D into the microcavity, without degrading the quality factor of the microcavities and the performance of the magnetostrictive material [3]. Furthermore, we also demonstrated quantum light enhanced cavity optomechanical magnetometry [4].

2. Experiment and results

2.1 Fabrication of the magnetometer and sensitivity improvement

We use the same method reported in Ref [1] to fabricate the magnetometer. A Terfenol-D particle is manually deposited into a high Q microtoroid using epoxy bonding. Figures 1(a) and (b) show the scanning electron microscope images of the microtoroid before and after the Terfenol-D particle deposition. We then gradually etch down the silicon pedestal (W_{ped}, shown in Fig. 1(c)) to decrease the pedestal's constraint on the mechanical motion of the cavity, and therefore improve the mechanical Q. The achieved peak sensitivity is around 26.5 pT/Hz$^{1/2}$, which is comparable to the similar-sized SQUID [2], but without using the cryogenic environment.

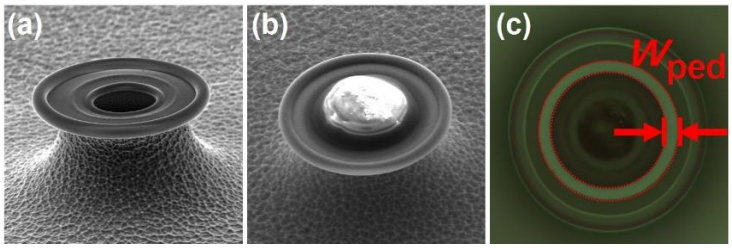

Figure 1. (a) and (b), SEM pictures of a microtoroid before and after the Terfernol-D deposition. (c) The top-view optical image of a magnetometer, with W_{ped} denoting the width of the silicon pedestal.

2.1 A new scalable fabrication method

While the above-mentioned epoxy bonding method allows proof-of-concept demonstrations, practical applications require more scalable and reproducible fabrication pathways. Here we developed a multiple-step method to scalably fabricate optomechanical magnetometers on a silicon chip, with reproducible performance across different devices [3]. The key step is to develop a process to sputter coat a magnetostrictive film onto high quality toroidal microresonators, without degradation of the optical quality factor. A peak sensitivity of 585 pT/pHz is achieved, which is comparable with previously reported results using epoxy-bonding. Figure 2(a) shows a silicon chip with an array of microdisks with Terfenol-D film embedded inside them, with the zoom-in of one of the devices shown in Fig. 2(b). Figure 2(c) shows one of the final devices: a silica microtoroid with Terternol-D film embedded in it.

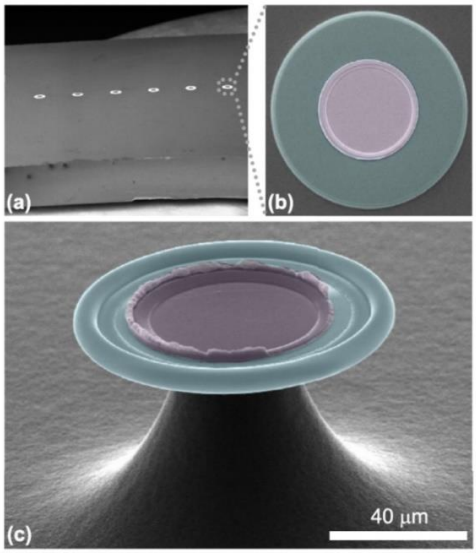

Figure 2. SEM pictures of the magnetometers fabricated by sputter coating Terfernol-D thin films into the microtoroids.

2.3 Squeezed light enhanced optomechanical magnetometry

In this cavity optomechanical system, one of the main noise sources is the shot noise from the probe laser, which could be suppressed by using squeezed light. In our work we demonstrated that by incorporating phase squeezed light into a cavity optomechanical magnetometer, shot noise from the probe light is suppressed by 2.2 dB, and therefore both the sensitivity and the bandwidth of the sensor are improved [4].

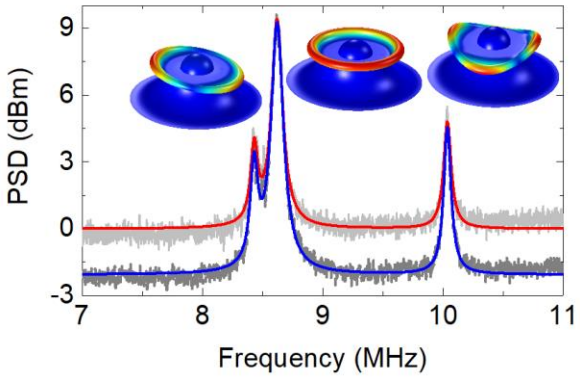

Figure 3. Power spectral density of the magnetometer with coherent probe (red curve) and squeezed probe (blue curve), showing the squeezed light suppressed noise floor, and therefore the improved sensitivity.

3. Summary

For a summary, we have realized high sensitivity magnetometry using a cavity optomechanical system and developed a scalable and reproducible fabrication method. We have also demonstrated quantum light enhanced magnetometry.

References

1. S. Forstner, S. Prams, J. Knittel, E. D. van Ooijen, J. D. Swaim, G. I. Harris, A. Szorkovszky, W. P. Bowen, and H. Rubinsztein-Dunlop, "Cavity Optomechanical Magnetometer," Phys. Rev. Lett. 108, 120801 (2012).

2. J. R. Kirtley, M. B. Ketchen, K. G. Stawiasz, J. Z. Sun, W. J. Gallagher, S. H. Blanton, and S. J. Wind, "High‐resolution scanning SQUID microscope," Appl. Phys. Lett. 66, 1138 (1995).

3. B.-B. Li, D. Bulla, V. Prakash, S. Forstner, A. Dehghan-Manshadi, H. Rubinsztein-Dunlop, S. Foster, and W. P. Bowen, "Invited article: Scalable high-sensitivity optomechanical magnetometers on a chip", APL Photonics 3, 120806 (2018).

4. B.-B. Li, J. Bilek, U. B. Hoff, L. S. Madsen, S. Forstner, V. Prakash, C. Schafermeier, T. Gehring, W. P. Bowen, and U. L. Andersen, Optica 5, 850 (2018).

WOMA

2022

Abstracts of Posters
(in alphabetical order)

Dispersion and nonlinearity engineering for hybrid waveguide comprised of chalcogenide and silicon oxynitride

SHIQI AI[1,2], DONGHAI ZHANG[2], YUHUA LI[1], SAI TAK CHU[1]*, XIN GAI[2]*

[1]*Department of Physics, City University of Hong Kong, Kowloon, Hong Kong, China*
[2]*Department of Electrical Engineering, City University of Hong Kong, Kowloon, Hong Kong, China*
saitchu@cityu.edu.hk & xingai@cityu.edu.hk

Abstract: Hybrid waveguide of chalcogenide and silicon oxynitride is designed as a new platform for nonlinear optical signal processing by taking the advantages of CMOS compatibility of silicon oxynitride and highly nonlinearity of chalcogenide glasses.

1. Introduction

Silicon oxynitride is a very attractive material for integrated optics application, because of its excellent optical properties, e.g. the large refractive index range (between 1.45 for silicon oxide and 2.0 for silicon nitride), and the availability of CMOS compatible low-cost fabrication technologies [1]. Chalcigenide glass is emerging family of materials in the last decade for all-optical signal processing because of its large nonlinearity and negligible nonlinear absorptions such as two-photon absorption and free carrier absorption [2,3].

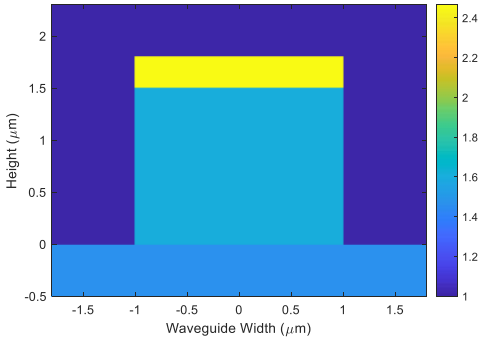

Fig. 1. Schematic graph of hybrid waveguide comprised of chalcogenide and silicon oxynitride.

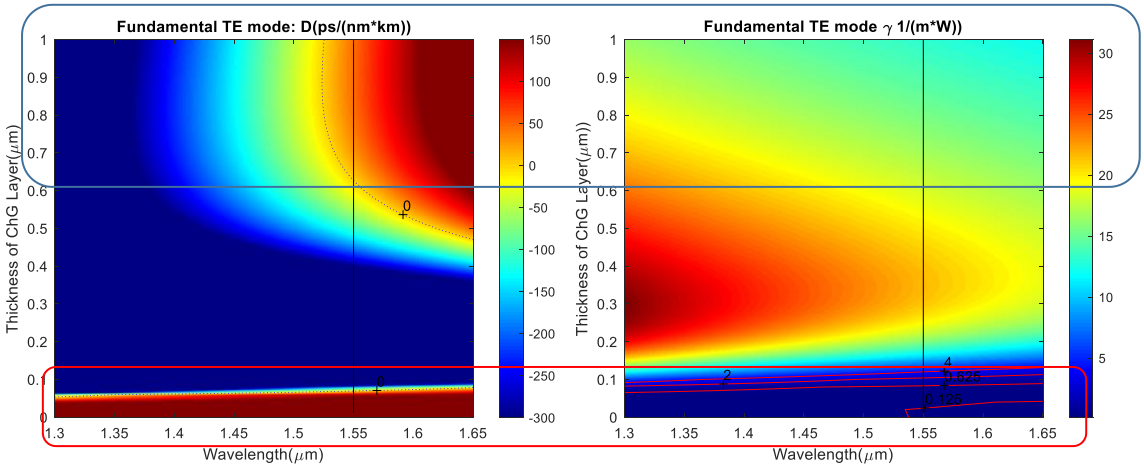

Fig. 2. Dispersion engineering and nonlinearity prediction for transverse electric mode of hybrid waveguide.

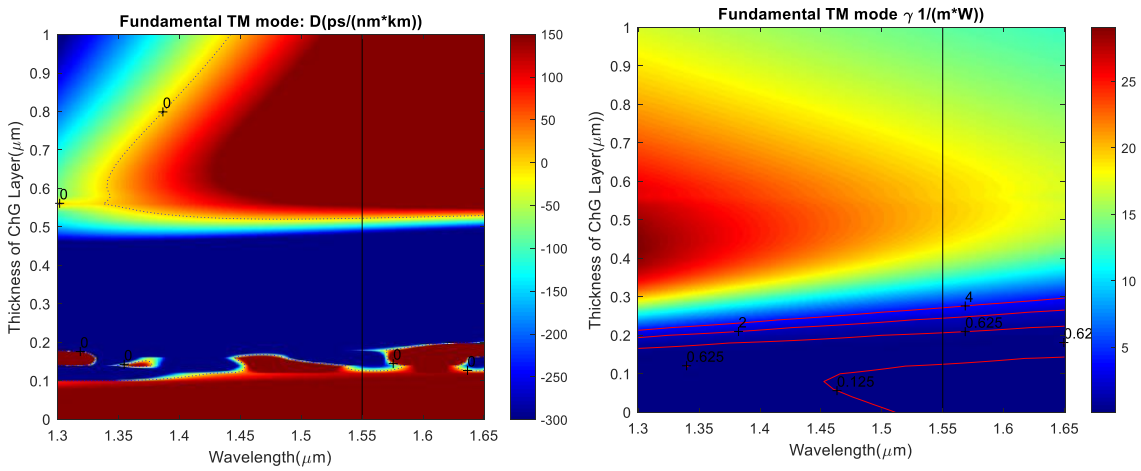

Fig. 3. Dispersion engineering and nonlinearity prediction for transverse magnetic mode of hybrid waveguide.

2. Summary

Dispersion and nonlinearity are systematically studied for hybrid chalcogenide-silicon-oxynitride waveguide. Anomalous dispersion and strong nonlinearity enhancement are observed at different thickness of chalcogenide top layer.

References

1. Zhizhou Lu, Weiqiang Wang, Wenfu Zhang, Mulong Liu, Leiran Wang, Sai T. Chu, Brent E. Little, Jianguo Zhao, Peng Xie, Xinyu Wang, and Wei Zhao, "Raman self-frequency-shift of soliton crystal in a high index doped silica micro-ring resonator [Invited]," Opt. Mater. Express 8, 2662-2669 (2018)
2. Xin Gai, Ting Han, Amrita Prasad, Steve Madden, Duk-Yong Choi, Rongping Wang, Douglas Bulla, and Barry Luther-Davies, "Progress in optical waveguides fabricated from chalcogenide glasses," Opt. Express 18, 26635-26646 (2010)
3. Yu, Y. , Gai, X. , Ma, P. , Choi, D. , Yang, Z. , Wang, R. , Debbarma, S. , Madden, S. J. and Luther‐Davies, B. (2014), A broadband, quasi‐continuous, mid‐infrared supercontinuum generated in a chalcogenide glass waveguide. Laser & Photonics Reviews, 8: 792-798.

BOSIM: Holistic Optical Switch Integration Model

XUANQI CHEN[1], ZHIFEI WANG[2], JUN FENG[3], ZHEHUI WANG[4], JIAXU ZHANG[5], SHIXI CHEN[6], JIANG XU[7]

[1,2,3,4,5,6,7]*Department of Electronic and Computer Engineering, The Hong Kong University of Science and Technology, Clear Water Bay, Kowloon, Hong Kong, China*

[1]*xuanqi.chen@connect.ust.hk*

Abstract: BOSIM is a SPICE-compatible electro-optical co-simulation model to systematically study optical switches using PN, PIN and MIS capacitor device technologies. It can model both transient and steady state properties, and have extensive validations by measured data.

1. Introduction

Silicon photonic networks are revolutionizing computing systems by improving the energy efficiency, bandwidth, and latency of data movements. Optical switches, such as microresonators (MR) and Mach-Zehnder Interferometers (MZIs), are the basic building blocks of silicon photonic networks. Fig. 1 shows our proposed SPICE-compatible electro-optical (EO) co-simulation flow. The mainstream EDA tools, such as Spectre, HSPICE or TSPICE, can simulate the electrical circuits. BOSIM serves the EO bridge, and provide both electrical SPICE model for active photonic switches and optical numerical model based on effective index method. It can holistically model both transient and steady state properties, such as switching speed, power, transmission spectrum, area and carrier distribution. Furthermore, the comprehensive quantitative comparisons of different types of switches are feasible using BOSIM, as shown in the radar chart of Fig. 1.

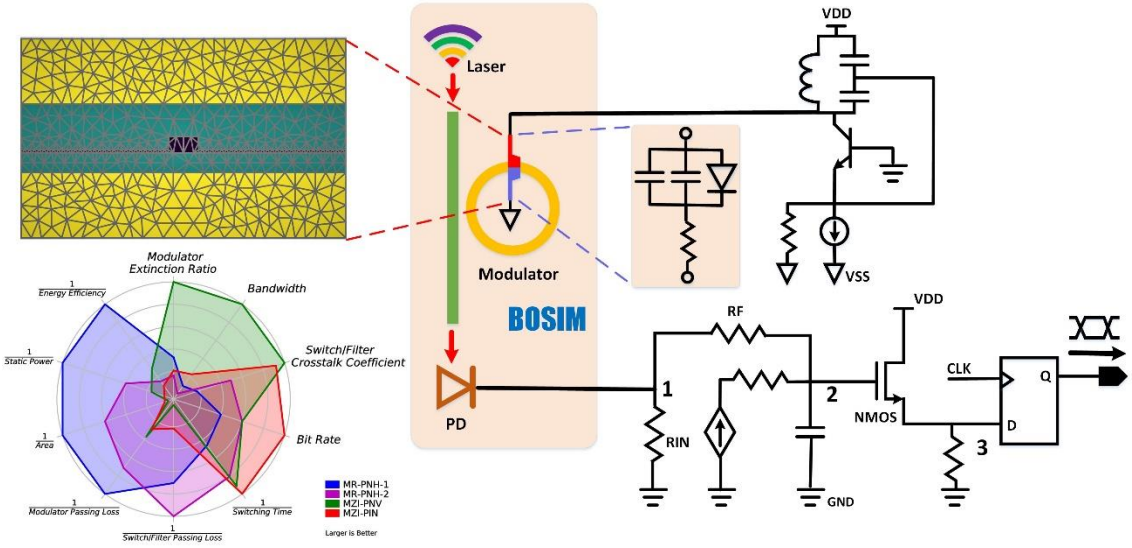

Fig. 1. SPICE compatible electro-optical co-simulation flow.

2. BOSIM

2.1 Overview

A system overview is shown in Fig. 1 (a), where the BOSIM analyzer inputs design details, selects related libraries and outputs performance results. The design details include electrical configurations, optical element structures, and device parameters. The input of the electrical configuration involves the driven voltage and circuit parameters, while optical element structure includes the geometry size, film height, etching depth, cladding height and PN interface offset. The device parameters include the doping concentration of the electrical element, its SPICE parameters, and the optical parameters like refractive index and absorption rate. The BOSIM library contains all the common objects. The electrical objects are a PN diode, PIN diode, and MIS capacitor, while the optical objects are a phase shifter, bus waveguide, directional coupler, and MMI. As for the outputs, BOSIM can evaluate latency, power, loss, signal to noise ratio (SNR), transmission spectrum, eye diagram, area consumption and carrier distribution.

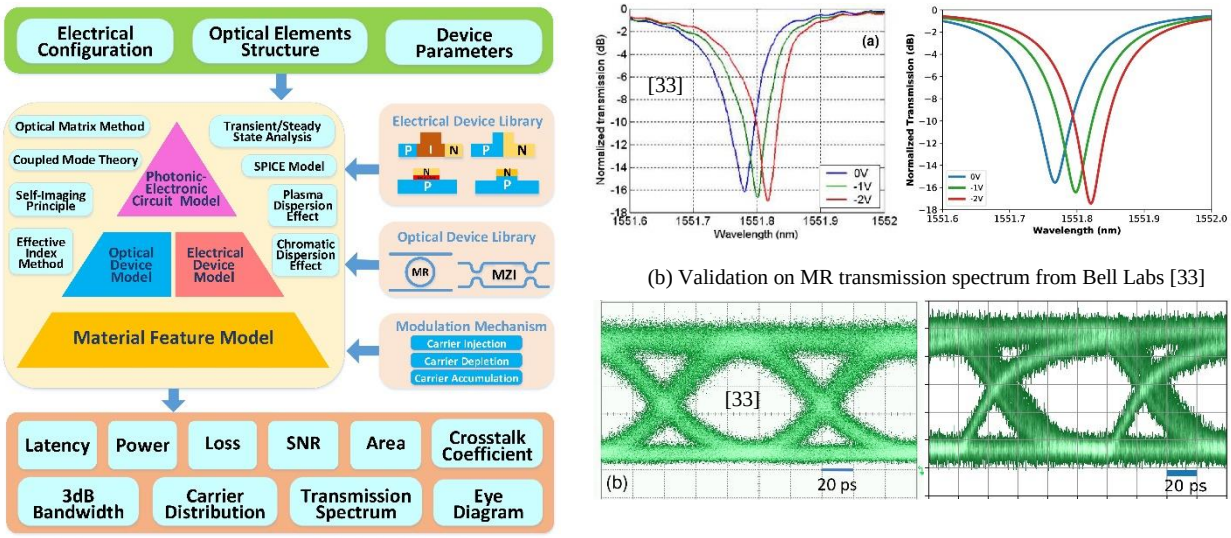

(a) Block diagram of BOSIM

(b) Validation on MR transmission spectrum from Bell Labs [33]

(c) Validation on MR eye diagram from Bell Labs [33]

Fig. 2. Block diagram and validation results of BOSIM.

The BOSIM analyzer has three levels: material, device and circuit level. In the material level, BOSIM precisely depicts critical physical quantities, such as refractive index and mobility. The device level adopts the classical model for electrical and optical elements with plenty of setup variables, and the circuit level integrates all the components and analyzes the optical modulators.

2.2 Validations and Applications

BOSIM is validated by the measured data from eight research groups and companies, including Intel, IBM, Bell Labs, PETRA, ETRI, CAS, Cornell University and University of Surrey. Fig. 2 (b) and (c) show the validation results of steady state and transient state separately for the carrier-depletion MR with 15μm radius from Bell Labs. When the driven voltage decreases from 0V to -2V, the transmission spectrum has red shift and the absolute value of minimal point increases, as shown in Fig. 2 (b). The Fig. 2(c) is the eye diagram result when MR works in 5 Gbps modulation rate. The BOSIM simulation results well match the experimental data, specifically the passing loss, crosstalk coefficient, 3dB bandwidth, the shift wavelength and the spectrum shape in Fig. 2(b); the bit rate, extinction ratio, passing loss and jitter in Fig. 2(c).

Currently, we have integrated our BOSIM simulator with the mainstream EDA tools and our heterogenous simulator, JADE [3]. There are four promising areas. Firstly, the silicon photonic EO-codesigns are feasible, and the SPICE compatible feature of BOSIM guarantees its good compatibility with electrical EDA tools, as shown in the circuit simulation overview of Fig. 1. Secondly, in the device level, BOSIM can help study different optical switches, as shown in the radar chart of Fig. 1 and Fig. 2(a). Thirdly, as a plugin of JADE, BOSIM solids and enriches advanced computer architecture researches involving photonics technique [4]. Last but not the least, the complicated but accurate device model will speed up the study of design space optimization and process variation.

3. Summary

We propose BOSIM, a basic silicon photonic switch integration model for silicon photonic network. Validations show that BOSIM is accurate in both transient and steady states for the carrier depletion MR from Bell Labs. Some possible applications of BOSIM are discussed as well. More information can be found in [1] [4].

References

1. Xuanqi Chen, Zhifei Wang, Yi-Shing Chang, Jiang Xu, Jun Feng, Peng Yang, Zhehui Wang, Luan HK Duong, "Modeling and Analysis of Optical Modulators Based on Free-Carrier Plasma Dispersion Effect," TCAD (2019).
2. Po Dong, Shirong Liao, Dazeng Feng, *et al*, "Low Vpp, ultralow-energy, compact, high-speed silicon electro-optic modulator," OE (2009).
3. Rafael K. V. Maeda, Peng Yang, Xiaowen Wu, Zhe Wang, Jiang Xu, Zhehui Wang, Haoran Li, Luan H. K. Duong, Zhifei Wang, "JADE: a Heterogeneous Multiprocessor System Simulation Platform Using Recorded and Statistical Application Models," AISTECS (2016).
4. Xuanqi Chen, Zhifei Wang, Yi-Shing Chang, Jiang Xu, Peng Yang, Zhehui Wang, Luan HK Duong, "A Comprehensive Electro-Optical Model for Silicon Photonic Switches," ISVLSI (2018).

Manipulating and Trapping of Micro-Particles on Microring Resonators

VICTOR W. L. HO[1*], BRENT E. LITTLE[2] AND SAI T. CHU[1]

[1]*Department of Physics, City University of Hong Kong, Kowloon Tong, Hong Kong*
[2]*State Key Laboratory of Transient Optics and Photonics, XIOPM, CAS, Xi'an, China*
[*]*wailokho2-c@my.cityu.edu.hk*

Abstract: Optical trapping and manipulation of micro size particles on an integrated optical ring resonator is demonstrated in a self-locked scheme with pulses. Furthermore, the evolution of these pulses can also be explored in sensing applications.

1. Introduction

Various demonstrations of optical trapping with planar microring resonators have previously been reported, *e.g.* [1] where the particles are trapped and manipulated by adjusting the input tunable lasers on and off resonances. Resonator is an energy storage system with a feedback system where the optical intensity is enhanced when it is on resonance. Compared to a waveguide trapping configuration, resonant cavity trapping presents two advantages [2]; the high field confinement in a cavity leads to strong optical force enhancement. Cavity perturbation induced by the trapped object could serve as a highly sensitive probe for analyzing the physical properties (size, refractive index, absorption) of the objects. However, the key issues with using a resonator to trap particles are the resonance is sensitive to temperature and environment. Misalignment of laser with resonance reduces the power on the ring and lost the trapping capability. Therefore, it is critical to keep track of the ambient shift of the resonance frequency otherwise the particles will no longer be under controlled if it can be drifted off resonance [3]. The optical ring resonator in a self-locked configuration, shown in Fig. 1a) where the ring resonator is enclosed inside an external cavity loop. The external cavity having a much smaller free spectral range (FSR) than the ring resonator keeps the signal on resonance for optical trapping regardless of the ambient variation and resonance frequency shift encountered in the experiment. The switch in the proposed configuration allows the selection of either clockwise or counter-clockwise propagation of the particles, while the propagation speed can be adjusted from the power of the amplifier. When it is on resonance, the excitation light circulates in the microring resonator by a number of times proportional to its Q-factor. As the circulating light cumulates, the optical field in the microring resonator can also be enhanced by orders of magnitude [4]. Thus, the electrical field in the ring is much higher than the bus waveguide in on resonance status. In this research, the new proposed scheme can trap PS beads of sizes in 3 mm (Fig. 1c and d) to with low power ranging with control the speed and direction.

2. Experimental Results

The time response from the tap indicates we have CW mode locking in the fiber loop cavity (Fig. 1b). The repetition rate of the CW pulses is approximately 5.5 MHz, corresponds to an external cavity loop of ~40 meters. The expanded optical image of the ring resonator prior to the EDFA being switched on at magnification of 10x. The pattern on the device is fillers that allow the device to be polished flat and this does not affect the optical performance. In the experiment, the particles start to migrate toward the ring resonator once the EDFA power is switched on, this is due to the gradient force that pulls the particles toward the waveguide. Once the particles are positioned on top of the ring waveguide, they are trapped and get push along the waveguide by the radiation force. In the example shown in Figs. 1 c) and d), the particles are initially separated into two groups, a single particle and a group of three particles. The two groups of particles travel at different speeds with the group of three travels faster than the single particle due to the peloton effect. After 30s, the group of three particles peloton has caught up with single particle (Fig. 1d). The measured speed is 19.7μm/s for single particle while the speed of the peloton is 23.6μm/s.

The speed of the particle can also be adjusted by controlling the power of the EDFA, Table 1 shows the measured speed of the 3 μm size PS particle at the different drop port power, along with the estimated power in the ring resonator. Here, one can adjust the speed from 59 um/s to 98 um/s by increased the power by 2.4 dB. Besides the power of the EDFA, the speed of the particle also depends on the size and composition of the particle, along with the viscosity of the solution which the particles are immersed.

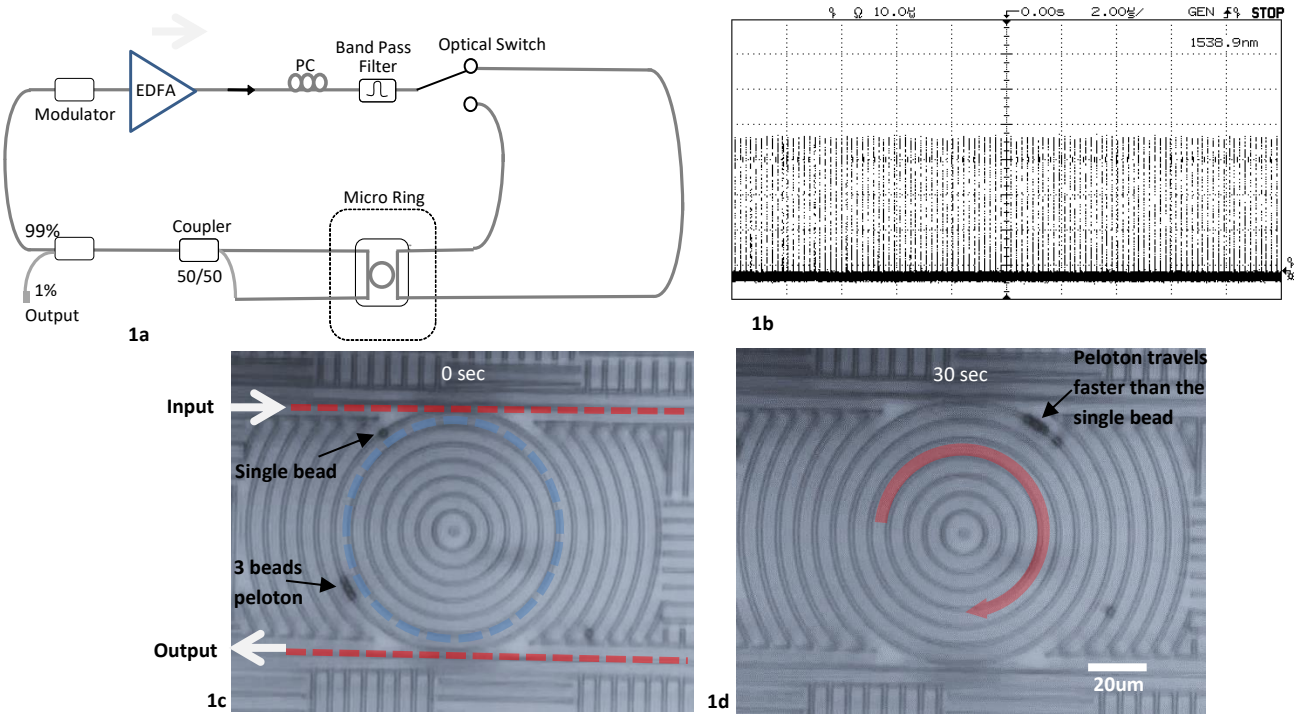

Fig. 1a: Optical ring resonator in a self-locked configuration (Radius of ring: 47 um, Core index: 1.70). Fig. 1b: The time domain from the optical output port. Fig. 1c and 1d: The particles are positioned on top of the ring waveguide, they are trapped and traveled along the waveguide in first 30s.

Table 1. Estimated power in the resonator base on the power in the drop port and the relative trapping speed.

Power in Drop Port (dBm)	Power in the resonator (dBm)	Speed (um/s)
-2.4	24.1	59.1
-2	24.5	84.4
-1.2	25.3	89.5
0	26.5	98.4

3. Summary

The proposed scheme allows the ring resonator to continue to trap the particles regardless the resonance frequency shift it encounters during the experiment. The particles are propelled around the ring circumference with velocity as high as 98um/s for over 10 minutes. We expect to realize all-optical on-chip manipulation such as routing, delivery and storage of nanoparticles and biomolecules using this configuration.

References

[1] S. Lin, E. Schonbrun and K. Crozier, 'Optical Manipulation with Planar Silicon Microring Resonators', Nano Letters, vol.160, pp. 2408-2411, 2010.

[2] Shiyun Lin, Ethan Schonbrun, and Kenneth Crozier, Nano Lett. 2010, 10, 2408—2411

[3] M. Peccianti, A. Pasquaze, Y. Park, B.E. Little, S.T. Chu, D.J. Moss and R. Morandotti," Demonstration of a stable ultrafast laser on a nonlinear microcavity", Nature Comm., DOI:10.1038/ncomms1762, 2012.

[4] Little, B. E. et al. Microring resonator channel dropping filters. J. Lightwave Tech. 15, 998−1005 (1997).

Highly sensitive detection with heterodyne waveguide interferometry

MING JIN[1, 2], XING-JUN WANG[1, 3], YUN-FENG XIAO[2,3]

[1]*State Key Laboratory of Advanced Optical Communications System and Networks, Department of Electronics, Peking University, Beijing, 100871, China.*
[2]*State Key Laboratory for Artificial Microstructure and Mesoscopic Physics, School of Physics, Peking University, Beijing 100871, China.*
[3]*Nano-optoelectronics Frontier Center of Ministry of Education at Peking University, Beijing, 100871, China.*

xjwang@pku.edu.cn; yfxiao@pku.edu.cn

Abstract: We introduce a CMOS-compatible waveguide interferometry for highly sensitive detection using optical dark-field scattering and heterodyne technique. The sensing performance is preliminarily demonstrated by fiber nanotip with the radius of 200 nm, and it shows a high signal-to-noise ratio of above 3×10^2 under a quite low pump (~ -8 dBm).

1. Introduction

The detection of nanoscale objects is important for applications in environment monitoring, medical diagnosis and biomolecule characterization. The optical evanescent sensors are widely used for nanoparticle detection due to their high sensitivity and label-free nature. In the past few years, the research mainly focuses on sensitivity enhancement using optical nanofiber, microcavity and plasmonic nanostructures. To date, the optical evanescent sensors have been able to detect single molecules and atomic ions [1-3]. Optical nanofiber sensors using elastic light scattering in the dark field even reached quantum limit and was able to track biomolecules as small as 3.5 nm [4-5]. However, most these sensors face the difficulty of mass manufacturing due to precise control on the fabrication. In our previous work, an on-chip spiral waveguide sensor has been demonstrated the ability of single nanoparticle detection [6]. Here, we introduce a waveguide interferometry for highly sensitive detection. Fiber nanotip with a radius of around 200 nm is used as benchmark. The signal-to-noise ratio is boosted up to 3×10^2 under a quite low pumping condition (~ -8 dBm).

2. Sensor Design

The waveguide sensor is fabricated on the standard silicon-on-isolator (SOI) platform of 220 nm in height. TE-polarized light is coupled into two orthogonal coupled waveguides (WG1, WG2), as shown in Fig.1a, using C-band grating couplers on top of 2 μm buried oxide (BOX). The widths of the waveguides are 500 nm and 1000 nm respectively. The gap between two waveguides is 1 μm. A 200-μm-long taper is added to smoothly change the width of WG2 from 500 nm at input port to 1 μm at output port for better inducing TE_0 mode. The tested insertion loss of grating coupler is about 7.5 dB/facet, considering the coupling condition between the single mode fiber and the grating coupler.

3. Experiment results

The Experiment schematic is shown in Fig.1a, which includes two parts, the on-chip heterodyne detection using orthogonal coupled waveguide sensor and the signal processing setup. The light from laser is divided into three flows. The first one goes through the acousto-optic modulator (AOM) under the driven of RF source 1 (modulation frequency is f_1 = 80.234 MHz) and outputs a blue-shifted probe light coupled into the WG2. The second one regarded as the local light of heterodyne scheme is directly coupled into the WG1. The third one is used as a balanced beam to better reduce the noise from laser amplitude and frequency fluctuation. The basic working principle is: the analytes in the gap between the WG1 and the WG2 scatter the red-shifted probe light from the WG2 to the WG1 as signal field, which is detected using a balanced photodetector. Then the signal travels through a high-pass filter for better noise control and is followed by an electrical amplifier. The amplified signal is divided into two paths, and they are separately mixed with two RF signals which have 90 degrees phase difference while maintaining the same frequency from the RF source 2 (f_2 = 80.184 Mhz). The mixers output is received by a data acquisition system (DAQ).

We use a fiber nanotip with a radius of 200 nm instead of the nanoparticles to benchmark the performance of the orthogonal coupled waveguide sensor. The nanotip (Fig. 2d) is controlled by a 3D translation stage. The Fig. 2c is a 3D simulation of the coupling region which also denotes the scan direction (x-direction) and the distance of the nanotip. The moving range of the nanotip is carefully set to ensure the scan loop starts at the position away from the WG2 and stops at the x-direction center of the WG2 output port. We observe two different drops at normalized amplitude in every single loop. The first one with symmetrically distribution proves the nanotip passes through the same side

boundary of coupling region twice a loop. If the nanotip horizontally scans across the whole coupling region, the drops will be asymmetric because when the nanotip passes through the half coupling region close to WG1's output port, the forward-scattering light dominates the output signal change. To the opposite, when the nanotip passes through the other half region, the back-scattering light will induce an asymmetric change compared to forward scattering. The second kind of drops occurs when the nanotip approaches the middle of the coupling region which is, due to the abrupt increase of direct reflection back into WG2.

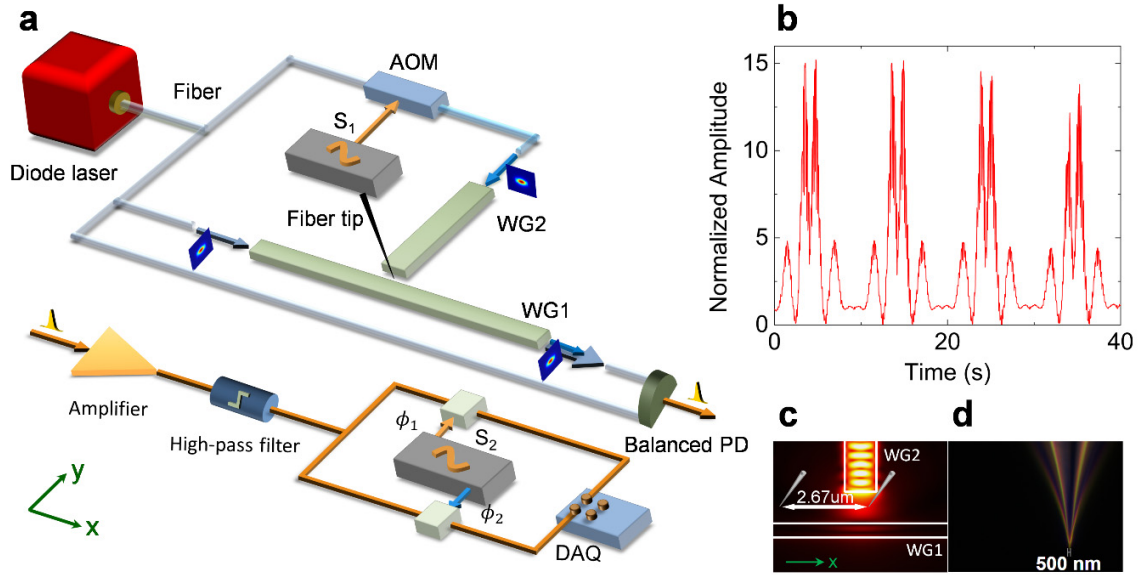

Fig. 1 **a,** Experiment setup. The orthogonal coupled waveguide sensor consists of WG1 and WG2, the frequency of source 1 (S_1), source 2 (S_2) are 80.234 MHz and 80.184 MHz respectively, 55 MHz High pass filter, $\phi_1 - \phi_2 = 90^\circ$ **b,** Normalized amplitude of the sensor output for the fiber nanotip horizontally scanning with a range of 2.67μm. **c,** mode profile of coupling region and scanning range schematic. **d,** Microscope image of fiber nanotip with a radius of 200nm.

4. Summary

In summary, we have demonstrated a CMOS-compatible orthogonal coupled silicon waveguide sensor. By using the heterodyne scheme, fiber nanotip with a radius of 200 nm can be detected. The signal to noise ratio reaches up to 3×10^2 under a quite low pump condition (~ -8 dBm). The measured background noise is at the level of 10^{-2} in the received signal. The combination of CMOS technology and heterodyne scheme makes our sensor possess the ability to detect nanoscale analytes in a more affordable way while maintaining a high sensitivity, which opens the gate towards the large-scale integration of optical sensors.

References

1. Zhu, J., Ozdemir, S. K., Xiao, Y.-F., Li, L., He, L., Chen, D.-R., & Yang, L. On-chip single nanoparticle detection and sizing by mode splitting in an ultrahigh-Q microresonator. Nature Photonics, 4, 46 (2009).
2. J. Xavier et al, Advances in optoplasmonic sensors – combining optical nano/microcavities and photonic crystals with plasmonic nanostructures and nanoparticles, Nanophotonics, 7, 1, 1-38, (2018).
3. Li, B. B., Clements, W. R., Yu, X. C., Shi, K., Gong, Q., & Xiao, Y. F. Single nanoparticle detection using split-mode microcavity Raman lasers. Proc Natl Acad Sci U S A, 111(41), 14657-1466, (2014).
4. Yu, X.-C., Zhi, Y., Tang, S.-J., Li, B.-B., Gong, Q., Qiu, C.-W., & Xiao, Y.-F. Optically sizing single atmospheric particulates with a 10-nm resolution using a strong evanescent field. Light: Science &Amp; Applications, 7, 18003, (2018).
5. Mauranyapin, N. P., Madsen, L. S., Taylor, M. A., Waleed, M., & Bowen, W. P. Evanescent single-molecule biosensing with quantum-limited precision. Nature Photonics, 11, 477 (2017).
6. Tang, S. J., Liu, S., Yu, X. C., Song, Q., Gong, Q., & Xiao, Y. F. (2018). On-Chip Spiral Waveguides for Ultrasensitive and Rapid Detection of Nanoscale Objects. Adv Mater, 30(25), (2018).

Lab-on-a-chip based pneumatically deformable microfluidic laser

JINUK KIM, KYUNGWON AN[1]

Department of Physics and Astronomy & Institute of Applied Physics, Seoul National University, Seoul 08826, Korea
[1]kwan@phya.snu.ac.kr

Abstract: We demonstrated a microfluidic laser based on lab-on-a-chip technique. The cavity shape can be adjusted continuously by air flow around liquid jet. Its flexibility is applicable for studies on chaotic microcavities and interactions between cavitymodes.

1. Introduction

Optofluidic microcavities fabricated by lab-on-a-chip technique have received a great deal of attention for a large variety of applications such as optofluidic dye lasers, single cell analyses, and single molecule detection [1]. Various type of cavities have been realized on the microfluidic chip by reproducible micron-scale fabrication technique: gratings[2], microrings[3] and Fabry-Perot cavities[4]. Tunability of gain medium is one of the advantages of optofluidic systems, however the shape of these cavities are basically fixed. On the other hand, the liquid jet laser of which cavity is formed by gain medium itself has a tunable cavity[6]. By combining advanced device fabrication technologies and tunablility of the liquid jet laser, a pneumatically tunable microfluidic laser is demonstrated.

2. Liquid jet laser based on silicon/glass chip

2.1 Silicon/glass chip

Three channels are engraved on a silicon wafer by photoresist patterning and dry etching. Middle channel is for the liquid which dye dissolved in. Pressurized liquid is ejected from the outlet of the chip. Outer channels are for the gas to press and deform the ejected liquid jet. Inlets for liquid and gas are patterned on a glass wafer by dry film resist and sanding. The silicon and glass wafers are bonded by anodic bonding.

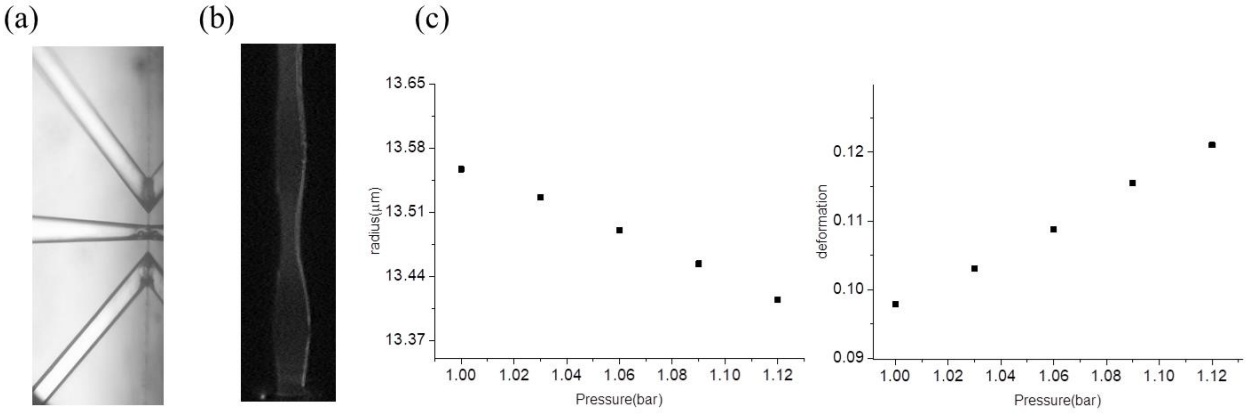

Fig. 1. (a) The microfluidic gas-deformable chip is shown. The gas channel (up and down), and the liquid channel (middle) are connected to outlets on the right side of the chip. (b) A CCD image of the liquid jet ejected from the chip. (c) Air pressure dependence of the radius and the deformation of the jet.

2.2 Pneumatic control of the cavity shape

Ejected liquid jet oscillates spatially because of surface tension and momentum given by air jet. The crosssection of the liquid jet at extreme position is described in polar coordinate by the below equation.

$$r = r_0(1 + \eta \cos 2\theta + 5/12\,\eta^2 \cos 4\theta)$$

Due to the refractive index difference between liquid and air, the boundary of liquid acts as a dielectric mirror. The shape of cavtiy is determined by two parameters: radius(r_0) and deformation(η). The parameters can be estimated

by observing the spectrum of the microfluidic laser. The radius is in inverse proportion to the air pressure, while the deformation parameter is directly proportional.

3. Summary

Microfludic laser based on a silicon/glass chip is demonstrated. The parameters for cavity shape are adjusted by pneumatic control. Its tunability can be used for exploring chaoticitiy of microcavities and intra cavity modes interactions. Furthermore, an exceptional point of liquid jet cavitymodes can be approached by adding refractive index control.

References

1. Y. Chen *et al.*, "Optofluidic microcavities: Dye-lasers and biosensors", BIOMICROFLUIDICS **4**, 043002 (2010).
2. C. Vannahme *et al.*, "Optofluidc dye laser in a foil", Opt. Express **18**, 9280 (2010).
3. W. Lee *et al*., "Tunable single mode lasing from an on-chip optofluidic ring resonator laser", Appl. Phys. Lett. **98**, 061103 (2011).
4. G. Aubry *et al*., "A multicolor microfluidic droplet dye laser with single mode emission", Appl. Phys. Lett. **98**, 111111 (2011).
5. S. Moon *et al*., "Experimental observation of Bohr's nonlinear fluidic surface oscillation", Sci. Rep. **6**, 19805 (2016).

Unilluminable room problem and wave chaos in an acoustic Penrose-cavity

JUMAN KIM,[1] TAKEHIRO FUKUSHIMA,[2] AND KYUNGWON AN[1†]

[1] *School of Physics and Astronomy, Seoul National University, Seoul 08826, Korea*
[2] *Department of Information and Communication Engineering, Okayama Prefectural University, 111 Kuboki, Soja, Okayama 719-1197, Japan*
[†] *kwan@phya.snu.ac.kr*

Abstract: The tunneling through dynamical barriers in the Penrose-cavity is simulated with an edge-cut Penrose-cavity. We also observed a half-illuminated mode in an acoustic Penrose-cavity experimentally. This mode can be explained as a coherent superposition of near-degenerate modes.

1. Introduction

Unilluminable room problem is a mathematical question of finding the billiard which always has dark regions regardless of the location of a light source [1]. Penrose-cavity uses the property of the ellipse to make an unillumiable room, which consists of elliptical top and bottom boundaries and mushroom-shaped protruded boundaries in the middle [2] [Fig. 1(a)]. There are three regions [colored in green, blue, and red, respectively in Fig. 1(b)] separated from each other by dynamical barriers in the PSOS (Poincaré surface of section) of the Penrose-cavity [3]. However, the divided regions can be coupled to each other by wave diffraction, Goos–Hänchen shift, and refraction (in an open cavity). Using the ray simulation in an edge-cut Penrose-cavity, we try to incorporate these effects and simulated the coupling mechanisms. In addition, by using the schlieren method [4], we have imaged acoustic resonance modes of an acoustic Penrose-cavity with the size parameter in the range of the long-wavelength regime. While most of them are excited symmetrically with respect to the mirror-symmetry axis, an unexpected half-illuminated mode is observed, where one side [the upper or the lower side in Fig. 1(a)] is bright while the other side is dark with high contrast. This mode can be explained as a coherent superposition of adjacent near-degenerate scar modes which have different parities within its linewidth. The half-illuminated modes at different size parameters are also compared.

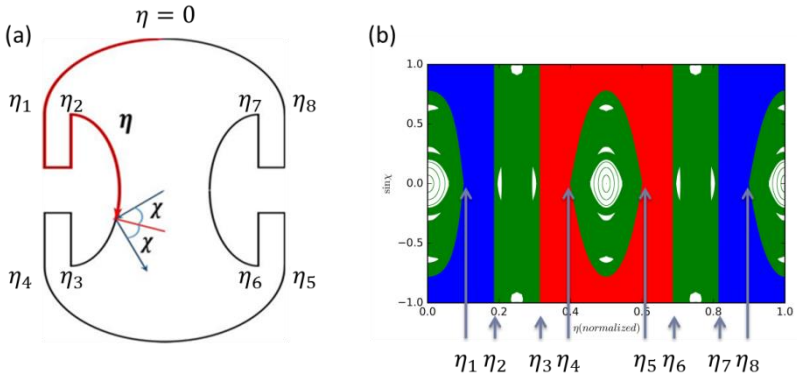

Fig. 1. (a) The shape of the Penrose cavity. Coordinate η is measured along the circumference. Significant locations are denoted as η_1, η_2, η_3, etc. (b) There are three divided chaotic regions (red, green, and blue) in the PSOS of the Penrose cavity. White regions represent island structures.

2. Results

2.1 Ray-dynamics in an edge-cut Penrose-cavity

The tunneling through dynamical barriers can be simulated to some degree by using the classical ray simulation in an edge-cut Penrose-cavity, where the edges around the foci (near η_2, η_3, η_6, and η_7) are slightly cleaved (Fig. 2(a)). The ray can escape through the opening and the escape rate is investigated to understand the coupling between two divided chaotic regions. The PSOS of the edge-cut Penrose cavity (Fig. 2(b)) shows the channels through which rays escape to the other regions. The mean number of reflections of a bundle of rays before escape is measured with changing the cut width and compared to the theory (Fig. 2(c)).

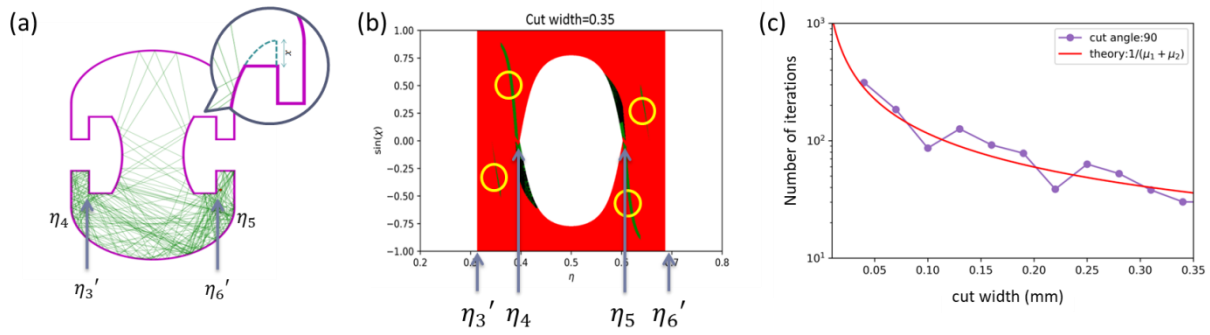

Fig. 2. (a) The edge-cut Penrose-cavity and its ray dynamical simulation. (b) A part of the PSOS of the edge-cut Penrose-cavity. A ray emitted from the red dot in (a) (which initially belongs to the red chaotic region) escapes to the green chaotic region after many reflections through the channels marked in green (highlighted with yellow circles). Here the black parts are new regions emerging from deformation. (c) Log-linear plot of the mean number of reflections measured with changing the cut width (purple dots) is well fit by the inverse of the sum of the areas of the escape channels (red solid line).

2.2 Half-illuminated modes in a Penrose-cavity

We observed an unexpected half-illuminated mode (HIM) of the acoustic Penrose-cavity in the low-frequency regime using the schlieren imaging method. This mode can be explained as a coherent superposition of the quasi-eigenmodes within the linewidth of the HIM. The acoustic modes are computed with the finite-element mode simulations. Figure 3(a) is the experimentally imaged HIM and Figure 3(b) is a superposition result of some near-degenerate modes near the HIM obtained by optimizing their coupling to the external source. Here modes are regarded as driven damped harmonic oscillators. Among them, a scar mode constitutes the largest proportion of the total intensity and some other modes which have different parities interfere with the scar mode constructively at the top and destructively at the bottom. It is also experimentally verified from interferential oscillation of the HIM as the external acoustic source is translated horizontally.

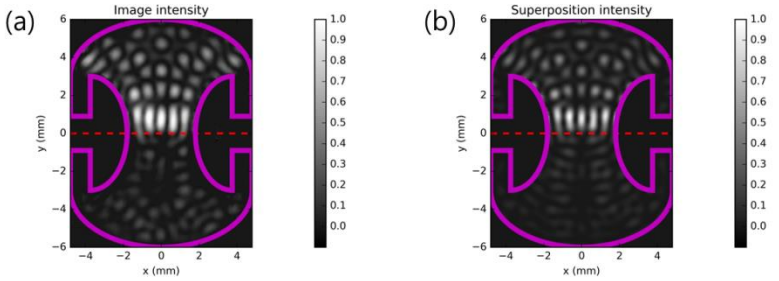

Fig. 3. (a) The half-illuminated mode imaged using the schlieren method in experiment. (b) The superposition of near-degenerated modes can reproduce the observed HIM.

3. Summary

Towards making a broadband unilluminable room which can trap chaotic acoustic wave in a localized region, we have investigated the tunneling through the dynamical barrier using the edge-cut Penrose-cavity and studied HIM to use this as an alternative in the low-frequency regime.

References

1. Lionel Penrose and Roger Penrose, *Puzzles for Christmas*, New Scientist **25**, 1580-1581 (1958).
2. Weisstein, Eric W. "Illumination Problem." From MathWorld--A Wolfram Web Resource. http://mathworld.wolfram.com/IlluminationProblem.html
3. T. Fukushima *et al.*, Opt Express **22**, 11912-11917 (2014)
4. P.A.Chinnery, Victor F. Humphrey, and C. Beckett, J. Acoust. Soc. Am. **101**, 250–256 (1997).

Silicon Oxynitride Hybrid Microresonator Lasers for Sensing

CHING CHI KWAN AND ANDREW W. POON

Photonic Device Laboratory, Department of Electronic and Computer Engineering, The Hong Kong University of Science and Technology, Clear Water Bay, Kowloon, Hong Kong, China
eeawpoon@ust.hk

Abstract: We design and fabricate dye-coated silicon oxynitride whispering-gallery-mode microdisk resonators with embedded grating for on-chip active optical sensing. We demonstrated that the lasing signals are spatially-dependent at the rims and at the inner ring regions. In the sensing experiment, the intensity of lasing reduce under a tapered glass fiber perturbate.

1. Introduction

Whispering-gallery-mode (WGM) microresonators have been intensively studied over the past four decades because of their capability to confine light by total internal reflection along the resonator curved sidewalls, resulting in optical resonances with a high quality (Q)-factor [1]. Such high-Q WGM microresonators on a chip have been demonstrated with high sensitivity to the micro-environment in the proximity of the WGM evanescent field [2] [3]. One way to enhance the sensitivity is to turn a passive microresonator to an active one by either using a light-emitting (gain) medium as the resonator [4] or integrating a gain medium inside or on the surface of the resonator [1] [5]. The fluorescence or lasing emission of such active microresonators can be linearly or nonlinearly perturbed by the micro-environment [3], and thus enable an active sensing mechanism.

In this work, we adopt silicon oxynitride (SiO_xN_y) as the passive platform for on-chip optical and bio-sensing. SiO_xN_y is transparent from the visible to mid-infrared wavelengths, enabling bio-compatible and environmental gas sensing. The refractive index of SiO_xN_y can be tuned between ~ 1.44 (SiO_2) to ~ 2 (Si_3N_4) by abjusting the oxide and nitride ratio. The relatively high refractive index enables compact photonic sensors in the environmental medium such as air and water. The device fabrication is compatible with the standard silicon complementary metal-oxide-semiconductor (CMOS) processes, which enable potentially low-cost photonic integration on a chip. To enable active SiO_xN_y WGM microresonators in the visible wavelengths, we spin-coat the SiO_xN_y photonic chip with a layer of fluorescent dye (Rhodamine-B) doped polymer (SU-8), and flood pump the dye-doped polymer-coated SiO_xN_y microresonator from the top surface.

2. Device design and fabrication

We adopt WGM microdisk resonator design with a thickness of ~350 nm and a dye-doped polymer with a thickness of ~ 100s nm in order to expose the evanescent field of the visible wavelengths to interact with analytes or nanoparticles on the top surface and the sidewall. The microdisk diameter of 100 μm is to enable a high-Q cavity by reducing the fabrication-imperfection-induced sidewall surface roughness. We believe that a lasing sensor can be turned on or off once there is a particle perturbation. With this sensing method of detecting a lasing signal, there is no need for a precision wavelength-tunable laser source nor a high-resolution detector as with passive sensors. Furthermore, radial gratings embedded with gain medium has been introduced in the microdisk for additional modal overlapping and grating wavevector influence. The additional of modal overlapping with gain medium may lower the threshold of the laser and provide further light-matter interaction.

3. Experimental results

The lasing signals from a flood pumped device is collected by using a manually tapered fiber as shown in Figure 1. The tapered fiber tip is touching the surface of the device to collection near field signals. Figure 1 shows the spatially-dependent lasing spectra. There are two cluster of peaks when the signals are collected from the rim of the device but only one cluster of peaks when collecting at the inner ring of the device.

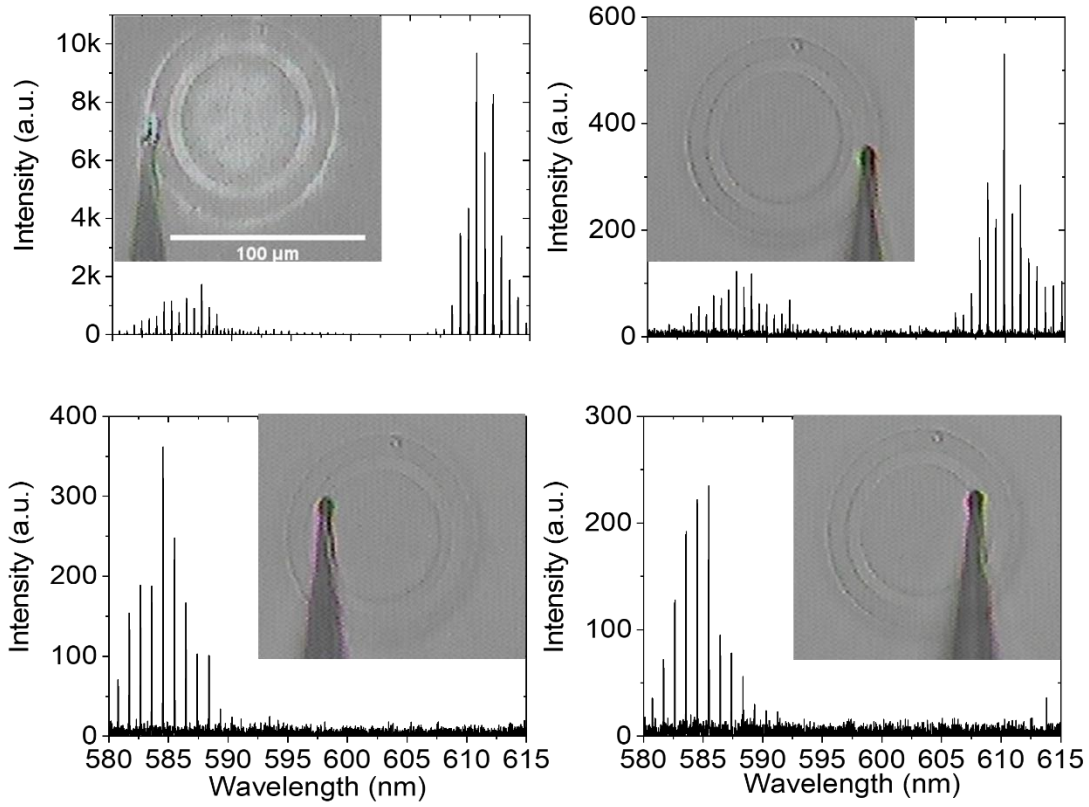

Figs. 1 Lasing signals collected from the rim and at the inner ring.

We acknowledge the financial support from the Research Grants Council (16211616) and the device fabrication support from the Nanosystem Fabrication Facility (NFF) of the Hong Kong University of Science and Technology.

References

[1] J. F. Owen, P. W. Barber, P. B. Dorain, and R. K. Chang, "Enhancement of fluorescence induced by microstructure resonances of a dielectric fiber," Phys. Rev. Lett. **47**, no. 15, pp. 1075–1078, 1981.

[2] K. A. Knapper, K. D. Heylman, E. H. Horak, and R. H. Goldsmith, "Chip-scale fabrication of high-Q all-glass toroidal microresonators for single-particle label-free imaging," Adv. Mater., **28**, no. 15, pp. 2945–2950, 2016.

[3] E. Kim, M. D. Baaske, and F. Vollmer, "Towards next-generation label-free biosensors: recent advances in whispering gallery mode sensors," Lab Chip, vol. 17, no. 7, pp. 1190–1205, 2017.

[4] S. K. Vanga and A. A. Bettiol, "Proton beam writing of dye doped polymer microlasers," Nucl. Instruments Methods Phys. Res. Sect. B Beam Interact. with Mater. Atoms, **348**, pp. 209–212, 2015.

[5] K. Gardner, Y. Zhi, L. Tan, S. Lane, Y.-F. Xiao, and A. Meldrum, "Whispering gallery mode structure in polymer-coated lasing microspheres," J. Opt. Soc. Am. B, **34**, no. 10, p. 2140, 2017.

[6] N. B. Rex, R. K. Chang, and L. J. Guido, "Threshold lowering in GaN micropillar lasers by means of spatially selective optical pumping," IEEE Photonics Technol. Lett., **13**, no. 1, pp. 1–3, 2001.

Three-dimensional microlasers: the square pyramid and beyond.

C. LAFARGUE[1], Y. SONG[2], M. GUIDRY[1], Y. MONCEAUX[1], A. GRIGIS[3], D. DECANINI[4], S. BITTNER[1], B. DIETZ[2], X. CHECOURY[4], J. ZYSS[1], AND M. LEBENTAL[1]

[1]*Laboratoire de Photonique Quantique et Moléculaire, UMR 8537, Ecole Normale Supérieure de Paris-Saclay, CentraleSupélec, CNRS, Université Paris-Saclay, 94235 Cachan, France.*
[2] *School of Physical Science and Technology, and Key Laboratory for Magnetism and Magnetic Materials of MOE, Lanzhou University, Lanzhou, Gansu 730000, China.*
[3]*Laboratoire d'Analyse, Géométrie et Applications (LAGA-UMR 7539), Université Paris 13, Villetaneuse, France.*
[4]*Centre de Nanosciences et de Nanotechnologies, CNRS, Université Paris-Sud, Université Paris-Saclay, C2N Marcoussis, 91460 Marcoussis, France*.

Lebental@ens-paris-saclay.fr

Abstract: Three-dimensional microlasers of various shapes are experimentally investigated, with a focus on the square pyramid, where the lasing modes are located on a genuine three-dimensional periodic orbit. Preliminary results for Möbius strip microlasers are shown.

Thanks to the Direct Laser Writing (DLW) technology, it is now possible to fabricate three-dimensional (3D) microcavities and -lasers with high quality [1]. In Ref. [2], we investigated the pyramid with square base and a ratio of 1:1 beetween the height and the square sidelength shown in Fig. 1(a). The photoresist is doped by a commercial laser dye, such that the pyramid becomes a microlaser. We measure its lasing spectrum and its angular emission pattern in 3D. We demonstrate that the lasing modes are localized on a genuine 3D periodic orbit, shown in Fig. 1(d). This isolated periodic orbit is reflected from the lateral faces at the critical angle, which results in two well-separated linear polarization states. The stability conditions of the periodic orbits are discussed based on the concept of the screw angle.

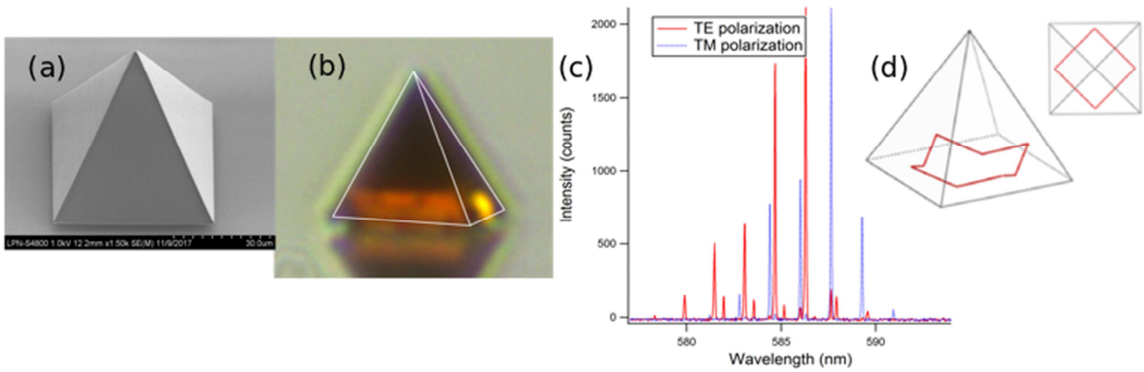

Fig. 1. (a) SEM image of a pyramid with square base. The scale bar is 50 µm. (b) Photo of a square pyramid under optical pumping. The green pump light is removed by a notch filter. The bright yellow spot on the bottom-right wall of the pyramid is the laser emission. (c) Experimental laser spectrum of a square pyramid. A linear polarizer is set in front of the spectrometer, showing that the laser emission is made of two combs with orthogonal polarizations. (d) Periodic orbit in the square pyramid, where the lasing modes are localized. Inset, top view of the same periodic orbit.

Other 3D microlasers will be presented as well, such as the engineering of laser beams with cylindrical cavities and Möbius strip microlasers, for which periodic geodesics seem to play a crucial role.

References

1. J. Fischer and M. Wegener, "Three‐dimensional optical laser lithography beyond the diffraction limit", Laser & Phot. Rev. **7**, 22 (2013).
2. M. A. Guidry, Y. Song, C. Lafargue, R. Sobczyk, D. Decanini, S. Bittner, B. Dietz, L. Huang, J. Zyss, A. Grigis, and M. Lebental, "Three-dimensional micro-billiard lasers: the square pyramid" , Europhys. Lett.**126**, 64004 (2019).

Active 3D FDTD simulation in limaçon transformation cavity

YONG-HOON LEE, INBO KIM, AND MUHAN CHOI

School of Electronics Engineering, Kyungpook National University, Daegu 41566, South Korea
mhchoi@ee.knu.ac.kr

Abstract: Generally, it is difficult to predict lasing modes by passive cavity simulation result because of lasing mode competition and mode coupling. In this study, lasing mode is confirmed in limaçon transformation cavity with active 3D FDTD simulation.

1. Introduction

Since, optical microcavities have various potential from basic researches to application devices, optical microcavities have been widely studied over the past several decades. Especially, in circular microcavities, whispering gallery modes (WGMs) are extremely long-lived modes through the total internal reflection (TIR) at the boundary of the cavity [1, 2]. However, although the circular microcavities have a number of advantages, the isotropic emission takes limitations for the application because of its perfect angular symmetry.

To overcome this problem, many researchers have studied various cavities in which the shape of a cavity is deformed or a scatterer is added inside the cavity so that the cavity has emission characteristics in a specific direction [3, 4]. However, if the boundary of the cavity is deformed or a scatterer is added, the Q-factor is greatly reduced due to the broken angular symmetry of the cavity shape [5]. Therefore, it has long been considered impossible to realize a cavity having directional light emission characteristics and high Q-factor simultaneously.

Transformation optics is an optical principle that realizes the general relativity of a path of light when a space expands or contracts, not in space distortion but in the real world through spatial control of permittivity and permeability of material. Recently, a transformation cavity (TC) research has been newly proposed in which the transformation optics are applied to the resonator [6]. The transformed cavity using the transformation optics maintains a high Q factor because it can maintain the WGMs even though the outer shape is deformed, and it has a directionality unlike the circular cavity.

2. Limaçon transformation cavity laser

Limaçon is the trajectory of the fixed point inside the rotated circle when the other circle is rotated against the fixed circle. Limaçon transformation is conformal mapping and the transformation is

$$\boldsymbol{z = \beta_l(w + \alpha_l w^2)}$$

where $\boldsymbol{\alpha_l, \beta_l}$ are deformation parameter and $\boldsymbol{w, z}$ are complex plane. But it is difficult to realize limaçon TC because a refractive index at certain region is too high. Before transformed to limaçon shape, cavity is transformed the center shift called the Möbius transformation. This makes it is to make spatial varying refractive index by maximum refractive index by lowering the maximum refractive index. The center shift Möbius transformation is

$$\boldsymbol{z = \alpha_m \frac{w + \delta_m}{1 + w\delta_m^*}}$$

where $\boldsymbol{\alpha_m}$ is radius of circle and $\boldsymbol{\delta_{\mathrm{m}}}$ is a point of shifted center by mapping.

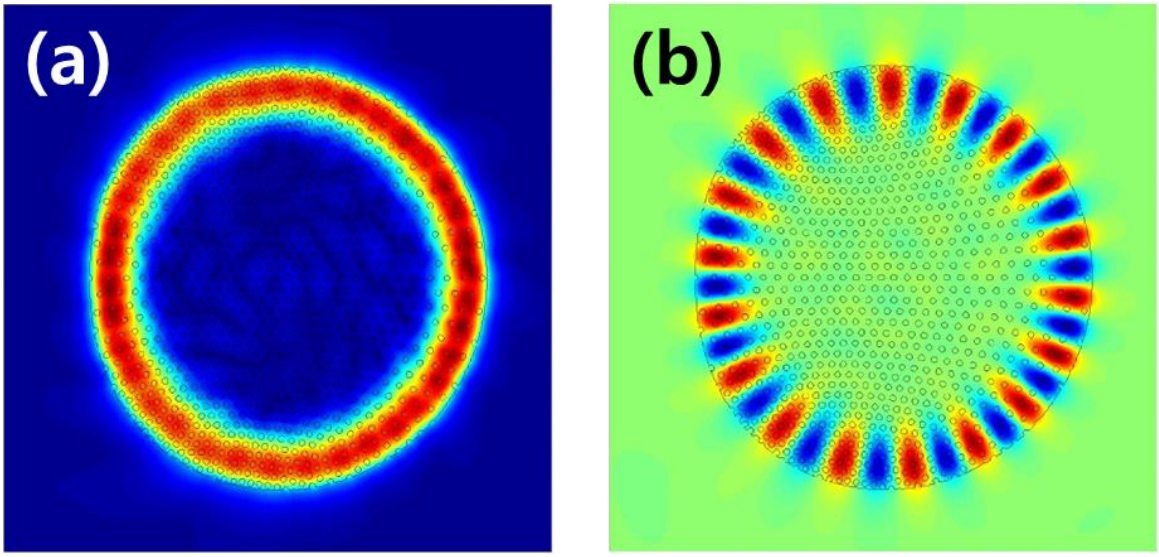

Fig. 1. TM-like mode. Lasing frequency is 1554.8[nm] and the mode number $(\boldsymbol{l}, \boldsymbol{m})$ is $(\mathbf{1}, \mathbf{18})$.

Spatial varying refractive index is implemented with holes and spacing between each holes. The thickness of the cavity is 300[nm]. The pumping wavelength was 980[nm] and the InGaAsP with gain center at 1550[nm] was used as active material. The pumping source was a continuous plane wave and fields and a spectrum were observed inside the cavity. Figure 1 shows lasing mode of limaçon TC.

3. Conclusion

Simulation of transformation laser cavity is calculated though FDTD solver. A 2D passive cavity have been studied extensively. However, it is difficult to predict lasing mode by passive simulation. In active cavity, there are mode coupling and mode competition because each modes shares same gain region. Even if it is designed by passive simulation, the active cavity should be verified by active FDTD simulation. In this study, lasing mode is confirmed in limaçon TC. The cWGM laser has a narrow linewidth and directional emission characteristic that the circular cavity does not have. For these characteristics, the cWGM lasers will be able to apply from basic research to various applications.

4. References

1. Vahala, K. J. *et al.,* Nature, 424(6950), 839–846 (2003).
2. Braginsky, V. B. *et al.,* Physics Letters A, 137(7-8), 393–397 (1989).
3. McCall, S. L. *et al.,* Applied Physics Letters, 60(3), 289–291 (1992).
4. Cao *et al.,* Applied Physics Letters, 76(24), 3519–3521 (2000).
5. Armani *et al.*, Science, 317(5839), 783–787 (2007).
6. Baaske *et al.*, Nature Nanotechnology, 9(11), 933–939 (2014).
7. Ulf Leonhardt *et al*, Transformation Optics and the Geometry of Light (2008).

Chirality in an Asymmetric Microcavity

SEUNG-WOO LEE[1], YANNI CHO[1], SUNJAE KWAK[2], HYUNDONG KIM[2], AND CHIL-MIN KIM[1,2*]

[1]*School of Undergraduate Studies, Daegu Gyeongbuk Institute of Science and Technology (DGIST), Daegu 42988, Republic of Korea*
[2]*Department of Emerging Materials Science, Daegu Gyeongbuk Institute of Science and Technology (DGIST), Daegu 42988, Republic of Korea*
Seung-Woo Lee and Yanni Cho have contributed equally to this work and share first co-authorship
[*]*chmkim@dgist.ac.kr*

Abstract: We study wave and ray-dynamical chirality near an avoided resonance crossing in an asymmetric microcavity composed of one half-ellipse and two quarter-ellipses. Through the study, we find that ray-dynamical chirality depends on cavity asymmetricity.

1. Introduction

In a microcavity, chiral properties of resonance modes have attracted much attention in relation with exceptional points (EPs). The chiral EP mode can be found when a mirror-symmetric microcavity is perturbed to induce non-Hermitian coupling of two modes (an even and an odd mode) [1,2,3]. In our study, asymmetricity is taken as an external perturbation and the chiral properties of ray dynamical emission are obtained. Next, to study the ray-dynamical chirality in relation with an avoided resonance crossing (ARC), we obtain an ARC, where an even and an odd mode interact with each other for strong (or weak) coupling. Around the ARC, we obtain the chirality of resonance modes and ray-dynamical emission. Through the study, we find that ray-dynamical chirality depends on cavity asymmetricity.

2. Ray-Dynamical Chirality in an Asymmetric Microcavity

For the study we contrive an asymmetric shape composed of one half-ellipse and two quarter-ellipses as shown in Fig. 1(a). The shapes of the ellipses are $x^2 + \frac{y^2}{g_1^2} = 1$ for the half-ellipse and $\frac{(x-(1-g_2))^2}{(2-g_2)^2} + \frac{y^2}{g_3^2} = 1$, $\frac{(x-(1-g_2))^2}{g_2^2} + \frac{y^2}{g_3^2} = 1$ for the first and the second quarter ellipse, respectively. In this condition, the boundary is smoothly connected to satisfy $C^{(1)}$ continuity. In this shape satisfying $C^{(1)}$ continuity, whispering gallery type (WGT) modes can be generated so that an even and an odd mode can be coupled for chiral EPs and chiral modes. In this shape, when $g_1 = 0.8$, $g_2 = 0.406$, and $g_3 = 0.974$, the chirality of the ray-dynamical emission reaches 0.6262 with CCW chirality as shown the survival probability distribution and ray-dynamical emission in the microcavity in Fig. 1 (b) and (c), respectively. As another example, when $g_1 = 0.8$, $g_2 = 0.881$, and $g_3 = 0.69$, the chirality of the ray-dynamical emission reaches 0.717 with CW chirality as shown the ray-dynamical emission in Fig. 1 (d). This means that classical dynamics also exhibits chiral emission of rays when our microcavity is asymmetrically deformed.

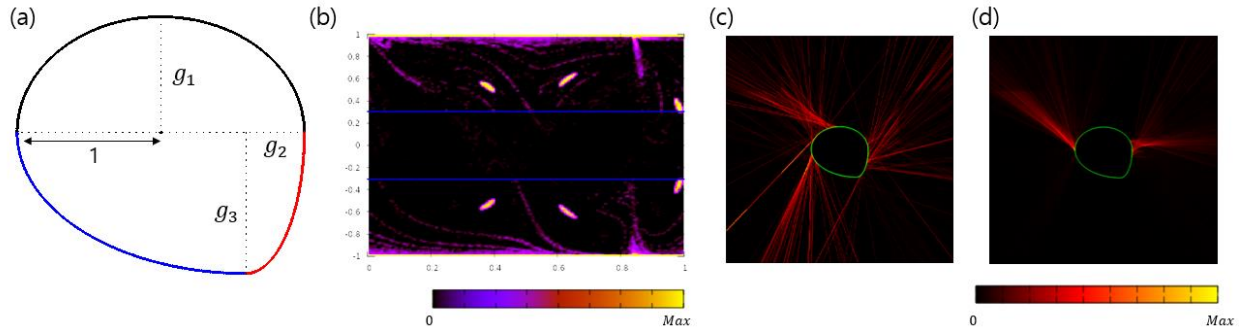

Figure 1. Cavity shape and ray-dynamical properties. (a) is the shape of our asymmetric microcavity. (b) and (c) are the survival probability distribution and emission of rays in the microcavity showing CCW chirality for $g_1 = 0.8$, $g_2 = 0.406$, and $g_3 = 0.974$. respectively. (d) shows CW chirality of ray dynamics at $g_1 = 0.8$, $g_2 = 0.881$, and $g_3 = 0.69$.

3. Chiral Properties around an Avoided Resonance Crossing

In our asymmetric microcavity, we obtain an avoided resonance crossing (ARC), where an even and an odd mode are coupled as shown in Fig. 2. The real eigenvalues are repulsed while the imaginary one's cross as shown in Fig. 2(a) and (b), respectively. For the ARC, an even and an odd mode are coupled as shown the two modes in Fig. 2. In this study we control g_2 for $g_1 = 0.8$ and $g_3 = 0.7375$, through which asymmetricity can be controlled.

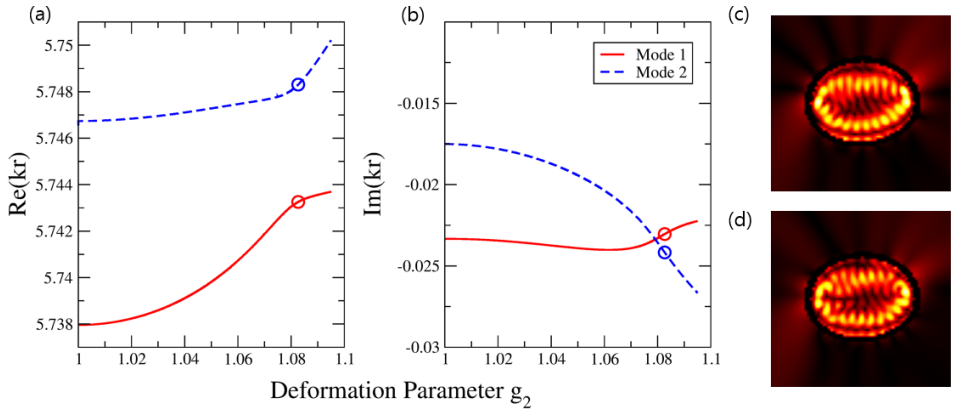

Figure 2. Avoided resonance crossing and the interacting modes. (a) are the real eigenvalues showing repulsion. (b) imaginary eigenvalues showing crossing. Mode 1 and mode 2 are similar to an odd and an even mode, respectively.

Now, we compare the chirality of the two interacting modes and ray-dynamical chirality. The chirality of the resonance modes is maximized around the ARC region; mode 1 and 2 are maximized at $g_2 = 1.08$ and $g_2 = 1.082$, respectively. However, ray-dynamical chirality is maximized around $g_2 = 1.14$. This result implies that wave chirality and ray-dynamical chirality are different, which should be solved next time.

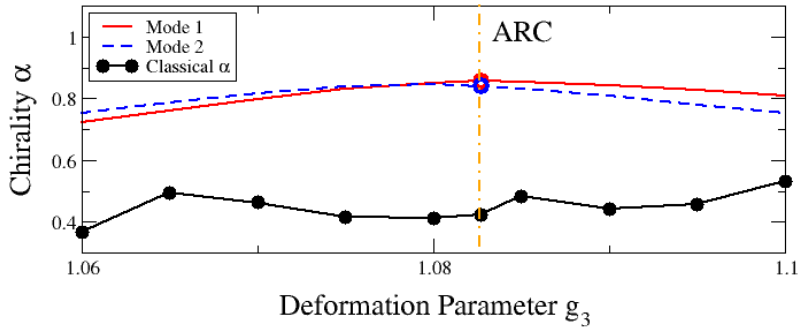

Figure 3. Chirality of resonance modes and ray-dynamical chirality around an ARC depending on g_2. The red solid and the blue dashed curve are the chirality of mode 1 and 2, respectively. The black dots are the ray-dynamical chirality.

4. Summary

In our asymmetric microcavity, we study chirality of waves and ray-dynamics. Although the coupling modes do not satisfy an EP condition, their properties are chiral due to the asymmetricity. Next, we will study the chirality when two modes are coupled at an EP.

References

1. J. Wiersig, Phys. Rev. A. 84, 063828 (2011)
2. B. Penga, et al, PNAS, 113, 6845–6850 (2016).
3. S. Gwak, et al, Opt. Lett. 46, 2980-2983 (2021).

Second-order Nonlinear and Quantum Photonics based on Integrated 3C-SiC-oninsulator Platform

JIAYANG LI[1], ANDREW W. POON[1,*]

[1]*Department of Electronic and Computer Engineering, The Hong Kong University of Science and Technology, Clear Water Bay, Kowloon, Hongkong, China*
[*]*eeawpoon@ust.hk*

Abstract: Silicon carbide is a new nonlinear and quantum optic platform. We develop an integrated 3C-SiC-on-insulator platform through the anodic bonding. We demonstrate the second-harmonic generation and the spontaneous parametric down-conversion in a microring resonator.

1. Introduction

Second-order nonlinear processes are keys to various applications, including frequency conversions, metrology and photon-pairs generation leveraging the spontaneous parametric down conversion (SPDC) process. The SiC polytypes are emerging photonic platforms for their second-order nonlinearities, wide bandgaps and being complementary metal oxide semiconductor (CMOS) compatible. Several groups have demonstrated integrated platforms on both hexagonal 6H/4H- and cubic 3C-SiC polytypes [1-3]. Researchers have demonstrated second-harmonic generation (SHG) with conversion efficiency of 360%/W on the 4H-SiC-on-insulator platform [2].

Among all the polytypes, 3C-SiC is the only form which can be epitaxially grown on silicon (Si) substrate, providing a promising large scalability. In this work, we develop a 3C-SiCoI platform through a modified anodic bonding process. We achieve a loaded Q of 1.1×10^5 at 1550 nm from our microring resonator. We demonstrate the SHG of the 3C-SiC material platform. We also demonstrate the SPDC process and measure the photon-pair generation rate between different signal and idler channels.

2. Device design and fabrication

The 3C-SiC polytype features a $4\bar{3}m$ symmetry which provides a theoretically decent $\chi^{(2)}_{zxy} = 34$ pm/V [4]. With the film been epitaxially grown on [001] direction, such a nonlinear susceptibility will generate new frequency polarizing in z-axis ([001]), which is a transverse magnetic (TM) mode, when pumped at a transverse electric (TE) mode having both x- and y-axis ([100] and [010]) field components through Type-I modal phase matched SHG or sum-frequency generation (SFG) process. When reverse pumping in the shorter wavelength, we can also have the pump photon with higher energy split into a photon pair through SPDC process.

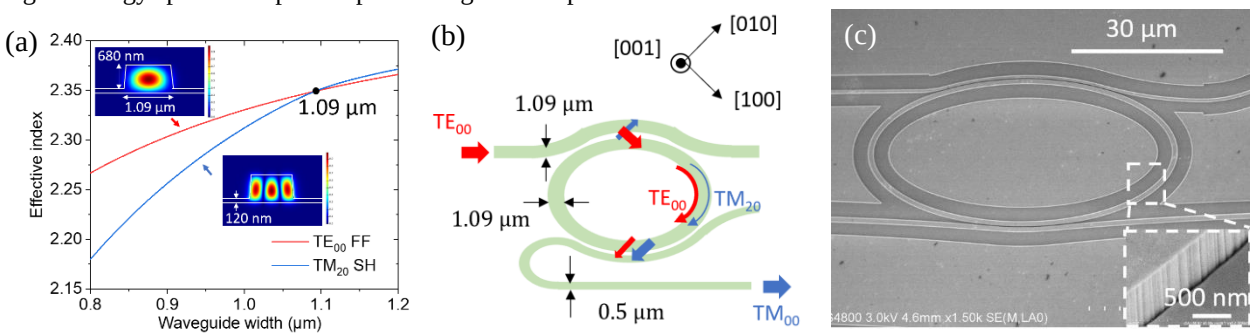

Fig. 1(a) The effective index of TE00,1575nm and TM20,787nm at different waveguide widths. (b) The schemetics of the resonator. (c) The SEM of a fabricated device.

Figure 1(a) shows the numerical simulation of the effective indexes of the $TE_{00,1575nm}$ and $TM_{20,787nm}$ waveguide modes with the width varying while the film and slab thickness fixed at 800 and 120 nm, respectively. We consider an 86° sidewall slope based on our etching recipe. At a waveguide width of 1.09 µm, we find a phase matching point between $TE_{00,1575nm}$ and $TM_{20,787nm}$ modes. We adopt this width for our microring resonator. Specifically, we design our microring in an elliptical shape with long and short axises of 30 and 15 µm, respectively, to suppress the reverse conversion caused by the 4-bar symmetry of the 3C-SiC crystal. We bond the commercial 3C-SiC-on-Si dies on a glass wafer through a modified anodic bonding process. We etch the devices by a SF_6 based etching recipe. Figure

1(b) shows the schemetics of the resonator. Figure 1(c) shows the scanning electron microscope (SEM) of the fabricated device.

3. Experimental results

Figure 2 (a) shows the device passive transmission spectra, revealing resonances around the pumping for TE and the corresponding SH wavelength for TM with loaded Q factors of 2.54×10^4 and 1.67×10^4, respectively. We pump TE polarized light at the 1575.4 nm resonance and demonstrate a double-resonance cavity-enhanced SHG from our device. Figure 2 (b) shows the transmitted pump wavelength and the SHG signal measured at the drop-port. The inset with log-log scale reveals the quadratic power dependence of the SHG on the pumping power, showing a non-depletion conversion. The estimated on-chip nonlinear conversion efficiency is $\eta_{SH} = P_{SH}/P_{FF}^2$ is 51%/W.

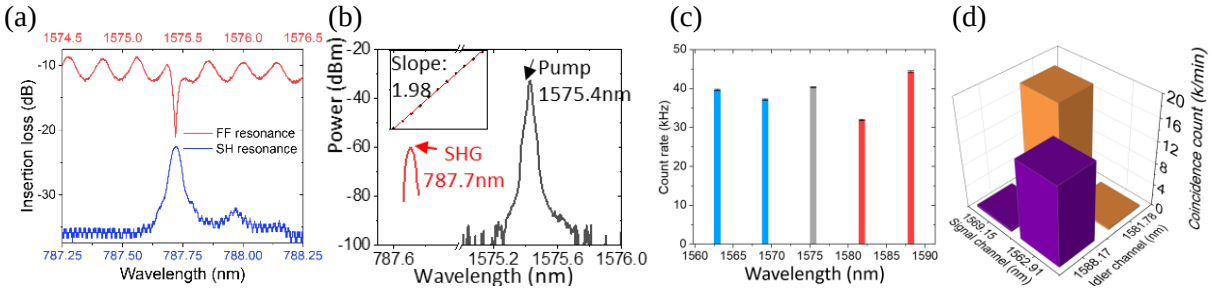

Fig. 2(a) The device passive transmission spectra around 1575 and 787 nm. (b) The spectra of the transmitted pump wave-length and the SHG signal. Inset: the SHG shows a quadratic power dependence on the pumping power. (c) The photon flux counts coming from different resonances with reverse pumping at 787.7nm. (d) The coincidence counts between different signal and idler channels.

We pump the microring resonator at 787.7 nm and demonstrate the first SPDC process of this material platform. Figure (c) shows the photon flux generated from different resonances. We obtain a flux rate of ~40 kHz with an estimated on-chip pumping power of 5.8 mW. We also measure the coincidence counts between different signal and idler channels.

4. Summary

We develop an integrated 3C-SiCoI platform based on a modified anodic bonding process. We demonstrate the first SHG and SPDC processes of the 3C-SiC polytype. We will improve the fabrication process to achieve a higher Q-factor for more efficient nonlinear and quantum conversions. Our work paves a way to future nonlinear and quantum PICs leveraging the 3C-SiC platform.

References

1. Shota Yamada et al. 2014. “Second-Harmonic Generation in a Silicon-Carbide-Based Photonic Crystal Nanocavity.” Optics Letters 39 (7): 1768.
2. Daniil M. Lukin et al. 2020. “4H-Silicon-Carbide-on-Insulator for Integrated Quantum and Nonlinear Photonics.” Nature Photonics 14 (5): 330–34.
3. Tianren Fan et al. 2020. “High-Quality Integrated Microdisk Resonators in the Visible-to-near-Infrared Wave-length Range on a 3C-Silicon Carbide-on-Insulator Plat-form.” Optics Letters 45 (1): 153.
4. I. J. Wu and G. Y. Guo. 2008. “Second-Harmonic Generation and Linear Electro-Optical Coefficients of SiC Polytypes and Nanotubes.” Physical Review B - Condensed Matter and Materials Physics 78 (3): 1–10.

Systematic z-scan measurements of the third order nonlinearity of chalcogenide glasses

Qiuli Li,[1] Rongping Wang,[1,*]

[1] *Laboratory of Infrared Materials and Devices, The Research Institute of Advanced Technologies, Ningbo University, Ningbo 315211, China*

liqiuli@163.com

Abstract: We report measurements of linear and nonlinear coefficient of three groups of chalcogenide glasses with compositions utilizing the Z-scan at the wavelength of 2μm、2.5μm and 3μm.

1. Introduction

The advent of integrated all-optic communication networks progressively requires faster functional devices [1] And, such requirements have evoked increasing interest on all-optical devices including optical switches, regenerators, cross-connects, amplification and pulse compression [2-5]. For such devices, chalcogenide glasses are of particular interest among the developing materials due to their large optical nonlinearity, n_2 (≈100-1000×silica) with ultrafast response time (<200 fs). Moreover, chalcogenide glasses have several advantages over inorganic crystals and organic materials: composition can be tunable easily, easy fabrication of optical waveguides including fibers and excellent optical homogeneity. As_2S_3, for example, have been successfully demonstrated from chalcogenide fiber by Asobe *et al* in 1992 [6]. However, the limited material nonlinearity may be insufficient for applications to small-scale photonic devices. Thus, glasses have higher nonlinearity particularly in the case of all-optical integrated photonic circuits.

2. Experiments and results

2.1 . Experiments

All optical and spectroscopic measurement were obtained at room temperament. Transmittance and absorption spectra of all samples were recorded using Lambda 950 (UV-VIS-NIR, PerkinElmer) in a range from 0.5 to 2.5μm. Fourier transform infrared (FT-IR) spectra of the ChGs were measured by a Nicolet 380 FTIR spectrometer. We explored the measurement of nonlinearities via the Z-scan technique. The nonlinear refractive index n_2 was evaluated from the nonlinear phase from “closed aperture” data and the nonlinear absorption coefficient β from “open aperture”. Excitation was provided by an optical parametric amplifier system (Coherent, Mira 900, Legend Elite and OperA Solo) femtosecond laser delivering linearity polarized 100 fs single pulses at 2μm、2.5μm and 3μm with 1kHz repetition rate. The incident energy of single laser pulse was kept at 128+10 nJ and the testing wavelength was determined by a difference frequency generator (DFG). The laser power was recorded by a highly sensitive pyroelectric power probe (Laser Probe, RkP-575). To minimize experimental error and ensure the accuracy of our Z-scan, the measurements were repeated ten times at different places on the glasses surface. Both nonlinear refractive (n_2) and nonlinear absorption coefficient of the samples were extracted from the best fitting using the well-established fitting procedure.

2.2 . Results

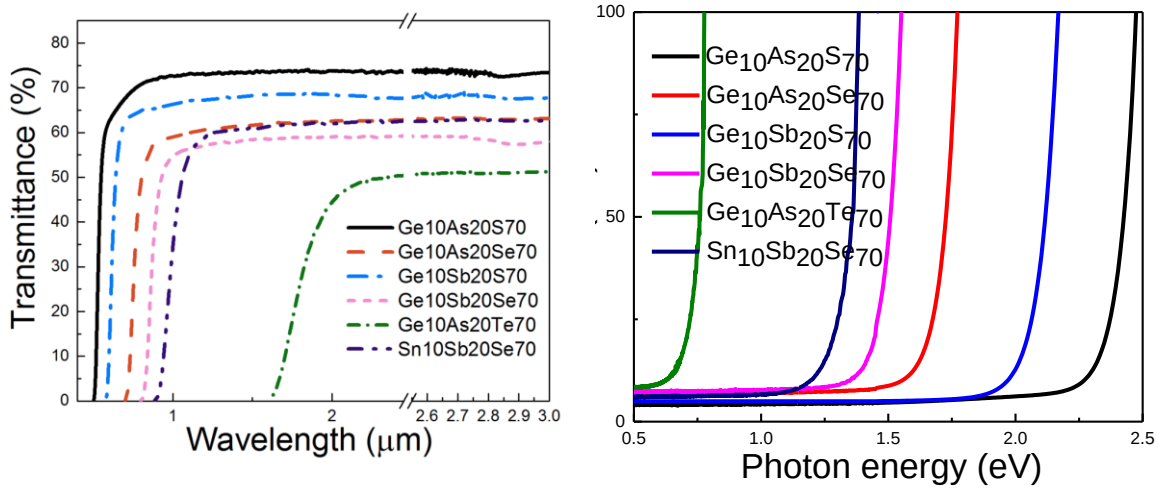

Fig1. Transmittance and absorption spectra versus of series II glasses

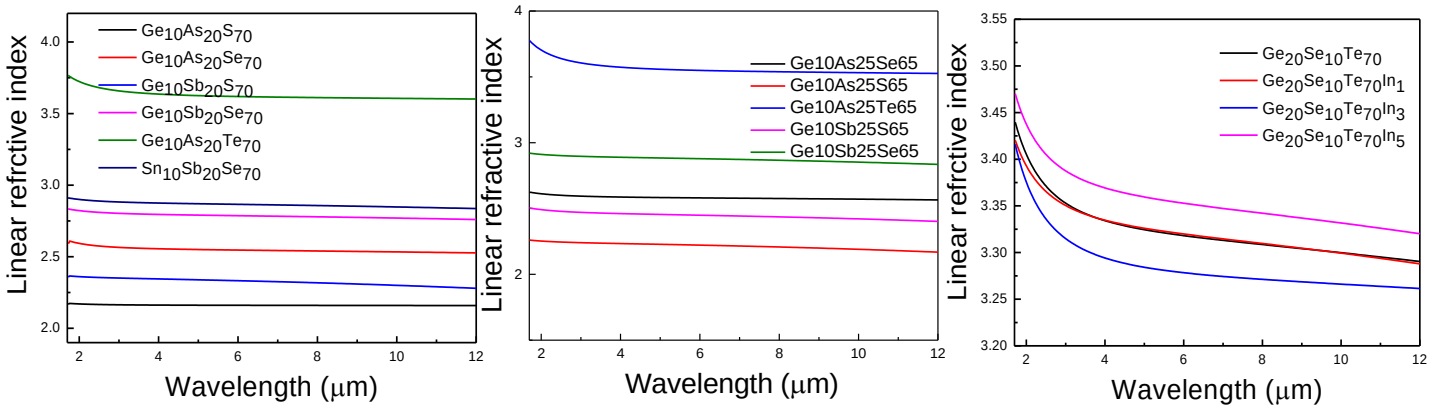

Fig2. The linear refractive index (n) spectra versus of series I and series II and series III glasses

3. Summary

We give the values of the linear indices as well as the nonlinear refraction coefficient (n_2) of these materials. An estimation of the energy gap (E_g) is also made at the absorption coefficient equals to 100 cm^{-1}. For each group of glasses, it is found that with the replacement of more polarizable elements (Se for S, Sb for As, Te for Se), the optical band gap is reduced and the nonlinear refraction is increased, which is related to the red shift of the absorption band gap. Furthermore, the addition of tellurium not only enhance significantly the nonlinear refraction coefficient but also exalts more the nonlinear absorption. The relationship between two-photon absorption and nonlinear refractive index is considered using two formalisms developed for crystalline semiconductors by Sheik-Bahae and Dinu respectively. The two models show that both n_2 and β are strongly dependent upon E_g as $n_2 \propto 1/E_g^4$ and $\beta \propto 1/E_g^3$. and these features of the dispersion curves and scaling rules of third-order nonlinearities predict wavelength dependence and may be an effective guidance for the design of linear and nonlinear optical devices in in chalcogenide materials.

References

1.T. Kamiya and M. Tsuchiya, Jpn. J. Appl. Phys. 44 (2005) 5875

2. R.W. Boyd, Nonlinear Optics 2nd Ed. (Academic Press, San Diego, 2003).

Efficiency-stable and ultra-narrow bandwidth-tunable add-drop filter based on quasicritical coupling between tapered fiber and microsphere

XIAOTING LI[1,2,*], PENGFA CHANG[1] , AND FENG GAO[2,3]

[1] *MOE Key Laboratory of Weak-Light Nonlinear Photonics, TEDA Institute of Applied Physics and School of Physics, Nankai University, Tianjin 300457, China*
[2] *Department of Electrical Engineering, City University of Hong Kong, Kowloon, Hong Kong, China*
[3] fenggao@nankai.edu.cn
[*] 2120160177@mail.nankai.edu.cn

Abstract: An efficiency-stable and bandwidth-tunable add-drop filter was demonstrated under the quasicritical coupling condition. The total tuning bandwidth was from 0.4 MHz to 327.1 MHz, during which the fluctuation of the efficiency was less than 10%.

1. Introduction

Whispering-gallery-mode (WGM)-based bandwidth tunable add-drop filters (ADFs) have been considered as a very promising candidate for applications in wavelength-division-multiplexing communications [1, 2], ultra-narrow-linewidth lasers [3, 4], nonlinear optics [5] and so on, because of their superb merits. In recent years, a great number of on-chip ADFs using microdisks [6] and microtoroids [7] with MEMS-actuated waveguides were proposed. Although these structures have realised bandwidth tunability, ADFs that simultaneously exhibit stable efficiency, narrow band, and bandwidth fine tunability have not yet been proposed. Here we demonstrated an efficiency-stable and ultra-narrow bandwidth-tunable ADF structure by using the few-mode tapered fiber coupling to WGMs, which introduced an additional loss channel to balance the variation of WGM intrinsic loss. It was observed that the bandwidth variation was monotonous to the gap change, and the coupling efficiency tended to be stable when the gap decreased close to zero.

2. Some details

2.1 Theory and simulation

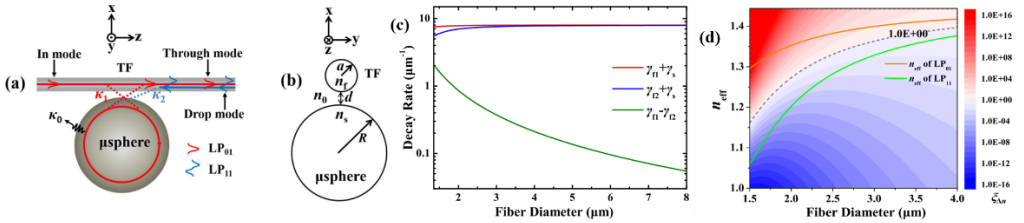

Fig.1. (a) Add/drop filter (ADF) structures based on coupling a microsphere resonator to a few-mode tapered fiber. κ_1 : cavity intensity decay rate due to coupling to LP_{01} fiber mode. κ_2 : cavity intensity decay rate due to coupling to LP_{11} fiber mode. κ_0 : cavity intensity decay rate due to intrinsic internal cavity losses. (b) Cross-sectional view of the configuration of a tapered fiber coupled to a microsphere. TF: tapered fiber. (c) Decay rates of evanescent waves of LP_{01} and LP_{11} fiber modes with different fiber diameters at λ =1550 nm. The red curve denotes the sum of evanescent wave decay rates of the microsphere WGM and LP_{01} fiber mode, while the blue curve denotes the sum of the WGM and LP_{11} fiber mode. The green curve denotes the difference. (d) The calculated ratio $\xi_{\Delta n}$, which is related to the phase matching condition of the WGM coupling. The color contour denotes the value of $\xi_{\Delta n}$. The orange curve and green curve denote ERIs of LP_{01} and the LP_{11} fiber modes, respectively. The dashed curve denotes the relationship between the ERI of the WGM and the diameter of fiber, to meet the condition of $\xi_{\Delta n}$ =1 .

We numerically calculated the feasibility of our ADFs in realizing the efficiency-stable tunability under quasicritical coupling [8] (Fig. 1 a,b). Through the derivation based on weakly guiding waveguide theory [9], the parameter $\xi=\kappa_1/\kappa_2$ which determines the transmission of the add/drop system can be written as.

$$\xi = \frac{\kappa_1(0)}{\kappa_2(0)} e^{-(\gamma_{f1}-\gamma_{f2})d} e^{-Rk_0^2[(n_{f1,\,\mathrm{eff}}-n_{s,\,\mathrm{eff}})^2/\gamma_{f1}-(n_{f2,\,\mathrm{eff}}-n_{s,\,\mathrm{eff}})^2/\gamma_{f2}]} = \frac{\kappa_1(0)}{\kappa_2(0)} e^{-(\gamma_{f1}-\gamma_{f2})d} \xi_{\Delta n} \quad (1)$$

where $\xi_{\Delta n} = e^{-Rk_0^2[(n_{f1,\,\mathrm{eff}}-n_{s,\,\mathrm{eff}})^2/\gamma_{f1}-(n_{f2,\,\mathrm{eff}}-n_{s,\,\mathrm{eff}})^2/\gamma_{f2}]}$ is related to the phase mismatching. Obviously, the coupling state between the TF modes and WGM strongly depends on the gap *d* between the fiber and microsphere and the ERIs of

them, whose calculation results is shown in Fig.1 (c) and (d). As shown in Fig.1c, suppose the diameter of the fiber is 2.5 μm, when the gap d increases from 0 to one wavelength (say 1.55 μm), $e^{-(\gamma_{f1}-\gamma_{f2})d}$ in Eq. (1) just decreases from 1 to 0.434. By contrast, in traditional add/drop systems, the corresponding $e^{-(\gamma_{f1}+\gamma_s)d}$ decreases from 1 to $e^{-12.29}$ (i.e. 4.6×10^{-6}), which means that we have successfully reduced the fluctuation by more than 10 orders of magnitudes. Meanwhile, dashed curve in Fig. 1(d) denotes the theoretical guidance on the relationship between the ERI of the WGM and the diameter of fiber to meet the quasicritial coupling condition.

2.2 Experiment and discussion

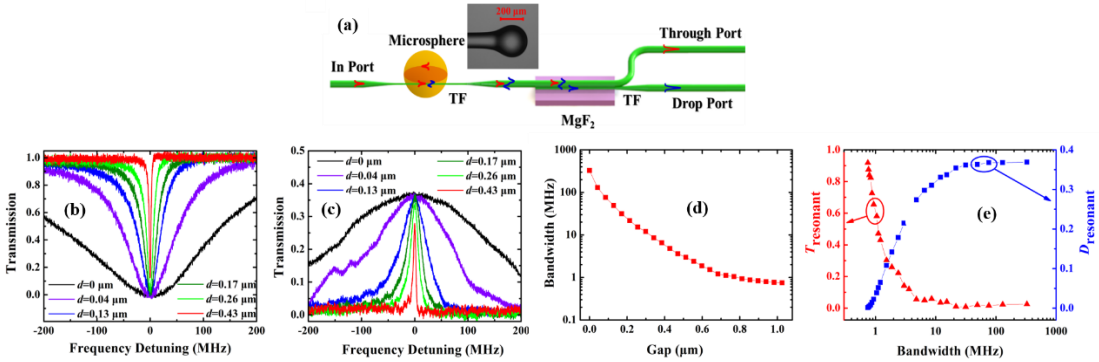

Fig. 2 (a) The experimental set-up for our ADFs. (b)Transmission spectra of the Through port and (c) transmission spectra of the Drop port when tuning the gap between the TF and microsphere. (d) The relationship between the ADF bandwidth and the gap. (e) The relationships between the ADF resonant transmissions and the bandwidth.

Based on the above theoretical analysis, we proposed an experimental configuration (Fig. 2a). The same setup in our previous work was used [8]. In the experiment, when decreasing the gap between TF and WGM through 3D nano-positioning stage, the bandwidth of the resonance peaks generally increased. When the gap between the microsphere and TF was tuned decreasing from about 1 μm to 0 μm, the typical transmission spectra at Through and Drop Port were measured (Fig. 2b,c). Meanwhile, the resonant coupling efficiencies of both the Through and Drop ports tended to be stable when the TF approached the microsphere, and the resonant-transmission-gap tuning relationship is shown in Fig. 2e. The Though and Drop ports achieved efficiency-stable-tuning bandwidths from 4.8 MHz to 327.1 MHz and from 15.3 MHz to 327.1 MHz, respectively.

3. Summary

In conclusion, the efficiency-stable and ultra-narrow bandwidth tunability in a microcavity-based add-drop filter can be achieved by maintaining the ratio of the two coupling decay rates constant in a single coupling fiber. In this proof-of-principle experiment, we realized the bandwidth tuning through controlling the gap between the WGM microsphere and few-mode TF under the quasicritical coupling condition. Our scheme could benefit its applications in ultra-narrow-linewidth lasers, microwave photonics and nonlinear optics.

References

1. L.-W. Luo, N. Ophir, C. P. Chen, L. H. Gabrielli, C. B. Poitras, K. Bergmen, and M. Lipson, "WDM-compatible mode-division multiplexing on a silicon chip," Nature Communications 5(2014).
2. Y.-D. Yang, Y. Li, Y.-Z. Huang, and A. W. Poon, "Silicon nitride three-mode division multiplexing and wavelength-division multiplexing using asymmetrical directional couplers and microring resonators," Optics Express 22, 22172-22183 (2014).
3. M. Cai, O. Painter, K. J. Vahala, and P. C. Sercel, "Fiber-coupled microsphere laser," Opt. Lett. 25, 1430-1432 (2000).
4. S. M. Spillane, T. J. Kippenberg, and K. J. Vahala, "Ultralow-threshold Raman laser using a spherical dielectric microcavity," Nature 415, 621-623 (2002).
5. A. Rasoloniaina, V. Huet, M. Thual, S. Balac, P. Féron, and Y. Dumeige*, "Analysis of third-order nonlinearity effects in very high-Q WGM resonator cavity ringdown spectroscopy," J. Opt. Soc. Am. B 32, 370-378 (2015).
6. M. Lee and M. Wu, "Variable bandwidth of dynamic add–drop filters based on coupling-controlled microdisk resonators," Opt. Lett. 31, 2444-2446 (2006).
7. J. Yao* and M. Wu, "Bandwidth-tunable add–drop filters based on micro-electro-mechanical-system actuated silicon microtoroidal resonators,"Opt. Lett. 34, 2557-2559 (2009)
8. X. Li, P. Chang, L. Huang, F. Gao, W. Zhang, F. Bo, G. Zhang and J. Xu, "Quasicritical coupling in a few-mode tapered-fiber coupled whispering-gallery-mode system," Phys. Rev. A 98, 053814-1-053814-5 (2018).
9. A. Snyder, and J. Love, Optical waveguide theory (Springer Science & Business Media, (2012).

High-harmonics generation in highly-doped silica micro-ring resonator

YUHUA LI [1], SHAO HAO WANG[2], ROY DAVIDSON[3], SHIQI AI[1], BRENT E. LITTLE[4], SAI T. CHU[1]

[1]*Department of Physics, City University of Hong Kong, Kowloon Tong, Hong Kong, China*
[2]*Department of Microelectronics Science and Technology, Fuzhou University, Qi Shan Campus, Fuzhou, 350108, China*
[3]*QXP Technology Inc., Xi'an, China*
[4]*State Key Laboratory of Transient Optics and Photonics, XIOPM, CAS, Xi'an, China*
[1]*saitchu@cityu.edu.hk*

Abstract: We demonstrate experimentally both second and third harmonic generation in a highly-doped silica micro-ring resonator. We report the observation of bright red and green emissions from the resonator under a continuous-wave pump in the C-band.

1. Introduction

Low-loss and high quality (Q) factor optical microcavities are effective structures for various nonlinear frequency conversion processes. Their ability to confine and recycle light in a small volume allows the enhancement of light-matter interaction. In general, the enhancement factor is proportional to the finesse of the cavity and it can reach a few orders of magnitude for ultra-high Q structures. Since the report of third-harmonic generation (THG) of visible emission in micro-droplets [1], there have been a number of demonstrations of THG in various micro-cavity structures [2, 3]. While most of the reported emission from the glass based microcavities are due to the THG process, Zheng *et. al*, have recently reported the observation of second-harmonic generation (SHG) on the silica microsphere that is due to the symmetry-breaking-induced nonlinear optics effect [4].

In this work, we design and fabricate a high-Q optical microring resonator based on the CMOS compatible highly-doped silica glass platform [5] and report on the observation of both SHG and THG from the resonator under a continuous-wave pump in the C-band.

2. Device structure and Experimental Results

The waveguide core of the fabricated micro-ring resonator (MRR) is a low-loss, high-index (n=1.70) doped silica glass, buried within a SiO_2 cladding. The fabricated waveguide has cross-sectional dimension of 1.9 μm by 1 μm, shown in Fig. 1a), with gap separation between the ring and the bus at 1.2 μm. At ring radius of 135 μm, it corresponds to a free-spectral range (FSR) of 201 GHz. The measured on/off chip loss from the through port response of the fiber pigtailed fabricated device in Fig. 1b) is below 1.5 dB across the C-band. The measured filter bandwidth from the drop response is 1.1 pm, corresponds to a loaded Q of 1.4×10^6 at around 1550 nm. Using the measured waveguide dimension from Fig. 1a), we calculated the dispersion of the fundamental TE and TM modes, shown in Fig. 1c), where it is found that both modes are in the normal dispersion regime in the C-band. Furthermore, the extracted coupling coefficient from the measured responses is around 2% in the C-band. For the SHG and THG wavelengths that are two and three times shorter than the pump wavelength, there is virtually no coupling between the ring and the bus at the THG wavelength but just a slight amount of coupling at the SHG wavelength. Thus the experimental setup, shown in Figure 1d), consists of a collimator positioned directly on top of the ring to collect the emitted light from the surface of the resonator. The collected emission is transferred to the spectrometer (OceanOptics USB2000+) by an optical cable for their spectral analysis. We placed the device on a thermoelectric cooler (TEC) to allow the adjustment of the resonance location by changing of the chip temperature.

We first investigated the dynamic phase-matching condition of the THG process in the MRR by sweeping the pump wavelength across a resonance at different chip temperature settings. This allows us to determine the Q-factor of the resonator at the THG wavelength from the walk-off between the pump and THG resonances. By fine tuning the chip temperature by TEC, the THG power dependence of the intracavity pump power was monitored. The measured Q-factor of the resonator at the THG wavelength is 1.1×10^5, which is one order of magnitude smaller than that of the pump resonance. The lower Q value is due to the higher propagation and scattering losses at the THG wavelength. The measured maximum conversion efficiency approaches 1.6×10^{-6}, which is comparable with the net THG conversion efficiency in the silicon nitride MRR [6].

We were also able to observe SHG in the same MRR that is due to the breaking of the inversion symmetry at the ring surface instead of from $\chi^{(3)}$ of the waveguide as in the THG. Figs. 2(a-c) show the measured THG and SHG spectra when uses ~1549 nm pump. Note that the optimal SHG and THG occur at the specific chip temperature where the input laser simultaneously aligns to the pump resonance as well as the SHG/THG resonances. By carefully

choosing the pump wavelength and chip temperature, we can generate a mixture of both THG and SHG emissions at the same time, as shown in Fig. 2c). When fine tuning the pump wavelength and TEC, we can further adjust the ratio of green (THG) emission to red (SHG) emission, which promises arbitrary color generation in chromaticity diagram between the two original colors.

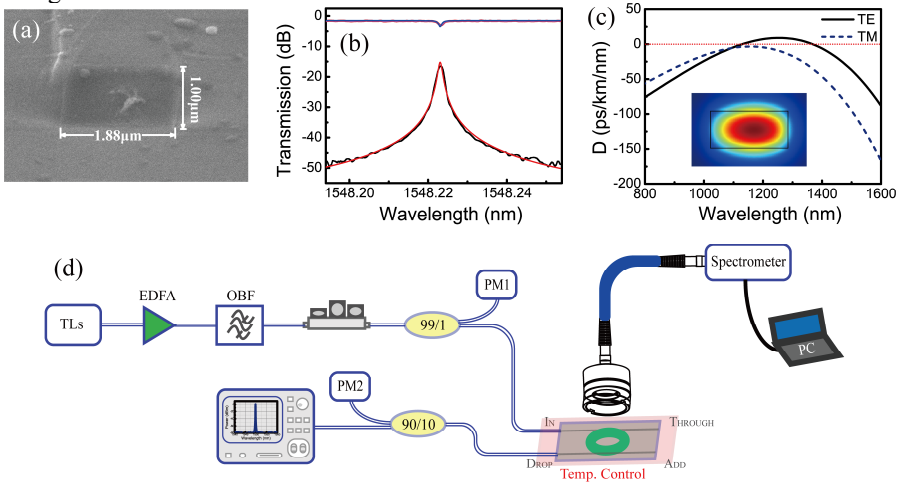

Fig. 1. (a) SEM image of cross-section of core waveguide. (b) Filter response (Black-dotted: TM drop; Magenta-dotted: TM through; Red-solid: drop fitting; Blue-solid: through fitting) characteristic of MRR. (c) Calculated dispersion of the fundamental TE and TM mode. Inset: Fundamental TM mode profile. (d) Schematic experimental setup for the harmonic generation. A collimator is positioned on top of MRR to collect scattered light. (TLs: tunable laser source; EDFA: erbium doped fiber amplifier; OBF: optical bandpass filter; PM: power meter.)

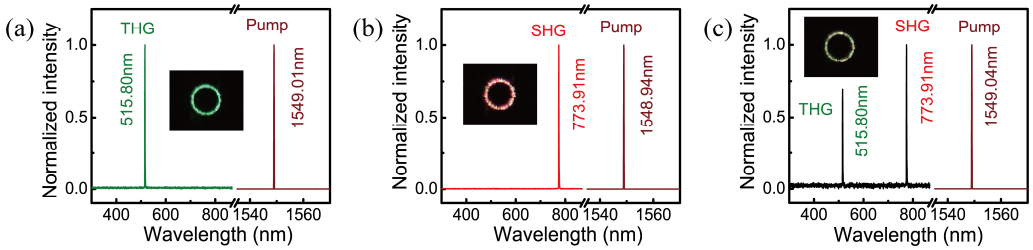

Fig. 2. (a) Measured THG signal at chip temperature of 19 °C. (b) Measured SHG signal at chip temperature of 29 °C. (c) Measured THG and SHG signals at chip temperature of 25 °C. By tuning the ratio of THG to SHG emissions, green, red and yellow light emissions can be achieved on a piece of MRR chip.

3. Summary

In conclusion, we have observed and investigated the second- and third-harmonic generation of visible emission in on-chip highly-doped silica glass MRR pumped in the C-band. The measured THG maximum conversion efficiency is 1.6×10^{-6} for MRR with loaded Q-factor of 1.4×10^{6}. The extracted intrinsic Q-factor at the THG wavelength of ~517nm is around 1.1×10^{5}. Future works include the optimization of the waveguide geometry for the generation of NIR and visible frequency comb.

References

1. W. P. Acker, D. H. Leach, and R. K. Chang, "Third-order optical sum-frequency generation in micrometer-sized liquid droplets," Opt. Lett. 14, 402-404 (1989).
2. T. Carmon and K. J. Vahala, "Visible continuous emission from a silica microphotonic device by third-harmonic generation," Nat. Phys. 3, 430 (2007).
3. H. Jung, R. Stoll, X. Guo, D. Fischer, and H. X. Tang, "Green, red, and IR frequency comb line generation from single IR pump in AlN microring resonator," Optica 1, 396-399 (2014).
4. X. Zhang, Q.-T. Cao, Z. Wang, Y.-x. Liu, C.-W. Qiu, L. Yang, Q. Gong, and Y.-F. Xiao, "Symmetry-breaking-induced nonlinear optics at a microcavity surface," Nat. Photonics 13, 21-24 (2019).
5. B. Little, "A VLSI photonics platform," in Optical Fiber Communication Conference, (Optical Society of America, 2003), ThD1.
6. L. Wang, L. Chang, N. Volet, M. H. Pfeiffer, M. Zervas, H. Guo, T. J. Kippenberg, and J. E. Bowers, "Frequency comb generation in the green using silicon nitride microresonators," Laser Photonics Rev. 10, 631-638 (2016).

This work was supported by the National Natural Science Foundation of China (Grant No. 61675231).

1.6 μm continuous-wave lasing from InAs/AlGaInAs quantum dash microdisk lasers grown on (001) silicon

LIYING LIN[1], WEI LUO[1], SI ZHU[1], AND KEI MAY LAU[1]*

[1]*Department of Electronic and Computer Engineering, The Hong Kong University of Science and Technology, Clear Water Bay, Kowloon, Hong Kong, China*
*eekmlau@ust.hk

***Abstract*-We present preliminary results of InAs/InAlGaAs 1.6μm quantum dash (QDash) microdisk lasers directly grown on (001) silicon. Continuous-wave (CW) single-mode lasing at 1.6 um under 1064 nm optical pumping is demonstrated with an average threshold of 0.96 mW.**

1. Introduction

To realize optoelectronic integrated circuits on the Si platform, efficient light sources with small footprint are in demand. The challenge to achieve III-V lasers directly grown on silicon originates from the high density of defects at the III-V/Si hetero-interface. Featured with less sensitivity to crystalline defects, stronger carrier localization and confinement compared to quantum wells [1], quantum-dots and QDashes have been regarded as promising gain materials for III-V lasers directly grown on Si [2]. Microdisk laser with whispering-gallery-modes (WGMs) shows its potential application in photonic integrated circuits (PICs) due to the small cavity volume and high efficiency [3]. Here we demonstrate QDash microdisk lasers directly grown on (001) Si operating at room temperature, with an average threshold of 0.96mW under 1064 nm continuous-wave (CW) optical pumping.

2. Experiments and results

A schematic of the laser structure is shown in Figure 1(a). The InP-on-Si (IoS) template was grown on nominal on-axis (001) silicon by Metal-Organic Chemical Vapor Deposition (MOCVD). The 1μm thick GaAs on planar Si serves as an intermediate buffer to mitigate the mismatch between Si and InP grown atop. The active region consists of three-layers InAs QDash grown in InGaAs well (DWELL) separated by InAlGaAs cap layers, sandwiched by symmetric InAlAs cladding layers to enhance optical confinement. The Photoluminescence (PL) of the as-grown sample is presented in Figure 1(b). It's noted that the PL was measured using a 514 nm excitation source. Colloidal lithography was adopted to ensure perfect circularity of the microdisk [1]. 4-μm diameter silica beads diluted in isopropyl alcohol (IPA) were spread on the as-grown sample with 200nm SiO_2 deposited on top by Plasma Enhanced Chemical Vapor Deposition (PECVD). The contour was then transferred to the SiO_2 hard mask by Fluorine-based dry etch. After removal of the beads by ultra-sonic bath, inductively coupled plasma (ICP) etching was performed to form the disk mesa, followed by InP pedestal formation using diluted hydrochloric acid. The suspended cavity efficiently prevents leakage of the optical mode into the substrate. Figure 1(c) displays a 70° tilted SEM image of the as-fabricated microdisk laser, revealing a perfect circularity which promises high-quality WGMs at the periphery.

The fabricated microdisk lasers were tested using a micro-photoluminescence (μ-PL) setup. A continuous-wave laser operating at 1064nm was used to pump the micro-disk laser optically. The optical pump power effectively absorbed by the microdisk laser was estimated to be 62% after taking into consideration multiple reflections and absorptions: $(1-R)(1-e^{-\alpha d})/(1-\mathrm{R}\times e^{-\alpha d})$ [4]. Figure 2(a) shows the representative lasing spectra of one microdisk laser with 4 μm in diameter. At a low pump level, the emission shows a strong transverse electric (TE)-polarized WGM at a wavelength of 1627nm, accompanied by other weak cavity modes. The mode at 1627 nm dominated and eventually lased under gradually increased pump power. Figure 2(b) displays a linear plot of output intensity versus input power (L-L curve) of the lasing mode. The kink of the L-L curve indicates the onset of lasing and the threshold can be estimated at around 0.8mW by linear fitting of a L-L curve in high excitation regime. The inset figure shows the L-L curve in log-log scale. A clear S-shape reveals the evolution from spontaneous emission to amplified spontaneous emission till lasing. Figure 2(c) presents the mode modulation under low pump power ($0.5 \times P_{th}$) and single-mode lasing at high excitation power ($2.5 \times P_{th}$). An extinction ratio of around 23 dB can be extracted from the single-mode lasing spectrum. The full width at half maximum (FWHM) of the lasing mode is extracted to be 0.45 nm by bi-Lorentz fitting [Figure 2(d)]. Quality factor can then be derived to be 3.6×10^3. Figure 2(e) indicates the emission peak shift with the increase of pump power, clear red-shift induced by thermal effect can be observed when pump power was increased beyond the threshold.

3. Summary

In summary, we have demonstrated continuous-wave lasing of optically-pumped microdisk lasers directly grown on CMOS-standard (001) Si emitting at 1.6 μm at room temperature. The average threshold of 20 microdisk lasers is around 0.96 mW. The low power consumption and small footprint of microdisk lasers pave the way towards dense and low-cost integration of light sources in silicon photonics.

Acknowledgements-The work was supported by the Research Grants Council of Hong Kong (16245216) and Innovation Technology Fund of Hong Kong (ITS/273/16FP).

References

[1]. Zhu, Si, Bei Shi, Yating Wan, Evelyn L. Hu, and Kei May Lau. "1.55 μm band low-threshold, continuous-wave lasing from InAs/InAlGaAs quantum dot microdisks." Optics letters 42, no. 4 (2017): 679-682.

[2]. Norman, Justin C., Daehwan Jung, Yating Wan, and John E. Bowers. "Perspective: The future of quantum dot photonic integrated circuits." *APL Photonics* 3, no. 3 (2018): 030901.

[3]. Ye, Yu, Zi Jing Wong, Xiufang Lu, Xingjie Ni, Hanyu Zhu, Xianhui Chen, Yuan Wang, and Xiang Zhang. "Monolayer excitonic laser." Nature Photonics 9, no. 11 (2015): 733.

[4]. Ide, Toshihide, Toshihiko Baba, Jun Tatebayashi, Satoshi Iwamoto, Toshihiro Nakaoka, and Yasuhiko Arakawa. "Room temperature continuous wave lasing in InAs quantum-dot microdisks with air cladding." Optics express 13, no. 5 (2005): 1615-1620.

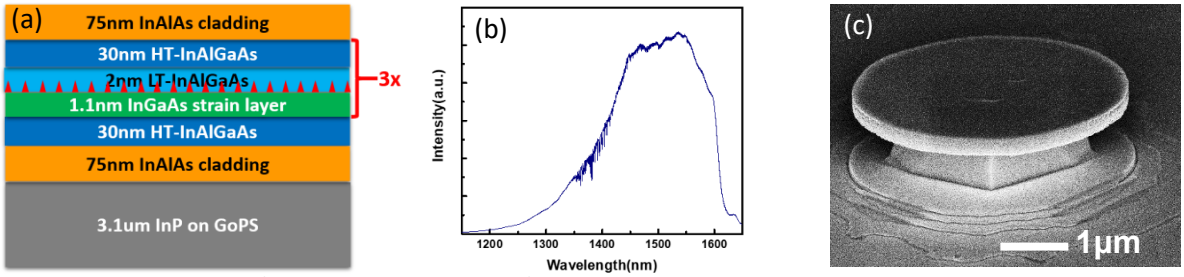

Figure 1 (a) Schematic illustration of the epitaxy structure, (b) PL of the as-grown sample optically pumped by a CW 514 nm Ar ion laser operating at room temperature, (c) 70° tilted SEM image of the 4μm diameter microdisk laser.

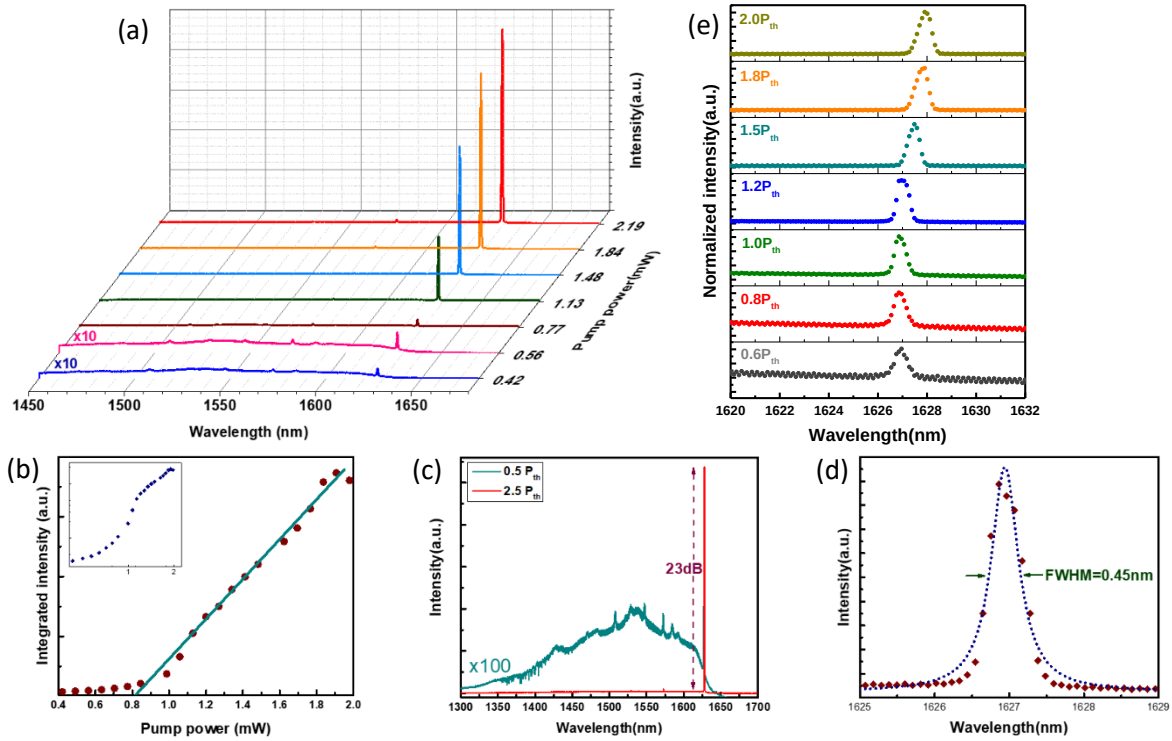

Figure 2. Characterizations of a 4μm diameter microdisk laser lasing at room temperature. (a) Power-dependent micro-PL spectra. Spectra at low pump power (0.42mW and 0.55mW) are magnified 10 times to show the spontaneous emission from the QDs clearly. (b) L–L curve in linear scale. The dark green line represents a linear fit to the experimental data. The threshold is extrapolated to be 0.8mW according to the fitting result. Inset: L–L curve in log-log scale. (c) Overlay of spectra measured below and above threshold. (d) High-resolution lasing spectrum pumped under 0.85mW (around threshold), indicating FWHM of the dominant mode 0.45 nm. The dark red diamonds represent the measured data, which are fitted to a Lorentzian line shape, as shown by the green dashed line. (e) Zoomed-in emission spectra taken at various pump powers, indicating a red-shift in wavelength as the pump power increases higher than the threshold.

Effective four-wave mixing in the lithium niobate on insulator microdisk by cascading quadratic processes

SHIJIE LIU[1,2], ZHIWEI FANG[3,4], YA CHENG[3,4,5], YUANLIN ZHENG[1,2,6], AND XIANFENG CHEN[1,2,7]

[1]*State Key Laboratory of Advanced Optical Communication Systems and Networks, School of Physics and Astronomy, Shanghai Jiao Tong University, Shanghai 200240, China*
[2]*Key Laboratory for Laser plasma (Ministry of Education), Collaborative Innovation Center of IFSA, Shanghai Jiao Tong University, Shanghai 200240, China*
[3]*State Key Laboratory of Precision Spectroscopy, East China Normal University, Shanghai 200062, China*
[4]*XXL-The Extreme Optoelectromechanics Laboratory, School of Physics and Materials Science, East China Normal University, Shanghai 200241, China*
[5]*State Key Laboratory of High Field Laser Physics, Shanghai Institute of Optics and Fine Mechanics, Chinese Academy of Sciences, Shanghai 201800, China*
[6]*Corresponding author: ylzheng@sjtu.edu.cn*
[7]*Corresponding author: xfchen@sjtu.edu.cn*

Abstract: We demonstrate effective FWM in a LNOI microdisk via cascaded quadratic nonlinear processes of SHG and DFG. The effective FWM process can be used as an OPA, and can mimic an effectively strong Kerr nonlinearity.

1. Introduction

In LNOI micro-resonators, quadratic nonlinear processes, such as SHG, SFG, parametric down conversion and cascaded wave mixing, have been reported in different schemes to for various application demonstration. Both modal phase matched SHG and difference frequency generation (DFG) processes have been demonstrated in the same LN microring resonator with a high conversion efficiency. Further more, by harnessing the cascading of quadraticnon linearity, it is feasible to achieve efficient third-order ones for nonlinear phase shift, third- and high-order harmonic generation. In many situations, the cascaded effect can outcompete a direct process. Thus, with the contemplate advances, there is more potential of LNOI microresonators for frequency conversion to be explored..

In this Letter, we report on the experimental realization of cascaded SHG and DFG (cSHG/DFG) to manifest an effective FWM based on second-order nonlinearity in a high-Q LNOI microdisk resonator. Through modal phase matching, efficient SHG in the visible range was observed with several milliwatt input power at telecom wavelengths. By introducing a second input (acting as signal light) into the microdisk, idler light from cascaded DFG of the SH and the signal light, also via modal phase matching, is observed at the output. By utilizing cascaded quadratic nonlinearity, a large effective third-order nonlinearity can be obtained. Thus, the cascading process can achieve an efficient FWM process by simultaneously performing the two nonlinear processes in one single quadratic microdisk.

2. Experimental details

2.1 Fabrication and experiment.

In our experiment, the microdisk was fabricated from commercial LNOI nano films (NANOLN Co.). The LN nano film is z-cut single crystalline with a thickness of 300 nm, bonded on top of a 2-um thick silica layer, and the bottom substrate is bulk LN of 0.5 mm thick. The LNOI microdisk microfabrication was performed at the Center for Advanced Electronic Materials and Devices(AEMD),Shanghai Jiao Tong University. The fabrication procedures include femtosecond laser micromachining, focused ion beam (FIB) milling and high temperature annealing. The diameter of the fabricated LNOI microdisk is 50 μm.

The first step in the cascading process is to generate efficient SHG. By injecting intense FW of 5 mW, we scan the FW wavelength (Laser1) to observe efficient SHG. The wavelength for efficient modal phase matching was found to be 1534.9 nm. When we tuned the pump into the resonance of TE(1, 169), efficient SHG via modal phase matching is observed. We then added a signal light from Laser2 and scanned its wavelength to observed the DFG of the signal and the SH. The DFG process occurs when signal is tuned at wavelengths of 1541.8 nm, correspond to TE(1, 168), and 1548.9 nm, corresponding to TE(1, 167). The idler counterparts sit at 1528.0 nm, corresponding to TE(1,170), and 1521.2 nm, corresponding to TE(1,171), respectively. The spectra of the two experimental results are shown in Fig. 1 in blue and black lines, respectively. Considering that the third order nonlinear coefficient of the LN crystal is small compared to the second-order one, the observed effective FWM process is a cascaded quadratic nonlinear process, i.e., cSHGDFG.

To reconfirm this, we collected the power of FW, signal and idle light via the OSA spectrum. As shown in Fig. 2, the signal light intensity is maintained at 5 mW, while the pump power is increased from 0 to 5 mW. The spectrum corresponds to the orange lines in Fig. 2.

The energy dependence is shown in Fig. 2(a). The experimental data exhibit a sinh relation between the two as predicted by the theoretical modelling based on the cascaded quadratic nonlinear processes of cSHG/DFG. For simplicity, one can easily find that $P_{Idl} \propto \sinh^2(P_p)$ for the output light, with P_{Idl} and P_p being the power of idle and pump, respectively. In addition, we also studied the relationship between idle and signal light. In the end, we can get a normalized conversion efficiency of approximately 10^{-4}. Although still at a low efficiency, the signal in this process is also amplified, that is OPA is achieved. The effective large Kerr nonlinearity during the cascading process in the LNOI microresonators maybe exploited for signal amplification or tunable wavelength conversion in telecommunication channels.

2.2 Figures and tables

The figures should be of high resolution. Make sure that every figure is cited in the paper [1,2].

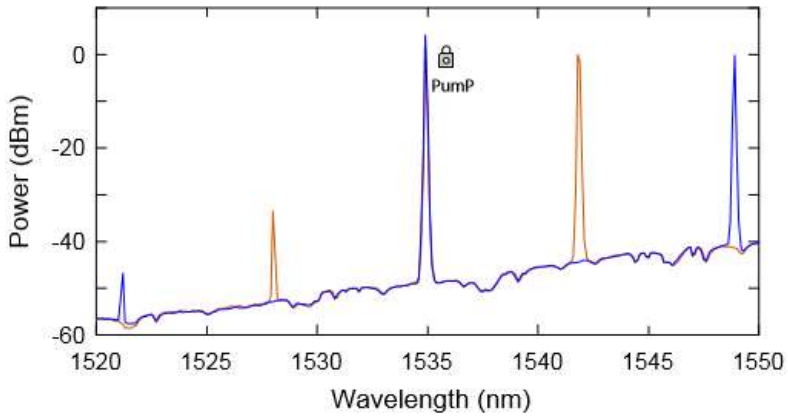

Fig. 1. Optical spectra of the cascading process

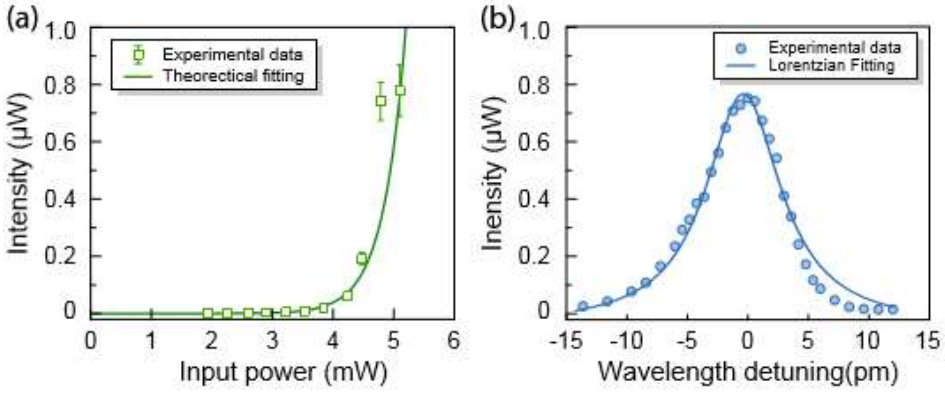

Fig. 2. Effective FWM process in the LNOI microdisk..

3. Summary

In summary, we have demonstrated an effective FWM in an on-chip LNOI microdisk resonator via cascading second order nonlinear processes (cSHG/DFG).

References

1. Shijie Liu, et al. “Effective four-wave mixing in the lithium niobate on insulator microdisk by cascading quadratic processes,” Optics Letters (2019).

Rainbow refractometry for deformed microjets: boundary profiling and chromatic dispersion measurement

SONGKY MOON[1], KYUNGWON AN[2]

[1]*Faculty of Liberal Education, Seoul National University, Seoul 08826, Korea*
[2]*Department of Physics and Astronomy & Institute of Applied Physics, Seoul National University, Seoul 08826, Korea*
[1]*kwan@phya.snu.ac.kr*

Abstract: We have developed a measurement technique of boundary modulation of a micro liquid device. It is based on spectroscopic observation of resonances of high quality factors, and applicable to microjets in operation. The results of the measurement is also useful to determine the chromatic dispersion of the liquid material.

1. Introduction

In employing an optofluidic micro device, it is important to know its shape and chromatic dispersion, which are closely related to its characteristics. However, the conventional boundary measurement techniques such as triangulation are inappropriate to optofluidic devices because their clear surfaces exhibit specular reflection [1]. Moreover, reported chromatic dispersions of a liquid material often disagree to each other [2,3]. We have developed a rainbow refractometry-type technique that measures the boundary modulation of a microcavity based on the global resonance structure of the cavity. It is applicable to a deformed liquid microjet in operation, and useful for determining the chromatic dispersion of the liquid material.

2. Rainbow refractometry for deformed liquid microcavity

2.1 Theoretical background

A resonance of a deformed microcavity corresponds to a solution of two-dimensional Helmholtz equation

$$\nabla^2\varphi = n^2k^2\varphi \,,$$

where n is the real index of refraction and k is the complex wave number. The boundary of the cavity can be described as the product of the mean radius (a) and the boundary modulation. When the boundary modulation is fixed, it can be shown that the set of resonant size parameters $\{ka \equiv X\}$ is unique. Moreover, if X_0 is a resonant size parameter with a high-quality(Q) factor for a refractive index n_0, then $X_0(n_0/n_i)$ is also a resonant size parameter of another cavity with the same boundary modulation but a slightly different index n_i, approximately. This can be understood from that a high-Q resonance can correspond to a periodic ray orbit close to the surface boundary. Consequently, the set of $\{nX\}$ for high-Q resonances is approximately determined by the boundary modulation only.

2.2 Liquid microjet : boundary modulation and index·radius curve

We make a microjet by ejecting ethanol from a deformed orifice, whose mean radius is about 14μm. The cross section at an extreme position of the jet oscillation can be regarded as a two-dimensional microcavity and is pumped by a 532nm cw-laser. Then typically 100 and more high-Q resonances are clearly visible within 550-670nm as the peaks of the cavity-modified fluorescence (CMF) spectrum. For each of such resonances, the following relation is held.

$$n_0X_0\lambda = 2\pi na \,,$$

where X_0 means the corresponding resonant size parameter obtained by numerical calculation with the same boundary modulation as the actual cavity and an arbitrary index n_0. The experimentally observed resonant wavelength is denoted by λ, and n means the refractive index. By using this relation as the fitting equation, one can find the boundary modulation of the actual microjet cavity and index·radius curve (na, namely the chromatic dispersion multiplied by a constant) simultaneously. Our results show that the surface modulations of the microjets are the Bohr type quadruoctapole as confirmed by a different method in our previous study [4], and the slope of the chromatic dispersion is in good agreement with that reported by Rheims [2].

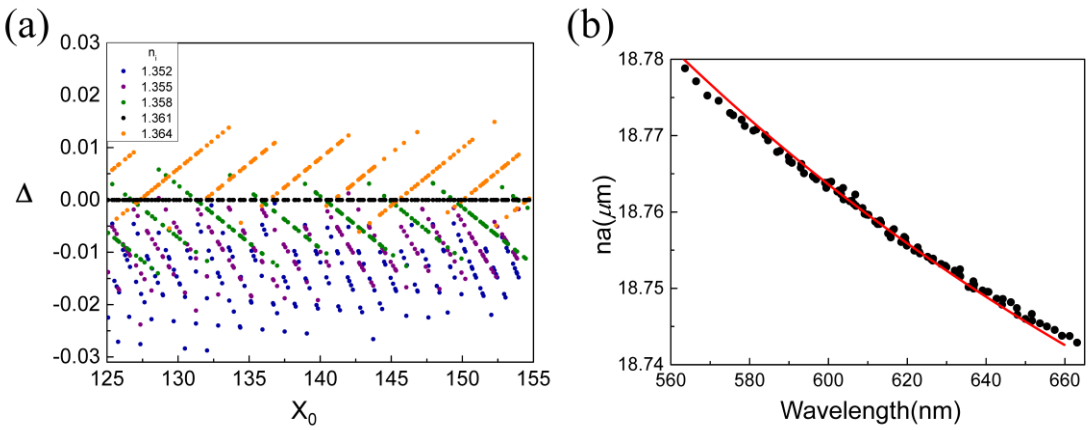

Fig. 1. (a) The deviation between $X_i(n_i/n_0)$ and X_0 (the vertical axis) versus X_0 (the horizontal axis) obtained by numerical calculations. Here, n_0 is set to 1.361 and n_i is varied. The accuracy of the size parameter in calculation is 0.01. The deviations are appeared to be very small. The comb-like diagonal structures are artifacts due to the calculation accuracy. (b) An example of index·radius curve. The experimental observation is taken at an ejection pressure of 1.011bar and room temperature of 23.5℃, and the resonances are fitted with the calculated resonant size parameters for the Bohr-type quadruoctapole with the quadrupolar deformation parameter of 0.100. The red solid curve is obtained by multiplying Rheims' chromatic dispersion of ethanol by a=13.80μm.

3. Summary

We have developed a rainbow refractometry-type measurement technique of boundary modulation that is applicable to liquid microjets. It is based on the global structure and of high-Q resonances of a two-dimensional microcavity. The technique is also useful for determining the chromatic dispersion of the liquid material.

References

1. D. Narita *et al.*, "Three-dimensional shape measurement of a transparent object using a rangefinding approach", Instrumentation and Measurement Technology Conference, IMTC 2003. Proceedings of the 20th IEEE 2, 1022 (2003).
2. J. Rheims *et al*., "Refractive-index measurements in the near-IR using an Abbe refractometer", Meas. Sci. Technol. 8, 601 (1997).
3. I. Z. Kozma *et al.*, "Direct measurement of the group-velocity mismatch and derivation of the refractive-index dispersion for a variety solvents in the ultraviolet", J. Opt. Soc. Am. B **22**, 1479 (2005).
4. S. Moon *et al*., "Experimental observation of Bohr's nonlinear fluidic surface oscillation", Sci. Rep. **6**, 19805 (2016).

REPETITION RATE TUNING OF SOLITON IN MICROROD RESONATORS

RUI NIU[1,3], SHUAI WAN[1,3], SHU-MAN SUN[1,3], TAI-GAO MA[1,3], HAO-JING CHEN[1,3], WEI-QIANG WANG[2,4], ZHI-ZHOU LU[2,4], WEN-FU ZHANG[2,4], GUANG-CAN GOU[1,3], CHANG-LING ZOU[1,3,*], CHUN-HUA DONG [1,3,*]

[1]*Key Laboratory of Quantum Information, CAS, University of Science and Technology of China, Hefei, Anhui 230026, P. R. China*
[2]*State Key Laboratory of Transient Optics and Photonics, Xi'an Institute of Optics and Precision Mechanics (XIOPM), CAS, Xi'an 710119, P. R. China*
[3]*CAS Center For Excellence in Quantum Information and Quantum Physics, University of Science and Technology of China, Hefei, Anhui 230026, P. R. China*
[4]*University of Chinese Academy of Sciences, Beijing 100049, P. R. China*
[*]*Corresponding author: clzou321@ustc.edu.cn, chunhua@ustc.edu.cn*

Abstract: We get single soliton in the microrod cavity through auxiliary-laser-assisted method. And we experimentally demonstrate the effective tuning of the repetition rate of DKS. We also get the single soliton in the SiN microring

1. Introduction

The dissipative Kerr soliton in microresonator has attracted great attentions in the recent years[1], which offers broadband low-noise frequency comb in frequency domain. Owing to the advantages of scalable, stable, portable and low power consumption, it has great potentials for dual-comb spectroscopy, optical clock, high precision optical ranging and so on. However, the stabilization and tuning of the repetition rate for a soliton still hold great challenge. In this study, we experimentally demonstrate the effective tuning of the repetition rate of DKS in a microrod cavity. The resonance frequency and free spectral range of the resonator can be effectively tuned by mechanically compressing the cavity[2]. Besides, by introducing an auxiliary laser, the cavity thermal response is effectively adjusted and the switching to the DKS can be stably achieved[3,4]. Our work allows precise tuning and locking of repetition rate of dissipative Kerr soliton in the microresonators and holds great potential for applications in spectroscopy and precision measurements.

2. Some details

2.1 Auxiliary-laser-assisted soliton generation

Fig. 1. illustrates the mechanism of the auxiliary-laserassisted DKS generation. Firstly, the pump and the auxiliary laser are settled at blue-detuning side of the cavity mode. In the experiment, pump power and auxiliary power were set at about 800mW. When the auxiliary laser drop out off a cavity mode, the cavity cools down rapidly and the resonance blue shifted, effectively scanning the pump to reach the DKS state. By applying such a thermal response control method, we eventually reached single soliton state.

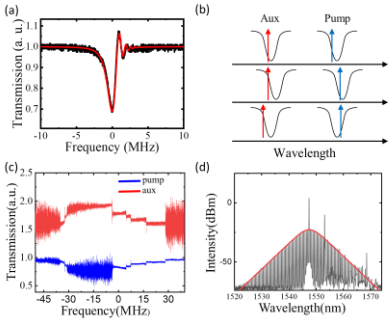

Fig. 1. Auxiliary laser assisted soliton generation

To validate the DKS microcomb generation in our experiments, we characterized the output frequency combs in detail by resuming the optical spectrum and the radio frequency (RF) beat note of comb lines. Limited by the detection range

of our detector and electrical spectrum analyzer (ESA), we used an electro-optic modulator (EOM) modulated with frequency of $\boldsymbol{\Omega}$ = 26GHz to down convert the beat note signal to less than 20GHz. Based on the preknowledge about the range of FSR in our cavity, we can exactly determine the $f_{rep} = f'_{rep} + 2\Omega$while f'_{rep} is the measured frequency in ESA.

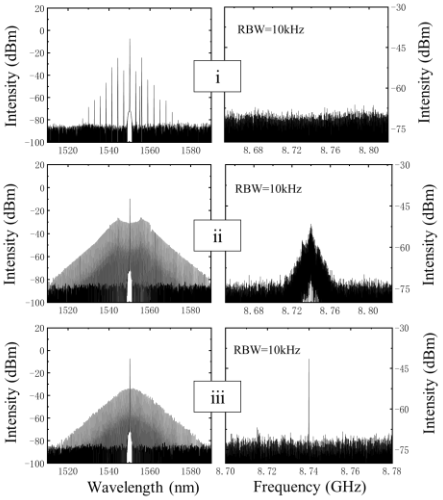

Fig. 2. Optical spectra and RF beat note of primary comb state (i), MI state (ii) and DKS state (iii).

2.2 Mechanical tuning

Since our system has the advantages of fast and convenient adjustment of the structure, we demonstrate a mechanism for tuning the repetition rate precisely through applying a mechanical force along the the vertical direction of the microrod. In our experiment, we applied voltages on the PZT, and adjusted the microrod cavity to critical coupling at each voltage.

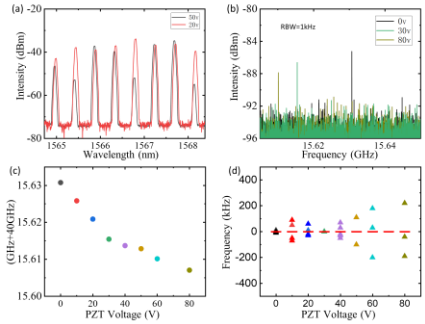

Fig. 3. The optical spectra and RF beat note with different PZT voltages.

3. Summary

Combining the mechanical tuning and auxiliary laser assisted soliton generation, the repetition rate of the soliton state can be precisely tuned over a broad band of 30MHz. Benefiting from the advantage of precisely and fast tuning of repetition frequency of DKS in the microresonator, our platform can lock the repetition rate stably and provide a promising candidate for applications such as metrology, spectroscopy and spectrometer calibration.

References

1. T. Herr, V. Brasch, J. D. Jost, C. Y. Wang, N. M. Kondratiev, M. L. Gorodetsky, and T. J. Kippenberg, Nat. Photonics **8**, 145 (2014).
2. S. B. Papp, P. Del'Haye, and S. A. Diddams, Phys. Rev. X **3**, 031003 (2013).
3. Y. Geng, X. Huang, W. Cui, Y. Ling, B. Xu, J. Zhang, X. Yi, B. Wu, S.-W. Huang, K. Qiu, C. W. Wong, and H. Zhou, Opt. Lett. **43**, 2406 (2018).
4. Z. Z. Lu, W. Q. Wang, W. F. Zhang, S. T. Chu, B. E. Little, M. Liu, L. Wang, C.-L. Zou, C.-H. Dong, B. Zhao, and W. Zhao, preparation.
5. R. Niu, S. Wan, S.-M. Sun, T.-G. Ma, H.-J. Chen, W.-Q. Wang, Z. Lu, W.-F. Zhang, G.-C. Guo, C.-L. Zou, and C.-H. Dong, arxiv:1809.06490

Programmable Heterogeneous Integrated III-V-on-Si microresonator-Based Switch Arrays

YUE NIU[1], ANDREW POON[1]

[1]*Department of Electronic and Computer Engineering, The Hong Kong University of Science and Technology, Clear Water Bay, Kowloon, Hongkong, China*
[1]*yniuaj@connect.ust.hk*

Abstract: As a datacenter router, microresonator-based switches based on the Free Carrier Disersion (FCD) effect contribute to the realization of intra- and inter-chip optical links and transmission. We aim to develop heterogeneously integrated III-V-on-Si microresonator-based switch arrays, leveraging the active gain of the III-V medium.

1. Introduction

Microresonators as one of the building blocks in the datacenter networks offer a functional router that redistributes the information from the input links to appropriate output links [2]. Emerging fields like neuromorphic computing and artificial intelligence serving for the next generation datacenter call for an urgent need of the ultra-high speed multi-channel data processing and matrix computing [3]. In this work, we propose a programmable heterogeneous integrated III-V-on-Si microresonator-based switch array, leveraging the active gain of the III-V medium, to serve as a functional router applied in datacenters as shown in Fig.1(b).

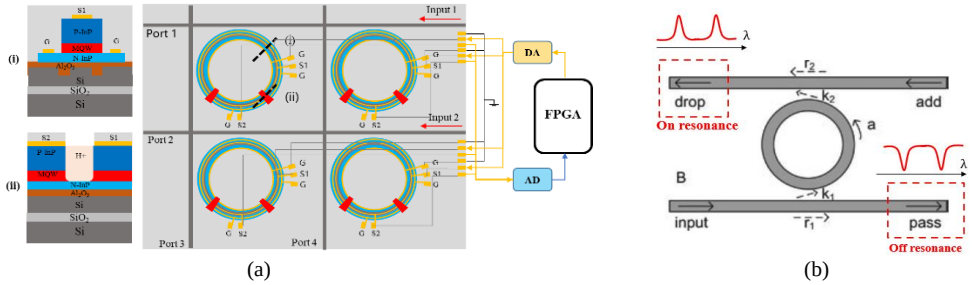

(a) (b)

Fig. 1. (a) Schematic of a rogrammable 2×2 microring resonator-based switch array controlled by the FPGA board. (b) Principle of a microring resonator-based switch

2. Principle

As shown in fig.1(b), when the effective refractive index of the silicon bus waveguide and the microresonator meet a phase match, part of the input laser beam will evanescently couple into the microresonator. Propagation within the microresonator leads to a phase shift on the coupled wave. When the phase shift reaches an integer time of 2 π, the waves in the cavity interfere constructively, contributing to a peak power, which is called “on resonance”. Ideally, a microresonator switches the peak power from the through to drop port on resonance. The phase shift is determined by the length of the microresonator, and the propagation constant of the coupled wave, which depends on the effective refractive index of the cavity. By heterogeneously integrating a III-V compound semiconductor with a doped PIN junction onto the silicon microresonator as shown in fig.2 (a), we adjust the effective index by injecting current in the III-V layer due to a free carrier dispersion effect.

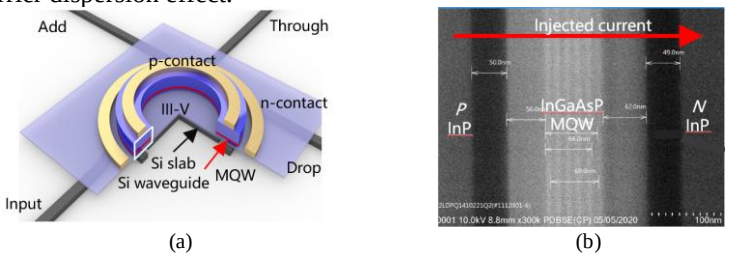

(a) (b)

Fig. 2. (a) Heterogeneous structure of a III-V-on-Si microring resonator-based (MRR) switch. (b) Heterogeneous structure of the III-V active medium.

As an active medium, III-V compound semiconductors possess a higher recombination-generation (R-G) rate, providing two additional functions with different bias of voltage applied on [1], at the same time of working as a switch

tuner. Heterogeneous structure of the III-V medium is shown in fig.2(b). Under a forward bias, III-V provides optical gain to compensate the propagation loss in the silicon waveguide. While under a reverse bias, photons are absorbed by the III-V compound and transferred to the photocurrent. Therefore, an isolated area in the III-V layer can be spared to serve as a photodetector.

3. Fabrication

Ebeam lithography is used to pattern the photoresist on the silicon substrate. The pattern is transferred to the silicon layer by DRIE etching. The integration of the III-V layer onto the etched silicon waveguide is implemented by the Atomic layer deposition (ALD) bonding. Al2O3 with a thickness of 30 nm is deposited on both the surface of the III-V and of the etched Si. Thus, the III-V and the etched Si will be seamlessly attached to stand a bonding process with a temperature of 300 °C, and a pressure of 1000 mBar for 3 hours.

We etched 1.4 um InGaAsP by RIE etching and deposited metal pads by a lift-off process. H ion will be implanted into the P-InP after the III-V etching for electrical isolation. At last, an oxide cladding of 500 nm was deposited by PECVD. which are shown in Fig.3(b), (c) show the width of the etched Si waveguides and a crossing in the SEM views

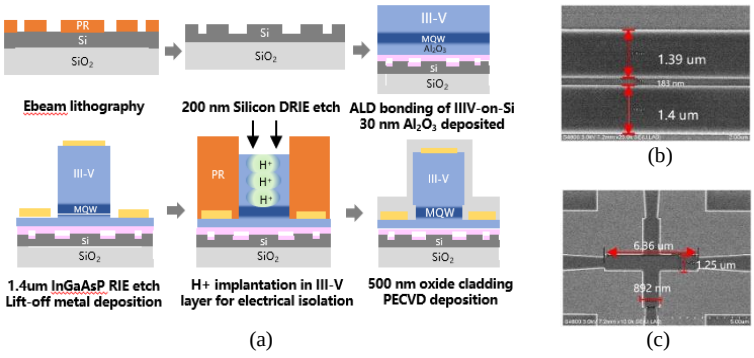

(a) (b) (c)

Fig. 3. (a) Process flow of a microresonator-based switch array. (b) SEM view of etched Si bus waveguide. (c) SEM view of a crossing in the switch array in the Si layer.

4. Results

Fig. 4(a) shows a transmission of the drop/through transmission of a Si microresonator-based switch with a linewidth of 0.045 nm and a FSR of 2.44 nm. Fig.4(b) illustrates the through port transmission of a MRR switch under the injection current of 0 mA, 4 mA, 7 mA, 8 mA, demonstrating a maximum blue shift of 0.15 nm. Fig. 4(c) shows an eye diagram of a MRR switch at a data rate of 10 Gbit/s [1].

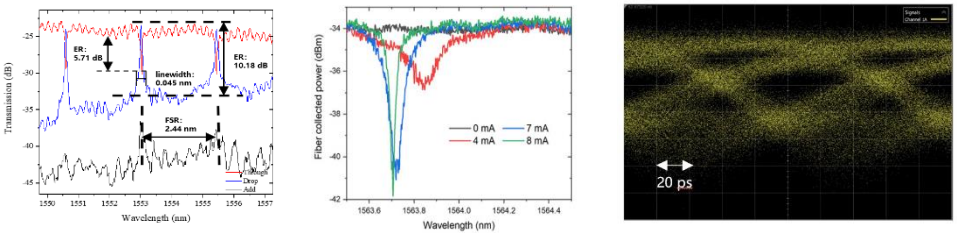

(a) (b) (c)

Fig. 4. (a) Drop/through transmission of a Si microresonator-based switch. (b)Through port transmission of a MRR switch under different injection current of the III-V medium. (c) Eye diagram of a MRR switch @10 Gbit/s

5. Summary

We show preliminary results of a programmable heterogeneous integrated III-V-on-Si microresonator-based switch array, demonstrated by the characterizations of a III-V-on-Si MRR switch and a Si microresonator-based switch.

References

1. Li J, Tan B X, Tian M, et al., “Heterogeneously integrated III–V-on-Si microring resonators: a building block for programmable photonic integrated circuits,” Journal of Optical Microsystems (2021).
2. Cheng Q, Rumley S, Bahadori M, et al., “Photonic switching in high performance datacenters,” Optics express (2018).
3. Mordor Intelligence, “Optical Switches Market Growth, Trends and Forecast (2019-2024),” (2019).

Gas Sensing through thermal effect in the high-Q microbubble resonators

ZHONG-DI PENG[1], CHANG-QIU YU[2], HONG-LIANG REN[3], CHANG-LING ZOU[1], GUANG-CAN GUO[1], CHUN-HUA DONG[1]

[1] *Key Laboratory of Quantum Information, University of Science and Technology of China, Chinese Academy of Sciences, Hefei 230026, P. R. China.*
[2] *School of Electronics and Information, Hangzhou Dianzi University, Hangzhou 310018, China*
[3] *College of Information Engineering, Zhejiang University of Technology, Hangzhou Zhejiang 310023, China*
[1] *chunhua@ustc.edu.cn*

Abstract: The gas sensing in the high-Q microbubble resonator is demonstrated through the thermal effect, which is induced that the heating of the strong pump laser. By passing gas with different speed, the thermal response is different, while the heating is dissipated by the flowing gas. In addition, the thermal oscillation can be observed at appropriate pressure for specially gas, which amplifies the slight thermal parameters difference for different gas. Therefore, we can distinguish the flowing gas in our experiment. These unique features establish a new avenue towards distinguishing more different kinds of gases.

1. Introduction

Whispering-gallery-mode microcavity have been widely investigated for a variety of applications such as optical sensing, nonlinearity optics, ultra-low-threshold lasing, cavity quantum electro dynamics (QED). Among these applications, WGM microcavity-based sensors hold great potential in high-resolution sensing for their high quality factor (Q) and small mode volume. The research field about WGM sensors have seen enormous growth these years and different reactive sensing mechanisms have been summarized such as resonant mode shift, resonant mode splitting and resonant mode broadening. Among different kinds of microresonators sensors, the microbubble resonator becomes distinguished as a sensing platform with high tunability because of its thin wall.

In this work, we have discussed the thermal response in microbubble resonators with different gas flowing rate as well as pressure, and demonstrate the potential for a sensitive gas sensing. The thermal response, representing by the linewidth of the mode with thermal effect, relates to the thermal relaxation time (γ_{ths}) and thermal absorbing rate (γ_{abs}). Due to the dissipation of the passing gas, the two factors of the cavity thermal behavior change with the gas flowing rate.

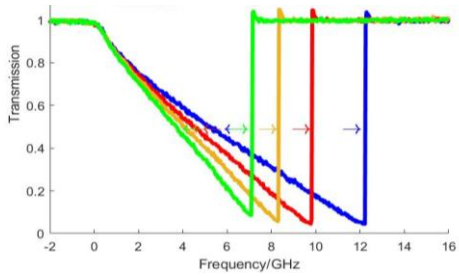

Fig. 1. Typical transmission of optical mode with thermal effect, with N_2 passing through the microcapillary by different flowing rate.

References

1. Vahala K J, “Optical microcavities” nature (2003).
2. Yang Y, Ward J, Chormaic S N, “Optimization of whispering gallery modes in microbubble resonators for sensing applications” International Society for Optics and Photonics (2014)
3. Carmon T, Yang L, Vahala K J, “Dynamical thermal behavior and thermal self-stability of microcavities” Optics express (2004)
4. Ward J M, Yang Y, Chormaic S N. “Flow sensor using a hollow whispering gallery mode microlaser”, International Society for Optics and Photonics (2016)
5. Kippenberg T J, Rokhsari H, Carmon T, et al. “Analysis of radiation-pressure induced mechanical oscillation of an optical microcavity” Physical Review Letters (2005)
6. He L, Xiao Y F, Zhu J, et al. “Oscillatory thermal dynamics in high-Q PDMS-coated silica toroidal microresonators” Optics express,(2009)

Whispering Gallery Mode sensor for the Detection and Characterization of Organophosphorus Agro-chemical at Ultra- lower Concentrations

K. M. Kalani G Perera[1], Dr. Siva Subramanian[1], Dr. Srikanth Pedireddy[1], Prof. Frank Vollmer[1]

[1] *University of Exeter, Living Systems Institute, Exeter, EX4 4QD, United Kingdom*

[1] *F.Vollmer@exeter.ac.uk*

Abstract: We demonstrate the detection and characterization of single molecules of glyphosate interacting with a whispering gallery mode gold nanoparticle hybridized resonator in real-time. Instead of conventional detection and characterization methods, we propose a method to identify the amino, phosphate, and carbonate functional groups of glyphosate through the changes in the signal patterns and the sensor kinetics at different pH conditions.

1. Introduction

Glyphosate (GLY) has been receiving increasing attention as an active synthetic organophosphorus herbicide since 1974, primarily due to the interruption of the shikimate pathway (which exists only in microorganisms and plants, never in animals) by inhibiting the 5-enolpyruvateshikimate-3-phosphatesynthase enzyme. [1] Even though there has been extensive research on the fate of GLY, emphasis on the detection of single molecules in environmentally relevant conditions has been minimal.[2] Hence, it is interesting to determine precise levels of glyphosate at ultra-lower concentration levels. Herein, we utilize a nanosensing strategy based on optical whispering gallery modes (WGMs) enhanced by a gold nanorods platform, which can directly detect and characterize the GLY molecules at a single molecular level in real-time.

2. Method

2.1 WGM Setup

An external cavity diode laser (Toptica TA pro 642 HP, Toptica GmbH, Munich, Germany) was used as the excitation laser. Total internal reflection at an N-SF11 prism surface was used for efficient coupling to the WGMs. A pulsed CO_2 laser (with a 10.6 μm emission line) was utilized to melt a commercial, single-mode optical fibre to fabricate the glass WGM microcavity. One end of the fibre was held in tension by the weight of a small ceramic ferrule. A stem was made by tapering to a width of 10 μm for a length of 500 μm. And the sphere (88 -95 μm) was formed after irradiation with a high-power cycle at the end of the taper. In addition to that, the bendings were adjusted by using the minute power of the laser. A polydimethylsiloxane (PDMS) V-shaped chamber was used to load the sample where the maximum volume it could hold was 400 μL.

2.1 Preparation of WGM sensor

The spherical glass resonator (diameter ~88- 95 μm) fabricated at the tip of a single-mode optical fibre acts as the WGM microcavity. The previously reported method was used to attach the plasmonic cetrimonium bromide capped gold nanorods (CTAB-AuNRs) [10 × 25 nm (LSPR wavelength 642 nm CTAB, Nanopartz Inc., USA) (1 oD/ 0.1 μL)] to the surface of the WGM cavity. The AuNRs attachment to the WGM cavity surface was monitored (7-8 NRs). After attaching the AuNRS, the remaining solution was removed, and the sample chamber was rinsed thrice with MiliQ water to remove excess free NPs in the chamber. After cleaning the chamber, the background record was carried out to ensure no detectable signal was found in the trace data.

2.1 Preparation of GLY

For single-molecule detecting and characterization, GLY was chosen. GLY molecule has five different ionic states, and it is known that the ionic state depends on the medium pH. Therefore, the detection was carried out at pH 10.6 (citrate buffer), 9.2 (citrate buffer), 7((phosphorus buffer), 5.6 (phosphorus buffer), and 3(citrate buffer). The concentration of the GLY was varied from 12.5 nM – 1000 nM to obtain the different functionality.

3. Results

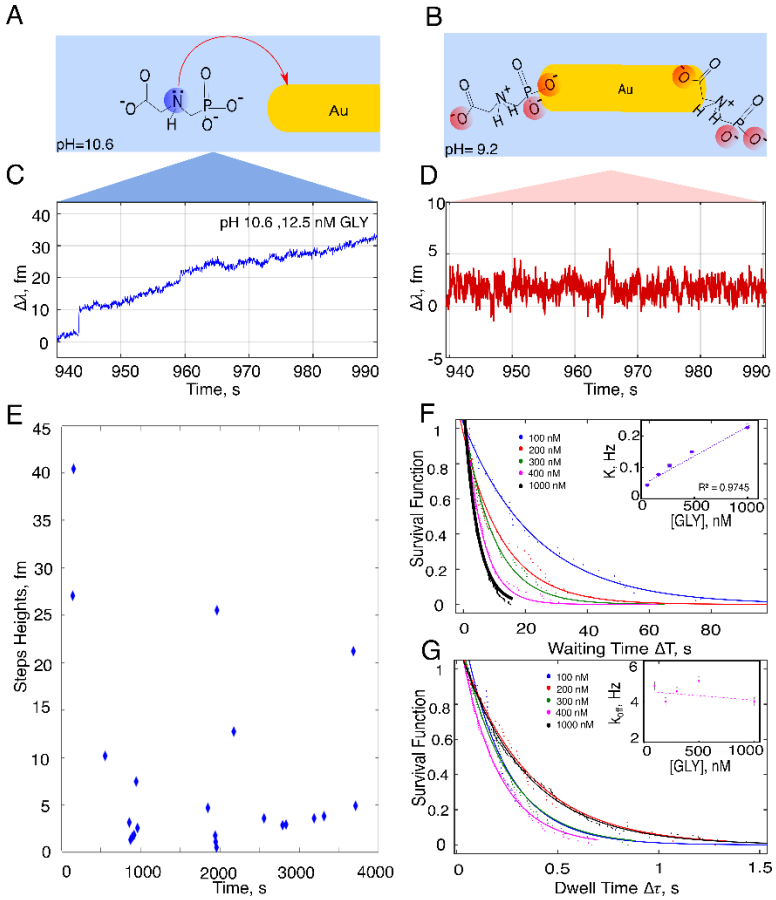

Figure 1. A Conceptual diagram of the GLY-amine gold interaction at pH 10.6. **B.** Conceptual diagram of the GLY oxyanion gold interaction at pH 9.2. **C.** Discrete signals in the WGM resonator trace from covalent bond formation of the NH_2 functional group with the Au surface at pH 10.6. **D.** sensor signals due to transient interaction GLY-oxyanion with the gold nanorod at pH 10.6. **E.** Plot of the height of step events over time obtained during the analysis. Each step indicates binding of a GLY molecule. **F**. Survivor function and corresponding exponential fit to the time separation of spike events; 100 nM GLY (Blue), 200 nM GLY (Red), 300 nM GLY (Green), 500 nM GLY (Pink) ,and 1000 nM GLY (Black). And the inset shows the regression slope of spike event rate versus GLY concentration (R^2 = 0.9746). **G.** Survivor function and corresponding exponential fit to the Dwell time of spike events; 100 nM GLY (Blue), 200 nM GLY (Red), 300 nM GLY (Green), 500 nM GLY (Pink) ,and 1000 nM GLY (Black). And the inset illustrates the behaviour of the offset rate versus GLY concentration Experiments were conducted at room temperature.

Table 1. Extracted offset-rate from the fitting data at pH 9.2,7, 5.6, and 3

[GLY]/nM	pH 9.2	pH 7	pH 5.6	pH 3
100	4.770	3.670	2.236	2.147
200	3.990	2.434	1.728	1.739
300	4.497	2.923	2.032	1.774

4. Summary

Quantitative structural characterization of a molecule at a single level is coming increasingly important in Analytical studies. This study concludes that the WGM technique opens the identification and characterization of functional groups in molecules such as GLY at ultra-low concentrations.

References

1. 1. Hu J, Lesseur C, Miao Y, Manservisi F, Panzacchi S, Mandrioli D, Belpoggi F, Chen J, Petrick L. Low-dose exposure of glyphosate-based herbicides disrupt the urine metabolome and its interaction with gut microbiota. Scientific reports. 2021 Feb 5;11(1):1-0.

2. Singh S, Kumar V, Datta S, Wani AB, Dhanjal DS, Romero R, Singh J. Glyphosate uptake, translocation, resistance emergence in crops, analytical monitoring, toxicity and degradation: a review. Environmental Chemistry Letters. 2020 May;18(3):663-702.

A phonon laser operating at an exceptional point

JING ZHANG[1,2,3], BO PENG[1,4], ŞAHIN K. ÖZDEMIR[1,5], KEVIN PICHLER[6,*], DMITRY O. KRIMER[6], GUANGMING ZHAO[1], FRANCO NORI[7,8], YU-XI LIU[3,9], STEFAN ROTTER[6], AND LAN YANG[1]

[1] *Department of Electrical and Systems Engineering, Washington University, St Louis, MO, USA*
[2] *Department of Automation, Tsinghua University, Beijing, China*
[3] *Center for Quantum Information Science and Technology, BNRist, Beijing, China*
[4] *IBM Thomas J. Watson Research Center, Yorktown Heights, NY, USA*
[5] *Department of Engineering Science and Mechanics, The Pennsylvania State University, University Park, PA, USA*
[6] *Institute for Theoretical Physics, Vienna University of Technology (TU Wien), Vienna, Austria*
[7] *Theoretical Quantum Physics Laboratory, RIKEN, Saitama, Japan*
[8] *Physics Department, The University of Michigan, Ann Arbor, MI, USA*
[9] *Institute of Microelectronics, Tsinghua University, Beijing, China*
[*] *Presenting author: kevin.pichler@tuwien.ac.at*

Abstract: We present a phonon laser operating at an exceptional point (EP), which offers valuable insights into the non-Hermitian physics of lasing. In particular, we find a significant broadening of the phonon laser linewidth in the vicinity of the EP.

1. Introduction

Non-Hermitian systems have attracted considerable attention because of their unconventional and often counter-intuitive behavior around exceptional points (EPs) – spectral singularities where at least two of the eigenvalues and also their corresponding eigenvectors coalesce. In recent years, numerous EP-related concepts have been studied, such as unidirectional lasing and invisibility [1,2], mode selection in lasers [3], enhanced sensing [4], or topological energy transfer [5,6]. One of the oldest theoretical predictions associated with EPs is an extreme broadening of the laser linewidth, due to the excess quantum noise induced by the non-orthogonality of the resonator modes [7,8]. A detailed experimental study of this effect, however, remained out of reach so far since it is not straight-forward to steer a laser to an EP and to measure its extremely narrow linewidth right there. Here we tackle this problem by working with a phonon laser, where the linewidth can be measured much more easily.

2. Experimental setup

Our phonon laser, which is based on a system implemented by Grudinin et al. [9], is schematically illustrated in Fig. 1. It consists of two whispering gallery mode micro-resonators which are evanescently coupled to each other. The first resonator supports a high-Q optical mode a_1 as well as a mechanical mode (phonon mode), whereas the second resonator supports a low-Q optical mode a_2. Light is coupled into the first resonator through a tapered optical fibre. Due to the inter-resonator coupling, two optical supermodes are formed, which act as a two-level system in which the transitions between the two levels are mediated by the phonon mode. We can tune the decay rate in the second resonator by approaching a chromium coated silica nanotip, which adds an additional loss γ_{tip} to the system. To reach an EP in the spectrum, we additionally tune the frequency difference between the two supermodes by varying the distance between the two resonators.

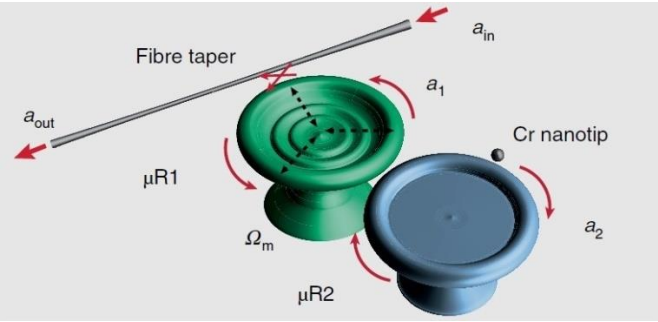

Fig. 1: Schematic of the phonon laser setup. Two coupled microtoroid resonators μR1 and μR2 support the optical modes a_1 and a_2. The first resonator additionally supports a mechanical mode with resonance frequency Ω_m. Laser light is coupled into the system through a tapered fibre that is evanescently coupled to the first resonator. The loss in the second resonator can be tuned by approaching a chromium coated silica nanotip.

3. Results and Discussion

In our experiments, we measured the threshold pump power as well as the linewidth of the phonon laser as a function of the additional loss γ_{tip}. Increasing γ_{tip} redistributes the two supermodes between the two resonators and alters the intracavity field intensity in the first resonator (which supports the mechanical mode) in such a way that the threshold first increases and then features a sudden drop when the system comes closer to the EP (see Fig. 2a). At the same time, the increasing overlap of the two optical modes leads to an enhancement of the optical noise, which becomes maximal at the EP, where the two supermodes are completely non-orthogonal. The noise inherent in these optical modes imprints on the phonon mode a linewidth that is maximally broadened at the EP (see Fig. 2b). Further increase of γ_{tip} pushes the system beyond the EP, where the threshold remains low and the linewidth broadening decreases again.

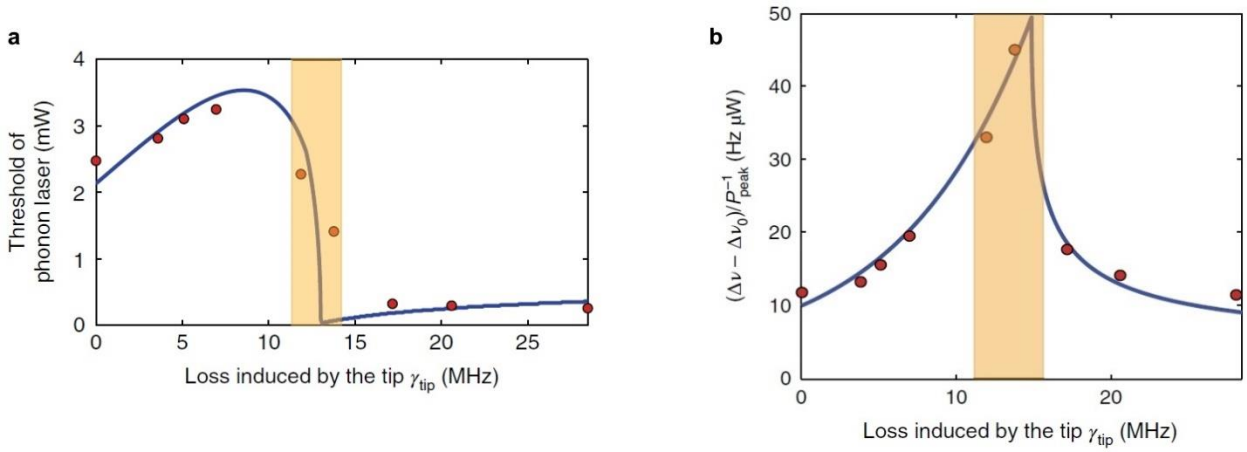

Fig. 2: **a)** Phonon laser threshold as a function of the additional loss γ_{tip}. The threshold first increases with increasing γ_{tip} and then experiences a sudden drop in the vicinity of the EP (orange shaded area). After the EP, the threshold remains low. **b**) Ratio between the normalized phonon laser linewidth and the inverse peak power $(\Delta\nu - \Delta\nu_0)/P_{peak}^{-1}$ as a function of the additional loss γ_{tip}. We find a pronounced linewidth enhancement in the vicinity of the EP (orange shaded area).

4. Conclusion and Outlook

We have experimentally investigated how a phonon laser is affected when being operated close to an EP. By steering the phonon laser across the EP, we have shown that its linewidth is greatly enhanced, which is attributed to the increased noise in the two optical supermodes that provide the gain for the phonon laser. Our study [10] provides direct experimental evidence showing that EP-enhanced optical noise can be transferred directly to mechanical noise, leading to a linewidth broadening in the phonon laser. This opens up new perspectives for the relation between noise and non-Hermitian physics and may find applications in various related fields such as signal processing technologies.

References

1. B. Peng, Ş.K. Özdemir, M. Liertzer, W. Chen, J. Kramer, H. Yilmaz, J. Wiersig, S. Rotter, L. Yang, "Chiral modes and directional lasing at exceptional points", Proc. Natl. Acad. Sci. USA **113**, 6845–6850 (2016).
2. Z. Lin, H. Ramezani, T. Eichelkraut, T. Kottos, H. Cao, D.N. Christodoulides, "Unidirectional invisibility induced by PT-symmetric periodic structures", Phys. Rev. Lett. **106**, 213901 (2011).
3. L. Feng, Z.J. Wong, R.-M. Ma, Y. Wang, X. Zhang, "Single-mode laser by parity–time symmetry breaking", Science **346**, 972–975 (2014).
4. W. Chen, Ş.K. Özdemir, G. Zhao, J. Wiersig, L. Yang, "Exceptional points enhance sensing in an optical microcavity", Nature **548**, 192–196 (2017).
5. J. Doppler, A.A. Mailybaev, J. Böhm, U. Kuhl, A. Girschik, F. Libisch, T.J. Milburn, P. Rabl, N. Moiseyev, S. Rotter, "Dynamically encircling an exceptional point for asymmetric mode switching", Nature **537**, 76–79 (2016).
6. H. Xu, D. Mason, L. Jiang, G.E. Harris, "Topological energy transfer in an optomechanical system with exceptional points", Nature **537**, 80–83 (2016).
7. K. Petermann, "Calculated spontaneous emission factor for double-heterostructure injection lasers with gain-induced waveguiding", IEEE J. Quantum Electron. **15**, 566–570 (1979).
8. A.E. Siegman, "Excess spontaneous emission in non-Hermitian optical systems. I. Laser amplifiers", Phys. Rev. A **39**, 1253–1263 (1989).
9. I.S. Grudinin, H. Lee, O. Painter, K.J. Vahala, "Phonon laser action in a tunable two-level system", Phys. Rev. Lett. **104**, 083901 (2010).
10. J. Zhang, B. Peng, Ş.K. Özdemir, K. Pichler, D.O. Krimer, G. Zhao, F. Nori, Y.-X. Liu, S. Rotter, L. Yang, "A phonon laser operating at an exceptional point", Nature Photonics **12**, 479–484 (2018).

Coupling in Optical Microcavities

TOM RODEMUND[1,2], **MARTINA HENTSCHEL**[1]

[1] *Professorship Theoretical Physics of Complex Dynamic Systems, Department of Physics, University of Applied Sciences Chemnitz, Reichenhainer Straße 70, 09126 Chemnitz, Germany*
[2] *tom.rodemund@physik.tu-chemnitz.de*

Abstract: Deformed microdisc cavities have proven their potential as microlasers. Here, we further enhance their properties by using arrays of several resonators, where coupling between the cavities can lead to a wide range of effects. This work seeks to characterize the coupling between two and more microresonators by calculating modes and resonant frequencies and by comparing the system to two coupled harmonic oscillators.

1 Introduction

Optical microcavity resonators posses great application potential as microlasers and novel photonic devices.[1, 2] Using arrays of slightly deformed circular cavities can lead to a strong directionality of the far field.[3] However, this drastically depends on the distance between the constituents of the array, especially in the case of strong coupling. For arrays of more than three microcavities, the directionality of the far field can reverse entirely.[3] This calls for a deeper investigation of the interaction between resonators and the effects involved. A way to characterize the coupling between resonators using a simple scalar or similar is needed. The objective of the present work is to explore possible avenues of achieving this.

2 Model System

The model system used in the following simulations consists of two circular microdisc cavities as shown in Fig. 1. Each is characterized by a radius of $R = 1$ and a refractive index of $n = 3.4$. The latter corresponds to the effective refractive index of GaAs. Both discs are embedded in vacuum or air with a refractive index of $n_0 = 1$. The microdiscs are separated by a distance D. All calculations are performed using the open-source library MEEP for `python 3`, which excells in FDTD calculations of the Maxwell equations.

3 Results

One metric by which the interaction between the two resonators can be grasped is the splitting of eigenfrequencies. The eigenfrequencies of the coupled resonators are expected to lie in the vicinity of the modes of the single resonator, as the values must coincide in the limit of large D/R. Whispering-gallery modes (WGMs) are of interest, as they possess the highest Q-factors and are therefore long-lived. Figure 2 shows the eigenfrequencies of the resulting system in dependence on the intercavity distance, where a clear splitting of frequencies for $D/R < 0.45$ can be observed. The symmetric modes shift to lower frequencies, while the energy of asymmetric modes decreases. The mode structures are displayed in Fig. 3, indicating that the symmetric modes like Fig. 3a lie at lower frequencies, as the coupling features allow the WGM to live closer to the cavity wall in the coupling region in comparison to the antisymmetric mode in Fig. 3b. Here, the uneven nature of the field requires a node in between the two resonators, which pushes the mode further into the cavity, which in turn increases its energy. This deformation of the mode in phase space can also be seen in the Husimi functions of the near-fields in Fig. 3c-d, which represent the phase space obtained by calculating the overlap of the wave function with a coherent state.[4]

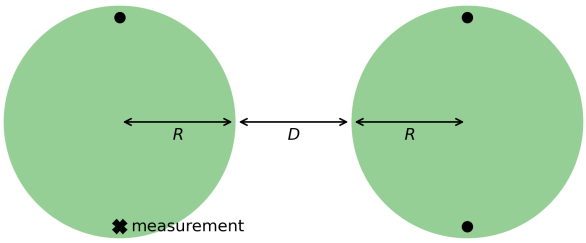

Figure 1: Model system, which is defined by the radius of the microdiscs R and the intercavity distance D. The dots and the cross represent the positions of the sources, of which there are four in total due to the use of symmetric planes. The cross represents the point at which the electric field is measured.

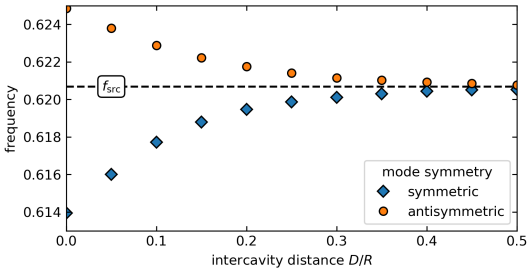

Figure 2: Resonant frequencies depending on the intercavity distance. The dashed line represents f_{src}, a resonance frequency of a single microdisc and the frequency, at which the system is excited.

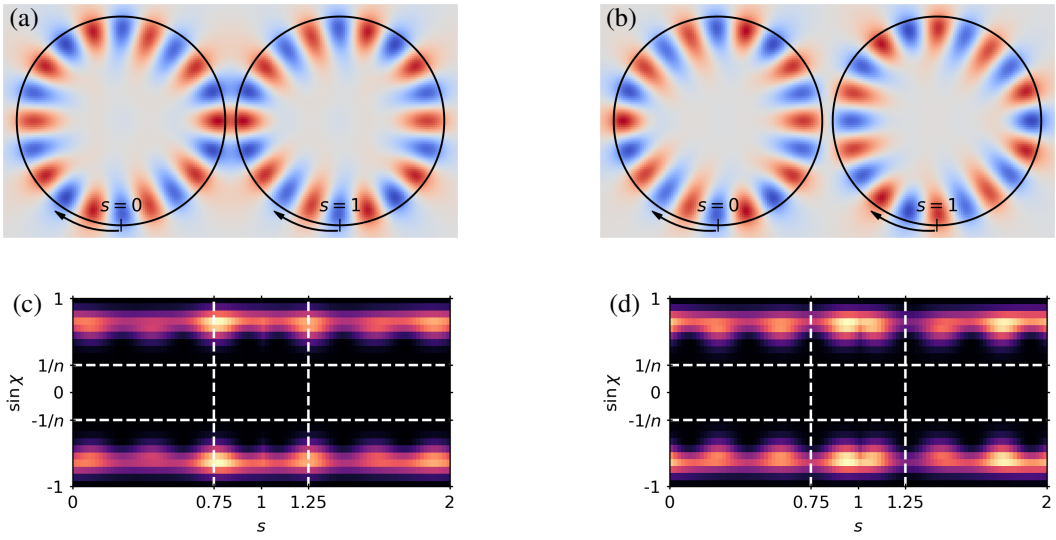

Figure 3: Mode patterns for a system with $D/R = 0.1$. Red denotes a positive sign while blue denotes a negative sign of E_z. The gray area marks the microdiscs. The patterns are obtained via frequency domain calculations using MEEP. (a) shows the symmetric configuration, where a significant overlap of the modes of the two resonators is found, which leads to a lower total energy as shown in Fig. 2. (b) shows the antisymmetric mode. (c) and (d) show the Husimi representations of the symmetric/antisymmetric modes respectively in Birkhoff coordinates $(s, \sin\chi)$. $s \in [0,1]$ corresponds to the left and $s \in [1,2]$ to the right resonator respectively, and χ to the angle of incidence. The ticks at $\pm m/k$ represent the theoretical value for WGMs of a closed disc. The vertical white, dashed lines show the surface points, where the two resonators are closest to each other.

The Husimi representations corresponding to Fig. 3a-b are shown in Fig. 3c-d respectively. The greater overlap of the modes in the symmetric configuration is visible as an increased value of the Husimi function near $s \approx 0.75$ and 1.25 where the two discs are closest to each other. The opposite holds for the antisymmetric case, where minima at $s \approx 1 \pm 0.25$ are found.

Another way of characterizing the coupling between resonators is by examining parallels to a system consisting of two coupled mechanical oscillators. When the spring constant of the coupling spring is increased, which corresponds to decreasing values of D/R in the microcavity case, a splitting of frequencies takes place. However, here the resulting lower frequency stays constant as the corresponding synchronous oscillation does not depend on the coupling. The corresponding lower frequency of the oppositely oscillating pendula increases with D/R as in the microcavity case. This is a limitation of the oscillator comparison. If one oscillator is excited, a periodic exchange of energy between the two pendulums can be observed. This is also the case for microcavity arrays, even though the mode structure of the latter is far more complex.

4 Summary and Outlook

Coupling between microcavities is an interesting field, which is yet to be explored fully. The ultimate goal is to find a concise manner in which the strength and the nature of coupling can be characterized. Numerical calculations show a behavior partly similar to a simple system of coupled harmonic oscillators with clear deviations already in the simplest case of coupled discs. In the future more complicated systems are to be examined, e.g. microdiscs with varying radii and whole arrays of cavities, which could also be deformed. In this context, the emergent dynamics in the complex system is of interest.

References

[1] Kerry J Vahala. Optical microcavities. *Nature*, 424(6950):839–846, 2003.

[2] Jens U Nöckel and A Douglas Stone. Ray and wave chaos in asymmetric resonant optical cavities. *Nature*, 385(6611):45–47, 1997.

[3] Jakob Kreismann, Jaewon Kim, Martí Bosch, Matthias Hein, Stefan Sinzinger, and Martina Hentschel. Superdirectional light emission and emission reversal from microcavity arrays. *Physical Review Research*, 1(3):033171, 2019.

[4] Jung-Wan Ryu, Soo-Young Lee, and Sang Wook Kim. Coupled nonidentical microdisks: Avoided crossing of energy levels and unidirectional far-field emission. *Physical Review A*, 79(5):053858, 2009.

Optical Microcavities with Sources

LUKAS SEEMANN[1,2], **MARTINA HENTSCHEL**[1]

[1] *Professorship Theoretical Physics of Complex Dynamic Systems, Department of Physics, University of Applied Sciences Chemnitz, Reichenhainer Straße 70, 09126 Chemnitz, Germany*
[2] *lukas.seemann@physik.tu-chemnitz.de*

Abstract: The geometry of optical microcavities is intimatly related to their far field emission. However, the presence of internal sources can add new features. We investigate these using ray-wave correspondence and extending the ray model by the phase information.

1 Introduction

Complex systems of mesoscopic optics are interesting both as model systems and because of their enourmes application potential [1,2]. Ray-wave correspondence provides a straightforward method to invastigate their properties, e.g. their far-field emission characteristics. In case of more complicated systems, e.g. microcavities with internal light sources or coupled microcavities, interference effects will become important. Phase information is necessary to be able to describe these interference effects. To this end we add the phase information to the ray picture by collecting the phase along the ray trajectory and investigate chances and possible limitations of this approach.

2 Model System

We consider a disk or limaçon microcavity resonator with refractive index n in air or vacuum. The light is either captured in the resonator by total internal reflection or a part of the light intensity can leave the cavity if the angle of incidence χ is less then the critical angle $\chi_C = \arcsin(1/n)$ of total reflection. Using the laws of reflection and refraction of light, the trajectory of the ray thus be traced.
The phase information of the light ray is usually not exploited. It contains, however, additional information that is appreciated in the optics community and can explain interference effects in mesoscopic optics [3]. To this end we do not only take the Fresnel coefficients that cover the change in intensity along the ray trajectory into account, but also investigate the phase shift along the optical path. A phase shift occurs due to the path traveled by the light. If s is the optical path length and λ ($\lambda_0 = n\lambda$) is the wavelength in (outside) the cavity, respectively, the phase shift is

$$\Delta\phi_P = 2\pi \cdot \frac{s}{\lambda}. \tag{1}$$

Total internal reflection leads to a further phase shift for angles of incidence $\sin\chi > \frac{1}{n}$ and depends on the polarization (TM or TE with Brewster angle feature). This phase shift reads

$$\Delta\phi_{TIR} = 2\arctan\left(\kappa\frac{\sqrt{n^2\sin\chi - 1}}{\cos\chi}\right) \tag{2}$$

where $\kappa = n$ for TE or $\kappa = 1/n$ for TM polarization. The total phase shift is

$$\Delta\phi = \Delta\phi_P + \Delta\phi_{TIR}. \tag{3}$$

In the ray picture, the far or mid field can be calculated by continuing to trace refracted rays outside the resonator that are not captured by total internal reflection.

3 Results

If the phase shifts are collected along the ray trajectory, the phase information can be plotted versus the number of reflection points. In the case of a disk resonator, the angle of incidence is conserved and thus is the path length between two successive reflection points. Consequently the phase shift is constant.
However, if the disk geometry is deformed, e.g. a limaçon is used, neither the angle of incidence nor the path between the reflections points remains constant. In the event of a slight deformation, regular behavior is still possible. In Fig. 1 the phase information for the displayed trajectory in a limaçon with a small deformation parameter is shown. Due to the changes in the angle of incidence and the path between the reflection points, the phase information exhibits an interesting but still regular behavior. If the deformation parameter is increased further, the trajectory and the phase information becomes irregular, see Fig. 1 (c,d).
The trajectories' phase information can also be used to reconstruct the field distribution outside the cavity, Fig. 2.

Here, an additional light source was placed inside the cavity. For the optical limaçon cavity in Fig. 2 (a) the typical far field emission is seen in addition to the source contribution. For comparison, Dirac fermion optics is shown on the right for an single-layer graphene billiards with an effective index of refraction $n_{\text{eff}} = -1$ [4]. Here, the source induces a distinct lensing effect that can be associated with short paths and dominates the mid field emission.

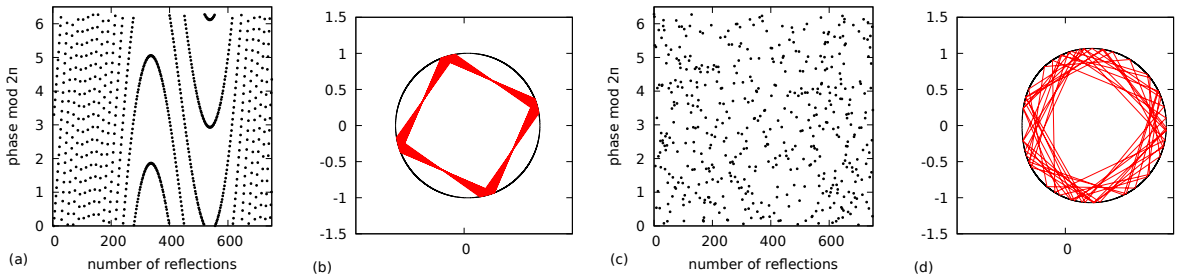

Figure 1: (a) Phase information with backfolding to $[0, 2\pi]$ for a regular trajectory (b) in a limaçon with small deformation parameter. Due to the slight change in the angle of incidence and the distance between the reflection points, the phase information changes as well. (c) Phase information for a irregular trajectory (d) in a limaçon.

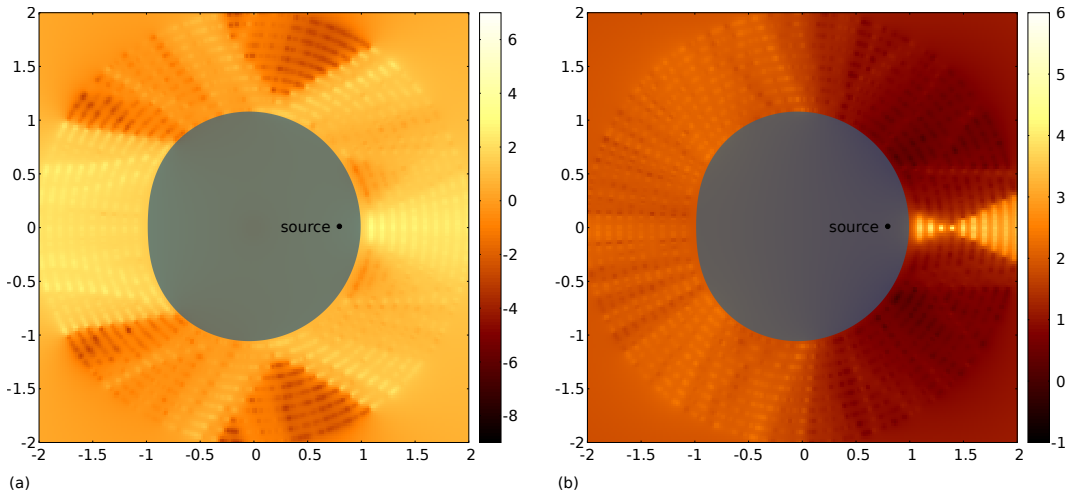

Figure 2: (a) Mid field region of a limaçon ($n = 3.3$) with an internal source. The rays are traced outside the limaçon and an intensity-weighted sum is formed in discrete bins. (b) Same as (a), but for Dirac fermions in graphene showing the mid field to be dominated by the lensing effect originating the source.

4 Summary and Outlook

The ray picture can be easily extended by the phase information to allow for modelling interference effects. In the future, this model will be used to study more complicated settings, such as resonators with different sources or arrays thereof. In comparison with FDTD calculations, the chances and limitations of this approach to ray-wave correspondence will be investigated.

References

[1] Kerry J. Vahala, "Optical microcavities", Nature (2003).
[2] Jens U. Nöckel, A. Douglas Stone, "Ray and wave chaos in asymmetric resonant optical cavities", Nature (1997).
[3] Martina Hentschel, Matthias Vojta, "Multiple beam interference in a quadrupolar glass fiber", Opt. Lett. (2001).
[4] Jule-Katharina Schrepfer, Szu-Chao Chen, Ming-Hao Liu, Klaus Richter, Martina Hentschel, "Dirac fermion optics and directed emission from single- and bilayer graphene cavities", Phys. Rev. B, 104, 155426 (2021).

FODON: Ultra-High-Radix Low-Loss Optical Switch Fabric

ZHIFEI WANG, ZHEHUI WANG, JIANG XU, XUANQI CHEN, JUN FENG, JIAXU ZHANG, SHIXI CHEN

Department of Electronic and Computer Engineering, The Hong Kong University of Science and Technology, Clear Water Bay, Kowloon, Hongkong, China

zhifei.wang@ust.hk

Abstract: To accomplish high-bandwidth low-latency high-efficient communications among hundreds of nodes, we propose FODON, a scalable integrated high-radix optical switch fabric. Analyses suggest FODON reduces numerous waveguide crossings and improves the scalability than other MIN-based fabrics.

1. Introduction

The rapid growth of web services, high-performance computing and big-data applications has resulted in an annual increase of ~30% in the amount of traffic in data centers [1]. The communications within data centers, mainly rack-level communications, contribute more than 75% of the total data center traffic [2]. Conventional electrical switches are currently facing challenges to meet the performance requirement under tight energy and thermal constraints [3]. Electronic switches typically boost the bandwidth by aggregating multiple pins to circumvent power-hungry high-speed electrical signals transmissions. This hinders the scale-up of electronic switches. Fortunately, the advancement of silicon photonics promises integrated optical switches to overcome the limitations of their electronic counterparts, and provide high-bandwidth, low-latency communications with high energy efficiency.

Crossbar is one of the most widely used space switch fabrics. A 32×32 PILOSS optical switch fabric based on the improved Crossbar structure has been demonstrated [4]. Apart from Crossbar, multistage indirect networks (MIN) topologies are also explored to switch optical signal, such as Baseline, Benes, Clos, Fat-tree, *etc*. However, on the worst-case path, signals have to pass a large number of switch elements in Crossbar-like switch fabrics or numerous waveguide crossings in MIN-based optical switch fabrics. Therefore, these integrated optical switch fabrics suffer from large loss, which limits the scalability of these fabrics. In this work, we propose FODON (Floorplan Optimized Delta Optical Networks), a scalable integrated high-radix optical switch fabric. By reducing the number of waveguide crossings, both the worst-case and the average loss of FODON are significantly reduced than other MIN-based optical switch fabrics, like Baseline, Benes, Fat-tree, etc.

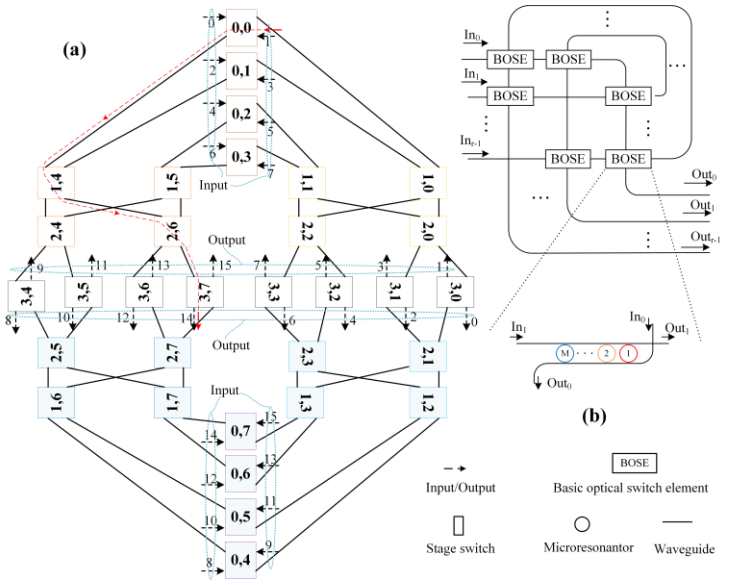

Fig. 1 (a) Floorplan of a 16-port FODON based on 2-radix stage switches. (b) Diagram of a stage switch based on the looped crossbar and the diagram of BOSE.

Algorithm 1 Routing algorithm of N-port FODON

Input: source s, destination d, stage switch radix r
Output: the path from s to d

$n \leftarrow \lceil \log_r N \rceil$ // calculate stage number
$bias \leftarrow 0$
$residual\_s \leftarrow s$
$residual\_d \leftarrow d$
for i = 0 to $n-1$ **do**
  $stage\_switch[i] \leftarrow residual\_s \,/\, r + bias$
  $in\_port[i] \leftarrow residual\_s \bmod r$
  $out\_port[i] \leftarrow residual\_d / r^{n-i-1}$
  $residual\_s \leftarrow residual\_s / r$
  $residual\_d \leftarrow residual\_d \bmod r^{n-i-1}$
  $bias = bias + out\_port[i] \times r^{n-i-2}$
end for
return $stage\_switch, in\_port, out\_port$ // can determine the path

2. Introduction

FODON is a MIN-based integrated optical switch fabric. The first and last stages are called input stage and output stage and they are located on the y-axis and x-axis on a plane, respectively. Other stages are located in the four

quadrants and the connection pattern between two adjacent stages is shuffle permutation. Fig. 1(a) depicts an example of the floorplan of a 16-port FODON based on 2-radix stage switches. In the figure, each rectangle denotes a 2-radix stage switch. The stage switches have various implementations. Basic optical switch elements (BOSEs), including microresonators (MRs) and Mach-Zehnder interferometers (MZIs), can be directly employed as the 2-radix stage switch, and a stage switch of more than radix 2 can be implemented as Crossbar, looped Crossbar [5], PILOSS [4], etc. Fig. 1(b) shows the stage switch based on looped Crossbar, within which an MR array is utilized as the BOSE to switching signals in multiple wavelength-division multiplexing (WDM) channels. The inputs and outputs can be implemented as grating couplers to couple in and out optical signals. In Fig. 1(a), the first number within the square denotes the index of stage and the second number denotes the index of stage switches in some certain stage.

The *N*-port FODON based on 2-radix stage switches can be treated abstractly as four *N*/4-port Baseline MINs located at four quadrants on a plane, and the input and output stages on y-axis and y-axis, respectively. By such a division, a significant number of waveguide crossings can be avoided, and thus the loss is considerably reduced compared to an *N*-port Baseline MIN. The number of waveguide crossings on the worst-case path in *N*-port FODON based on *r*-radix stage switches can be summarized as $r^n/4 - nr + n + r - 1$, where n is the number of stages. Algorithm 1 illustrates the routing algorithm of FODON, and the red dashed line in Fig. 1(a) shows an example of the path from port 1 to 14.

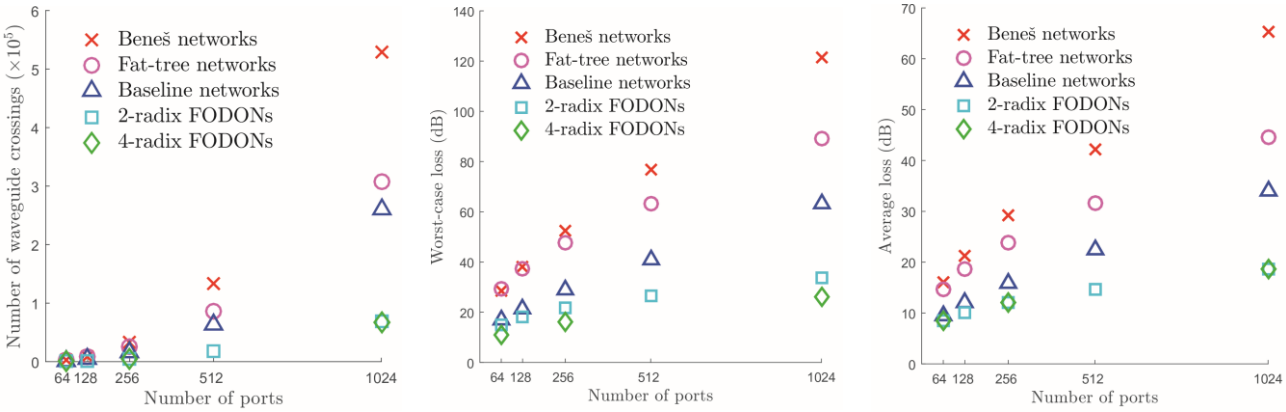

Fig. 2 The quantitative comparisons among 4-radix FODON, 2-radix FODON, Baseline MIN, Fat-tree and Benes in terms of number of waveguide crossings (left), worst-case loss (middle), average loss (right). *r*-radix FODON represents a FODON based on *r*-radix stage switches.

With the MR model based on the scattering matrix method, we obtain the insertion loss and passing loss of MR are around 2.25dB and 0.24dB for the case of 32 WDM channels. We assume the loss of a waveguide crossing is around 0.04dB [6]. Based on the developed the loss models of integrated optical switch fabrics, we analyze the worst-case loss and average loss of FODON, Baseline MIN, Fat-tree and Benes, and the results are shown in Fig. 2. The figure also presents the quantitative comparison regarding the number of waveguide crossings in these optical switch fabrics. One can note that the worst-case loss of 1024-port FODON based on 4-radix stage switches is around 26dB, around 95dB, 63dB and 37dB smaller than that of Benes, Fat-tree and Baseline MIN at the same scale, respectively. In addition, the number of waveguide crossings in the 1024-port FODON are reduced 74%, 78% and 87% compared to Benes, Fat-tree and Baseline MIN.

3. Summary

This work has presented FODON, a type of MIN-based optical switch fabrics. The floorplan and routing algorithm of *N*-port FODON have been discussed. With the developed models of the integrated optical switch fabrics, analyses show FODON reduces numerous waveguide crossings and thus significantly reduces both the worst-case and average loss than other MIN-based fabrics, making it promise to be an ultra-high-radix integrated optical switch fabric.

References

[1] Cisco System, Inc., "Cisco global cloud index: Forecast and methodology, 2016–2021," 2018.

[2] T. Benson, A. Akella, and D. A. Maltz, "Network Traffic Characteristics of Data Centers in the Wild," in *10th ACM SIGCOMM Conference on Internet Measurement*, New York, USA, 2010

[3] P. Yang *et al.*, "Inter/intra-chip optical interconnection network: opportunities, challenges, and implementations," in *2016 IEEE/ACM NOCS*

[4] K. Tanizawa *et al.*, "Silicon photonic 32 x 32 strictly-non-blocking blade switch and its full path characterization," in *2016 21st OECC held jointly with PS*

[5] Z. Wang *et al.*, "Low-Loss High-Radix Integrated Optical Switch Networks for Software-Defined Servers," *Journal of Lightwave Technology*, Sep. 2016.

[6] Y. Ma *et al.*, "Ultralow loss single layer submicron silicon waveguide crossing for SOI optical interconnect," *Optics Express*, Dec. 2013.

Dual Si_3N_4 microresonators for polarization entangled photon generation

KAIYI WU, QIANNI ZHANG AND ANDREW W. POON

Photonic Device Laboratory, Department of Electronic and Computer Engineering, The Hong Kong University of Science and Technology, Clear Water Bay, Kowloon, Hong Kong, China
eeawpoon@ust.hk

Abstract: We design and fabricate dual Si_3N_4 microring resonators for on-chip polarization entanglement generation. We demonstrate two-photon interference for the polarization-entangled photon pair source with visibility of > 60%.

1. Introduction

Polarization-entangled photon sources generated through nonlinear crystals (such as β-barium borate (BBO) and periodically poled lithium niobate (PPLN)) are widely adopted in quantum communications [1] and quantum teleportation [2]. Photonic integrated circuits offer excellent platforms for entangled photon sources and circuits, with the advantages of compactness, scalability, and stability upon proper control. Previous work demonstrated an on-chip polarization-entangled photon source using a silicon waveguide integrated with a polarization rotator in between [3]. In this paper, we report our idea of generating polarization entangled photons using dual Si_3N_4 microresonators supporting transverse-electric (TE) and transverse-magnetic (TM) polarizations respectively. By aligning the pump, signal and idler to the dual microrings, we demonstrate polarization-entangled photon pair generation with two-photon interference fringe.

2. Device Characterization

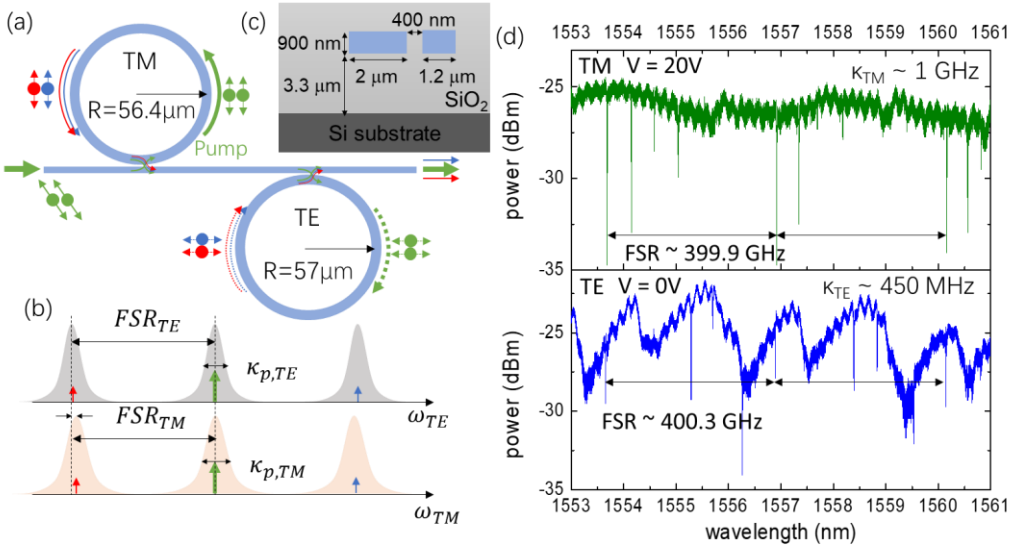

Fig. 1. (a) Schematic of dual microring resonators with slightly different radii supporting TM and TE polarizations respectively. (b) Schematic of the triple resonances alignment for the dual microrings, with a tolerance of misalignment within the resonance linewidth. (c) Cross-sectional view of the device under test. (d) Transmission spectra for the device measured at TM and TE polarizations.

Figure 1(a), (b) schematically illustrates our design. We adopt dual microrings with slightly different radii to achieve a similar free spectral range (FSR) for fundamental TE and TM modes supported by the two rings respectively. We launch the pump with diagonal (45 degree) polarizations, where half of the pump couples into the TM-ring while another half couples into the TE-ring. Spontaneous four-wave mixings occur inside the dual microrings and generating photon pairs. We measure the photon pairs one FSR away from the pump, whose polarizations are in the superposition between the TE and TM. Note that the two microrings can exhibit different photon-pair generation rate for our desire modes, we slightly adjust the pump polarization in order to obtain the same rate. We adopt microrings with a width of 2 μm and a height of 900 nm, as illustrated in Fig. 1(c).

We measure the transmission spectra of the waveguide-coupled dual microrings at either TE or TM polarizations, as shown in Fig. 1(d). The relative wavelengths are calibrated using a free space Mach-Zehnder interferometer with an

FSR of ~42.36 MHz [4]. The FSR is ~400.3 GHz for the TE-ring and ~399.9 GHz for the TM. The difference of ~400 MHz in FSR is within the resonance linewidth of ~1 GHz for TM-ring. To align the triple resonances, we apply ~235 mW electrical power on the TM-ring through an integrated Mo microheater on top of the microring.

We characterize the polarization entanglement through two-photon interference experiment. The experimental setup is illustrated in Fig. 2(a). We use a wavelength tunable laser and an erbium-doped fiber amplifier (EDFA) for the pump, with multiple stages of filters in the upstream to suppress the amplified spontaneous emission (ASE) noise. We use a polarization controller (PC) after the laser to adjust the input polarization. The wavelength of the tunable laser is locked to the cavity resonance by a simple power lock [4]. We adopt polarization-maintaining lensed fiber for input and output coupling. In the downstream, we first use a sets of four dense wavelength division multiplexing (DWDM) filters for pump rejection, followed by a de-multiplexer (DMUX) to separate the signal and idler photons. The polarization entanglement analysis (PEA) unit mainly consists of a half-wave plate (HWP) and a polarizing beam splitter (PBS) to serve as a polarizer. The PBS is tuned to either TE or TM polarizations and the PC in the PEA is tuned to align to the PBS polarization. While rotating the HWP with an angle φ, effectively the angle of the polarizer is rotated by 2φ. We use two superconducting nanowire photon detectors (SNSPDs) to detect the photon pairs, with a time-to-digital convertor to register the photon arrival time for coincidence measurement.

Two-photon interference are preformed when fixing the one of the polarizers at a certain angle, while rotating another polarizer. Fig. 2(b) shows our measurement results. Due to the quantum interference, we observe cosine square dependence as we fix the HWP at the idler arm while rotating the HWP at the signal arm. The quantum interference occurs when the two polarizers are not aligning to the polarization basics (eg. When the idler HWP is at 22.5 degree and 67.5 degree), which is different from the classical behavior. We obtain interference fringes with visibility of >60%.

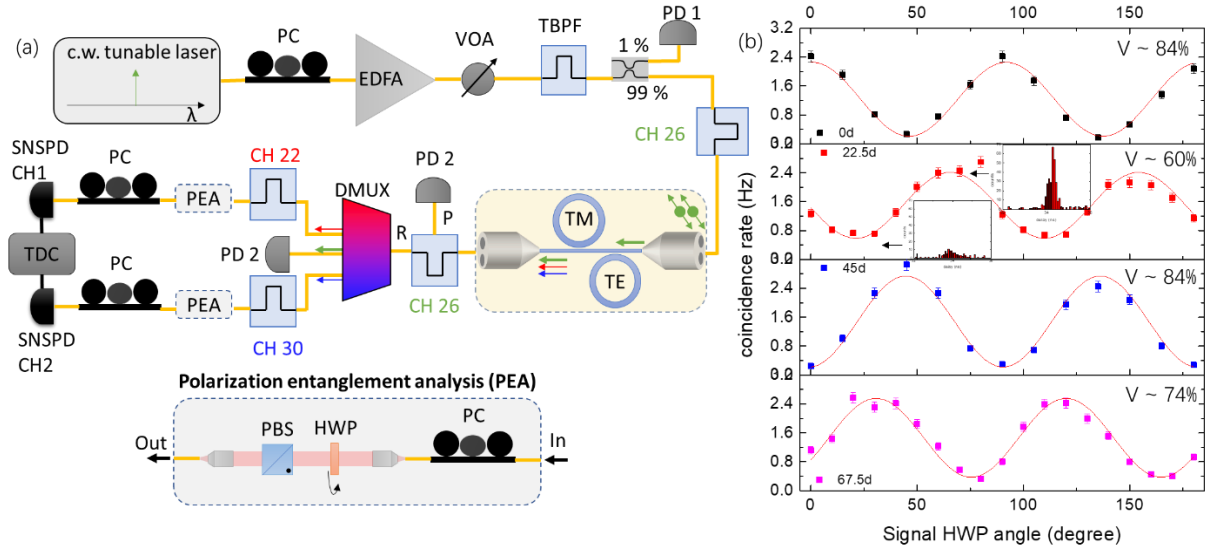

Fig. 2. (a) Experimental setup for characterizing two-photon interference of polarization-entangled photon source (b) Two-photon interference fringe obtain by fixing the HWP angle at the idler arm to 0 degree, 22.5 degree, 45 degree and 67.5 degree, while varying the HWP angle at the signal arm. Symbols are from measurement. Lines are fitting with Sine function. The insets show the coincidence spectra at the destructive and constructive interferences. TBPF: tunable band-pass filter, PD: photodiode, CH: channel, P: pass-port, R: reflection-port.

Acknowledgement

This work is supported by the Research Grants Council of the Hong Kong Special Administrative Region (HKSAR) under projects 16202615 and 16203317. We thank the Nanosystem Fabrication Facility (NFF) of the HKUST for device fabrication and helpful discussions.

References

[1] Z. S. Yuan, et al, "Entangled photons and quantum communication," Phys. Reports-review Sect. Phys. Lett. 497(1), 1–40 (2010).

[2] J. Yin, et al. "Quantum teleportation and entanglement distribution over 100-kilometre free-space channels," Nature 488(7410), 185–188 (2012).

[3] N. Matsuda, et al. A monolithically integrated polarization entangled photon pair source on a silicon chip. Sci Rep 2, 817 (2012).

[4] K. Wu, et al, "Integrated Si3N4 microresonator-based quantum light sources with high brightness using a subtractive wafer-scale platform," Opt. Express 29(16), 24750 (2021).

Second harmonic generation in a lithium tantalate microdisk resonator

XIONGSHUO YAN[1],YI'AN LIU[1], LICHENG GE[1], YUPING CHEN[1,2] AND XIANFENG CHEN[1,3]

[1]*State Key Laboratory of Advanced Optical Communication Systems and Networks, School of Physics and Astronomy, Shanghai Jiao Tong University, 800 Dongchuan Road, Shanghai 200240, China*

[2]*ypchen@sjtu.edu.cn*

[3]*xfchen@sjtu.edu.cn*

Abstract: Lithium tantalate (LT) is an important complementary material to lithium niobate (LN). Recently optical grade LT nano scale film has been developed. Here a high-quality factor (~ 10^5) LT microdisk resonator based on LT on insulator film was fabricated utilizing femtosecond laser direct writing assisted with focused ion beam. The LT film has higher optical damage threshold than LN while the resistance to ion etching is relatively poor. On-chip second harmonic generation was demonstrated in the fabricated device with the efficiency about $1.22 \times 10^{-6}/\mathrm{mW}$. This work may pave the way to hybrid integration of LN photonic chips.

1. Introduction

Ferroelectric oxide crystalline materials like LN and LT are becoming more and more important in the field of nonlinear optics and integrated optics for the large nonlinear index and light spectrum acceptance. LT crystal possesses higher optical damage threshold which implies that LT has more potential in high-power optical devices. In this way LT will become an important complimentary material to LN in optical integrated chips.

2. Experiment and results

2.1 Transmission spectrum of LT microdisk

The LT microdisk was fabricated by femtosecond laser direct writing assisted by focused ion beam milling[1]. To characterize the optical mode structure of the disk, a telecommunication band tunable laser was sent into a tapered fiber which was used to coupled light into and out of the disk. Fig.1 (a) shows the transmission spectrum between 1540 and 1550nm. The inset shows the optical image of the LT microdisk. Fig.1 (b) shows the Lorentzian fitting of the mode indicated by a red arrow in (a), exhibiting a quality (Q) factor about 2.01×10^5.

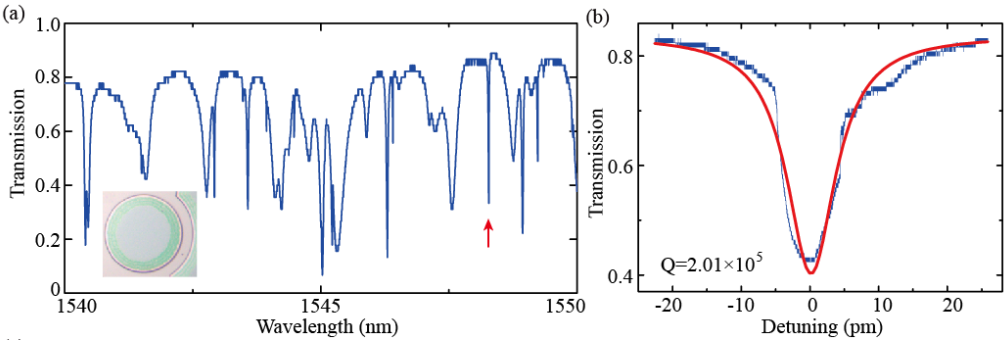

Fig. 1. (a) Transmission spectrum of a 55um diameter z cut LT microdisk. The inset is the optical microscope of the disk. (b) Lorentzian fitting of a measured mode indicated by a red arrow in (a), exhibiting a Q factor of 2.01×10^5.

2.2 Second harmonic generation (SHG) in LT microdisk

The nonlinear optical properties of LT disk are tested with larger pump intensities in LT microdisk. An erbium-ytterbium-doped fiber amplifier (EDFA) was used to amplify the seed laser. After EDFA the power of pump laser can be adjusted by a variable optical attenuator. Then the light was coupled into the microdisk through a tapered fiber. A 780/1550 wavelength division multiplex (WDM) was used to separate the fundamental and second harmonic waves. A spectrometer was used to detect second harmonic signal. Fig.2 (a) shows the signal centered at 770.48nm,

corresponding to a fundamental wavelength at about 1540.96nm. The inset shows the photomicrograph of the excited second harmonic light. Fig.2 (b) shows the relationship of SHG power and fundamental power, which is in good quadratic fitting. When the pump power is 6mW, the second harmonic power is measured to be 44.02nW, corresponding to the conversion efficiency about $1.22 \times 10^{-6}/\mathrm{mW}$.

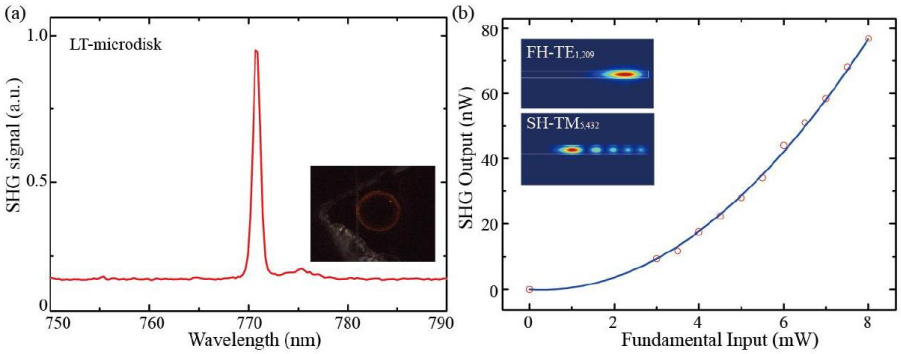

Fig. 2. (a) SHG signal of LT microdisk. The inset is the optical image of generated second harmonic. (b) Quadratic fitting of second harmonic power and input fundamental power. The inset shows the simulated mode distribution of fundamental and second harmonic modes.

Finite element analysis was carried out to further identify optical modes of fundamental harmonic (FH) and second harmonic (SH) waves. We find that the fundamental mode is $TE_{1.209}$ while the second harmonic mode is $TM_{5,432}$ as is shown in the inset in Fig.2 (b).

3. Summary

In conclusion we have fabricated LT microdisk utilizing femtosecond writhing assisted with focused ion beam milling. The Q factor of the disk can reach 10^5. SHG was observed in LT microdisk with the efficiency about $1.22 \times 10^{-6}/\mathrm{mW}$. It will be of great importance in hybrid integration of LN photonic chips especially for high-power devices.

References

1. Lin J, Xu Y, Fang Z, et al. Fabrication of high-Q lithium niobate microresonators using femtosecond laser micromachining[J]. Scientific reports, 2015, 5: 8072.
2. Yan X, Liu Y, Ge L, et al. Second harmonic generation in a lithium tantalate microdisk resonator, in preparation.

Plasmonic-cavity integrated graphene photodetector

DONGHAI ZHANG[1], XIN GAI[1]

[1]*Department of Electronic Engineering, City University of Hong Kong, Kowloon, Hong Kong, China*

zhangdh0920@gmail.com, xingai@cityu.edu.hk

Abstract: A plasmonic cavities integrated graphene photodetector is proposed and experimentally achieved for polarization detection and performance improvement.

1. Introduction

Polarization detection is a powerful tool to enhance the information recognition of objects, while photodetectors based on graphene are typically polarization insensitive. The plasmonic structure to confine subwavelength light and enhance localized field shows potential application in improving performance of 2D materials based optoelectronic and photonic devices.

2. Discussion and Summary

The plasmonic cavity enhances the photoresponse of transverse magnetic waves and restrains that of transverse electric waves, leading to a remarkable polarization extinction ratio as high as 30. In addition, for the selected polarization, the photoresponse is enhanced by more than one order of magnitude due to the enhanced localized field by plasmonic cavities. By adjusting the geometry of the metal stripe and the thickness of the insulator, the MIM structure could be pushed into the critical coupling status and the incident light at resonance could be fully trapped and absorbed.

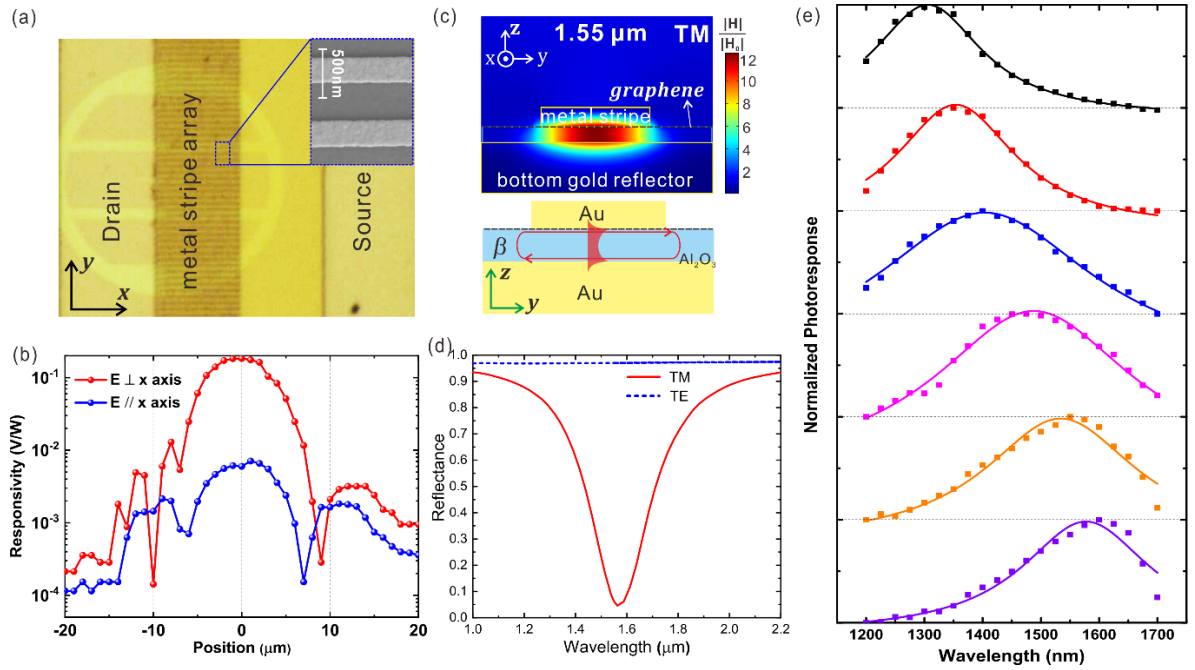

Fig. 1. (a) Plasmonic cavities integrated graphene phototransistor. (b) Scanning photoresponse mapping of graphene channel. (c) Magnetic field distribution of a plasmonic cavity and a sketch of the MIM structure. (d) Simulated reflectance spectra with the resonant wavelength of 1.55 μm. (e) Photoresponse spectra with different metal stripe widths.

References

[1] D. Zhang, J. Zhou, C. Liu et al, Enhanced polarization sensitivity by plasmonic-cavity in graphene phototransistors. J. Appl. Phys. (2019).

Photon Sources Generation in Silicon Nitride Whispering-gallery-mode Microring Resonators

QIANNI ZHANG[1], ANDREW POON[1*]

[1]Department of Electronic and Computer Engineering, The Hong Kong University of Science and Technology, Clear Water Bay, Kowloon, Hongkong, China

[*] eeawpoon@ece.ust.hk

Abstract: We demonstrate photon-pair and heralded-single-photon sources generation in dispersion-engineered, wide-width, whispering-gallery-mode (WGM) Si_3N_4 microring resonators. The measured wide-width microresonators exhibit an average quality(Q)-factor of ~1×10^6 without inner sidewall scattering.

1. Introduction

The quantum integrated circuits (QPICs) enable the implementation of both sources and quantum circuit in a compact footprint for developing large-scale quantum computing and information technology [1,2]. The nonlinear optical effects, such as spontaneous parametric down-conversion (SPDC) and spontaneous four-wave mixing (SFWM) processes, are main methods for on-chip photon source generation under room temperature [3,4]. Among the various material platform, silicon nitride shows a broad transparency window (0.25-8 μm) and gets rid of the two-photon absorption (TPA) loss at the 1.3/1.55μm telecommunication-wavelengths and the free-carrier absorption (FCA) loss. Si_3N_4 photonics with a low propagation loss and the complementary metal oxide semiconductor (CMOS-) compatible fabrication technologies seem promising for scalability and commercialization.

In this paper, we demonstrate photon-pair generation through SFWM process in Si_3N_4 microresonators. We adopt wide-width microring resonator with high quality (Q)-factor to enhance the weak spontaneous frequency conversion process under a lower pump power. We measure pair generation rate of TE-polarized photon pairs generated from a waveguide-coupled, wide-width microring resonator with the loaded Q-factor of ~ 1.2×10^6. We also measure the cross-correlation of signal and idler photons and second order coherence $g^{(2)}(0)$ to characterize the heralded single photon sources.

2. Results

2.1 Device design

Fig.1 (a) illustrates the schematic structure of devices. We design a 115μm-radius waveguide-coupled microring with a width of 8 μm supporting several low-radial-order WGMs. The stimulated mode-field distribution, shown as Fig 1(b), is along the outer sidewall of waveguides avoiding the scattering loss from inner sidewall and leading to a higher Q factor. We use a finite difference eigenmode (FDE) solver to stimulate the film-thickness dependence of the dispersion. With a film thickness larger than 825 nm, we can obtain the zero-dispersion-wavelength (ZDWL) located around 1550 nm. We fabricate this thick-film Si_3N_4 layer by pre-etched stress-release-pattern at under-cladding oxide layer. The stress-release patterns help release the stress generated during Low Pressure Chemical Vapor Deposition (LPCVD) by introducing periodic disturbance.

2.2 Quantum measurements

We pump the device with a continuous wave (c.w.) laser at ~1556.7 nm. We measure the pump-power dependence of both the single-channel count rate and the coincidence count rate between signal and idler channel. The measured count rates include the SFWM-generated photon pairs following a quadratic dependence with respect to the pump power, the noise counts contribute to the linear noise term and the SNSPD dark count that independence on the pump power. We can obtain the photon pair generation rate by extracting the quadratic terms from the power dependence of single photon count rate and the coincidence count rate. The measured single photon count rate and coincidence count rate are illustrated in Fig. (c-d) under an on-chip power of 0.2~1.3 mW (below optical parametric oscillator threshold). The calculated pair generation rate (R) is ~181 kHz/mW^2. Fig 1 (e) exhibit the cross correlation of photon pairs with a $g_{si}^{(2)}(0)$ of ~258 upon pump power of ~2 mW.

We measure the heralded single photon with a Hanbury Brown–Twiss setup. We separate the photon pairs in spectral domain and employ idler photons as the heralding photon. We use one channel of superconducting nanowire single photon detectors (SNSPD) as a trigger to indicate the photon-pair arriving time. We use a single photon avalanche detector and one channel of SNSPD to detect the photon at two signal-photon arms after 50:50 beam splitter. We

adopt a Time Digital Convertor (TDC) to record the fire time of three detectors. The three-fold coincidence count is rare and ideally only comes from the dark count noise of detector. The measured $g_H^{(2)}(0)$ is ~ 0.018 with a 14.58ns system delay time between two signal arms as shown in Fig. 1 (f).

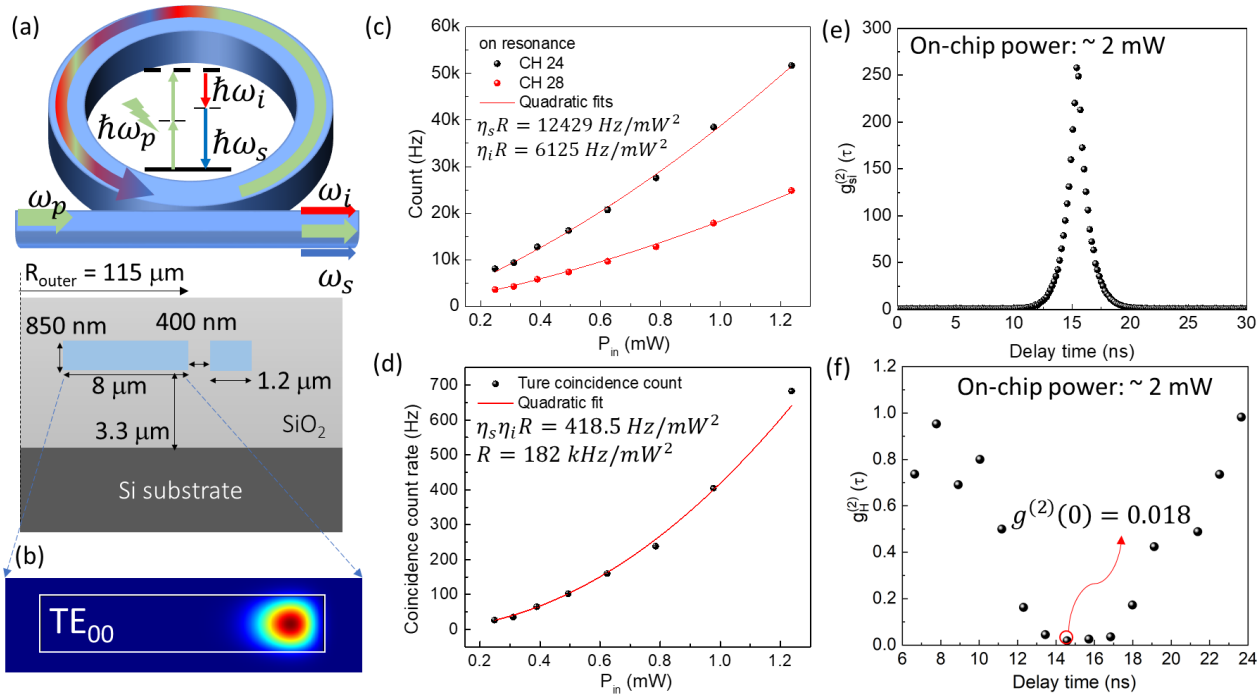

Fig. 1 (a) Schematic illustrations of the single-waveguide coupled, wide-width microring resonator and the cross-section of coupling region, (b) stimulated fundamental-TE-mode filed amplitude distribution in microring waveguide, the power dependence of (c) single count rate and (d) coincidence count rate with the corresponding quadratic fitting curves, (e) the cross correlation of signal and idler photons upon an on-chip power of ~2 mW, (f) the second order coherence function measurement for heralded single photon.

3. Summary

We characterize the TE-polarized photon-pair generation from wide-width WGM microring resonators in C-band. The extracted pair generation rate is ~181 kHz/mW^2 with a cross-correlation $g_{si}^{(2)}(0)$ of ~258. The measured $g_H^{(2)}(0)$ of heralded single photon is ~ 0.057.

References

1. D. Llewellyn, Y. Ding, I. I. Faruque, S. Paesani, D. Bacco, R. Santagati, Y.-J. Qian, Y. Li, Y.-F. Xiao, M. Huber, M. Malik, G. F. Sinclair, X. Zhou, K. Rottwitt, J. L. O'Brien, J. G. Rarity, Q. Gong, L. K. Oxenlowe, J. Wang, and M. G. Thompson, Chip-to-chip quantum teleportation and multiphoton entanglement in silicon, Nat. Phys. 16, 148 (2019).
2. G. Moody, L. Chang, T. J. Steiner, and J. E. Bowers, Chip scale nonlinear photonics for quantum light generation, AVS Quantum Sci. 2, 041702 (2020).
3. C. Joshua E., et al. "Time-energy Entangled Photon Pairs Generated via SFWM in an AlGaAsOI Ring Resonator." Optical Fiber Communication Conference. Optical Society of America, (2021).
4. O. Slattery, L. Ma, K. Zong, X. Tang, "Background and review of cavity-enhanced spontaneous parametric down-conversion." Journal of Research of the National Institute of Standards and Technology, 124, 1-18 (2019).
5. Kaiyi Wu, Qianni Zhang, and Andrew W. Poon. "Integrated Si_3N_4 microresonator-based quantum light sources with high brightness using a subtractive wafer-scale platform." Optics Express 29.16 (2021): 24750-24764.

Cavity Enhancement of Four-wave Mixing in a Silicon Racetrack Resonator

YAOJING ZHANG, WEN ZHOU, DAN YI, ZUNYUE ZHANG, YEYU TONG, RAKESH RANJAN KUMAR, YI WANG AND HON KI TSANG

Department of Electronic Engineering, The Chinese University of Hong Kong, Shatin, New Territories, Hong Kong
hktsang@ee.cuhk.edu.hk

Abstract: We experimentally demonstrated efficient four-wave mixing in a cavity structure: a silicon racetrack resonator. Carefully adjusting both pump and signal into resonances, we observed the change on the number of orders of four-wave mixing.

1. Introduction

Third-order optical nonlinearities of silicon have been widely studied in silicon-on-insulator (SOI) wafers. Four-wave mixing (FWM) as one of the third-order optical nonlinearities has applications in optical time lens [1] and all optical signal regeneration [2]. Cavity structures due to the advantage in build-up of light intensities have been extensively used in the study of FWM with low power and small footprint [3]. Recently we experimentally observed efficient FWM in a silicon racetrack resonator with multiple orders of FWM [4] despite the resonator's normal group-velocity dispersion. Here we present some further experimental results showing that the fine tuning of both pump and signal can have large effects on the number of orders of FWM produced.

2. Structure and Measurement

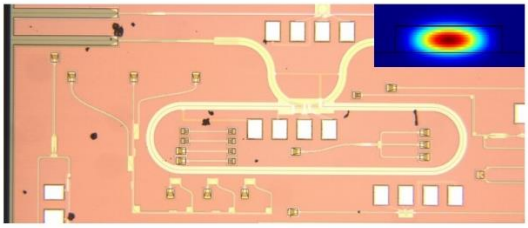

Fig. 1. Structure of the fabricated silicon racetrack resonator and the simulated transverse electric (TE)-like mode.

The silicon racetrack resonator used in the experiment is shown in Fig. 1, which was fabricated on a 220-nm SOI wafer by *IMEC INT*. The height and width of the resonator were designed as 220 nm and 2 μm, respectively. The bend radius of the racetrack is 130 μm. The length of the straight waveguide of the racetrack is 1000 μm. A symmetric lateral PIN diode of the waveguide was used to deplete the free carriers generated by two-photon absorption. Two edge couplers and lens fibers were used to couple light in and out of waveguide which offer large bandwidth. The total loss of the resonator was measured as -12 dB.

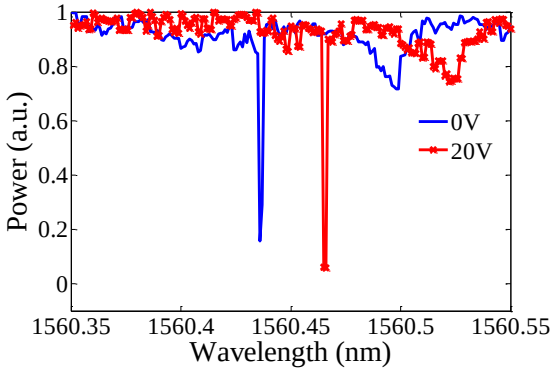

Fig. 2. Measured transmission spectra of the resonator with bias voltage of 0 V and 20 V.

We first measured the I-V curve of the resonator. When we applied bias voltage of 20 V, the current was obtained as -15 nA. Therefore, we chose 20 V as the bias voltage to apply onto the resonator. Then we experimentally scanned

a tunable laser and obtained the transmission spectra of the resonator as shown in Fig. 2. Applied with bias voltage of 20 V, same resonance of the resonator shifts to longer wavelength compared to that with bias voltage of 0 V, due to the change of free carriers with higher bias voltage.

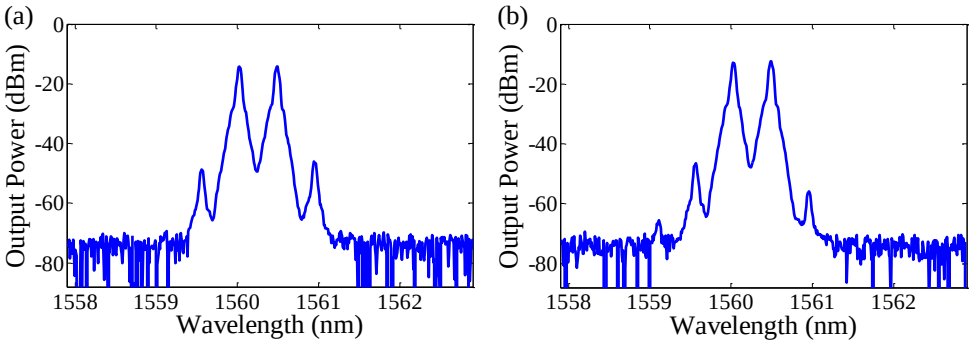

Fig. 3. The process of generated cascaded four-wave mixing with carefully tuning both lights into resonances.

Next, we experimentally demonstrated FWM in the resonator. We used two tunable lasers as light sources. Two polarization controllers adjust the polarizations of the two lights which were combined with a 3-dB fiber coupler as the input of the resonator. An optical spectrum analyzer (OSA) was used to record the output spectrum from the resonator. Fig. 3 shows the observed FMW from the OSA. Carefully tuning the two lights into two resonances, we observed additional idler comparing Fig. 3(a) and Fig. 3(b). The coupled pump power used in the measurement was 0.12 mW. For the resonator, we have not yet done anything about dispersion engineering. The simulated group-velocity dispersion (GVD) of the resonator is shown in Fig. 4 and the resonator has normal GVD at wavelength of 1560 nm. Previous literature showed that anomalous GVD has higher efficient FWM [5].

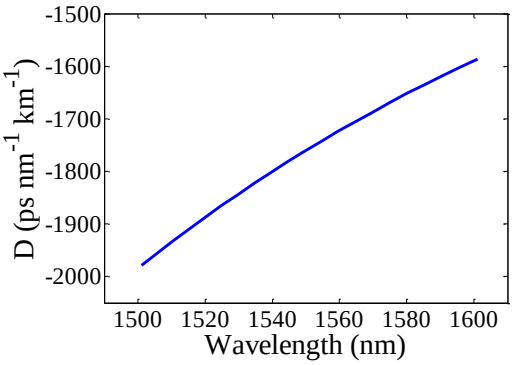

Fig. 4. Simulated GVD of the silicon racetrack resonator.

3. Summary

Taking advantage of build-up of light intensities in a cavity, we experimentally demonstrated efficient FWM in a silicon racetrack resonator with coupled pump power of 0.12 mW, even though the resonator has normal GVD. Experimentally results indicated that tuning both pump and signal into resonances enabled the increased number of idlers which is the base of cascaded FWM and further for the optical comb generation.

The authors would like to thank IMEC for device fabrication and funding support from RGC grant 14207314. The authors would like to thank Yuchen Zhang from Nankai university for the help of experiment. Yaojing Zhang and Wen Zhou would like to thank the support from the Postdoctoral Hub-Innovation and Technology Fund (PH-ITF).

References

1. R. Salem, M. A. Foster, A. C. Turner, D. F. Geraghty, M. Lipson, and A. L. Gaeta, "Optical time lens based on four-wave mixing on a silicon chip," Opt. Lett. **33**, 1047-1049 (2008).
2. R. Salem, M. A. Foster, A. C. Turner, D. F. Geraghty, M. Lipson, and A. L. Gaeta, "Signal regeneration using low-power four-wave mixing on silicon chip," Nat. Photonics **2**, 35 (2008).
3. A. C. Turner, M. A. Foster, A. L. Gaeta, and M. Lipson, "Ultra-low power parametric frequency conversion in a silicon microring resonator," Opt. Express **16**, 4881-4887 (2008).
4. Y. Zhang, W. Zhou, D. Yi, Z. Zhang, Y. Tong, R. R. Kumar, Y. Wang and H. K. Tsang, " Highly efficient cascaded four-wave mixing in a silicon racetrack resonator," in Asia Communications and Photonics Conference (2019). (under review)
5. M. A. Foster, A. C. Turner, J. E. Sharping, B. S. Schmidt, M. Lipson, and A. L. Gaeta, "Broad-band optical parametric gain on a silicon photonic chip," Nature **441**, 960 (2006).

High Resolution Spectrometer Using Arrayed Waveguide Gratings with Micro-ring Resonators

ZUNYUE ZHANG AND HON KI TSANG[1]

[1]*Department of Electronic Engineering, The Chinese University of Hong Kong, Shatin, NT., Hong Kong, China*
[1]*hktsang@ee.cuhk.edu.hk*

Abstract: We analyze and measure the performance of a high-resolution spectrometer formed by integrating micro ring resonators (MRR) with arrayed waveguide gratings (AWG). The two MRRs and two identical AWGs operating with center wavelength around 850 nm have 0.75 nm spectral resolution and 60 nm operating bandwidth.

1. Introduction

Broadband high-resolution spectrometers are desired in bio-sensing and bio-imaging systems, such as the spectral domain optical coherence tomography (SD-OCT) system [1]. While to combine the high spectral resolution and broad operating bandwidth in a single spectrometer is very challenging as the large number of channels will not only consume large chip areas but also induce more loss and degrade the performance of the spectrometers. For example, in the most commonly used dispersive device, AWG, the footprint increases nonlinearly with the number of channels. Even if the chip area can be reduced by a tandem configuration of a high-resolution AWG with several low-resolution AWGs [2], the high-resolution primary-stage AWG is still challenging to implement because the high resolution would require relatively long optical path length which will increase the insertion loss and crosstalk from the accumulated large phase errors.

In this paper, we analyze the performance of combining MRRs with AWGs in tandem. Compared with high resolution AWG, the use of MRR occupies a much smaller chip area and can reduce the insertion loss and inter-channel crosstalk because of lower accumulated phase errors. An 80-channels spectrometer with double MRRs and two identical AWGs are demonstrated on silicon nitride platform at 850 nm center wavelength. The overall footprint is 1.4 * 1.1 mm^2.

2. Principle

The principle of the tandem MRR-AWG spectrometer is illustrated in Fig.1 (a). The four port MRRs are designed to have a uniform resonance wavelength shift, the shifted spacing determines the resolution of the whole spectrometer. The precise resonance wavelength shift can be obtained either by a single MRR with tunable thermal heater or by multiple identical MRRs under ion implantation and laser annealing process [3]. The dropped wavelengths from the MRR (shown in Fig. 1 (b)) are then sent to secondary-stage low-resolution AWG. To precisely separate the wavelengths from the primary-stage ring resonators, the channel spacing of the secondary-stage AWG is designed to match with the FSR of the MRR (shown in Fig. 1 (c)). In such a tandem integrated spectrometer, the bandwidth of the whole spectrometer is defined by the broadband AWG while the channel spacing is defined by the resonance wavelength shift spacing. Fig. 1 (d) shows the simulation spectrum of the integrated spectrometer with single MRR and an AWG. When the resonance wavelength of the MRR is tuned across the full FSR, the output spectrum will fill one channel of the AWG, which is shown in Fig.2 (a).

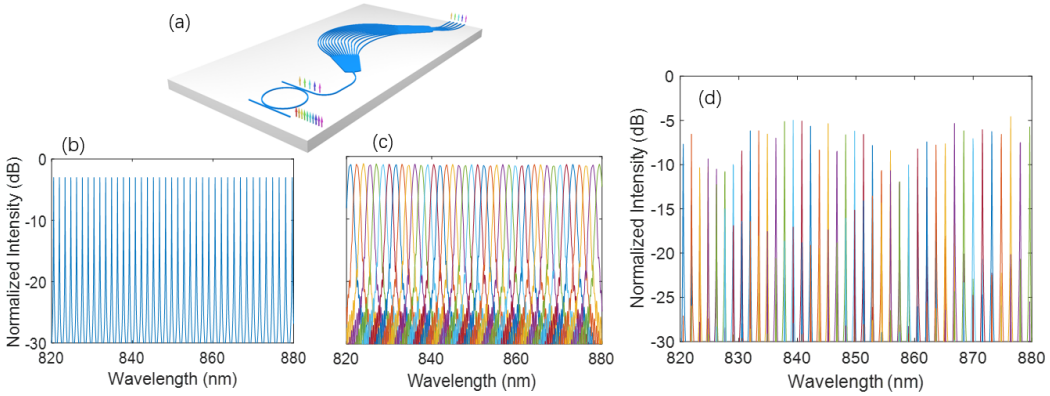

Fig. 1. (a) Principle illustration of the integrated spectrometer. (b) Normalized spectrum of the MRR (c) Normalized spectrum of 40-channel AWG (d) Normalized spectrum of the integrated spectrometer

3. Device design

As an initial demonstration of this tandem MRR-AWG spectrometer, we designed and fabricated a passive spectrometer with double MRRs connected with two identical 40-channel AWGs on silicon nitride platform at 850 nm central wavelength. Instead of using ion implantation and laser annealing process, we tune the resonance wavelengths of the MRRs by changing a small amount of waveguide width.

3.1 MRR design

We start the design of the four port MRRs by simulating the group index of the silicon nitride waveguides with Lumerical Mode Solutions. The radius of the MRRs are designed as 38 μm to make the FSR 1.5 nm. The waveguide width is changed by 4 nm to give a 0.75 nm resonance wavelength shift.

3.2 AWG design

A 40-channel AWG is designed with 149 arrayed waveguides in the array. The waveguide length increment is designed as 5.15 μm and the length of the free propagation region is designed as 418 μm to make the operating bandwidth 60 nm and channel spacing 1.5 nm, which matches with the FSR of the primary-stage MRRs.

4. Results and discussion

The device is fabricated on air/ silicon nitride/ silicon oxide/ silicon platform, the overall footprint is 1.4 * 1.1 mm^2. The spectrometer is tested with a superluminescent diode working at 850 nm central wavelength and optical spectrum analyzer. The normalized spectrum of the central 6 channels of the device is shown in Fig. 2 (b).

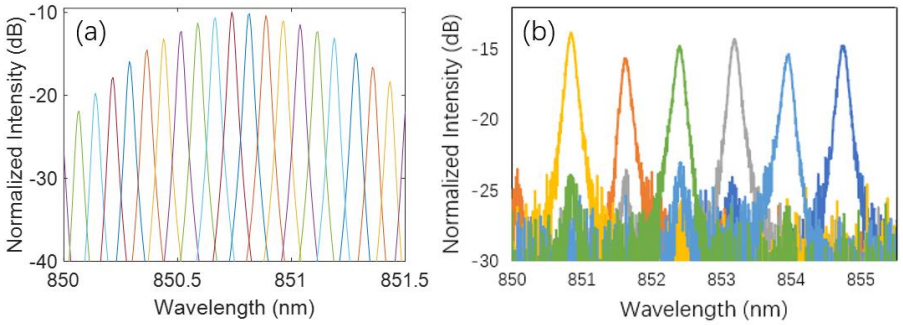

Fig. 2 (a) Normalized spectrum in single FSR of MRR. (b) Normalized spectrum of the tandem MRR-AWG spectrometer [4].

The experimental results show a channel spacing of 0.75 nm, which agrees well with the design. The crosstalk of the spectrometer is 10 dB, which is limited by the crosstalk of the AWG. With an optimized AWG design [5], the crosstalk level of the integrated spectrometer can be further reduced. An active tunable MRR will enable a more flexible and precise control of the spectral resolution of the spectrometer and laser trimming of the MRRs will make it possible for large-scale integrated spectrometers up to hundreds of channels.

5. Summary

We propose that by integrating MRRs with AWGs in tandem, a broadband and high-resolution spectrometer can be achieved with relatively small footprint. This tandem spectrometer was demonstrated with two MRRs and two identical AWGs on silicon nitride platform at 850 nm central wavelength. A 0.75 nm spectral resolution is obtained. This work shows a great potential for cost-effective integrated spectrometers with high spectral resolution and large operating bandwidth to be used in bio-imaging systems.

References

1. B. I. Akca, *et al*., “Toward Spectral-Domain Optical Coherence Tomography on a Chip,” IEEE J. Sel. Top. Quantum Electron (2012).
2. B. I. Akca, *et al*., "Advanced integrated spectrometer designs for miniaturized optical coherence tomography systems," Optical Coherence Tomography and Coherence Techniques VI, SPIE Proceedings (2013).
3. M. M. Milosevic, *et al*., "Ion Implantation in Silicon for Trimming the Operating Wavelength of Ring Resonators," IEEE Journal of Selected Topics in Quantum Electronics (2018).
4. Z. Zhang, *et al*., “High Resolution Silicon Nitride Spectrometer by integrating Micro-rings and Arrayed Waveguide Gratings in Tandem,” accepted by IEEE Group Four Photonics conference (2019).
5. Z. Zhang, *et al.* “Ultracompact 40-Channels Arrayed Waveguide Grating on Silicon Nitride Platform at 850nm,” European Conference on Integrated Optics (2019).